

# STINFO COPY

AFRL-PR-ED-TR-2006-0040

AFRL-PR-ED-TR-2006-0040

## Supercritical and Transcritical Shear Flows in Microgravity: Experiments and Direct Numerical Simulations

Dustin W. Davis  
Bruce Chehroudi

ERC, Inc.  
10 E. Saturn Blvd.  
Edwards AFB CA 93524-7680

Douglas G. Talley

AFRL/PRSA  
10 E. Saturn Blvd.  
Edwards AFB CA 93524-7680

Josette Bellan  
Nora Okong'o

Jet Propulsion Laboratory  
4800 Oak Grove Drive  
Pasadena, California 91109

August 2006  
Final Report

APPROVED FOR PUBLIC RELEASE; DISTRIBUTION UNLIMITED.



**AIR FORCE RESEARCH LABORATORY  
AIR FORCE MATERIEL COMMAND  
EDWARDS AIR FORCE BASE CA 93524-7048**

UNCLASSIFIED

# REPORT DOCUMENTATION PAGE

Form Approved  
OMB No. 0704-0188

Public reporting burden for this collection of information is estimated to average 1 hour per response, including the time for reviewing instructions, searching existing data sources, gathering and maintaining the data needed, and completing and reviewing this collection of information. Send comments regarding this burden estimate or any other aspect of this collection of information, including suggestions for reducing this burden to Department of Defense, Washington Headquarters Services, Directorate for Information Operations and Reports (0704-0188), 1215 Jefferson Davis Highway, Suite 1204, Arlington, VA 22202-4302. Respondents should be aware that notwithstanding any other provision of law, no person shall be subject to any penalty for failing to comply with a collection of information if it does not display a currently valid OMB control number. **PLEASE DO NOT RETURN YOUR FORM TO THE ABOVE ADDRESS.**

<b>1. REPORT DATE (DD-MM-YYYY)</b> 20-07-2006		<b>2. REPORT TYPE</b> Final Report		<b>3. DATES COVERED (From - To)</b> 10 Jun 2003 – 30 Sep 2006	
<b>4. TITLE AND SUBTITLE</b> <b>Supercritical and Transcritical Shear Flows in Microgravity: Experiments and Direct Numerical Simulations</b>				<b>5a. CONTRACT NUMBER</b> F04611-99-C-0025	
				<b>5b. GRANT NUMBER</b>	
				<b>5c. PROGRAM ELEMENT NUMBER</b> 00000	
<b>6. AUTHOR(S)</b> Dustin W. Davis and Bruce Chehroudi (ERC, Inc.);  Douglas G. Talley (AFRL/PRSA); Josette Bellan and Nora Okong'o (Jet Propulsion Laboratory)				<b>5d. PROJECT NUMBER</b> 1011001V	
				<b>5e. TASK NUMBER</b> NASA0315	
				<b>5f. WORK UNIT NUMBER</b> 549739	
<b>7. PERFORMING ORGANIZATION NAME(S) AND ADDRESS(ES)</b>  ERC, Inc. 10 E. Saturn Blvd. Edwards AFB CA 93524-7048				<b>8. PERFORMING ORGANIZATION REPORT NO.</b>	
<b>9. SPONSORING / MONITORING AGENCY NAME(S) AND ADDRESS(ES)</b>  Air Force Research Laboratory (AFMC) AFRL/PRSA 10 E. Saturn Blvd. Edwards AFB CA 93524-7048				<b>10. SPONSOR/MONITOR'S ACRONYM(S)</b>	
				<b>11. SPONSOR/MONITOR'S REPORT NUMBER(S)</b> <b>AFRL-PR-ED-TR-2006-0040</b>	
<b>12. DISTRIBUTION / AVAILABILITY STATEMENT</b> Approved for public release; distribution unlimited. Public Affairs Number AFRL-ERS-PAS-2006-284 (04 Dec 06).					
<b>13. SUPPLEMENTARY NOTES</b>					
<b>14. ABSTRACT</b> Experiments and direct numerical simulations (DNS) were conducted on shear layers at subcritical to supercritical pressures. The experiments were performed on single-component coaxial jets, where the slower inner flow was liquid nitrogen, the faster outer flow was cold gaseous nitrogen, and the environment was room temperature gaseous nitrogen. The experiments were performed with and without the effects of transverse acoustic waves. Careful attention was given to measuring all the initial and boundary conditions, including the initial jet temperatures. Automatic image processing allowed a large number of shadowgraph images to be processed, giving statistically significant measurements of the mean and root mean square (RMS) variations of the observed dark core lengths. It was found that acoustic waves could have an appreciable effect on the jets, causing them to develop wavy structures having mean core lengths that were always shorter than when the acoustic waves were not present. However, the magnitude of the effect depended strongly on the velocity ratio and on whether the jets were supercritical or subcritical. In particular, it was found that the jets were relatively insensitive to the acoustic waves at large outer-to-inner velocity ratios. It was postulated that this effect could explain the mechanism behind the temperature ramping method of assessing the combustion stability margin in liquid rocket engines. The numerical work consisted of assessing the suitability of existing numerical schemes for conducting DNS of supercritical shear layers obeying real fluid equations of state and characterized by steep density gradients, at Mach numbers as low as $10^{-5}$ . It was found that existing schemes could not be extended to Mach numbers having such a low value. Therefore it was decided to use DNS databases that were developed for higher Mach numbers (0.35) to better understand how to develop subgrid-scale models for large eddy simulations (LES) of such flows. Using an existing DNS database of supercritical binary-species temporal mixing layer simulations, explicit mathematical forms (i.e. models) for the small-scale fluxes and simplifying assumptions for the remaining filtered terms were assessed. Coefficients of proportionality calibrated on the DNS database yielded good quantitative agreement with the small-scale fluxes for two of the three types of mathematical forms; however, comparison among the several realizations in the DNS database revealed that, statistically speaking, the calibrated coefficients were not generally valid. Additionally, anticipating future detailed measurements of supercritical flows for model validation, a numerical criterion was developed to identify vortices in supercritical flows. Finally, in order to understand how such flows behave in microgravity, a drop tower experiment was designed. However, resources were not sufficient to allow the experiment to be fabricated. The design is nevertheless documented herein.					
<b>15. SUBJECT TERMS</b> liquid rocket engine; supercritical; shear layer; acoustics; direct numerical simulation; DNS; coaxial flow					
<b>16. SECURITY CLASSIFICATION OF:</b>			<b>17. LIMITATION OF ABSTRACT</b>	<b>18. NUMBER OF PAGES</b>	<b>19a. NAME OF RESPONSIBLE PERSON</b> Dr. Douglas G. Talley
<b>a. REPORT</b>	<b>b. ABSTRACT</b>	<b>c. THIS PAGE</b>			<b>19b. TELEPHONE NO</b> (include area code) N/A
<b>Unclassified</b>	<b>Unclassified</b>	<b>Unclassified</b>	A	314	

# STINFO COPY

## NOTICE

USING GOVERNMENT DRAWINGS, SPECIFICATIONS, OR OTHER DATA INCLUDED IN THIS DOCUMENT FOR ANY PURPOSE OTHER THAN GOVERNMENT PROCUREMENT DOES NOT IN ANY WAY OBLIGATE THE US GOVERNMENT. THE FACT THAT THE GOVERNMENT FORMULATED OR SUPPLIED THE DRAWINGS, SPECIFICATIONS, OR OTHER DATA DOES NOT LICENSE THE HOLDER OR ANY OTHER PERSON OR CORPORATION; OR CONVEY ANY RIGHTS OR PERMISSION TO MANUFACTURE, USE, OR SELL ANY PATENTED INVENTION THAT MAY RELATE TO THEM.

## FOREWORD

This special report, entitled "Supercritical and Transcritical Shear Flows in Microgravity: Experiments and Direct Numerical Simulations," presents the results of a research study performed under JON NASA0315 by ERC, Inc., AFRL/PRSA, and NASA Jet Propulsion Laboratory. The Project Manager for the Air Force Research Laboratory was Dr. Douglas G. Talley

This report has been reviewed and is approved for release and distribution in accordance with the distribution statement on the cover and on the SF Form 298.

                  //signed//                    
DOUGLAS G. TALLEY  
Project Manager

                  //signed//                    
INGRID J. WYSONG  
Chief  
Aerophysics Branch

                  //signed//                    
PHILIP A. KESSEL  
Technical Advisor  
Space & Missile Propulsion Division

This Page Intentionally Left Blank

## TABLE OF CONTENTS

<b>INTRODUCTION.....</b>	<b>1</b>
<b>EXPERIMENTAL SUMMARY.....</b>	<b>2</b>
<b>NUMERICAL SIMULATION SUMMARY .....</b>	<b>4</b>
<b>REFERENCES.....</b>	<b>6</b>
<b>APPENDIX A: High Pressure Windowed Research Vessel for Supercritical and Transcritical Laminar Nitrogen Jet Studies in Microgravity .....</b>	<b>A.1</b>
<b>APPENDIX B: On the Behavior of a Shear-Coaxial Jet, Spanning Sub- to Super-critical Pressures, with and Without an Externally-Imposed Transverse Acoustic Field (PhD Thesis).....</b>	<b>B.1</b>
<b>APPENDIX C .....</b>	<b>C.1</b>
<b><i>A Priori</i> Analysis of Subgrid-Scale Models for Large Eddy Simulations Of Supercritical Binary-Species Mixing Layers .....</b>	<b>C.2</b>
<b>Vortex Identification in High-Pressure Flows .....</b>	<b>C.17</b>

## GLOSSARY

ARB	ARB, Inc., Bakersfield, CA
ASME	American Society of Mechanical Engineers
DR	density ratio
DNS	direct numerical simulations
FEA	finite element analysis
LES	large-eddy simulations
MAWP	maximum average working pressure
PCC	Precision Components Corporation, York, PA
PE	professional engineer
RMS	root mean square

## INTRODUCTION

Presently, the direction of almost all power- and thrust-producing devices is to increase the operating chamber pressure. The rationale for this increase in chamber pressure is to create gains in efficiency and thrust output. As chamber pressure is increased, the fluids inside the injector or combustion chamber may no longer remain below the thermodynamic critical point and become supercritical. At pressures much lower than the critical pressure, the liquid breaks up into ligaments and drops, leading to spray combustion. The vast majority of what is currently understood about spray combustion applies to these conditions, where the gas-to-liquid density ratio (DR) is very small, in the range of 0.002 to 0.03. However, as the combustion chamber pressure increases, the DR becomes larger and can approach unity. A solid fundamental understanding of the processes that occur under supercritical conditions is limited.

The objective of this research was to determine the fluid physics governing transport and mixing in non-reacting transcritical and supercritical shear layers. A combined experimental and modeling approach was proposed wherein transport and mixing could be studied. The proposed experimental approach was to produce inertially dominated laminar jets of cryogenic nitrogen injected into room-temperature nitrogen in microgravity. The modeling approach considered here was to perform direct numerical simulations (DNS) of the experiments.

A drop tower experiment was designed to satisfy the objectives of the program. However, because of the complexities introduced by satisfying safety standards associated with performing drop tower experiments on pressure vessels with windows containing cryogenic fluids at high pressures, it was discovered that the cost of resources required to fabricate the experiment were prohibitive. Consequently, the objectives of the program were modified. On the experimental side, it was decided to expand on supercritical experimental studies already begun in an existing normal-gravity facility. Rather than try to produce inertially dominated shear flows in the absence of buoyancy in normal gravity, it was decided instead to study the interaction of subcritical and supercritical shear flows – specifically, shear-coaxial jets – with acoustic waves. This was motivated by a need to understand the physics behind combustion instabilities in liquid rocket engines.

Then, since experimental data was not going to be available for comparison with the model, and since adding acoustic capability to the model was beyond the scope of the resources available, the objectives of the modeling effort were modified as well. It was decided to (i) inquire into the numerical issues that occur in DNS of supercritical incompressible flows, such as in the experiment, as compared to equivalent large-eddy simulations (LES) in which the small turbulent scales are not computed as in DNS but instead are modeled; (ii) determine the behavior of the small turbulent scales that were resolved in DNS but modeled in LES; and (iii) explore what would be the quantity/quantities to measure in an ideal experiment to compare to the numerical solution to ensure that code validation is meaningful. Results from this research program are briefly summarized below. Reference is made to the considerable detail which may be found in the Appendices.

## EXPERIMENTAL SUMMARY

The initial task was to design a high-pressure experimental chamber to inject a laminar cryogenic jet while the entire test setup was released in the 2.2-sec NASA drop tower. NASA has very stringent safety requirements for chamber operation at pressures of interest to us (2000 psi). To ensure a safe design, an external firm was contracted to perform detailed design of the apparatus. All design calculations were performed by a professional engineer (PE) including a finite element analysis (FEA) of the structure. Details of the FEA analysis are reported in **Appendix A**. As stated in NASA Technical Memorandum 107090 [1], all components were designed to withstand four times maximum average working pressure (MAWP) – i.e., 8000 psig. Because of the rigid weight constraints, it was necessary to select a material that had a high strength-to-weight ratio to minimize chamber weight and yet not compromise safety. In addition to having a high strength-to-weight ratio, the alloy selected (Ti Grade 23) remains ductile at cryogenic temperatures of interest in this work [2]. Detailed machine shop drawings of the chamber – which includes the injection pump for the cryogenic nitrogen – have been completed, along with step-by-step details of the design equations and FEA analysis. These are given in Appendix A.

Two companies possessing an ASME Boiler and Pressure Vessel Code were contacted to fabricate the device. The ARB, Inc. Company (Bakersfield, CA) is capable of producing ASME Boiler and Pressure Vessel certified pressure vessels under Section VIII, Division I of the code. However, ARB stated that the apparatus discussed here was beyond the scope of Division I. Another company, Precision Components Corporation (PCC, York, PA), which is certified for Section VIII, Divisions I, II, and III, was able to fabricate an ASME-certified vessel under Division II, if the necessary material for the fabrication was approved by the ASME. However, Ti Grade 23 was not approved by ASME Section VIII, and our calculations showed that no other material could produce a low enough chamber weight to meet the weight limitation and produce meaningful scientific data. PCC also stated that it was capable of producing this chamber in an “ASME-like” manner, which would include following the ASME code, except for the material, but including testing of the final machined parts. The term “ASME-like” manner means that the guidelines followed for the manufacturing of the chamber are those recommended by the ASME codes and that the chamber is built by a machine shop possessing ASME Section VIII Division 1 or 2 code stamp, with the exception of the selected material. Considering that this chamber was intended to withstand four times the MAWP, that it had to be made from the highest strength-to-weight ratio titanium alloy to meet the weight limitation, and had internal dimensions less than the required values by the NASA Glenn Safety Manual, and that it had to be manufactured in an “ASME-like” manner, we consequently wrote a memo to NASA and requested reconsideration of the ASME Code Stamp requirement for this project.

More importantly, it was projected by PCC that the total cost of the “ASME-like” fabrication would be greater than \$100,000. This set a budgetary limitation, and was greater than our level of available funds at that time by at least \$50,000. NASA was approached for additional funding, which proved not to be available. Therefore, the experi-

mental work continued in an existing normal gravity facility, where the emphasis was changed to understanding the interaction between acoustic waves and shear-coaxial jets.

To gain a better understanding of some of the underlying physics associated with the interaction of high-amplitude acoustic waves with a coaxial-jet injector similar to those used in cryogenic liquid rockets, a non-reacting-flow experimental investigation was conducted under sub-, near-, and supercritical chamber pressures, with and without acoustical excitation. The flow from the inner jet of this coaxial injector was liquid nitrogen (or liquid-like, if at supercritical pressures), and cold gaseous nitrogen flowed from the outer annular jet, both injected into a chamber pressurized with nitrogen at room temperature. The jet was excited with a high-amplitude acoustic driver, with the jet located at a velocity anti-node (pressure node) of the established acoustic field. Past research on this subject has shown both the relevance and importance of geometrical changes in an injector's exit-area and its nearby physical and fluid mechanical processes. On this basis, special attention was paid to collecting spatially-resolved mean temperatures and documenting the aforementioned interactions at the exit of this injector. Short-duration and high-speed digital photography, at framing rates up to 18 kHz, provided information on the dynamic behavior of this jet under a variety of conditions. Mean and root mean square (RMS) values of the coaxial-jet dark-core length fluctuations were measured from the acquired images via a computer-automated method. The conclusions of this work are summarized below. Additional details may be found in References [3-9]. Reference [3] is reproduced in its entirety in **Appendix B**.

1. The existence of high-amplitude acoustic waves alters the behavior of the shear-coaxial jet. The resulting structure of the jet exhibits a periodic shape corresponding to the transverse-velocity field created by the acoustic waves. The periodic oscillations imposed on the dark core of the jet are predominately in the direction of the transverse acoustic velocity. No helical mode for the jet was observed.
2. The root mean square (RMS) variation of the dark-core length decreases with increasing outer-to-inner-jet velocity ratio at a given chamber pressure and asymptotically approaches a constant level. The RMS of the dark-core length is greatest at subcritical pressures. To the best of the authors' knowledge, this behavior has not previously been reported in the literature.
3. Previous research showed that an episode of so-called "temperature ramping," used for rocket combustion stability rating, could lead the engine to an unstable behavior. Also, from other work, it has been shown that coaxial injectors with high outer-to-inner jet velocity ratios (greater than  $\sim 10$  for LOX/H<sub>2</sub> engines) are more stable. In the current work, the observation that the RMS of the dark-core length fluctuations decreased at high velocity ratio, is considered to be a potential explanation for the temperature ramping effect. Reducing the hydrogen temperature increases its density and therefore reduces its velocity. It is possible that the increases in the RMS fluctuations that this causes enable a key feedback mechanism for the self-excitation process that drives combustion instability in liquid rocket engines. Ultimately, this hypothesis requires further testing in a multi-element, fired rocket experimental facility, for validation purposes.

4. The quantitative behavior of the dark-core length of the coaxial jet at near- and supercritical pressures follows a similar momentum flux ratio ( $M$ ) dependency reported for the single-phase shear-coaxial jets (i.e.,  $12M^{-0.5}$ ). The dark-core length for the subcritical chamber pressures, however, scales with  $M^{-0.2}$ .
5. Within a range of momentum flux ratios between 1 and 10, the dark-core lengths for the coaxial jet under the subcritical (two-phase) ambient pressure used here appear longer than those measured at the supercritical (single-phase) condition. This range represents relevant values for liquid rocket engines. The subcritical data reported herein was conducted in parameter ranges that have not been reported previously.

## NUMERICAL SIMULATION SUMMARY

The modeling and simulation tasks were as follows.

1. At the very low Mach number of the experiments, it was expected that the acoustic waves would have little impact on the flow phenomena of interest, and only flow developments on the scale of the flow velocity would need to be resolved. The goal was to obtain an algorithm where the time step is constrained by the flow velocity and not by the acoustic speed. Because we wished to perform computations at Mach number values of  $5 \times 10^{-5}$ , we first conducted an extensive literature search for low-Mach number algorithms, either applicable to or that could be adapted to, the present study. As a result, we implemented a variety of low-Mach number schemes. The low-Mach number schemes that were considered included computing the pressure implicitly [10, 11], and preconditioning with pseudo-time integration [12]; these schemes involved modifying the numerical scheme while retaining the original governing equations. Our studies determined that neither approach was successful in the supercritical setting where real-gas equations of state must be used, and where we knew that there were regions of high-density-gradient magnitude which must be solved in DNS. In contrast, no such requirement is imposed on LES, which use presumed submodels; in LES pre-conditioning techniques are possible.

Therefore we explored an alternative approach based on low Mach number asymptotics [13, 14]. The goal was to modify the governing equations of the compressible formulation to eliminate the acoustic waves while incorporating physically reasonable assumptions to allow the governing equations to be solved with larger physical time steps than those possible for the original governing equations. This is the advantage of the low-Mach-number asymptotics, which we formally derived: the modified governing equations (“low-Mach-number formulation”) can be solved at larger time-steps than required by the original equations. The scheme derived solves the original governing equations (“compressible formulation”), by integrating different variables, in a numerically stable manner at low Mach numbers. Whereas the assumptions used to derive the low-Mach-number formulation from the compressible formulation were verified to be reasonable based on simulations using the compressible formulation, the low-Mach-number formulation did not yield physically consistent results with the

compressible formulation. The lack of agreement was attributed to failure of the low-Mach-number formulation to properly represent the pressure field. Therefore at this juncture, it appears that the low-Mach-number approach is not feasible for this problem, and such calculations should proceed with the compressible formulation. Because for all low-Mach-simulations it was observed that the results at the lowest reasonable Mach number for the compressible formulation (0.05) were very similar to those at the target experimental Mach number ( $5 \times 10^{-5}$ ), except for the pressure field which scales as Mach number squared, the indications are that the Mach=0.05 results will be generally applicable to the lower Mach numbers. The success of these studies was to show that existing numerical methodologies for LES are not applicable to DNS for high-pressure incompressible flows. Since the LES equations are obtained from filtering the DNS equations, thereafter making modeling assumptions neglecting several terms obtained through the filtering of the DNS equations, and then hypothesizing the mathematical form of the small-scale fluxes, it is appropriate to question the validity of the LES approximations made so far in the literature, particularly because the corresponding DNS results for incompressible flows are not yet available for comparison. With the future advent of numerical techniques applicable to high-pressure, incompressible flow DNS, comparisons between experimental results and simulations will be performed, at which point the issue of LES fidelity compared to DNS may be revisited.

2. To understand the characteristics of supercritical flows, with focus on the differences between DNS and LES discussed above, a study was conducted examining the small-scale features of such flows from DNS. Using an existing DNS database of supercritical binary-species temporal mixing layer simulations, explicit mathematical forms (i.e. models) for the small-scale fluxes and simplifying assumptions for the remaining filtered terms were assessed. Coefficients of proportionality calibrated on the DNS database yielded good quantitative agreement with the small-scale fluxes for two of the three types of mathematical forms; however, comparison among the several realizations in the DNS database revealed that, statistically speaking, the calibrated coefficients were not generally valid. The study has been presented in detail in Reference [15]. This shows the complexity of the small turbulent scales behavior that is different under supercritical conditions from equivalent results obtained under subcritical conditions [16]. Additionally, the implication is that the coefficients cannot be considered constant during LES calculations.
3. In the goal of future objective comparisons between ideal experiments and simulations, we have focused on the necessary identification of vortical structures as a criterion for comparing experiments and simulations; this is a necessary but not sufficient condition for model validation. We have obtained a quantitative criterion to distinguish vortical structures in images, such as would be provided by ideal experiments, and showed that unlike other criteria proposed for incompressible low-pressure flows, the selected criterion can identify the coherent structures expected from high-pressure experiments. A manuscript has been submitted for Publication [17].

References [15 and 17] are reproduced in **Appendix C**.

## REFERENCES

1. Lekan, Jack; Gotti, Daniel J.; Jenkins, Andrew J.; Owens, Jay C.; Johnston, Michael R., *Users Guide for the 2.2 Second Drop Tower of the NASA Lewis Research Center*, NASA-TM-107090; E-9968; NAS 1.15:107090, 19960501; May 1996.
2. Salmon, D.R., *Low Temperature Data Handbook Titanium and Titanium Alloys*. 1979, National Physical Laboratory: Teddington England.
3. Davis, D. W., 2006. *On the Behavior of a Shear-Coaxial Jet, Spanning Sub- to Supercritical Pressures, with and Without an Externally-Imposed Transverse Acoustic Field*, PhD Thesis, Mechanical Engineering Department, The Pennsylvania State University, University Park, Pennsylvania. (**Attached as Appendix B**).
4. Chehroudi, B., Davis, D., and Talley, D., 2003. "Initial Results from A Cryogenic Coaxial Injector In An Acoustic Field," 41st AIAA Aerospace Science Meeting and Exhibit, AIAA 2003-1339, Reno, NV, January 6-9. DTIC ADA410882.
5. Davis, D. and Chehroudi, B., 2004. "The Effects of Pressure and Acoustic Field on a Cryogenic Coaxial Jet," 42<sup>nd</sup> AIAA Aerospace Sciences Meeting and Exhibit, Paper No. AIAA-2004-1330, Reno, Nevada, January 5-8. DTIC ADA419454.
6. Davis, D. and Chehroudi, B., 2005. "Measurements in an Acoustically-Driven Coaxial Jet under Supercritical Conditions," 43<sup>rd</sup> AIAA Aerospace Sciences Meeting and Exhibit, Paper No. AIAA-2005-0736, Reno, Nevada, January 10-13. DTIC ADA443865.
7. Davis, D. W., and Chehroudi, B., 2005. "Experiments on a Coaxial Injector Under Externally-Forced Acoustic Field." 53rd JANNAF Interagency Propulsion Committee Meeting, 2<sup>nd</sup> Liquid Propulsion, 1<sup>st</sup> Spacecraft Propulsion Subcommittee, Monterey, California, Dec. 5-8. (Recipient of LPS Best Student Paper Award). DTIC ADA445032.
8. Davis, D. W., and Chehroudi, B., 2006. "Shear-Coaxial Jets from a Rocket-Like Injector in a Transverse Acoustic Field at High Pressures." 44<sup>th</sup> AIAA Aerospace Sciences Meeting and Exhibit, Paper No. AIAA-2006-0758, Reno, Nevada, January 9-12. DTIC ADA445316.
9. Davis, D. W. and Chehroudi, B., 2005. "Measurements in an Acoustically-Driven Coaxial Jet under Supercritical Conditions," *AIAA J. of Propulsion and Power*. (submitted). DTIC ADA443865.
10. C. Wall, D. Pierce, and P. Moin. "A Semi-implicit Method for Resolution of Acoustic Waves in Low Mach Number Flows." *Journal of Computational Physics*, 181:545-563, 2002.
11. C.-C. Rossow. "Extension of a Compressible Code Towards the Incompressible Limit." AIAA Paper 2003-0432. 41st AIAA Aerospace Sciences Meeting and Exhibit, January 6-9, 2003, Reno NV.
12. I. Mary, P. Sagaut, and M. Deville. "An Algorithm for Low Mach Number Unsteady Flows." *Computers & Fluids*, 29:119-147, 2000
13. A.W. Cook and J.J. Riley. "Direct Numerical Simulation of a Turbulent Reactive Plume on a Parallel Computer." *Journal of Computational Physics*, 129:263-283, 1996.
14. F. Nicoud. "Conservative High-Order Finite Difference Schemes for Low-Mach Number Flows." *Journal of Computational Physics*, 158:71-97, 2000.

15. N. Okong'o and J. Bellan. "LES of Supercritical Temporal Mixing Layers: A Priori Analysis," paper AIAA-2005-0155, presented at the 43<sup>rd</sup> Aerospace Sciences Meeting and Exhibit, Reno, January 2005. **(Attached as Part 1 of Appendix C).**
16. N. Okong'o and J. Bellan. "Consistent Large Eddy Simulation of a Temporal Mixing Layer Laden with Evaporating Drops. Part 1: Direct Numerical Simulation, Formulation and *a priori* Analysis," *J. Fluid Mech.*, 499, 1-47, 2004
17. N. Okong'o and J. Bellan. "Vortex Identification in High-pressure Flows." Submitted to *Physics of Fluids*, 2005. **(Attached as Part 2 of Appendix C).**

This Page Intentionally Left Blank

# **APPENDIX A**

**High Pressure Windowed Research Vessel for  
Supercritical and Transcritical  
Laminar Nitrogen Jet Studies in Microgravity**

**Design Specifications and Statement of Work**

Prepared by:  
Dustin Davis, Bruce Chehroudi, and Doug Talley  
February 26, 2003

## Table of Contents

<b>1.</b>	<b>GENERAL REQUIREMENTS</b>	<b>3</b>
<b>2.</b>	<b>MAIN CHAMBER REQUIREMENTS</b>	<b>3</b>
<b>3.</b>	<b>INJECTOR ASSEMBLY REQUIREMENTS</b>	<b>5</b>
<b>4.</b>	<b>LN2 BATH AND FLUID DELIVERY SYSTEM REQUIREMENTS</b>	<b>6</b>
<b>5.</b>	<b>TEST ARTICLE INTEGRATION WITH NASA DROP FRAME</b>	<b>8</b>
<b>6.</b>	<b>WORK TO BE PERFORMED BY IES AND FINAL DELIVERABLES</b>	<b>8</b>
<b>7.</b>	<b>FIGURES</b>	<b>10</b>

A conceptual design is shown in Figure 1, and the nomenclature used in Figure 1 will be used through out this document, unless otherwise stated. The figures in this document are intended to clarify points made in the text, show the general function of the component, or show specifications that are not easily communicated with text alone, and are in no way meant to be the final design unless otherwise explicitly stated.

## **1. GENERAL REQUIREMENTS**

The general requirements are to ensure the safety of the personnel operating the apparatus and facility where the apparatus will be used, to ensure that the apparatus can be used in the 2.2 sec. Drop Tower at NASA GRC, and to specifically state a general operating requirement.

*1.1.* The entire apparatus will be designed to ASME Boiler and Pressure Vessel Code, whenever possible, and the intent of the code when not possible. In particular, a factor of safety of four (4) or greater shall used for all structural parts, except the windows where the factor of safety shall be six (6) or greater.

### *1.1.V. Verification Procedure*

Inspection: The final calculations, including a finite element analysis (FEA) will be inspected to verify the ASME Boiler and Pressure Vessel Code has been me, whenever possible, by IES and AFRL.

*1.2.* The requirements and guidelines in the NASA Tech. Memo 107090 and the NASA Glenn Safety Manual (located at: [http://microgravity.grc.nasa.gov/drop2/pdf/2.2\\_handbook.pdf](http://microgravity.grc.nasa.gov/drop2/pdf/2.2_handbook.pdf) and [http://osat-ext.grc.nasa.gov/gso/manual/chapter\\_index.shtml](http://osat-ext.grc.nasa.gov/gso/manual/chapter_index.shtml), respectively) shall be followed. In particular, the entire apparatus shall survive 2000 (apparatus life of 10 years assuming 200 drops per year), short duration (of the order 0.1 s), 30g impacts when the drop vehicle reaches the bottom of the drop tower.

*1.3.* The maximum weight of the apparatus, conceptually shown in Figure 1, shall be 115 lbs +3 lb/-115 lb. It is believed by AFRL that an alpha beta titanium alloy or beta titanium alloy will be the only choice to meet the requirements. However, the material is not specified

*1.4.* The apparatus shall be able to withstand a maximum ambient temperature of 322 K, and a minimum local temperature of 77 K.

*1.5.* Special consideration to shall be given to the large temperature gradient within the apparatus (77 K to 322 K).

*1.6.* IES shall work closely with AFRL throughout the design process to meet the end goal of designing the apparatus.

## **2. MAIN CHAMBER REQUIREMENTS**

The following requirements relate to the physical requirements and operation of the main chamber. These requirements are derived from the required end result of visu-

alization of supercritical and transcritical jet phenomena in a microgravity environment.

**2.1.** The maximum allowable working pressure (MAWP) of the main chamber shall be 2000 psig.

*2.1.V. Verification Procedure*

Analysis: The results of a FEA will be verified that the design meets specifications 1.1, 1.2, and 2.1.

**2.2.** The internal height of the main chamber shall be 7.00" +0.000" / -0.125", and the internal cross-section shall be circular (except where the windows prevent the contour from being circular) with a diameter of 6.00" +0.000" / -0.125", as shown in Figure 2.

**2.3.** The main chamber shall have a minimum of four (4) windows. The windows shall be oriented such that the distance radially from the axis of the chamber to the centerline of the window on the inner surface of the window is one half the diameter stated in specification 2.2. The angle between the centerline of a window, the axis of the chamber, and an adjacent window shall be  $90^\circ \pm 2^\circ$ .

**2.4.** The dimensions for the visible portion of the windows when assembled shall be a width of 1.50" +0.50"/-0.25" and a length (along the centerline) of 5.5" +0.50"/-0.00", and the radius at the top and bottom of the window opening shall be equal to one half the width.

**2.5.** The top of the window openings and associated window attachment devices shall be positioned such that the injector tip (Figure 1.) is 0.25"  $\pm$ 0.125" below the top of the visible portion of the window.

**2.6.** The windows shall be rectangular with a height of 5.75"  $\pm$ 0.5" and a width of 1.75"  $\pm$ 0.5". Physical property data of the sapphire and fused silica materials from Esco Products Inc. will be faxed to IES.

**2.7.** The window attachment mechanism shall be able to accommodate both fused silica (quartz) and Al<sub>2</sub>O<sub>3</sub> (sapphire). The estimated thickness of the quartz and sapphire windows is 1.5" and 0.5", respectively. Different flanges for the sapphire and quartz windows may be designed, if necessary to accommodate the different material thicknesses.

**2.8.** The windows shall seal on the face of the window with a leak rate such that the loss in pressure from the chamber is less than 1.0% of the chamber pressure over a five (5) minute period, while the apparatus is both at ambient temperature and in the completely chilled down state. It is desirable to have the sealing mechanism that consists of an external flange that bolts into position that holds the window in place. If weight becomes prohibitive, alternate methods for sealing the windows may be considered.

**2.9.** The windows shall have an elastomer o-ring or other suitable object that is located on the perimeter of the window to provide a cushion as to minimize breakage of the window when exposed to the 30 g deceleration at the bottom of the drop tower.

- 2.10. The main chamber shall have a minimum of six (6) 7/16"-20 ISO straight thread ports capable of accepting Swagelok fittings part number Ti-400-1-OR or similar part from another manufacturer, for filling, venting, measuring pressure, the pressure balance line, and two safety relief devices
- 2.11. The main chamber shall have one (1) 5/16"-24 ISO straight thread port (Figure 2), that will accept a fitting such as Swagelok part number Ti-100-1-OR or similar part from another manufacturer, so a thermocouple may be passed through to measure the temperature of the wall of the injector tubing at a location of 0.125"±0.063" from the injector tip.
- 2.12. The bottom plate shall have a hole that is 4.0" in diameter, with a flange that seals an insert such as the ones depicted in Figure 3. There shall be at least three types of inserts, a blank (Figure 3), one with nine (9) 5/16"-24 ISO straight thread ports, that will accept a fitting such as Swagelok part number Ti-100-1-OR or similar part from another manufacturer (Figure 3), and one that will have ports for hermetic thermocouple feed-through (not shown) to be determined.

### 3. INJECTOR ASSEMBLY REQUIREMENTS

The following requirements relate to the physical requirements and operation of the injector assembly. These requirements are derived from the required end result of visualization of supercritical and transcritical jet phenomena in a microgravity environment.

- 3.1. Part 3 in Figure 4 shall be 316 Stainless Steel (S.S.) 1/16" outside diameter (OD), 0.020" inside diameter (ID) with a minimum length of 5.0" such as obtainable from Supelco part# 5-6727 or similar from another supplier.
- 3.2. Part 4 in Figure 4 shall have the dimensions stated in Figure 4.
- 3.3. Part 4 in Figure 4 shall have a hole bored axially the entire length, such that part 3 in Figure 4 as described in specification 3.1, may pass through. An interference fit is not necessary, but the radial gap between parts 3 and 4 shall be minimized.
- 3.4. The top of part 4 in Figure 4 shall have a 5/16"-24 ISO straight thread port that will accept a fitting such as Swagelok part number Ti-100-1-OR bored through or similar part from another manufacturer to provide the seal between parts 3 and 4 and the main chamber.
- 3.5. Parts 4 and 5 in Figure 4 shall have a hole that shall be used in conjunction with the port described in specification 2.10 to pass a thermocouple through to measure the temperature on the wall of part 3 without violating specifications 2.1 and 3.6. Parts 4 and 5 shall be keyed so that alignment of the holes is easily accomplished.
- 3.6. Parts 5 and 6 shall be connected in some manner (such as welding) to produce a sealed cavity (labeled Cavity 1 in Figure 4) that is capable of holding a vacuum to a pressure of 1.0 psia.

- 3.7. Cavity 1 in Figure 4 shall have two (2) 5/16"-24 ISO straight thread ports, that will accept a fitting such as Swagelok part number Ti-100-1-OR or similar part from another manufacturer.
- 3.8. The annulus formed between parts 4 and 6 in Figure 4 shall be 0.25"+0.125"/-0.00", as shown in Figure 4, to allow for proper thermal conditioning of the injector. It is envisioned that part 4 will be held in place by a nut threaded onto the top of part 4 drawn tight against the shoulder of part 6. Regardless of the method of attachment, LN2 shall be able to enter the annulus region.
- 3.9. The region labeled "Cavity 2" in Figure 4 is part of the LN2 bath, and the MAWP shall be 400 psig, and a minimum temperature of 77 K. Note the bottom of the injector assembly is exposed to the main chamber, which has a MAWP of 2000 psig.

*3.9.V. Verification Procedure*

Analysis: The results of a FEA will be verified that the design meets specifications 2.1 and 3.9.

- 3.10. The o-ring seal, as indicated in Figure 4, shall be capable of sealing at ambient temperatures as high as 322K and at the completely chilled down conditions of 77K. The seal may be of some other method other than an o-ring if necessary. However, in either case the seal must not allow the LN2 bath pressure to rise at a rate of 1% of the pressure of the LN2 bath in a 5 minute period, by allowing the greater pressure chamber fluid to enter the bath through the seal.

#### **4. LN2 BATH AND FLUID DELIVERY SYSTEM REQUIREMENTS**

- 4.1. The LN2 bath, when assembled shall be one internal volume with a MAWP of 400 psig.

*4.1.V. Verification Procedure*

Analysis: The results of a FEA will be verified that the design meets specifications 3.9 and 4.1.

- 4.2. The internal volume of the LN2 bath shall be a minimum of 1.9L.
- 4.3. The internal cross-section of the LN2 bath shall be circular with a minimum diameter of 3.0". Note that in the envisioned LN2 bath the external cross-section of part 8 in Figure 5, which forms a portion of the LN2 bath, should be square such that part 9 in Figure 5 and part 6 in Figure 4 mate properly to seal the LN2 bath.
- 4.4. Parts similar in nature to parts 7 and 9 in Figure 5 shall be included to maximize access to the bath without disassembly. The accesses port where part 9 will mate shall be rectangular with dimensions of 3.0" by 5.0". The access port where part 7 attaches shall be circular and be 3.0" in diameter.
- 4.5. Part 7 in Figure 5 shall have hermetic feed through to be determined to provide power to the perturbation mechanism in Figure 1.

- 4.6.** The LN2 bath shall have seven (7) 5/16"-24 ISO straight thread ports, that will accept a fitting such as Swagelok part number Ti-100-1-OR or similar part from another manufacturer. Four (4) these ports may be located on part 9 Figure 5. One of the ports shall be located at 3.0"±1.5" in part 12 Figure 5 measured from the end of part 12 that mates with part 13 in Figure 5. The remaining two ports shall be located so that they may be used in conjunction with the ports specified in specification 4.7.
- 4.7.** The LN2 bath shall have two (2) 7/16"-20 ISO straight thread ports, that will accept a fitting such as Swagelok part number Ti-400-1-OR or similar part from another manufacturer for the installation of a safety relief valve and/or burst disk holder.
- 4.8.** Part 10 in figure 5, labeled "Injection Reservoir Housing" in Figure 1, shall have a minimum internal volume of 10 mL, with a circular cross-section of capable of allowing part 17 in Figure 5 labeled "Pump Rod" in Figure 1, as specified in specification 4.5, to traverse the designed length for the displacement of the fluid contained in the "Injection Reservoir" in Figure 1.
- 4.9.** The "pump rod seal" location in part 10 in Figure 5 shall be designed to accept a seal from the Bal Seal Company. The detailed seal drawings from Bal Seal will be faxed to IES The same seal may be used in Parts 13 and 15 in Figure 5. The leak rate from the "injection reservoir" through the "pump rod seal" shall be less than 4 µL/min at 77 K and 2000 psig.
- 4.10.** The outlet from part 10 in Figure 5 shall be a male 1/8" AN (AND 10056) with 5/16"-24 UNF-3A threads to accept 37° flared 1/8" tubing.
- 4.11.** Part 10 in Figure 5 shall have two (2) 7/16"-20 ISO straight thread ports, that will accept a fitting such as Swagelok part number Ti-400-1-OR or similar part from another manufacturer, which are located such that one may be used to fill the "injection reservoir" and the other may be used to measure temperature. The two ports shall be used in conjunction with the ports specified in specification 4.5.
- 4.12.** Part 14 in Figure 5 shall have two (2) 7/16"-20 ISO straight thread ports, that will accept a fitting such as Swagelok part number Ti-400-1-OR or similar part from another manufacturer, such that the "pressure balance line" (Figure 1) may be attached and a port to vent the opposite side of the "pressure balance piston" (Figure 1).
- 4.13.** Part 17 in Figure 5 labeled "Pump Rod" in Figure 1 shall have a diameter of 0.400" +0.000"/-0.001" over the portion of the length that pass into the "injection reservoir".
- 4.14.** The "Pressure Balance Piston" shown in Figure 1 shall be an integral part of the "pump rod". The dimensions of this piston shall be sized to produce a net force of 5 lbf ±5 lbf (neglecting friction) in the direction opposite to the motion of the "pump rod" when used in conjunction with the "pressure balance line" when the chamber is a MAWP.

#### 4.14.V. Verification Procedure

Analysis: Calculate the net force on the “pump rod” when the chamber is at MAWP with the dimensions from the drawing.

- 4.15. The “pump rod” (part 17 Figure 5) shall have 0.125” radius on the ends to allow for seal installation.
- 4.16. The end of the “pump rod” (part 17 Figure 5) that mates with the motor connection shall be such that it may be connected to the motor via the “pump to motor linkage” (Figure 6) without interfering with seal installation.

### 5. TEST ARTICLE INTEGRATION WITH NASA DROP FRAME

- 5.1. The maximum dimensions shall be less than the size of the drop frame (Figure 6 and [http://microgravity.grc.nasa.gov/drop2/pdf/rectang\\_drop\\_frame.pdf](http://microgravity.grc.nasa.gov/drop2/pdf/rectang_drop_frame.pdf) ) 38” long, 33” high, and 16” deep.
- 5.2. The bottom plate shall be elevated 3.5”  $\pm 0.5$ ” above the drop frame floor by “chamber stands” (Figure 6). The “chamber stands” shall bolt to the bottom plate of the main chamber and not interfere with the access to the fittings to be located on the flange assembly referred to in specification 2.11. The “chamber stands” shall bolt to the drop frame. The “chamber stands” may be made from an aluminum or titanium alloy. An example of chamber stands may be found at: [http://microgravity.grc.nasa.gov/drop2/photo\\_pages/124\\_m.htm](http://microgravity.grc.nasa.gov/drop2/photo_pages/124_m.htm)
- 5.3. The chamber shall be supported such that it will be able to withstand the 30g impact. Envisioned “chamber support locations” are shown in Figure 6. However, it is impossible to determine at this time to determine the exact dimensions for the supports, because of the variability of the other components to be located on the drop rig. The locations and the required load bearing capability of each of the supports shall be determined by IES.
- 5.4. The “pump to motor linkage” (Figure 6) shall be such that it connects the motor (to be determined) to the “pump rod” with a deflection of less than 0.001” when the motor is operated at a velocity of 0.1 mm/s under the MAWP of the chamber.

### 6. WORK TO BE PERFORMED BY IES AND FINAL DELIVERABLES

- 6.1. A FEA of the main chamber, window assembly, and any other critical components shall be performed.
- 6.2. A report of the final design calculations shall be given to AFRL.
- 6.3. Machine shop drawings of the final design conforming to ASME Y14.5M-1994 in both print and electronic format shall be given to AFRL.
- 6.4. Determine if non-destructive testing of the Ti alloy stock is necessary prior to fabrication.

7. FIGURES

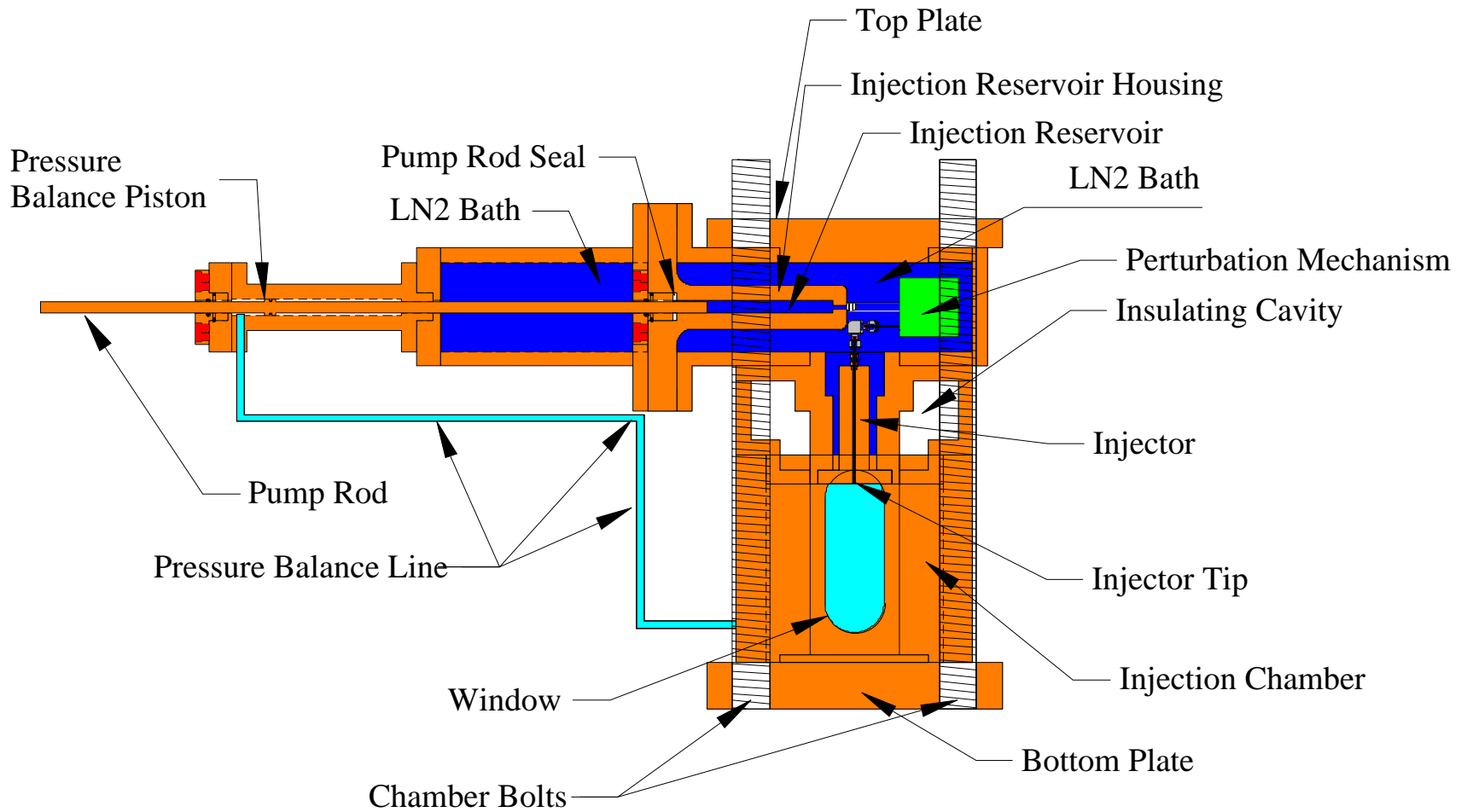


Figure 1. Baseline conceptual design of injection chamber; orange is titanium, blue is liquid nitrogen (LN2), light blue is gaseous nitrogen (GN2), red is bolt locations, and green is the perturbation mechanism.

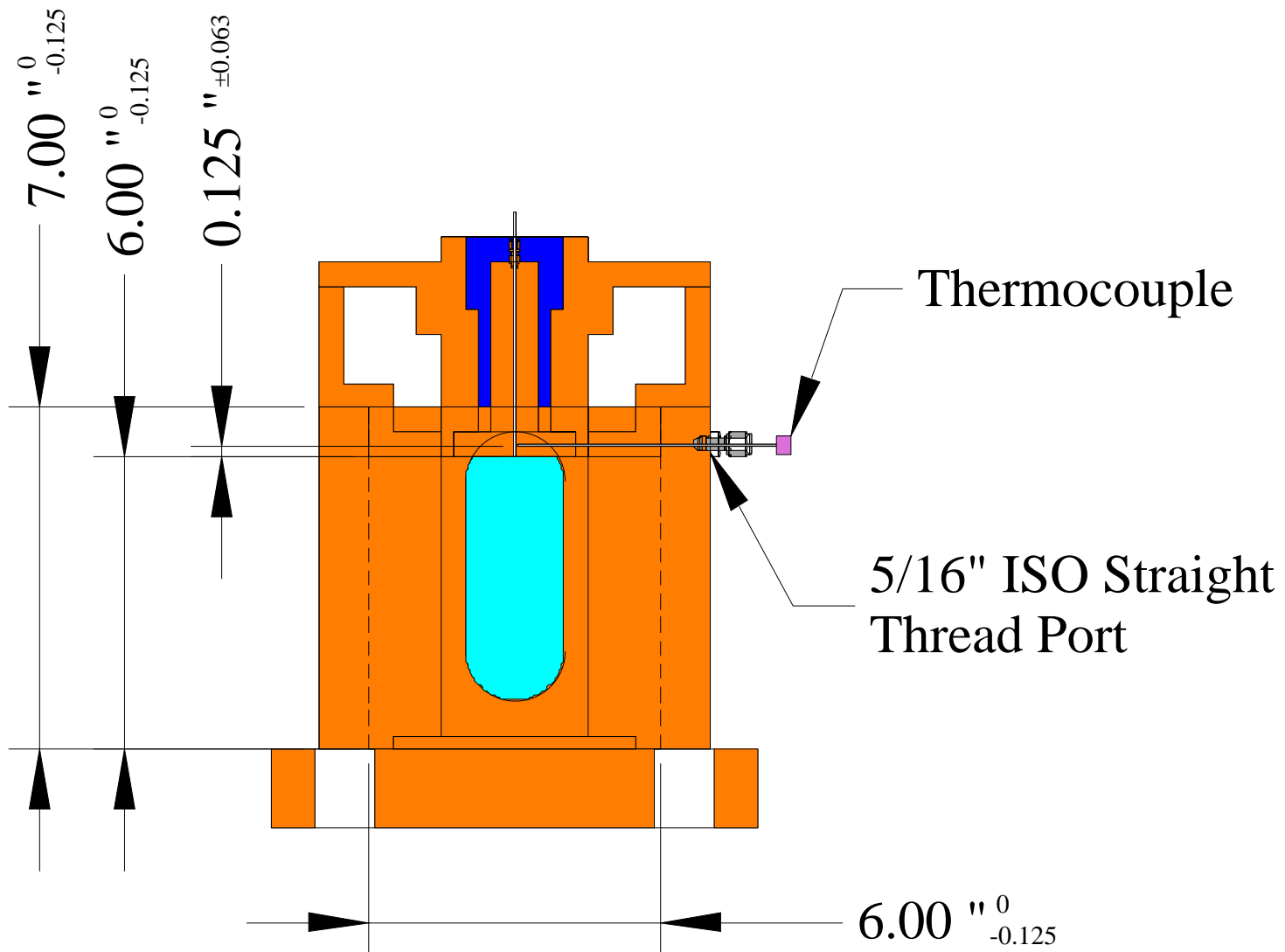


Figure 2. Thermocouple port location in main chamber

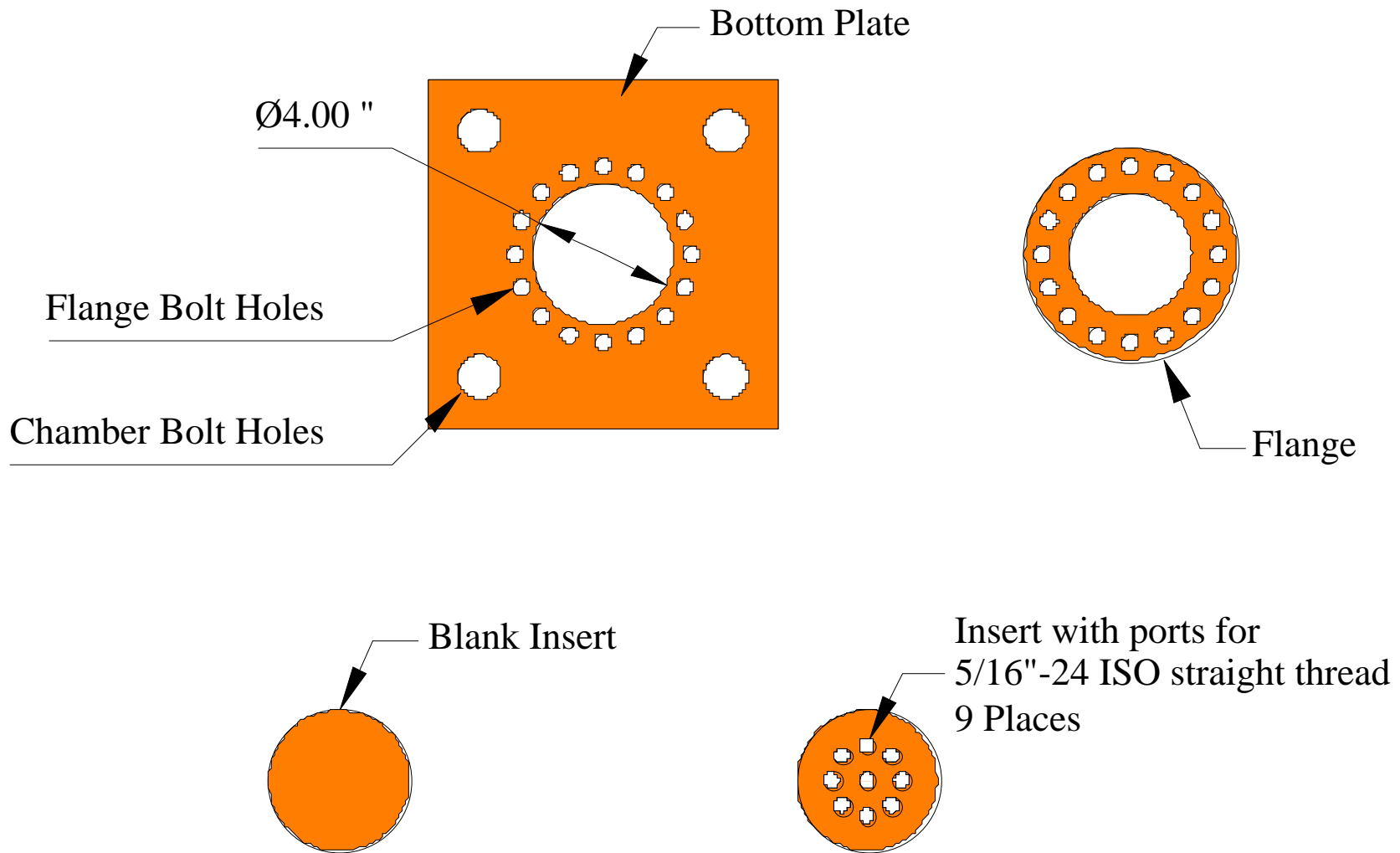


Figure 3. End view of Bottom Plate with flange and inserts.

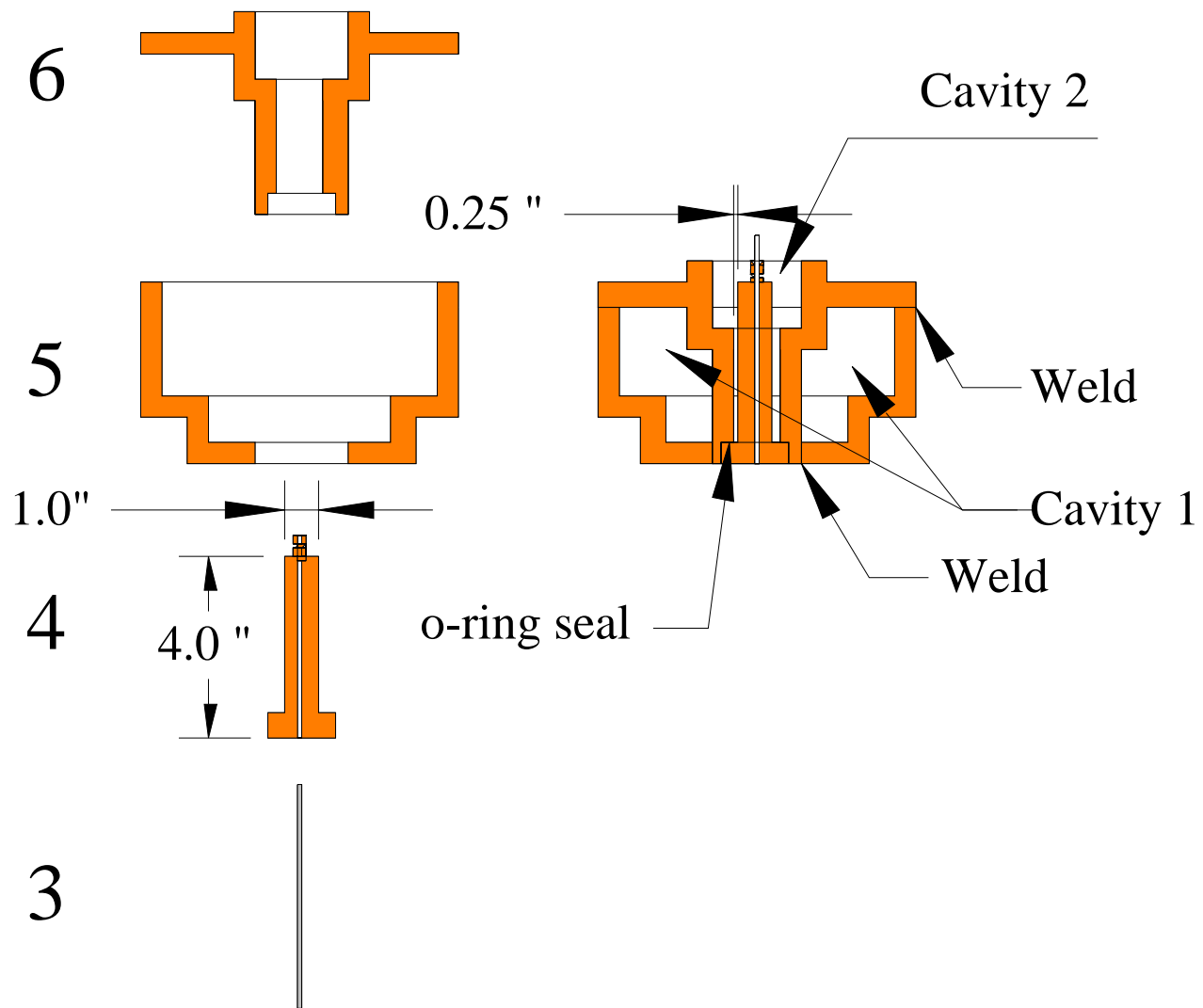


Figure 4. Injector assembly

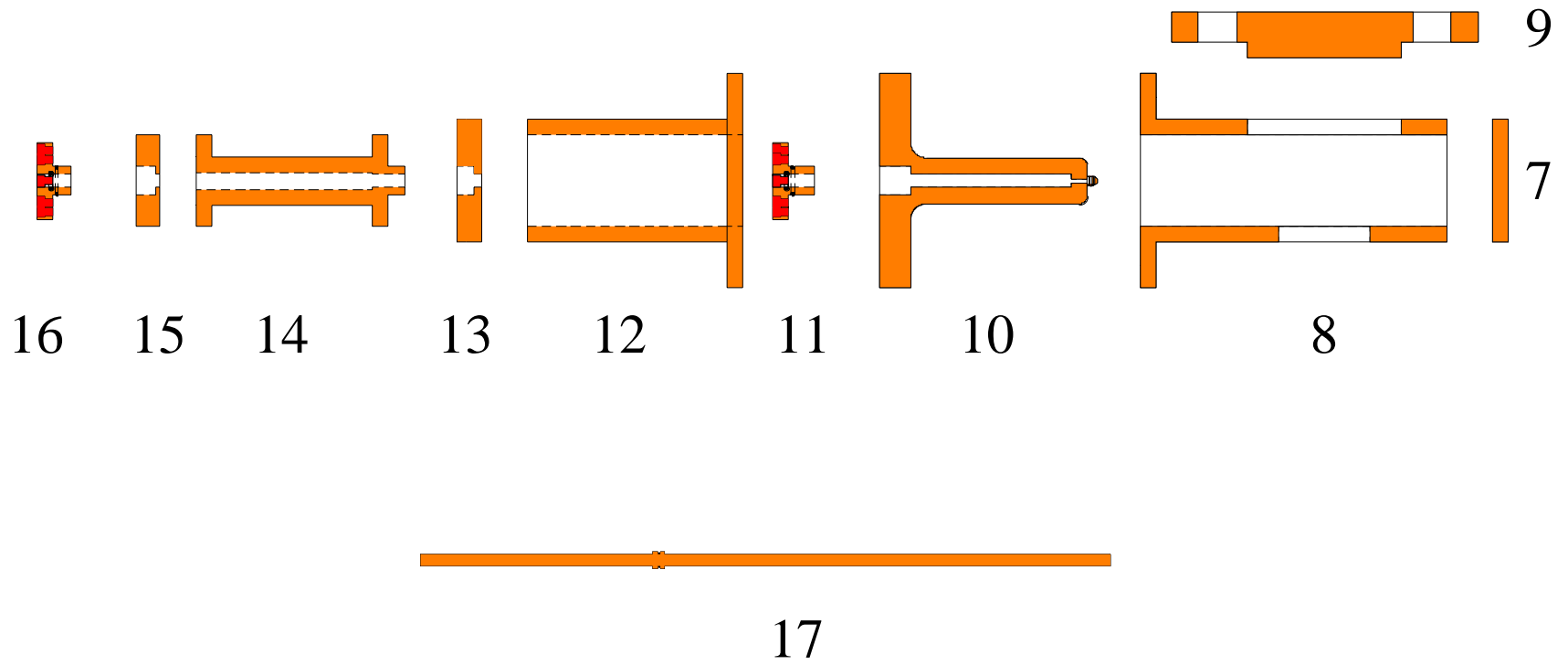


Figure 5. LN2 bath and fluid delivery system assembly

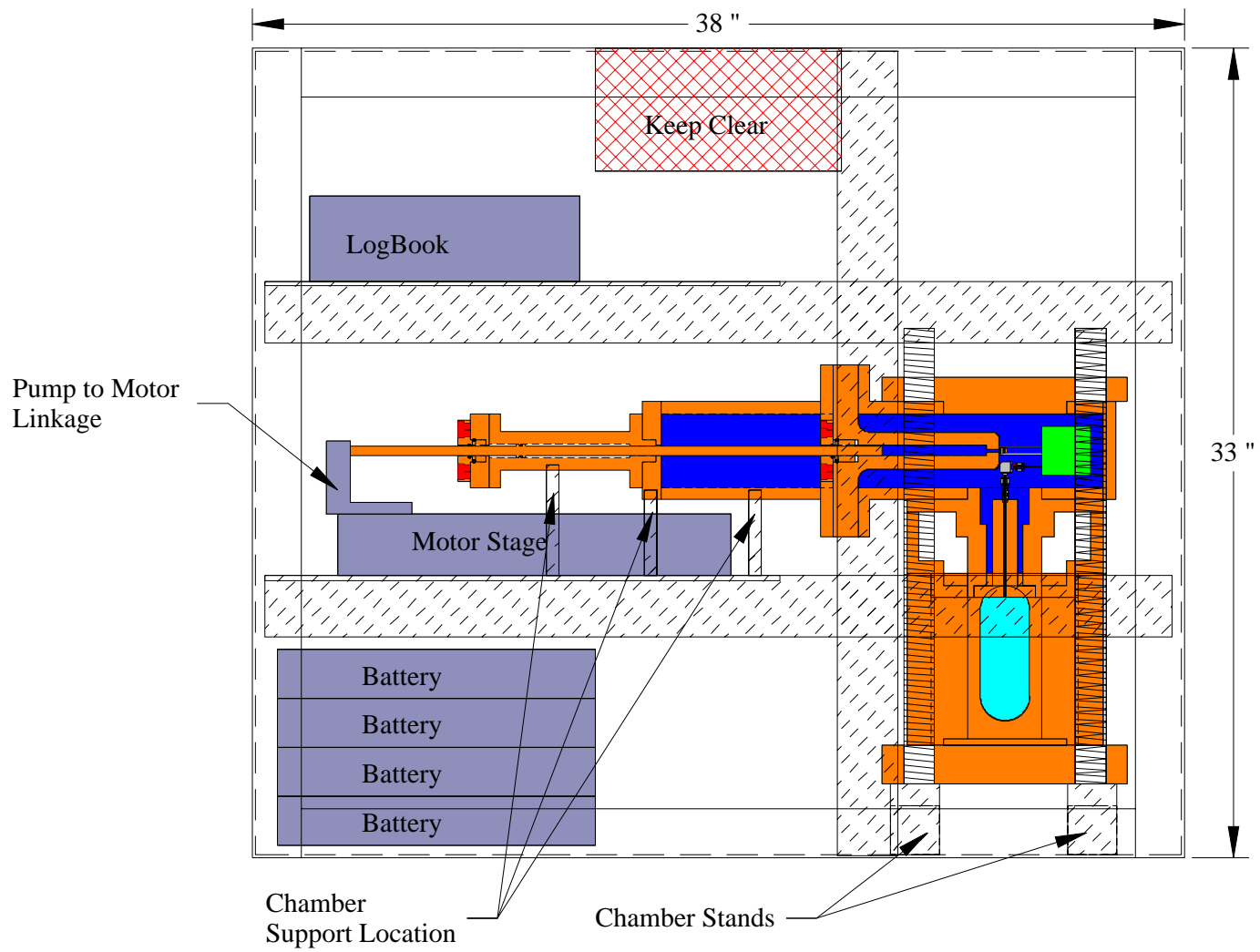


Figure 6. Test apparatus in envisioned location inside drop frame.

# **APPENDIX B**

Davis, D. W., 2006. On the Behavior of a Shear-Coaxial Jet, Spanning Sub- to Supercritical Pressures, with and Without an Externally-Imposed Transverse Acoustic Field, PhD Thesis, Mechanical Engineering Department, The Pennsylvania State University, University Park, Pennsylvania.

The Pennsylvania State University  
The Graduate School  
Department of Mechanical and Nuclear Engineering

**ON THE BEHAVIOR OF A SHEAR-COAXIAL JET,  
SPANNING SUB- TO SUPERCRITICAL PRESSURES, WITH AND WITHOUT  
AN EXTERNALLY IMPOSED TRANSVERSE ACOUSTIC FIELD**

A Thesis in  
Mechanical Engineering  
by  
Dustin Wayne Davis

© 2006 Dustin Wayne Davis

Submitted in Partial Fulfillment  
of the Requirements  
for the Degree of

Doctor of Philosophy

May 2006

The thesis of Dustin Wayne Davis was reviewed and approved\* by the following:

Robert J. Santoro  
George L. Guillet, Professor of Mechanical Engineering  
Thesis Advisor  
Chair of Committee

André L. Boehman  
Associate Professor of Fuel Science

Bruce Chehroudi  
Chief Scientist, ERC, Inc.  
Special Member

Domenic A. Santavicca  
Professor of Mechanical Engineering

Vigor Yang  
Distinguished Professor of Mechanical Engineering

H. Joseph Sommer III  
Professor of Mechanical Engineering  
Head of the Department of Mechanical and Nuclear Engineering

\*Signatures are on file in the Graduate School

**ABSTRACT**

In the past, liquid rocket engines (LRE) have experienced high-frequency combustion instability, which impose an acoustic field in the combustion chamber. The acoustic field interacts with the fluid jets issuing from the injectors, thus altering the behavior of the jet compared to that of stable operation of the LRE. It is possible that this interaction could be a substantial feed back mechanism driving the combustion instability. In order to understand the problem of combustion instability, it is necessary to understand the interaction of the jet with the acoustic waves. From past combustion instability studies of the liquid oxygen and hydrogen propellant combination in a shear-coaxial injector configuration, a design guideline of outer-to-inner jet velocity ratio greater than about ten was proposed in order to avoid high-frequency acoustic combustion instability problems. However, no satisfactory physical explanation was provided. To promote this understanding, a cold-flow experimental investigation of a shear-coaxial jet interacting with a high-amplitude non-linear acoustic field was undertaken under chamber pressures extending into the supercritical regime. Liquid nitrogen (LN<sub>2</sub>) flowed from the inner tube of a coaxial injector while gaseous nitrogen (GN<sub>2</sub>) issued from its annular region. The injector fluids were directed into a chamber pressurized with gaseous nitrogen. The acoustic excitation was provided by an external driver capable of delivering acoustic field amplitudes up to 165 dB. The resonant modes of the chamber governed the two frequencies studied here, with the first two modes being about 3 and 5.2 kHz. High-speed images of the jet were taken with a Phantom CMOS camera. The so-called “dark core” of the jet is among the most salient features in the

acquired images, and therefore, was defined and measured. The core length was found to decrease with increasing velocity and momentum flux ratio. Because of the ability of the camera to capture thousands of images and an automated routine to measure the dark core of the jet, meaningful statistics and time histories of the core length were determined. The root mean square (RMS) fluctuation of the dark-core length decreases and approaches a low constant value as the velocity ratio of the jet increases. The RMS of the dark core length, in some fashion is related to variations in mixture ratio within the combustion chamber. By decreasing this variation, at high velocity ratios under cold-flow conditions, this may lead to a physical explanation of the observed stable behavior of the LRE at high velocity ratios. The decreased RMS fluctuations at high velocity ratios reduce mixture ratio variations, which in turn leads to a more uniform heat release zone in the chamber, thus possibly weakening a key feed back mechanism to drive the combustion instability. Comparisons of the dark core length measured here to those reported by others for both single-phase coaxial jets (i.e. gas-gas or liquid-liquid) and two-phase coaxial jets (i.e. water-air or  $\text{LN}_2\text{-GN}_2$ ) establish two regimes on the dependence of this length to the outer-to-inner jet momentum flux ratio ( $M$ ). The core length of single-phase jets quantitatively agrees with the dark-core length and its  $M$ -dependence measured in our studies under supercritical conditions. However, under subcritical conditions the dark core tends to be much longer and depends more weakly on  $M$  than when under supercritical conditions. At  $M < 1$  the two regimes meet and approach the values reported for single round turbulent jets (at the limit of  $M = 0$ ). However, at higher values of  $M$ , divergence between the two regimes is observed.

## TABLE OF CONTENTS

LIST OF FIGURES .....	vii
LIST OF TABLES.....	xv
NOMENCLATURE .....	xvi
ACKNOWLEDGEMENTS.....	xix
Chapter 1 Introduction.....	1
1.1 Motivation.....	1
1.2 Objectives .....	6
1.3 Method of Approach.....	7
Chapter 2 Literature Review.....	9
2.1 Thermodynamics of High-Pressure Systems.....	9
2.2 Experiments in Supercritical Cold-Flow Jets and Sprays.....	15
2.3 Shear-Coaxial Jets .....	20
2.3.1 Core-Length of Single-Phase Shear-Coaxial Jets.....	21
2.3.2 Core-Length of Two-Phase Shear-Coaxial Jets .....	28
2.4 Interaction of a Transverse Acoustic Waves with Jet Flows.....	32
2.5 Velocity Measurements from High-Speed Shadowgraph Images.....	35
Chapter 3 Experimental Facility, Apparatus, and Technique.....	37
3.1 High Pressure Chamber .....	39
3.2 Fluid Systems.....	42
3.3 Shear-Coaxial Injector.....	47
3.4 Acoustic Driver.....	49
3.5 Instrumentation .....	52
3.6 Imaging Set-up.....	58
Chapter 4 Results and Discussion.....	61
4.1 Uncertainty Analysis .....	65
4.2 Exit-Plane Temperature Measurements.....	69
4.3 Flow Visualizations .....	82
4.3.1 Qualitative Behavior of Single Round Jets .....	82
4.3.2 Qualitative behavior of Shear-Coaxial Jets .....	91
4.4 Characterization of Acoustic Wave – Jet Interaction Mechanism.....	100
4.4.1 Acoustic Pressure Measurement.....	100
4.4.2 Acoustically-Driven Mode of the Shear-Coaxial Jet.....	105

4.4.3 Acoustic Velocity Measurements.....	113
4.4.4 Acoustic Wave Jet Interaction Mechanism .....	135
4.5 Dark-Core Length.....	146
4.5.1 Adaptive Thresholding Measurement of Dark-Core Length.....	153
4.5.2 Influence of Velocity Ratio on the Dark-Core Length.....	163
4.5.3 Scaling of the Dark Core with Momentum Flux Ratio .....	171
Chapter 5 Summary, Conclusion, and Recommendations for Future Work .....	185
5.1 Summary and Conclusions .....	185
5.2 Recommendations for Future Work .....	191
Bibliography .....	194
Appendix A Experimental Procedure and Flow Diagram .....	202
Appendix B Tabular Data .....	229

## LIST OF FIGURES

Figure 1.1: Critical pressures and critical temperatures for species of interest to combustion systems. Superimposed, are the operating conditions of liquid oxygen/hydrogen engines (x symbols), and the range of operating conditions for liquid oxygen/RP-1 rocket, and existing and future jet engines. The critical properties of jet fuels and RP-1 are shown as a range and do not exist as a single point because these fuels are mixtures of many hydrocarbons. ....	5
Figure 2.1: $T, P$ diagram for a pure fluid. Adapted from Smith et al.[10].....	10
Figure 2.2: Mixture critical pressure (a) and temperature (b) variation with composition for the $N_2 - H_2$ system, and phase diagram (c). The supercritical regime is indicated by the dotted arrows. Mixture critical data (hollow points) from Street and Calado [12] and saturation curve from NIST RERPROP [14]. The dashed-double-dotted lines denote the possible three-phase equilibria regime, and are hypothetical but typical of Type III critical point systems. ....	13
Figure 3.1: Photograph of the EC-4 Supercritical Facility. ....	39
Figure 3.2: Drawing of Main Chamber. All dimensions are in mm and approximate. ....	41
Figure 3.3: Process Flow Diagram of the AFRL Supercritical Facility. Larger format of this figure presented in the Appendix. ....	45
Figure 3.4: Photograph of Shear-coaxial injector (a) without gas manifold and insulation, (b) with gas manifold and PTFE insulation. Scale cross-section drawing (c) of injector exit-plane area also indicating relative size and position of thermocouple used for temperature measurement. Dimensions in mm. ....	48
Figure 3.5: Piezo-Siren, high-amplitude high pressure acoustic driver.....	49
Figure 3.6: Plan view cross-section drawing of acoustic driver housing, wave guide, and assembly for attachment to main chamber.....	50
Figure 3.7: Photograph of Inner-chamber.....	51
Figure 3.8: Acoustic Wave Guide.....	52
Figure 3.9: Calibration of the chamber pressure transducer. Difference between the measured pressure (using the linear fit) and the set pressure of the precision calibration device. The circle symbols indicate the increasing	

pressure, followed by decreasing the pressure (square symbols), finally increasing the pressure a second time (triangle symbols). .....	54
Figure 3.10: Traversing stage for Kistler transducer .....	55
Figure 3.11: Thermocouple Calibration Curve .....	57
Figure 3.12: Optical layout for the two Phantom camera arrangement. ....	60
Figure 4.1: Density – Temperature ( $\rho - T$ ) diagram displaying the pair of conditions of the inner and outer-jets of the shear-coaxial jet. The red circles are the outer-jet conditions, and the blue diamonds are the inner-jet conditions. The numbers listed near the points correspond to the case number listed in Table 4.1. ....	63
Figure 4.2: Thermocouple (TC) and the support mechanism used to perform radial temperature measurements in the coaxial jet. The thermocouple bead diameter is 0.10 mm. The resolution of the radial distance is 0.01 mm. The distance from the injector exit-plane to the thermocouple bead is 0.14 mm or $0.28 D_j$ . ....	71
Figure 4.3: Radial profiles of the measured average temperature and calculated density. Conditions of cases are listed in Table 4.1. The chamber nominal pressure in the top row is 1.5 MPa, in the middle row is 3.5 MPa, and in the bottom row is 4.9 MPa. The nominal outer-jet temperatures in the left and right columns are about 140 K and 190K, respectively, see Table 4.1 for exact values. The letters “T” or “D” in the inset of the figures refers to temperature or density, respectively, the next number indicates the particular case number for the data corresponding to the case listed in Table 1, and the number in parenthesis is the corresponding outer-to-inner jet velocity ratio. ....	72
Figure 4.3(a). Radial temperature and density profiles of subcritical pressure and low outer-jet temperature. ....	73
Figure 4.3(b) Radial temperature and density profiles of subcritical pressure and high outer-jet temperature. ....	74
Figure 4.3 (c). Radial temperature and density profiles of nearcritical pressure and low outer-jet temperature. ....	75
Figure 4.3 (d) Radial temperature and density profiles of nearcritical pressure and high outer-jet temperature. ....	76
Figure 4.3 (e) Radial temperature and density profiles of supercritical pressure and low outer-jet temperature. ....	77

- Figure 4.3 (f) Radial temperature and density profiles of supercritical pressure and low outer-jet temperature..... 78
- Figure 4.4: Subcritical liquid nitrogen single round jet injected into gaseous nitrogen. Nine sequential frames, starting at the top left, with a time interval between frames of 222  $\mu$ s are shown. Time increases down the column. The chamber pressure was 1.50 MPa, and the velocity of the jet was 2.2 m/s. The acoustic driver is off. The scale can be determined from the injector tip outer diameter of 3.18 mm..... 84
- Figure 4.5: Droplet formation and ejection from liquid jet surface. Fifteen sequential frames are shown starting at the top left, with a time interval between frames of 56  $\mu$ s. Time increases across a row. The pressure was 1.50 MPa, and the velocity of the jet was 2.2 m/s. The acoustic driver is off..... 86
- Figure 4.6: Acoustic wave interaction with subcritical liquid nitrogen single round jet injected into gaseous nitrogen. The pressure was 1.50 MPa, and the velocity of the jet was 2.2 m/s. The acoustic driver is on at 3.03 kHz, amplitude is about 170 dB. The top of the frame is about 10  $D_1$  down stream of the injector exit-plane..... 88
- Figure 4.7: Near-critical cryogenic nitrogen single round jet injected into gaseous nitrogen. Fifteen sequential frames, starting at the top left, with a frame-to-frame time interval of 222  $\mu$ s. Time increases across a row. The pressure was 3.47 MPa, and the velocity of the jet was 2.2 m/s. The acoustic driver is off. The scale can be determined from the injector width of 3.18 mm. .... 90
- Figure 4.8: Shadowgraph images of coaxial jet at subcritical chamber pressure ( $\sim$ 1.5MPa) and at the *high outer-jet temperature* ( $\sim$  190 K) corresponding to cases 1 – 4 listed in Table 4.1 from left to right. The acoustic driver is off for images in the top row and on for the bottom row at  $\sim$ 3 KHz. The velocity ratio is the same for each column and increases from left to right. .... 94
- Figure 4.9: Shadowgraph images of coaxial jet at subcritical chamber pressure ( $\sim$ 1.5MPa) and *low outer-jet temperature* ( $\sim$  140 K) corresponding to cases 13 – 15 listed in Table 4.1 from left to right. The acoustic driver is off for images in the top row and on for the bottom row at  $\sim$ 3 KHz. The velocity ratio is the same for each column and increases from left to right. The lowest flow rate condition was unattainable experimentally. .... 95
- Figure 4.10: Shadowgraph images of a coaxial jet at nearcritical chamber pressure ( $\sim$ 3.5 MPa) and at a *high outer-jet temperature* ( $\sim$  190 K) corresponding to cases 5-8 listed in Table 4.1 from left to right. Images in

the top row the acoustic driver is off, and the bottom row the acoustic driver is on at $\sim 3$ KHz. The velocity ratio increases from left to right. ....	96
Figure 4.11: Consecutive frames from high-speed shadowgraph images of case 3, 7, and 11 (from Table 4.1 ) with the acoustic driver turned on and off. Time increases from left to right with an interval of $55.6 \mu\text{s}$ between frames. The first two rows are at a subcritical chamber pressure ( $\sim 1.5$ MPa, case 19 of Table 4.1 ), the third and fourth rows are at a near-critical chamber pressure ( $\sim 3.5$ MPa), and the fifth and sixth rows are at a supercritical chamber pressure ( $\sim 4.9$ MPa). The acoustic driver is off for the first, third, and fifth rows and on for the second, fourth, and sixth at $\sim 3$ kHz. ....	99
Figure 4.12: Variations of the RMS of acoustic pressure oscillations (in kPa on the left axis, and in dB on the right axis) along the length of the inner-chamber. The static chamber pressure was 1.49 MPa, and the temperature was ambient $\sim 300\text{K}$ . The acoustic driver is located at the far left position. ....	102
Figure 4.13: Variation of the RMS of the acoustic pressure with the chamber pressure, measured 1.75 mm to the right of the injector centerline in the direction away from the acoustic driver. ....	104
Figure 4.14: Synchronized images viewed both perpendicular and parallel to acoustic velocity direction. Columns 1 and 2 acoustic driver is off, 3 and 4 on at 3.03 kHz. ....	108
Figure 4.15: Consecutive images framed at 18kHz of case 3 of Table 4.1. Column 1 acoustics off, column 2 acoustics on at 2.98 kHz, column 3 acoustics on at 5.16 kHz. ....	110
Figure 4.16: Ratio of the wavelength measured from the dark core of the jet multiplied by the frequency of the acoustic driver for the second resonance frequency (subscript 2) to the first resonance frequency (subscript 1) as a function of momentum flux ratio. ....	112
Figure 4.17: An image frame from a movie with boxes indicating the locations of the source windows for the spatial cross-correlation calculations (a), and (b) shows the spatial cross-correlation space for the fifth source window from the left in (a). ....	116
Figure 4.18: Power spectrum of the transverse velocity signal normalized by the dc component. The acoustic driver frequency was (a) 3.06 kHz and (b) 5.16 kHz, respectively. ....	118
Figure 4.19: Spatial cross-correlation space for image resolution of $512 \times 256$ . ....	120

- Figure 4.20: Transient transverse velocity after start of the acoustic driver, at chamber pressures of (a) 1.49 MPa and (b) 3.56 MPa, respectively. The acoustic driver frequency was (a) 3.01 kHz and (b) 3.04 kHz, respectively. .... 122
- Figure 4.21: The instantaneous transverse velocity measured at  $1.4 D_1$  downstream of injector exit-plane, at progressively closer radial distances to the injector centerline: (a)  $4.86 D_1$  from the centerline of the jet in the chamber fluid, (b)  $2.24 D_1$  from the centerline at the edge of the outer-jet, and (c)  $0.73 D_1$  from the centerline at the edge of the inner-jet. The chamber pressure was 1.49 MPa. .... 124
- Figure 4.22: RMS of the velocity signal variations with transverse direction ( $x$ ). The error bars on the figure correspond to the  $n^{\text{th}}$  order uncertainty as described in the beginning of chapter 4. The vertical gridlines are the four important radii of the shear-coaxial injector. The chamber pressure was 1.49 MPa. .... 125
- Figure 4.23: Power spectra of the acoustic velocity signals shown in Fig. 4.21 at distances from the centerline of the jet of: (a),  $4.86 D_1$  in the chamber fluid; (b),  $2.24 D_1$  at the edge of the outer-jet; and (c),  $0.73 D_1$  at the edge of the inner-jet. The chamber pressure was 1.49 MPa. .... 127
- Figure 4.24: Amplitude of the transverse acoustic velocity fluctuations from the chamber pressure measurements (circle symbols) and directly measured from the images (square symbols). The solid and dashed lines represent curve fits using the equation indicated in the figure. .... 130
- Figure 4.25: Variation of acoustic momentum flux ( $\rho U^2$ ) with the outer-to-inner jet momentum flux ratio. The words sub, near, and super in the figure inset correspond to subcritical, near-critical, and supercritical chamber pressure, respectively. The words “high” and “low” in the figure inset are for the nominal high and low outer-jet temperature cases. The hollow diamond symbols (“Sub, High”) are cases 1-4; the hollow circles (“Near, High”) are case 5-8; the hollow triangle symbols (“Super, High”) are cases 9-12; the solid diamond symbols (“Sub, Low”) are case 13-15; the solid cycle symbols (“Near, Low”) are cases 16-19. The case numbers correspond to Table 4.1. .... 132
- Figure 4.26: Variation of the ratio of acoustic momentum flux ( $\rho U^2$ ) to the momentum flux of the inner-jet with the outer-to-inner-jet momentum flux ratio. The words sub, near, and super in the figure inset correspond to subcritical, near-critical, and supercritical, respectively. The words “high” and “low” in the figure inset are for the nominal high and low outer-jet temperature cases. The hollow diamond symbols (“Sub, High”) are cases 1-4; the hollow circles (“Near, High”) are case 5-8; the hollow triangle symbols

("Super, High") are cases 9-12; the solid diamond symbols ("Sub, Low") are case 13-15; the solid cycle symbols ("Near, Low") are cases 16-19. The case numbers correspond to Table 4.1.....	133
Figure 4.27: Variation of the ratio of acoustic momentum flux ( $\rho U^2$ ) to the momentum flux of the outer-jet with the outer-to-inner jet momentum flux ratio. The words sub, near, and super in the figure inset correspond to subcritical, near-critical, and supercritical, respectively. The words "high" and "low" in the figure inset are for the nominal high and low outer-jet temperature cases. The hollow diamond symbols ("Sub, High") are cases 1-4; the hollow circles ("Near, High") are case 5-8; the hollow triangle symbols ("Super, High") are cases 9-12; the solid diamond symbols ("Sub, Low") are case 13-15; the solid cycle symbols ("Near, Low") are cases 16-19. The case numbers correspond to Table 4.1.....	134
Figure 4.28: Annotated consecutive images of a subcritical pressure shear-coaxial jet.....	140
Figure 4.29: Annotated consecutive images of the shear-coaxial jet at subcritical chamber pressure. Images show magnified views of the near-injector region. Horizontal arrow length is quantitative and proportional (amplified by 10 for clarity) to velocity measured in Fig. 4.21 (a). Two parallel vertical lines in the center show the inside diameter of the inner tube. The chamber pressure was 1.49 MPa (subcritical), and the acoustic driver frequency was at 3.01 kHz.....	144
Figure 4.30 Magnified view of frame number 10 from Fig. 4.29. The dashed curves denote the approximate boundary of the recirculation zone, and the arrows within the recirculation region indicate the direction of the rotation. The vortex structures that form on the outer rim of the injector are identified by the arrows pointing to the outer edge of the injector tip. The two vertical lines with the dimension D2 denote the extent of the outer diameter of the inner tube, $D_2 = 1.59\text{mm}$ .....	145
Figure 4.31: The image of (a) coaxial jet as captured, (b) threshold applied for injector, (c) threshold applied for dark core.....	156
Figure 4.32: Histogram of image in Fig. 4.31 (a).....	157
Figure 4.33: Dark core length (in pixels) versus velocity ratio (outer-to-inner jet) comparing the visual measurement with that of the algorithm programmed for automated measurement of this length using an average image representative for each of the conditions. The error bars represent a sensitivity analysis, varying the automatically-selected threshold level by $\pm 10\%$ . The diamonds and the up-triangles are for manual visual	

- measurements under sub- and nearcritical chamber pressures and the squares and circles are for corresponding pressures using automated computer measurements. .... 160
- Figure 4.34: Comparison of the average dark-core length measured from of set of individual images versus the dark-core length measured from the average image of the same set..... 162
- Figure 4.35: Plot of the averaged dark-core length (a) and the RMS of the length variations (b) normalized by the inner diameter. The solid symbols and lines represent the data for when the acoustic driver is OFF, and the hollow symbols and dotted lines show the data when the acoustic driver was operated at  $\sim 3\text{kHz}$  (ON). The diamond, square, and up-triangle symbols are sub-, near and supercritical chamber pressures, respectively. All cases are for the high nominal outer-jet temperature of  $\sim 190\text{ K}$ . .... 164
- Figure 4.36: Plot of the averaged dark-core length (a) and the RMS of the length variations (b) normalized by the inner diameter. The solid symbols and lines represent data for when the acoustic driver off, and the hollow symbols and dotted lines show results when the acoustic driver is operated at  $\sim 3\text{kHz}$  (ON). The diamond and square symbols are for sub- and near-critical chamber pressures, respectively. All cases are for the lower nominal outer-jet temperature of  $\sim 140\text{ K}$ ..... 165
- Figure 4.37: Comparison of measured core length data vs. velocity ratio (outer /inner). Data series indicated by (\*) denotes this work. References for the data taken from other work listed in Table 4.2. DR denotes density ratio of the outer-jet to the inner-jet. .... 170
- Figure 4.38: Dark core length versus momentum flux ratio. The diamond, circle, and up-triangle symbols represent sub-, near-, and supercritical chamber pressure, respectively. The hollow symbols are at a high outer-jet temperature ( $\sim 190\text{ K}$ ) and solid symbols are at a low outer-jet temperature. The error bars on the data points in Fig. 12 for the dark core length represent on standard deviation from the mean, and the error bars for the momentum flux ratio are the  $n^{\text{th}}$  order uncertainty as described at the beginning of this chapter. The dashed line is  $25/M^{0.2}$  and the dotted line is  $12/M^{0.5}$ ..... 173
- Figure 4.39: Comparison of dark core length, intact core length, or potential-core length for single-phase coaxial jets. This work (denoted by \*), Favre-Marinet and Camano Schettini [60], Rehab et al. [52], Au and Ko [48]. DR denotes density ratio of the outer-jet to inner-jet. .... 176
- Figure 4.40: Comparison of the dark-core length, intact core length, or potential-core length for two – phase coaxial jets. This work (denoted by \*), Eroglu et

al. [8], Engelbert et al. [63], Woodward [62]. Porcheron et al. [65] did not report core length measurements because of the measurement technique of liquid probability presence, but only an equation, see Table 4.2 for a summary of the work, and Chapter 2 for more details. Dashed-dotted line is the equation of Porcheron et al. evaluated at the average conditions of the subcritical data of this work with the LPP = 50%, and the dotted line is their equation evaluated at the same conditions except LPP = 2.5%.....	180
Figure 4.41: Comparison of the dark-core length, intact core length, or potential-core length vs. momentum flux ratio for shear-coaxial injectors, both single-phase and two-phase shear-coaxial jets. The same symbol definitions and references used here as Fig. 4.39 and Fig. 4.40 .....	182
Figure 4.42: Comparison of dark core length, for $M < 1$ , with Eq. 4.9 developed for single round jets. ....	184
Figure A.1: Process Flow Diagram of the AFRL Supercritical Facility. Regions denoted with "A" corresponds to Fig. A.1(A) and so on.....	203

**LIST OF TABLES**

Table 3.1: Fluid Subsystem Number Designation.....	46
Table 4.1: Summary of conditions for coaxial jet.....	64
Table 4.2: Summary of published operating conditions, geometries, measurement techniques, and proposed equations from the literature, measuring or correlating core length for shear-coaxial jets.....	148
Table B.1: Radial temperature and density profiles.....	230
Table B.2: Dark Core Length Data.....	241

## NOMENCLATURE

$A$	cross-sectional area
$c$	speed of sound
$C, c$	a constant
$D_1$	inner-diameter of the inner-jet
$D_2$	outer-diameter of the inner-jet
$D_3$	inner-diameter of the outer-jet
$D_4$	outer-diameter of the outer-jet
$E$	energy density of acoustic wave integrated over one time period
$E_R$	kinetic energy ratio $\equiv \frac{\rho_o U_o^3 (D_3^2 - D_2^2)}{\rho_i U_i^3 D_1^2}$
$f$	frequency, region of interest in an image
$g$	region of interest in an image
$H$	ratio of fluid of interest to that of nitrogen $\equiv \frac{\sqrt{\gamma} R}{\sqrt{\gamma_{N_2} R_{N_2}}}$
$L$	core-length, dark-core length, length
$M$	momentum flux ratio of the outer-jet to inner-jet $\equiv (\rho_o U_o^2) / (\rho_i U_i^2)$
$M_R$	momentum ratio of the outer-jet to inner-jet $\equiv (\rho_o U_o^2 A_o) / (\rho_i U_i^2 A_i)$
$p$	relative coordinate in the transverse direction
$P$	pressure
$\mathcal{P}$	amplitude of the acoustic pressure
$q$	relative coordinate in the axial direction

$R$	radius, gas specific gas constant, cross-correlation
$Re$	Reynolds number $\equiv \frac{\rho U D}{\mu}$
$St$	Strouhal number $\equiv \Lambda f / u$
$t$	time
$T$	temperature
$u$	velocity, characteristic velocity
$U$	average axial velocity
$\mathcal{U}$	is the amplitude of the acoustic velocity
$V_r$	velocity ratio
$We$	Weber Number $\equiv \frac{\rho_o (U_o^2 - U_i^2) D_1}{\sigma}$
$x$	transverse dimension
$y$	axial dimension
$Z$	Ohnesorge Number $\equiv \frac{\mu_i}{\sqrt{\rho_i \sigma D_1}}$

### Greek Symbols

$\alpha$	a constant
$\gamma$	ratio of specific heats
$\kappa$	a constant
$\Lambda$	wavelength measured from the core of the jet

$\mu$	viscosity
$\rho$	density
$\sigma$	surface tension
$\tau_A$	characteristic time associated with core wavelength

**Subscripts**

$e$	denoting entrainment quantity
$i$	denoting a quantity relating to the inner-jet
$o$	denoting a quantity relating to the outer-jet
$post$	denoting a dimension of the inner tube

**Superscript**

'	denoting root-mean-square fluctuating velocity
$sat$	denoting saturation condition

## ACKNOWLEDGEMENTS

I wish to thank my thesis advisor, Dr. Robert Santoro, particularly for many helpful discussions, and permitting me to go to AFRL to perform the experiments with Dr. Bruce Chehroudi and Dr. Douglas Talley. I would like to extend my appreciation to Dr. Chehroudi for his close mentorship and guidance during this work. The patient and gentle nature of Dr. Chehroudi was instrumental in the transition from a mentor to a friend, and I sincerely value his friendship. I would also like to thank the rest of my committee, Dr. Boehman, Dr. Santavicca, and Dr. Yang, for their interest in this research.

Without the support of the people at AFRL, this work would not have been possible. I would like to extend my appreciation to Dr. Talley for his interest, leadership, and support. Also, I would like to express my gratitude our mechanical crew, particularly Mr. Mike Griggs, for his valuable insight and experience. Mr. Griggs was a cornerstone in the modification and building of the experimental facility, and his opinion was always held in high esteem. Additionally, the AFRL Librarian, Jennie Paton, is thanked for her efforts to make literature available in a timely manner. The funding for this work from AFOSR, Dr. Mitat Birkin program manager, and NASA, Walter Duvall contract monitor, was greatly appreciated.

My deepest gratitude is to my wife Holly and sons Drew and Parker for enduring the long journey required to complete the degree. Also I would like to thank my parents, and grandparents for their support, especially my maternal grandfather, Homer Miller, for his inspiration to wonder how things work.

In all your ways acknowledge Him, and He shall direct your paths. Prov. 3:6



## Chapter 1

### Introduction

#### 1.1 Motivation

Combustion instability in liquid rocket engines was the problem in mind at the onset of this study, and the motivation starts there. Culick and Yang [1] indicated that combustion instability has plagued almost all liquid rocket engine programs since the late 1930's. Three types of combustion instabilities have been identified based on the frequencies involved. Low frequency instability (chugging) corresponds to when the wavelength is much longer than the characteristic dimension of the chamber and the feed system. Generally, chugging frequencies are less than a few hundred Hz. High frequency instability (screaming) is the second type, which is also referred to as acoustic instability, due to the closeness of the measured pressure oscillation frequencies to the computed acoustic resonance modes of the thrust chamber. High-frequency combustion instability is the most destructive type, and generally agreed that it is not influenced by the propellant feed system of the rocket engine. An intermediate frequency (buzz) consists of the lumping of the instabilities that do not fall into either chugging or screaming categories, see Harrje and Reardon [2].

With acoustic instabilities being the most destructive [2], they pose the greatest risk to preventing the development of a new engine, or may lead to a loss of vehicle and payload, or worse, to a loss of human life. A great deal of research primarily in the

1950's and 1960's during the space race [2] was undertaken attempting to gain fundamental understanding of combustion instability. This was later somewhat revitalized briefly in the 1990's [1]. Now, in part, enhancing our fundamental understanding is under consideration again. A large portion of the initial combustion instability research often involved a trial and error approach to the design of a new injector or a new combustion chamber. Many times, design and development of a new large-scale LRE starts with subscale models that proves to be stable, but an acoustic instability appears when a full-scale testing of this new LRE begins for flight verification. Historically, in these situations, the solution to the problem often has been to eliminate instability with baffles and Helmholtz resonators or modify the injectors (or both). Consequently, the modifications make the combustion chamber more complex, and add cost, time delays, and most importantly, additional mass to the vehicle. Despite these previous efforts, the fact of the matter is that a fundamental understanding of high-frequency combustion instability does not exist even today. The impediments to a full understanding of combustion instability in a rocket engine are due, in part, to the complex nature of the system itself, and mainly to a lack of fundamental understanding of the sub-processes such as liquid atomization, combustion, and their couplings with the acoustic waves.

Considering that the experiments in this study are done in a non-reacting environment, it would be an unjustifiable statement to claim, as an objective of this study, a quest for a full understanding of combustion instability. However, fundamental understanding about the sub-process associated with combustion instability may be gained. Hulka and Hutt [3] compiled an extensive review of combustion instability data

for liquid rocket engines using liquid oxygen (LOX) / hydrogen (H<sub>2</sub>) propellants. Because of the complex nature of combustion instability, the development of liquid rocket engines has focused and emphasized mapping of the stability margins of the engine, instead of understanding of the fundamental cause of the combustion instability. General observations about the stability regions of LOX / H<sub>2</sub> rocket engines indicates that higher hydrogen temperature, velocity ratios (outer-to-inner or H<sub>2</sub>-to-LOX), and momentum ratios (outer-to-inner) had a stabilizing effect. Because of the complex nature of a rocket engine, exceptions were found, but for the majority of the data, velocity ratios greater than about 10 proved to produce stable engines. One method for determining the stability margin of an engine is the so-called “temperature ramping” method. The temperature ramping method consists of lowering the hydrogen temperature feeding the engine at a constant hydrogen flow rate until a combustion instability event is initiated. Hulka and Hutt [3] point out that during the J-2 engine development, when the temperature was ramped down to somewhere between 28 and 42 K, combustion instabilities were observed even for high velocity ratios. The critical temperature of hydrogen is 33.2 K (DCAPII [4]), which is near the middle of this range. Note that in this range, small (~5K) changes in temperature produce large changes in density (factor of 2 to 3). It was not always clear where, with respect to the injector, the hydrogen temperature was measured. However, it is certain that it was not at the exit-plane of the injector. Physical mechanisms have been proposed on how temperature ramping causes combustion instability, but all have limited ranges of applicability (see Hulka and Hutt [3]).

Liquid rocket engines, burning cryogenic propellants of liquid oxygen (LOX) / hydrogen ( $H_2$ ), often use shear-coaxial injectors. Examples are the designs presently employed in the Space Shuttle Main Engine (SSME) or the Ariane 5 Vulcain engine (Vingert et al. [5]), and the RL-10 and J-2 engines from the late 1950's (Hulka and Hutt [3]). One method for eliminating acoustic instability in liquid rocket engines is to modify the spray combustion field, which is usually achieved through modifications to the injector design (see Harrje and Reardon [2]). One such modification to the Ariane 5 Vulcain reported by Vingert et al. [5], increased the mean droplet diameter size and improved the stability of the engine. Changes to the injector design ultimately influence the mixing characteristics of the propellant streams in the thrust chamber.

The fundamental physics of the breakup of a liquid jet and its subsequent mixing with other fluids have been studied since Rayleigh's study in 1878 [6]. Significant progress has been made since then, and as a result the scientific community is approaching a fundamental understanding of fluid jet break up and atomization processes, see for example Lefebvre [7]. However, Eroglu et al. [8] make it clear that a full understanding is not yet reached.

Interestingly enough, the majority of non-reacting flow studies related to propulsion applications were performed at low pressure, even though many liquid rocket engines are operated at pressures well above the critical pressures of the propellants or the major products of combustion, with the exception of water. Figure 1.1 shows the critical pressures and temperatures for possible chemical species of interest to combustion systems. Superimposed on the plot is the chamber pressure and fuel inlet temperature of several liquid oxygen/hydrogen rocket engines, the regime of liquid

oxygen/kerosene engines, and the current and proposed operating regime of jet engines. What is important to note in Fig. 1.1 is that many rockets and future jet engines are at supercritical pressures with respect to the propellants. Despite this observation, much less work has been done regarding mixing and atomization processes at elevated pressures as compared to atmospheric pressure.

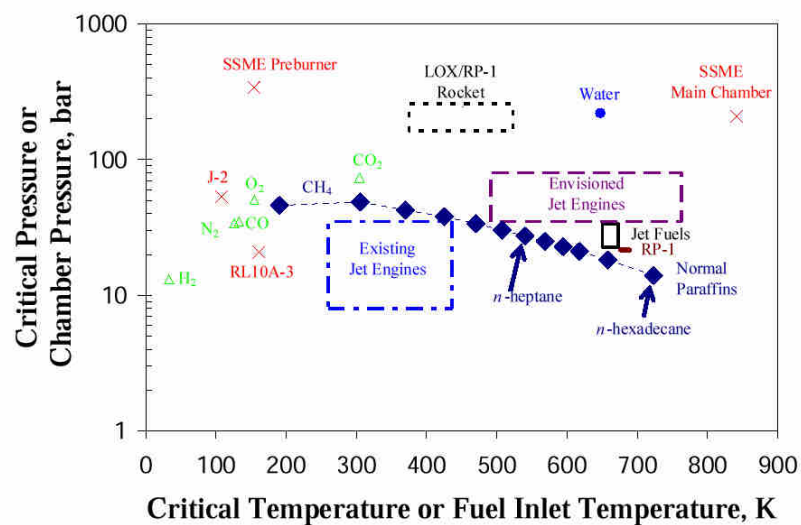


Figure 1.1: Critical pressures and critical temperatures for species of interest to combustion systems. Superimposed, are the operating conditions of liquid oxygen/hydrogen engines (x symbols), and the range of operating conditions for liquid oxygen/RP-1 rocket, and existing and future jet engines. The critical properties of jet fuels and RP-1 are shown as a range and do not exist as a single point because these fuels are mixtures of many hydrocarbons.

## 1.2 Objectives

Because of the observations of Hulk and Hutt [3] regarding the relationship of the hydrogen temperature (during the ramping exercise) and velocity ratio to combustion stability, several questions were pondered. Why does temperature ramping cause an onset of combustion instability? Why are engines more stable at high velocity ratios? How does the shear-coaxial jet behave during combustion instability? Does the nearcritical conditions of the hydrogen account for temperature ramping observations? Clearly the complex nature of combustion instability is far too large of a problem to answer in one dissertation. But perhaps, something can be learned from a cold-flow study of a shear-coaxial jet, in which similar conditions to those in liquid rocket engines during a combustion instability event are created. This could provide an opportunity to understand how the character of the jet may change during such an event. Therefore, the objectives of this study are:

1. To eliminate ambiguity in the real exit-plane temperature conditions making accurate temperature measurements at the injector exit-plane to determine initial conditions of the jet with high precision.
2. Determine if any one of the dynamic behaviors of the shear-coaxial jet could be a potential trigger for combustion instability, which would also be consistent with the observed stability impact of the velocity ratio.
3. Determine how the jet may behave during a combustion instability event, by driving the jet with externally-imposed high-amplitude transverse acoustic waves.

4. Assess the impact of the velocity and momentum flux ratios on the core of the shear-coaxial jet (physically related to mixing) both with and without the presence of acoustic waves.

One may expect to find a hypothesis statement to come at this point. However, at the onset of the study because of the complex nature of the problem, the outcome was quite unpredictable. Nevertheless, past efforts have shown that the core of the jet is an important component defining the character of the jet and could potentially be related to combustion instability. Therefore, special emphasis is put on the behavior of the core of a shear-coaxial jet.

### **1.3 Method of Approach**

The approach is then to create a shear-coaxial jet in a chamber with pressures spanning subcritical to supercritical. Using only a single chemical species, nitrogen, to remove any ambiguity about the conditions being subcritical or supercritical associated with the composition dependence on mixture critical properties. Make accurate temperature measurements so the initial conditions of the jet are well known. Adjust the temperature of the outer-jet to two nominal temperatures to simulate temperature ramping effects while maintaining independent control over velocity ratio. One temperature is selected to be in a region where small changes in temperature produce only small changes in density, and the other temperature where small changes could produce large changes in density. At these conditions, study the behavior of the jet both with and without acoustic forcing to simulate the effect of what might happen during transverse combustion

instability. Assess the behavior and mixing characteristics of the jet by taking images at framing rates fast enough to capture the dynamic behavior of the jet. From the images establish a repeatable method for determination of the effects of mixing in a consistent and repeatable fashion. One assessment for mixing of coaxial jets in the past has been core length. This parameter may also be of use to injector designers. Therefore, the assessment of mixing will be core length of the jet.

Chapter 2 presents a review of relevant literature. In particular, the review focuses on the core length measurements obtained by other researchers. However, relevant concepts concerning supercritical jets are also reviewed. Additionally, information concerning past studies involving the interaction of high-amplitude acoustic waves and jet flows are also presented.

The equipment used to perform the experiments in this work is presented in Chapter 3. A concise description of the experiment is presented first, then followed by details about the specific equipment used. A complete experimental procedure is contained in Appendix A.

Chapter 4 presents the experimental results and discussion. Chapter 4 is broken into several sections, but three sections contain the bulk of the information. Section 4.3 discusses general observations from the visualizations of the jet. Section 4.4 presents the characterization of the interaction mechanism of the acoustic wave and the jet. Finally, the discussion on the dark-core of the jet is placed in section 4.4.

Finally, the conclusions and recommendations for extensions to the study are presented in Chapter 5.

## Chapter 2

### Literature Review

#### 2.1 Thermodynamics of High-Pressure Systems

Considering a broader pool of readers, beyond that of the propulsion community, a brief review and discussion of high-pressure thermodynamics is presented first. The intent of this section is not to produce a comprehensive review of the literature on supercritical flows and applications, but rather present the relevant concepts which may be unfamiliar to those working outside the propulsion community.

Typically, fluids are divided into two classes, gases (or vapors) and liquids. However, in the supercritical regime a clear distinction between liquid and gas cannot be drawn. Moran and Shapiro [9] define the critical temperature ( $T_c$ ) of a pure chemical substance as a temperature above which vapor and liquid phases cannot simultaneously co-exist in equilibrium. The pressure at the critical point is called the critical pressure ( $P_c$ ). Figure 2.1 shows a phase diagram for a pure fluid, including a saturation curve in  $T$ - $P$  space. The critical point is the terminal point of the saturation curve. According to Smith et al. [10], pure fluids at conditions of  $T < T_c$  and  $P$  greater than the saturation pressure ( $P^{\text{sat}}$ ) are referred to as liquids, if  $P < P^{\text{sat}}$  then the fluid is referred to as a gas (or a vapor if  $T < T_c$ , also). The dashed and dotted lines on Fig. 2.1 do not represent physical phase boundaries, but rather identify different regions, as a result of semantics associated with the words liquid and gas [10]. For pure fluids, several anomalies occur

with the physical properties of the fluid as the critical point is approached. For example, the heat capacity diverges and becomes theoretically infinite. Additionally, the latent heat of vaporization and surface tension become zero. However, this subject becomes more complicated when multiple chemical species are added to the system as is the case in a reacting system.

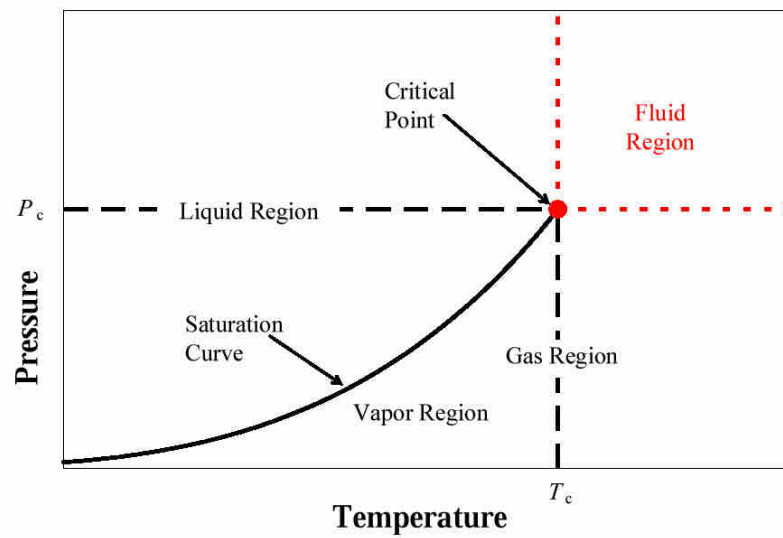


Figure 2.1:  $T, P$  diagram for a pure fluid. Adapted from Smith et al.[10].

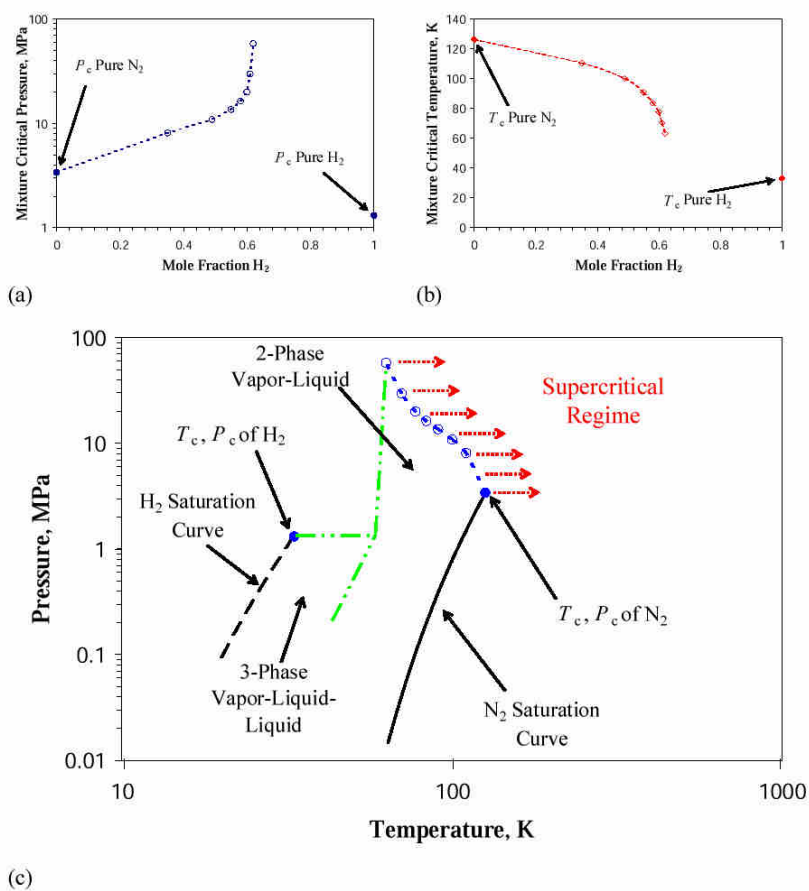
The critical point of a mixture of two or more pure species is expanded to critical lines or surfaces depending on the number of species in the mixture, and is called the critical locus. Multi-component fluid systems have phase diagrams that fall into one of the six fundamental types, first classified by van Konynenburg and Scott [11] with critical loci of phases other than vapor-liquid equilibrium critical phases (such as liquid-liquid). The vapor-liquid critical locus is the most relevant to liquid rocket engines, but the propellant combination may exhibit other types of phase behavior other than the simple vapor-liquid co-existence curve.

The critical locus of the mixture depends on the composition of the mixture. The critical pressure of a mixture can exceed many times the critical pressure of any component in the mixture. In the case of  $\text{H}_2 - \text{O}_2$  system, because of the reactive nature of the system, mixture critical point measurements are not easily attainable. However,  $\text{N}_2$  is similar in thermodynamic behavior to that of  $\text{O}_2$  and it is often used as a simulant. Mixture critical properties were measured for the  $\text{N}_2 - \text{H}_2$  system by Street and Calado [12] and are shown in Fig. 2.2. Figure 2.2 (a) and (b) show the variation in mixture critical pressure and temperature with composition, respectively. Figure 2.2 (c) is a phase diagram for the  $\text{N}_2 - \text{H}_2$  system, with the supercritical regime indicated by the red arrows. Although the liquid – liquid equilibrium (LLE) or vapor – liquid – liquid (VLLE) data are not available at the lower temperatures for this system, the phase diagram most likely exhibits Type III critical locus behavior (as classified by van Konynenburg and Scott [11]), due to the sharp divergence in the critical pressure with increasing composition (see Fig. 2.2(a)). For reference, the critical pressures and temperatures for pure  $\text{N}_2$  and  $\text{H}_2$  are 3.4 MPa, 126.2 K and 1.313 MPa, 33.19 K,

respectively (DCAPII [4]). The maximum measured critical pressure in the  $H_2 - N_2$  system is 58 MPa (~8400 psi), which is 17 times greater than the critical pressure of pure  $N_2$ .

In general, the composition in a combustion device varies both spatially and temporally. Therefore, the critical pressure and temperature of the mixture are functions of space and time, and are not fixed quantities as is the case for a pure fluid. It can then be expected that in a high-pressure combustion environment, especially near the injector exit-plane region where the temperature may be relatively low, the fluids could have regions which are subcritical. Additionally, if one of the products of combustion is water, with a critical pressure of 22.06 MPa [4] then the equilibrium two-phase region is likely to be expanded. As the water is transported away from the flame (especially in the direction of the lower temperatures) it is possible that more two-phase regions are created in the flow of the mixture.

The importance of the discussion in the last paragraph is that surface (or interfacial) tension may not be zero, and this can play a role in the mixing and atomization processes. For example, Zuo and Stenby [13] used a modified form of the Soave Redlich Kwong equation of state along with the assumption of a linear density gradient through the interface to compute non-zero interfacial tensions up to 60 MPa for the  $N_2 - n$ -octane system, well above the critical pressure for either pure species in the mixture ( $P_c$  of  $N_2 = 3.4$  MPa,  $P_c$  of  $n$ -octane = 2.49 MPa [4]). The computed results agreed fairly well with the experimental measurements of Gielessen and Schmatz [15] over the same range. A much more detailed computation of surface tension using



(c) Figure 2.2: Mixture critical pressure (a) and temperature (b) variation with composition for the  $N_2 - H_2$  system, and phase diagram (c). The supercritical regime is indicated by the dotted arrows. Mixture critical data (hollow points) from Street and Calado [12] and saturation curve from NIST RERPROP [14]. The dashed-double-dotted lines denote the possible three-phase equilibria regime, and are hypothetical but typical of Type III critical point systems.

molecular dynamics was done by Lee [16] for the  $O_2 - He$  system up to 8 MPa ( $P_c$  of  $O_2 = 5.043$  MPa,  $P_c$  of He = 0.2275 MPa [4]). Lee [16] demonstrated good agreement between the simulation and experimental results of Vieille [17] over the pressure range tested.

Caution should be exercised when referring to supercritical region to avoid ambiguity, and to ensure that some of the relevant physics are not neglected in the problem of interest. The supercritical system can be defined as the impossibility of two phases being simultaneously present as defined by Harstad and Bellan [18]. However, the impossibility of two phases existing when the system is at conditions greater than  $T_c$  or  $P_c$  is only true for systems consisting of a single pure substance. For a mixture it is not necessarily true as indicated by Fig. 2.2. Specifically, for  $N_2 - H_2$  system the temperature and pressure of the system must be greater than  $T_c$  and  $P_c$  of  $N_2$  to ensure that the system is at a supercritical condition by relying on only the critical properties of one of the components in the mixture, see Fig. 2.2. If the temperature of the system is less than that of the  $T_c$  of  $N_2$  and the pressure is greater than  $P_c$  of  $N_2$  the possibility of the coexistence of two equilibrium phases exists, depending on the specific values of the temperature of the system and the composition.

In some liquid rocket engines, gas-turbines, and diesel engines the fuel and/or oxidizer in the injector may be at a pressure greater than the critical pressure and a temperature below the critical temperature, and is introduced into a combustion chamber that is also at a supercritical pressure, but at a temperature supercritical with respect to the propellants. For instance, Woodward and Talley [19] call this “transcritical” injection. For a single chemical species undergoing a transcritical injection process the

impossibility of crossing a phase boundary is true. However, for a multiple chemical species system the potential for portions of the flow in different locations to be both subcritical and supercritical at the same time exists.

## 2.2 Experiments in Supercritical Cold-Flow Jets and Sprays

While much can be learned from the study of droplets under supercritical conditions, a thorough review is beyond the scope of this work and will not be discussed in great detail here. Extensive reviews on the subject of supercritical droplets have been done in the past by Givler and Abraham [20], Yang [21], and Bellan [22], to name a few. The review articles of Yang [21] and Bellan [22] do not restrict themselves to droplets only, but include other relevant flows for propulsion applications such as jets and sprays. In particular, both address difficulties associated with modeling supercritical flows.

One of the earlier jet studies under nearcritical conditions was done by Newman and Brzustowski [23]. A single round jet of liquid carbon dioxide ( $\text{CO}_2$ ) at 295 K was injected into a gaseous  $\text{N}_2$  environment under (chamber) pressures around the critical pressure of  $\text{CO}_2$  ( $P_c = 7.383$  MPa,  $T_c = 304.2$  K). Shadowgraph images of the jet were taken with a  $0.5 \mu\text{s}$  strobe flash at three chamber pressures of 6.21, 7.58, and 8.96 MPa and a variety of chamber far-field temperatures spanning sub- to supercritical values, with respect to the pure  $\text{CO}_2$ . The results of the photographic study under isothermal conditions indicated that the atomization of the jet near the critical pressure of the pure  $\text{CO}_2$  was similar to previous observations at high, but well below the critical pressure. Therefore, they concluded that in an isothermal system, the fact that the chamber pressure

was near or greater than the critical pressure of pure CO<sub>2</sub> is of no consequence for the atomization, and is only related to the fluid dynamic processes. The composition of the chamber fluid was found to have an effect on droplet size distribution (qualitatively determined). Their results indicated that increased concentration of CO<sub>2</sub> in the gas resulted in the formation of larger droplet sizes at a given axial distance from the injector. This was attributed to processes associated with evaporation. Under conditions of higher chamber temperatures, the atomization of the jet is controlled by the decreased surface tension associated with heat transfer to the jet [23]. Finally, they concluded that at low evaporation rates and at velocities that produce small (qualitative) droplet sizes, the jet can be characterized as a single-phase variable-density turbulent jet, spanning sub- to supercritical chamber pressures (with respect to the CO<sub>2</sub>). A discussion about the effect of the mixture critical properties of the N<sub>2</sub> – CO<sub>2</sub> system was not presented. It is possible (and is most likely) that the system, although reported supercritical, was in fact subcritical in nature. Additionally, axial velocity measurements of the jet were made from high-speed film movies. It is unclear from the report as to how these measurements were made, but perhaps by tracking structures in the movie.

Woodward and Talley [19] produced cryogenic nitrogen jets under subcritical and supercritical conditions injected into gaseous nitrogen (N<sub>2</sub>) and N<sub>2</sub> and helium (He) mixture. The injector was a long ( $L_{\text{post}} / D \sim 300$ ) tube with a diameter of 0.25 mm. Chamber temperatures ranged from 280 to 310 K and injection temperatures were between 88 and 115 K. Back-lit and Raman scattering images of the jet were made. From the shadowgraph results at subcritical injection temperatures and supercritical pressures (transcritical) for N<sub>2</sub>-into-N<sub>2</sub> injection (i.e., a single component system),

droplets were not present. However, once even a small amount of He gas was introduced into the chamber, the jet underwent the classical break-up mechanism as a result of presence of surface tension. These observations are consistent with the discussion of the thermodynamics of critical phenomena of single component and multi-component mixtures given above. If a single component system is at a pressure greater than the critical pressure, but at a subcritical temperature, then as the temperature is increased at relatively constant pressure (as is the case in this type of flow) then the fluid does not pass through the two phase region (see Fig. 2.1). Consequently, without passing through the two phase region, a surface tension cannot exist. However, as shown in Fig. 2.2(c) phase boundaries can be crossed for a transcritical injection process of a multi-component system. Recall, that a transcritical injection process is when the pressure is greater than the critical pressure of both of the chemical species, and the initial temperature is less than the critical temperature of one of the species at injection. After injection, the fluids are subsequently heated to a supercritical temperature.

Chehroudi and co-workers [24-37] extended the preliminary laminar-jet work of Woodward and Talley [19] at the Air Force Research Laboratory (AFRL) to higher Reynolds numbers and turbulent jets of interest to practical applications in propulsion systems. The single round-jet studies by Chehroudi et al. [24-30] were produced from two different injectors made from 50 mm long sharp-edged tubes with the inner diameters ( $D_I$ ) of 0.254 mm and 0.508 mm, ( $L_{\text{post}}/D_I$  of 200 and 100, respectively). Pure  $\text{N}_2$  and  $\text{O}_2$  were injected separately into  $\text{N}_2$ , He, Ar, and mixtures of CO and  $\text{N}_2$ . The single round jets were studied with shadowgraphs and Raman imaging. It was determined that the initial growth rate (initial spreading angle) of a supercritical jet was

different from that of a subcritical jet. Furthermore, they quantitatively proved for the first time that the initial growth rate of a supercritical jet behaved similar to a variable-density gas jet [27]. From this observation, a phenomenological model of the initial growth rate based upon time scale arguments was proposed that agreed well with the results acquired under sub- and supercritical conditions [28]. It is also important to note that Chehroudi et al. [28] showed that the growth rate measured from shadowgraphs was about twice as large as the growth rate of the jet measured from Raman imaging of the jet, based on the full-width at half-maximum (FWHM) jet thickness (diameter) values. The fractal dimension of the initial region of the jet under sub- and supercritical conditions was also measured by Chehroudi et al. [25, 28, and 30] and compared to liquid and gas jets in a similar fashion to that of the growth rate. A transition of the fractal dimension from values associated with a liquid jet under subcritical conditions to values associated with those of a gas jet under supercritical conditions was observed.

Similar research work to that of Chehroudi et al. has been undertaken at Deutsches Zentrum für Luft und Raumfahrt (DLR). Recently, a joint article by Chehroudi and co-workers at AFRL and Oswald and co-workers at DLR summarized the work performed at both laboratories, see Oswald et al. [37]. Independent confirmation of the results published by Chehroudi and his colleagues was shown in this article. Both laboratories had difficulties making Raman scattering measurements at subcritical conditions, and reported that under supercritical conditions, Raman scattering information was more useful. Correspondence between the spreading rates from shadowgraph and Raman scattering images using twice the FWHM rule might not be universally true at all axial locations from the injector exit-plane [37, 38]. This was

found to be especially true for single round jets under supercritical conditions approaching self-similar profiles at about 10 diameters downstream from the injector exit. Oswald and Micci [38] have shown that the spreading rate from the shadowgraph images is approximately twice the spreading rate from the Raman images using FWHM for  $15 < x/D < 32$  in the DLR experimental setup. Oswald and Schik [39], using Raman scattering demonstrated the effects of the initial temperature of the jet, considering whether it was initially below or above the “pseudo-boiling” temperature (this temperature is also called the transposed critical temperature in other supercritical literature). The pseudo-boiling temperature is an extrapolation of the saturation curve in  $T$ - $P$  space based upon the temperature at which a maximum in the heat capacity exists for a given pressure greater than the critical pressure. They reported that the temperature of the jet, measured along its centerline, remained roughly constant many diameters downstream if the initial temperature was below the pseudo-boiling temperature. However, if the initial temperature was greater than the pseudo boiling temperature, the jet temperature decreased from the injector exit-plane.

Zong et al. [40] and Zong [41] performed a large-eddy simulation of the supercritical cryogenic nitrogen jet studied experimentally by Chehroudi et al. [27-28]. Real fluid transport properties and thermodynamic properties were used in the model, and the subgrid scales were addressed using modified Smagorinsky models extended for compressible flow. The simulations produced good quantitative agreement with the experimentally-measured visual spreading angle of the jet to within 5%. The dynamics of the jet were largely governed by the local thermodynamic state of the fluid [40]. Classification of the supercritical jet could be broken into three regimes: potential-core,

transition regime, and a variable-density gas jet downstream. Therefore, Zong [41] notes simulating the entire jet as an incompressible variable-density jet could produce errors in the near-field region of the jet computation.

### 2.3 Shear-Coaxial Jets

Shear-coaxial jets are characterized by a flow issuing from an inner central tube, surrounded by a second outer tube, defining an annular opening from which an additional flow exits the injector. Typically, in shear-coaxial injectors for rocket applications, the oxidizer forms the inner-jet and the fuel defines the outer-jet region. Improved combustion stability characteristics of liquid oxygen (LOX) / hydrogen ( $H_2$ ) engines were observed when the outer-jet to inner-jet velocity ratio ( $V_r$ ) was greater than about 10, as indicated by Hulka and Hutt [3]. Therefore, many LOX /  $H_2$  liquid rocket engines have velocity ratios in this range and thus ratio of the momentum flux ratio ( $M$ ) typically falls into range  $1 < M < 10$ . For example the Space Shuttle main engine (SSME) preburner and main chamber velocity ratios are about 10 and 11.5, respectively, and momentum flux ratios are about 3.4 and 1.2, respectively [42,43].

Core length of the shear-coaxial jets is an important physical structure for the present study, particularly when the velocity ratio and momentum flux ratio are in the range relevant to that of liquid rocket engines. A summary of the studies that reported core length measurements or an equation correlating core length is presented in Table 4.2 in Chapter 4. This summary includes the fluids used, operating conditions, relevant injector dimensions, the diagnostic tools used in the study, the physical quantity

measured, and the correlation equation for the core length. This table is comprehensive, and to the best of the author's knowledge includes all of the relevant core length measurements and data in the open literature for non-reacting shear-coaxial jets.

### 2.3.1 Core-Length of Single-Phase Shear-Coaxial Jets

The term "single-phase" coaxial jet is defined as a shear-coaxial jet where all three fluid components (i.e., the inner-jet, the outer-jet, and the chamber or ambient fluid) are the same phase, either all gas, all liquid or all supercritical fluid.

One of the first experimental studies in the U.S. on coaxial gas jets was published by Forstall and Shapiro [44], shortly after WWII. Two different inner-jet tubes were used in this work with diameters of 6.4 mm and 25.4 mm, through which air with 10 ppm of helium (He) as a tracer gas flowed. The jet was studied with a Pitot tube, which was also used as a gas sampling tube. The gas samples were analyzed with a thermal conductivity cell measuring the He concentrations. The potential-core length was determined from the axial He concentration profiles. The length of the potential-core was found to increase with velocity ratio ( $V_r = U_o / U_i$ ) for velocity ratios of less than one. Additionally, it is interesting to note that in the limit of  $U_2 = 0$  (i.e., single round jet), the length of the potential-core predicted by their equation is  $4 D_i$ .

Chigier and Beer [45] also studied air – air coaxial jets at atmospheric pressure. Both the inner-jet diameter and the outer-jet annular gap were tapered to smaller dimensions near the injector exit-plane. Static pressure measurements were made with an impact tube and disk-type static probe, and velocities were calculated from these static

measurements. Carbon dioxide was used as a tracer gas to measure the axial concentration profile, similar to Forstall and Shapiro [44]. By extending the range of velocity ratios up to 9.22 (well beyond that of Forstall and Shapiro [44]), Chigier and Beer [45] determined that both the axial velocity and the concentration on the centerline decay as velocity ratio was increased. Therefore, they concluded that the potential-core length decreased as a velocity ratio increased, which is opposite to what Forstall and Shapiro [44] found for their lower velocity ratios studies ( $U_o / U_i < 1$ ).

Effects of the velocity ratio range spanning 0 to 10, for coaxial all-air jets, was investigated by Champagne and Wygnanski [46]. Velocity and turbulence intensities were measured using two hot wire anemometers. The potential-core for the outer-jet region was determined not to vary with velocity ratio. However, the potential-core of the inner-jet was strongly dependent on velocity ratio and the area ratio. They pointed out that for  $0 < U_o / U_i < 1$ , the length of the potential-core was extended as velocity ratio increased, and for  $U_o / U_i > 1$ , the potential-core decreased with increases in velocity ratio. Thus confirming the explanation offered by Chigier and Beer [45] for the disagreements between their data on the behavior of the core length variation with velocity ratio compared to that reported by Forstall and Shapiro [44].

Au and Ko [47-48], also studied shear-coaxial jets using air as the only fluid. The velocity field was measured with a hot-wire anemometer and static pressure fluctuations were measured with a microphone. Vortices were found to shed from the lip of the inner tube, with alternating direction when the velocity ratio was less than 1.25. Once the velocity ratio was increased to a number greater than 2, the vortices originated from the outer edge of the inner tube lip with a rotation direction inwards toward the inner-jet.

These inward-rotating vortices were considered the reason for the decrease in the core length as velocity ratio increased. The velocity ratio was adjusted by varying the inner-jet velocity while maintaining a constant initial velocity for the outer-jet (50 m/s). Changing the inner-jet velocity had little impact on the potential-core of the annular outer-jet, which remained roughly constant at a value 1.7 times larger than the outer-jet diameter. Upon comparing their work to others, they concluded that the outer-jet potential-core was relatively unaffected by the velocity ratio and was a function of the area ratio between the inner and outer streams. Finally, the inner potential-core length was found to be inversely proportional to the velocity ratio, and for the first time was reported in the form of an equation (see Table 4.2) indicating this inverse proportionality. It is also important to note that for a shear-coaxial jet with equal inner-jet and outer-jet densities, the velocity ratio is equal to the square root of momentum flux ratio.

Coaxial water jets with equal densities injected into a tank filled with water were studied by Dahm et al. [49]. The injector was contoured inward to the inner-tube exit diameter of 53.3 mm and the annular gap inner and outer diameters were 54.6 and 76.5 mm, respectively. The velocity ratio covered a range of  $0.59 < U_o / U_i < 4.16$ . The flow was visualized using planar laser induced fluorescence (PLIF) with a different color fluorescent dye in each fluid issuing from the inner and outer-jets. The fluorescent dyes were excited with a “thin” continuous wave argon ion laser sheet. The jets were imaged with 35 mm film, and 16 mm movie camera framing at 60 Hz. The shear layer between the inner- and outer-jet, and the outer-jet and the stagnant chamber fluid can be seen very clearly with this visualization technique. The vortex structure changed significantly over the small range of velocity ratios studied. The vortices evolving from each layer can be

wake-like (alternating rotation), shear-layer-like (single direction of rotation turning into the slower velocity region) with either axisymmetric or helical modes. They determined that the changes in potential-core length are governed by the near-injector vortex dynamics. Also, they found that this length did not depend on velocity ratio alone, and that it did not behave in a monotonic fashion with velocity ratio. Finally, a coupling between the instability, roll-up and vortex structure interactions in the outer shear layer (between the outer-jet and the chamber fluid) and vortex structures located in the inner shear layer (between the inner-jet and outer-jet) was observed.

The momentum flux ratio, in particular  $M^{-0.5}$ , has been taken to be an important parameter for coaxial jets by one group of researchers [50-58]. Recall that the velocity ratio is equal to the square root of momentum flux ratio ( $M = \rho_o U_o^2 / (\rho_i U_i^2)$ ) when the density ratio is unity. A review of coaxial jet literature considering the works of this group and others is given by Lasheras and Hopfinger [54] covering both single-phase experiments and two-phase experiments of coaxial jet flows.

Villermaux et al. [50] performed experiments on coaxial jets with water issuing from both the inner-jet and outer-jet, into a chamber filled with water studying the self pulsation phenomenon of the jet. The injector inner tube diameter was 40 mm, with an outward taper of  $6^\circ$  to a knife edge tip. The outer diameter of the annular gap was 55 mm. Oscillations were measured with a pressure transducer and a hot film anemometer. For velocity ratios between 1 and 6, they reported the potential-core length to be inversely proportional to velocity ratio (see Table 4.2). At velocity ratios greater than 6, a recirculation bubble was observed at the end of the potential core. Using a mixing layer argument and the pressure drop caused by the mixing layer, a criterion for the onset of

the recirculation was derived as  $\sqrt{M} > 6$ . The recirculation bubble caused oscillations that are convected downstream in the jet. The oscillation Strouhal number based on the inner diameter and the outer-jet velocity was fixed at a value approximately equal to 0.3.

Rehab et al. [51] expanded upon the work of Villermaux et al. [50] making measurements with a hot-film anemometer, a Pitot tube, and flow visualizations from a single-dye PLIF images excited by an argon ion laser. A definition of potential core was offered, clarifying that the flow in the potential core is not necessarily irrotational flow, but indicates a region of weak turbulence intensity where small-scale dissipation is nearly zero. The length of the potential core was defined as the distance from the injector exit to the axial location where the velocity on the centerline of the jet reached a minimum value, and was stated to follow the inverse proportionality to the velocity ratio. A theoretical analysis of the length of the potential core was given starting with the same estimate of pressure drop for the mixing layer as Villermaux et al. [50]. The pressure drop in the mixing layer is given by:

$$\Delta P = \rho u'^2 / 2 \quad (2.1)$$

Where,

$\rho u'^2 / 2$  is the dynamic turbulent pressure.

The assumed that the potential core is an inverted cone in shape with the inner diameter (of inner tube) defining the base, and the length of the potential core for its height. Also, they hypothesized that the entrainment velocity ( $u_e$ ) is proportion to the root-mean-square

(RMS) fluctuating velocity ( $u'$ ). The entrainment velocity ( $u_e$ ) is an averaged velocity that satisfies the equation for the conservation of mass for the core of the jet. From their measurements, they showed that  $u' \approx 0.17 (U_o - U_i) = 0.12 U_o$ , and in general assumed that  $u' \approx \alpha U_o$ . Then, applying conservation of mass on this conical control volume, the resulting length of the potential core was determined and given by Eq. 2.2.

$$\frac{L}{D_1} \approx \frac{1}{2} \left( \frac{1}{C^2 \alpha^2 \frac{U_o}{U_i}} - 1 \right)^{1/2} \approx \frac{1}{2C\alpha \frac{U_o}{U_i}} \quad (2.2)$$

Where,

$C$  is a constant approximately 0.5

With  $\alpha = 0.17$ , the term  $1/(2 C \alpha)$  is 5.88, and when  $\alpha = 0.12$ , the term  $1/(2 C \alpha)$  is 8.33, which is consistent with their data. If the RMS of the velocity fluctuations is given by  $u' \approx \alpha (U_o - U_i)$ , the resulting expression for the potential core length is given by the Eq. 2.3. A comment was made that for fluids of unequal densities the velocity ratio term should be replaced with  $M^{0.5}$ . Rehab et al. [51] stated that Eq. 2.3 is limited to the range  $1 < U_o / U_i < 8$ , without any statement about momentum flux ratio. However, if the same limitation were to apply, then the momentum flux ratio range of applicability would be  $1 < M < 64$ .

$$\frac{L}{D_1} \approx \frac{1}{2} \left( \frac{1}{C^2 \alpha^2 \left( \frac{U_o}{U_i} - 1 \right)^2} - 1 \right)^{1/2} \quad (2.3)$$

Favre-Marinet and co-workers [59, 60] investigated the effects of the density ratio on coaxial gaseous jets spanning a wide range of velocity, density, and momentum flux ratios (see Table 4.2 for the values). The variations in density ratio were achieved using different gas combinations of air, He, and sulfur hexafluoride ( $\text{SF}_6$ ). Favre-Marinet et al. [59] performed flow visualization by illuminating the jets with a 1mm thick laser sheet from a pulsed copper vapor laser operating at 10 kHz, and images were recorded with a video camera at 50 Hz. The shutter speed was set at 1/4000 s, therefore each frame captured two pulses from the laser. The flow was seeded with incense smoke, except when He and  $\text{SF}_6$  were used as the fluids, for this case, the inner-jet was seeded with “very-small” droplets of a mixture of water, glycerin, and fluorescein dye. A Laser Doppler Velocimetry (LDV) system used for the air-air and He-air jets, were combined with results using a hot-wire probe. Favre-Marinet and Schettini [60] used the same apparatus, but with a different diagnostic method and were able to measure the density field of the jet. The measurement was made with an aspirating probe, which is a “very thin” tube with a hot-wire at its end. This tube is connected to a vacuum pump and when the pressure reaches a critical value, the hot-wire is no longer sensitive to velocity, but only to density variation. The results of these two works indicated that the onset of the recirculation bubble at the end of the potential core begins at  $M \approx 50$ , which is larger than that reported by Villermaux et al. [50]. For  $M < 50$ , they claimed that the potential core length varied with  $M^{-0.5}$ . However, at the same  $M$  value but at different density ratios the potential-core lengths of the jet are different values.

### 2.3.2 Core-Length of Two-Phase Shear-Coaxial Jets

The term “two-phase” coaxial jet here means a shear-coaxial jet where the inner-jet is liquid phase, and the outer-jet and the chamber (i.e. ambient fluid) are gas phases.

Eroglu, Chigier, and Farago [8] measured liquid intact lengths for a coaxial water-air jet at atmospheric pressure, and later Farago and Chigier [61] classified the break-up of the liquid jet according to the value of Weber number ( $We$ ). Note that Eroglu et al. [8] used a definition of  $We$  which has a factor of 2 in the denominator. This expression is different than the definition given by Farago and Chigier [61] and the definition listed in the Nomenclature section of this dissertation. To be clear, all values and equations reported in this work are consistent with the definition of  $We$  presented in the Nomenclature section. Images of the coaxial jet were acquired with a 35 mm camera back-lit with a  $0.5 \mu\text{s}$  pulse duration strobe light. The injector had an inner-tube inside diameter of 0.971 mm. The inner and outer diameters at the exit of the annular gap were 1.262 mm and 10.36 mm, respectively, which was obtained by contracting a 16 mm duct in order to produce a flat velocity profile at the exit. The area ratio (outer-to-inner) of this injector was about 112, which is much greater than a rocket-type coaxial injector (for example, SSME injector area ratio is about 2.8). The inner tube of the injector used in many rocket engines is recessed back into the outer tube. However, the inner tube, in this case protruded (a negative post recess) beyond the outer tube by 0.6 mm, but they reported no noticeable effects of moving the inner-jet by  $\pm 1\text{mm}$ . The inner tube flow was in the laminar regime when  $Re < 6000$ , with transition occurring somewhere within the range  $6 \times 10^3 < Re < 10^4$ , and fully turbulent regime occurring for  $Re > 10^4$  [61]. The

$Re$  in this study was in the range  $1097 < Re < 9328$ , and therefore, being less than  $10^4$ , it is likely that the exit-plane velocity profile from the inner tube was not a fully-developed turbulent profile. Eroglu et al. [8] measured the intact liquid length by analysis of four to seven images taken at each condition for six different  $Re$  numbers. Mean values were then computed, and it was noted that the individual measurements values can be as much as  $\pm 15\%$  from the mean value. A correlation equation (see Table 4.2) of the intact liquid lengths was deduced from these measurements, and found to depend on the  $Re$  and  $We$ .

Three liquid breakup modes were found by Farago and Chigier [61]: (1) Rayleigh breakup for  $We < 25$ , (2) jet disintegration via membrane-type ligaments for  $25 < We < 70$ , and (3) jet disintegration via fiber-type ligaments for  $100 < We < 500$ . The Rayleigh breakup regime was further divided into two sub-categories, axisymmetric Rayleigh breakup for  $We < 15$ , and non-axisymmetric for  $15 < We < 25$ . Each of the breakup modes had sub-modes of pulsating and super-pulsating. The authors determined that the atomization process was always a pulsating process. The super-pulsation mode existed when the liquid mass flow rate was “low” and the gas flow rate was “very high”.

Woodward [62] made liquid core measurements from a coaxial jet with real time x-ray radiography. The inner tube of the injector had an undisturbed entrance length of 85 inner diameters, sufficiently long to produce a fully-developed turbulent velocity profile at the inner tube exit. The outer-jet fluids were nitrogen ( $N_2$ ) and helium (He), and the inner-jet fluid was an aqueous solution of potassium iodide ( $KI_{(aq)}$ ) to attenuate the x-rays. The chamber was initially pressurized with the same fluid as that used for the outer-jet from 0.1 to 2.17 MPa, which is still well below the critical pressure of water ( $H_2O P_c = 22.06$  MPa). It is important to note that the study of Woodward [62] is the

only study in the open literature, other than this work, to experimentally investigate the core length of shear-coaxial jets at pressures greater than atmospheric (see Table 4.2). The intact core measurements from the x-ray radiography were correlated (Eq. 2.4) using  $Re$  and  $We$ , similar to that of Eroglu et al. [8], but the additional parameters of density ratio, and a ratio ( $H$ ) involving the square root of the ratio of heat capacities and the specific gas constant of the fluid of interest to the same quantities evaluated for the nitrogen. At a constant temperature, this parameter ( $H$ ) is essentially the ratio of sound speeds for the outer flow compared to that of  $N_2$ . Woodward notes that this could imply a Mach number effect for coaxial jet liquid breakup, but states that the real physical significance is not known.

$$\frac{L}{D_1} = 0.0095 \left( \frac{\rho_o}{\rho_i} \right)^{-0.36/H} Re^{0.68} We^{-0.22/H} \quad (2.4)$$

Where,

$$H = \frac{\sqrt{\gamma R}}{\sqrt{\gamma_{N_2} R_{N_2}}},$$

$\gamma$  is the ratio of heat capacities =  $C_p/C_v$ , and

$R$  is the specific gas constant.

Englebert et al. [63] examined shear-coaxial jets with water as the inner-jet liquid and air as the outer-jet gas. The area ratio (outer-to-inner) was about 40, which again is much larger than a typical injector used in rocket engines (SSME injector area ratio is about 2.8). Images of the jet were taken with a high-speed 16 mm camera framing at 12 kHz, and back-lit with a continuous halogen lamp. Breakup length was correlated as a

function of  $We$ , kinetic energy ratio ( $E_R$ , see Eq. 2.5 ), and momentum ratio ( $M_R$ , see Eq. 2.6 ). With the velocity of the inner-jet at a constant value of 4 m/s, the breakup lengths were fitted to a function of  $We$ , with a similar exponent to that of Woodward [62], but were much shorter in length. The correlations of their data involving  $E_R$  and  $M_R$  were normalized by the annular gap-width (i.e.  $(D_3 - D_2)/2$ ). The dependence on the  $M_R$  to the -0.3 power was observed. Notice that  $M_R$  is the momentum ratio and incorporates the area ratio of the injector, and is not to be confused with  $M$ , the momentum flux ratio, which does not include the area ratio of the injector.

$$E_R = \frac{\rho_o U_o^3 (D_3^2 - D_2^2)}{\rho_i U_i^3 D_1^2} \quad (2.5)$$

$$M_R = \frac{\rho_o U_o^2 (D_3^2 - D_2^2)}{\rho_i U_i^2 D_1^2} \quad (2.6)$$

Carreau et al. [64] and Porcheron et al. [65] studied coaxial jets with a fiber optic probe to measure what they refer to as the “liquid-presence probability (LPP).” The probe had a sapphire tip, and an infrared light at 850 nm, modulated at 2.5 MHz, passed through it. In principle, because the shape of the probe end, if liquid was present, then the light would pass through of the tip, however, if gas was present at the tip, the light would be internally reflected back through the fiber optics and the signal would be recorded. A double-thresholding technique was used to determine the amount of time the probe was in contact with liquid and gas. The fraction of time the voltage signal was high indicated the gas time, and the fraction of time the signal was low indicated the

amount of time the probe was in contact with liquid. The LPP was computed from these measurements. The experiments were done with LOX and either He, N<sub>2</sub>, or Ar, and water – air. The LPP was correlated as a function of axial distance, as well as other parameters. Upon defining the LPP to be 0.5 at the end of the breakup length, a breakup length correlation could be determined. Note that changes in the selection of the LPP value from 0.5 at the breakup length would only result in variations in the constant used in their proposed correlation. The initial correlation (see Table 4.2) presented by Carreau et al. [64] was for LOX with either He, N<sub>2</sub>, or Ar, and was of the same form as that by Woodward [62]. Later Porcheron et al. [65] included water-air and LOX-inert-gas experiments and modified their earlier correlation by replacing explicit dependencies on  $We$  and  $Re$  to those of Ohnesorge number ( $Z$ ) and  $M$  parameters.

#### 2.4 Interaction of a Transverse Acoustic Waves with Jet Flows

The number of reports involving the interaction of transverse-acoustic waves and fluid jets are limited. One of the earliest studies was done by Miesse [66] with single round jets. Two “sound sources” (acoustic drivers) were positioned along a common axis, perpendicular to the flow of the jet, opposing one another. The phase angle between the two drivers was adjusted to be 180° to maximize the “push-pull” effect on the jet, using frequencies of less than 200 Hz. Images showed that the amplitude of the jet deflection in the transverse direction decreased with increase in both the frequency of the driver and pressure drop across the injector (i.e. flow rate). It was also noted that the sound field considerably reduced the length of the solid stream. Maximum dispersion of

the jet was observed at the natural frequency of the jet. The intact length of the jet decreased when excited by the acoustic drivers.

Newman [67] studied laminar single round jets in an externally-imposed acoustic field inside a resonant chamber at a frequency of 880 Hz. The mean chamber pressure varied up to about 0.6 MPa (70 psig). The breakup length of the jet was measured from images both with and without the presence of the acoustic field. The jet was placed at both a pressure node and a velocity node. At low mean chamber pressures (atmospheric pressure) the differences between the two nodal placements of the jet exhibited a small effect on the breakup length. However, at higher chamber pressures the pressure oscillations were more effective at decreasing the breakup length. Overall, the effect of the acoustic field diminished with increasing chamber pressure.

Buffum and Williams [68] investigated the interaction of externally imposed transverse acoustic waves at frequencies ranging from 100 to 500 Hz on a turbulent liquid jet at atmospheric pressure. The primary physical quantity measured was the oscillatory displacement of the liquid jet as it passed through an acoustic standing wave field in a resonant tube. Resonance effect at different frequencies was achieved through variations of the tube length in this study. It was found that the peak-to-peak jet deflection distance decreased when jet diameter or velocity was increased due to increased fluid mass in the acoustic field. The jet deflection was unobservable below 130 dB and immeasurable below 140 dB. At about 161 dB the acoustic waves induced shearing atomization of the jet, which produced large scale periodic structures. These periodic structures were proposed to act as reactant sources in a combustion case to sustain or amplify combustion instabilities. The drag coefficients for turbulent liquid jets in transverse acoustic field

were about an order of magnitude larger than that of a solid cylinder having a diameter the same as that of the injector orifice. This caused enhanced jet deflections in the acoustic field and may be one source for sustaining the instability in liquid rocket engines.

Heidmann and Groeneweg [69] produced images of unstable liquid oxygen (LOX) / hydrogen ( $H_2$ ) combustion. The LOX was injected in the form of a round jet from a multi-element ring surrounding the perimeter of disk-shaped combustion chamber. In a diffuse manner,  $H_2$  flowed from slots both above and below the LOX jets. The propellants were injected inward in the radial direction from the perimeter of the combustor, and the burned gases turned 90 degrees to flow through the nozzle located on the bottom plate. Time varying jet length was observed to be coupled with the acoustic field which raised suspicion that unstable combustion was directly related to the dynamic behavior of the liquid jet.

More recently, Rhys [70] considered the interaction of acoustic waves with flat liquid (water) sheets and swirl-coaxial jets (water and air). The amplitude of the surface waves on the flat liquid sheet decreased in magnitude as the frequency was increased over the range of 600 to 1700 Hz. The author indicated that the preferred frequency of the surface waves on the liquid sheet of the swirl-coaxial spray increased as  $We$  increased up to a values of about  $10^4$ , where the atomization character of the driven sheet changed. When  $We$  is greater than about  $10^4$  the liquid sheet disintegration of the swirl-coaxial spray made a transition from surface-wave breakup to aerodynamic stripping mode. Additionally, Rhys stated that for swirl-coaxial injectors high velocity ratios eliminate

fundamental atomization frequencies. Therefore, he postulated that the surface wave combustion instability pathway could be eliminated by operating at high velocity ratio.

### 2.5 Velocity Measurements from High-Speed Shadowgraph Images

An early report of velocity measurements from shadowgraph images was done by Newman and Brzustowski [23] in the experimental work reviewed in section 2.2 above. Measurements of the axial velocity of a single round jet were reported. However, no details were presented on how the measurements were made. One may only surmise that they visually tracked fluid structures on the core of the jet to estimate velocities.

Ota et al. [71] and Okamoto et al. [72] investigated supercritical carbon dioxide flow over a heated wall. The flow was driven by a pump vertically upward, but the fluid near the heated wall experienced a buoyant acceleration. Shadowgraph images were taken with a high-speed charge coupled device (CCD) camera framing at 250 Hz. The light source was a pulsed infrared laser with a wavelength 808 nm. The laser pulses were frame straddled, that is, the first pulse occurred near the end of one frame exposure time and the next pulse near the start of the next frame, and so on. Therefore, the effective time difference between frames was reduced to 0.48 ms, rather than 4 ms. A spatial cross-correlation was then computed for two consecutive images, using a 32 by 32 pixel interrogation source window. In the images, there were pixels that their intensities did not vary between images, and they were considered as noise points and not included in the spatial cross-correlation calculations. The intensity variations, caused by the density gradients in the shadowgraph served as fluid elements (or particles) for the spatial cross-

correlation. The authors refer to this process of velocity measurement using unseeded shadowgraphs as a “new technique”. Instantaneous two-dimensional velocity fields were constructed indicating a higher velocity near the heated wall. Also, the transient velocity signal at one point in space revealed the unsteady nature of the flow, which corresponded to the frequency of the diaphragm pump used to drive the flow. The uncertainties of the measurement are not specifically addressed in these reports and it is stated that error elimination should be part of future work.

## Chapter 3

### Experimental Facility, Apparatus, and Technique

The experiments presented in this work were performed in test cell EC-4 at the Air Force Research Laboratory (AFRL) at Edwards Air Force Base, CA. Portions of the experimental apparatus preexisted prior to the work described in this thesis, but the facility required significant upgrades and modifications, which will be outlined in the following sections of this chapter.

A concise operational description of the facility shown in Fig. 3.1 is given here. Detailed descriptions of key components appear in the subsequent sections. Also, the detailed standard operating procedure developed for this work is presented in Appendix A.

The experimental apparatus and system components were designed to achieve a cold flow injection of cryogenic liquid (when subcritical) or liquid-like (when supercritical) nitrogen through the inner tube of a shear-coaxial type injector with cold nitrogen gas passing through the annular region of this injector. The fluids from the injector flow into a main chamber pressurized with gaseous (or gas-like, if supercritical) nitrogen. All flows entering the chamber including those from the injector are supplied by the high pressure nitrogen line to the facility. The flow rates are monitored and controlled while still in gaseous phase because of the difficulties associated with controlling and measuring high-pressure cryogenic flows. The high-pressure gaseous nitrogen is liquefied by passing the gas through heat exchangers, chilled with low-

pressure liquid nitrogen. During the “chill down” procedure, the temperature of the outer-jet is monitored by a thermocouple positioned near the exit-plane of the injector in the outer-jet fluid. Adjustments to the outer-jet temperature are made by changing the liquid nitrogen flow rate to a secondary heat exchanger. Once a steady-state operating condition within the chamber has been achieved, radial temperature profiles near the injector exit-plane area were measured using a very fine (bead diameter 0.10 mm) exposed-bead thermocouple. Upon completion of these temperature measurements, the thermocouple was traversed out of the jet to a far-field position, and images of the jet were captured using either a low-speed camera with a framing rate of 10 Hz, or a high-speed camera with a framing rate of 18 kHz. Most of the images and movies were taken with a back-lit illumination arrangement producing shadowgraphs, but in some instances it was necessary to illuminate the jet from the front. An acoustic driver was driven with a sinusoidal signal to excite the first resonance mode of the inner-chamber, which is approximately 3 kHz, depending on the chamber temperature and pressure. The inner-chamber is embedded inside the main chamber, and is used to reduce the cross-sectional area of the main chamber to keep the amplitude of the acoustic waves high in the vicinity of the jet. Images of the excited jet were then acquired. Subsequently, the acoustic driver frequency was then set to the second resonance mode of the inner-chamber, at approximately 5 kHz, and then the imaging process was repeated. In other test runs, several variations of this imaging process were executed in order to gain additional information about startup transients or modal behavior of the jet.

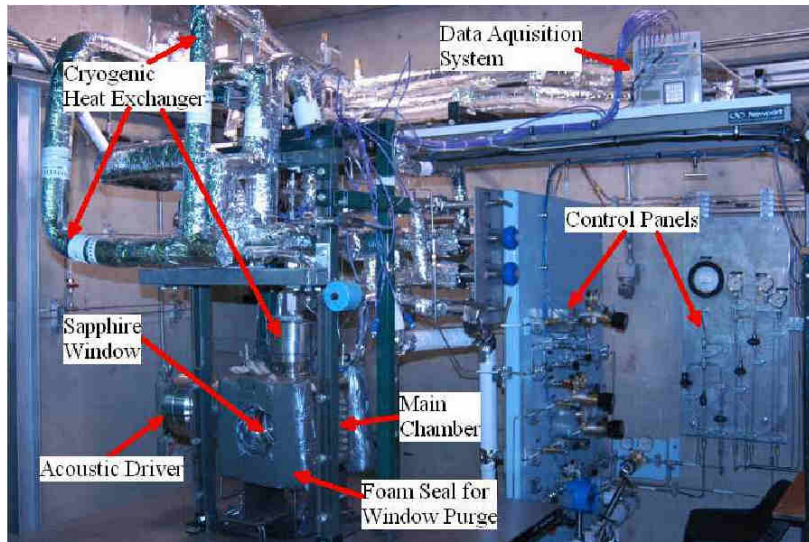


Figure 3.1: Photograph of the EC-4 Supercritical Facility.

### 3.1 High Pressure Chamber

The main chamber (Figs. 3.1 and 3.2) was originally designed by General Physics Corp. for the purpose of studying supercritical droplets at AFRL and was completed in 1995. The main chamber was designed in accordance with the American Society of Mechanical Engineers (ASME) Boiler and Pressure Vessel Code capable of withstanding 13.8 MPa (2000 psig) over a temperature range of 76 K to 473 K (-323°F to 392°F). The main chamber is made of 304 stainless steel. The chamber has four ports for providing optical access to the injector region (see Fig. 3.2). The two larger circular openings have round sapphire ( $\text{Al}_2\text{O}_3$ ) windows, and the smaller oblong shaped window openings can be

used to house fused silica (quartz) windows, the acoustic driver (discussed below), the thermocouple traversing stage (discussed below), or the piezoelectric pressure transducer traversing stage (discussed below). The opening at the top of the chamber is used to mount the cooling tower used to cool and/or liquefy (when the pressure is subcritical) the gaseous nitrogen ( $\text{GN}_2$ ) into liquid nitrogen ( $\text{LN}_2$ ) that is then injected into the chamber through the shear-coaxial injector. The chamber is equipped with multiple ports for flow connections and instrumentation such as thermocouples and pressure transducers.

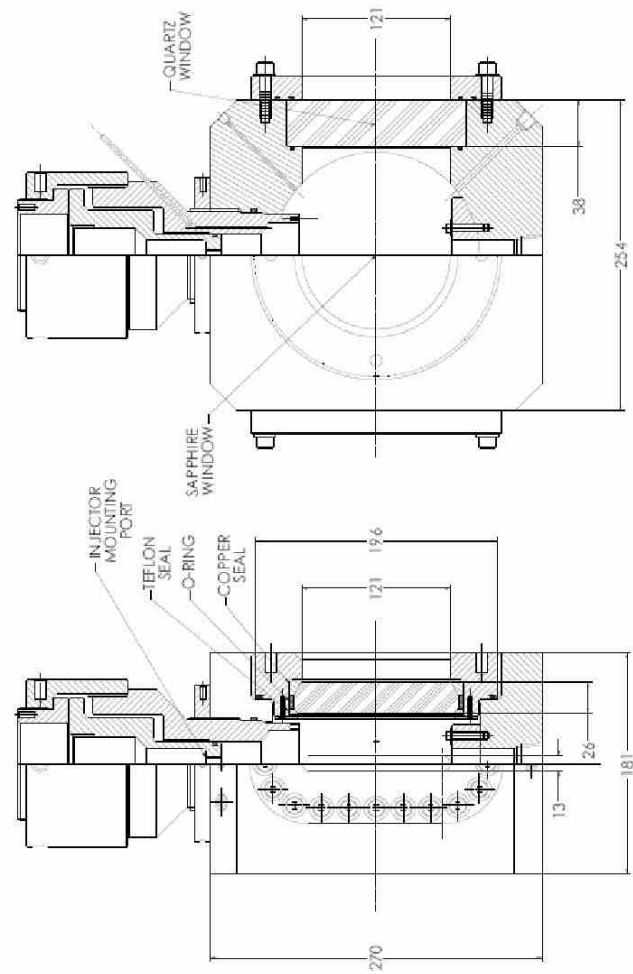


Figure 3.2: Drawing of Main Chamber. All dimensions are in mm and approximate.

The sapphire windows are contained within a specially-designed stainless steel window retainer. With approximately 121 mm diameter optical access, the retainer is fitted with acme threads on the outer diameter, and screws into the chamber resulting in a face-sealed design against the main chamber with an o-ring. The sapphire windows are beveled at the edge that are used in conjunction with the seals. The sealing of the window is assured using a combination of three types of seals, see Fig. 3.2. The edge facing inside the main chamber is sealed within the retainer using a Teflon seal ring that acts as a primary seal. To provide an additional seal, the outer edge is sealed using a copper gasket inside the window retainer. Between the two beveled edges there is an o-ring with a backup ring on both side of it to enhance the sealing action. The window retainer entirely encapsulates the large and expensive sapphire windows to provide protection from physical damage during removal and assembly. The window retainer is also sized in a manner to prevent stress on the window from thermal gradients causing changes in the critical dimensions.

### **3.2 Fluid Systems**

It was necessary to make several upgrades to the plumbing system of the facility prior to the start of this work in order to produce the desired flow rates and temperature conditions. A process flow diagram (PFD) of the modified plumbing system is shown in Fig. 3.3. Magnified versions are presented in Appendix A. The fluid handling components in Fig. 3.3 are systematically labeled with a two or three letter designation followed by a dash and a four-digit number. The letters indicate the type of fluid

component, such as, HV for hand valve and PSV for pressure safety valve. A detailed list of the letter designation for the flow controls is in Appendix A. The first digit of the number indicates the fluid in the line, for example, 0 designates nitrogen and 1 designates helium. Helium was not used in this work, but was included in the system for ease of upgrades in the future. The second digit, ranging from 0 – 9 listed in Table 3.1, indicates the fluid subsystem based upon its function. The last two digits indicate the component number.

Gaseous nitrogen ( $\text{GN}_2$ ) is introduced into the facility from a supply line available at AFRL and regulated to a nominal high pressure of 17 MPa (2500 psi) and a nominal low pressure of 0.85 MPa (125 psi). The high-pressure  $\text{GN}_2$  is split to feed the subsystems 1 – 4. The flows sent to the injector are first thermally conditioned using heat exchangers cooled with low-pressure liquid nitrogen ( $\text{LN}_2$ ). It is more convenient to control flow rates while the nitrogen is in the gaseous phase than to liquefy and then meter the high-pressure  $\text{LN}_2$ . Four heat exchangers (designated by the letters HE) are used in the system (see Fig. 3.3) to fully control the temperatures of the flows to the injector. The heat exchangers are of counter-flow design, with the exception of HE-0107, which has the ability to operate either in counter-flow or co-flow modes. The purpose for retaining the co-flow operating mode is to provide the ability to repeat tests that were conducted prior to all the upgrades made in this system. The temperature of the annular flow is controlled by adjusting the flow rate of the low-pressure  $\text{LN}_2$  into the heat exchangers. However, due to heat transfer within the injector passages, the exit temperature of the flow issuing from the inner tube depends upon the mass flow rates of the inner and outer flows, the temperature of the outer flow at the inlet to the injector, and

the chamber pressure. It was discovered that flow from the external LN<sub>2</sub> tank produced fewer and lower oscillations in temperature than the flow from the Dewar. Therefore, for all of the data presented in this work, the chilling operation used only the external LN<sub>2</sub> tank as the flow source for the heat exchangers.

The chamber pressure can be adjusted to within  $\pm 0.14$  bar (2 psi), using a combination of three valves controlling the vent system. The three “hand valves”, see Fig. 3.3, HV-0604, HV-0605, and HV-0606 are a Hoke ¼” ball valve with a  $C_V = 0.8$ , a Parker ¼” needle valve with a  $C_V$  ranging from 0.0 – 0.43, and a Swagelok ¼” needle valve with a  $C_V$  ranging from 0.0 – 0.04, respectively. This large range in  $C_V$  values for the three valves allows accurate control of the venting of the chamber fluid, thus controlling the chamber pressure within a tight tolerance ( $\pm 0.14$  bar).

Even with the dry climate in the desert where experimental facility is located, significant frost build up on the apparatus occurs due to freezing of moisture in the laboratory air. Therefore, in order to eliminate obscuring of visual access inside the chamber it was necessary to purge the windows with dry nitrogen to eliminate frost formation. A low pressure, 1.12 bar (1.5 psig), dry nitrogen purge was introduced through the void created by a 10 cm (4”) foam seal between the main chamber and an acrylic shield as shown in Fig. 3.1.

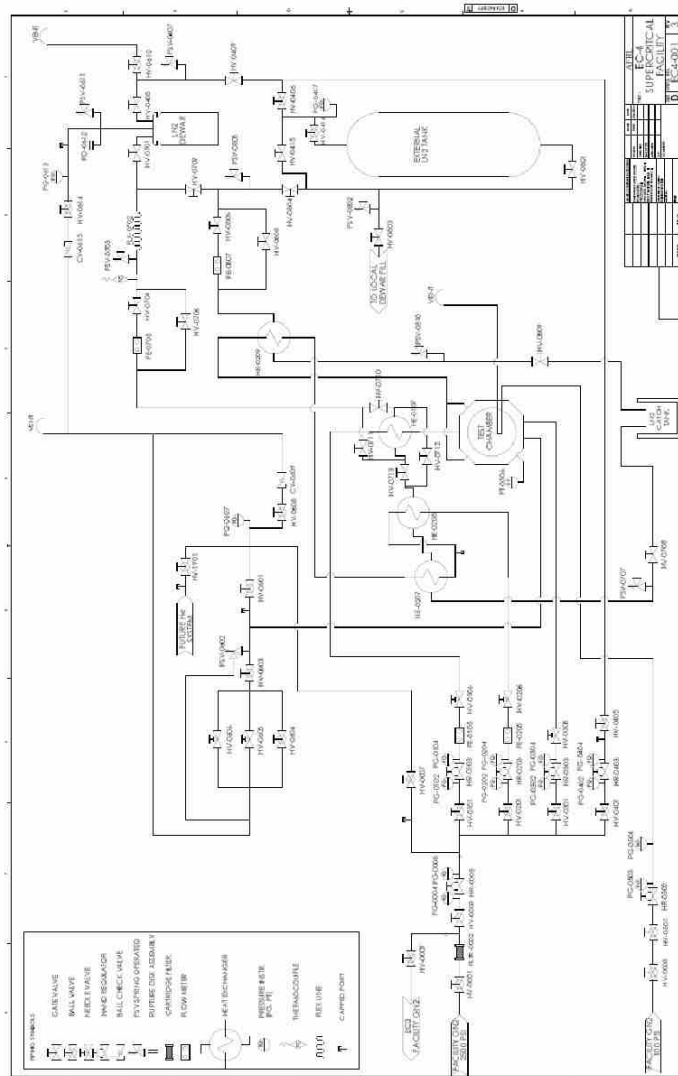


Figure 3.3: Process Flow Diagram of the AFRL Supercritical Facility. Larger format of this figure presented in Appendix A.

Table 3.1: Fluid Subsystem Number Designation.

Subsystem Number	Function
0	High Pressure Facility GN <sub>2</sub>
1	N <sub>2</sub> to Feed Center Post of Injector
2	N <sub>2</sub> to Feed Annular Flow of Injector
3	N <sub>2</sub> to Pressurize the Chamber
4	N <sub>2</sub> for Pressurization of LN <sub>2</sub> Systems
5	Low Pressure GN <sub>2</sub> for Window Purge
6	GN <sub>2</sub> Vent
7	LN <sub>2</sub> from Dewar
8	LN <sub>2</sub> from External Tank
9	Future He System

### 3.3 Shear-Coaxial Injector

The shear-coaxial injector used in this study (Fig. 3.4) was based on the well-characterized design of the single-jet injector used in this facility previously described by Chehroudi and co-workers [24-30]. The cryogenic nitrogen feeding the inner tube, producing the inner-jet, flows into the cooling tower in the injector mounting port as indicated in Fig. 3.2. The cold, but still gas or gas-like, nitrogen flow generating the annular outer-jet is introduced into two ports in a manifold ring (see Fig. 3.4). The fluid in the manifold ring is then split into four tubes flowing into the annular passage through four holes located 28 mm (1.1") upstream of the injector exit area. Teflon<sup>®</sup> (PTFE) was used as an insulating material for the injector to minimize heat transfer from the warm chamber to the cold injector assembly.

The inner-tube (center-post) was made from a stainless steel tube with an inside diameter ( $D_1$ ) of 0.51 mm (0.020") and an outside diameter ( $D_2$ ) of 1.59 mm (0.063") with a length of 50.8 mm (2.00"). The resulting length-to-inside-diameter ratio ( $L_{\text{post}}/D_1$ ) is 100, which is sufficiently long enough to ensure fully-developed turbulent pipe flow conditions at the exit. The outer stainless steel tube creating the annular passage had an inside diameter ( $D_3$ ) of 2.42 mm (0.095") and an outside diameter ( $D_4$ ) of 3.18 mm (0.125"). The resulting mean gap width of the annular passage, the hydraulic diameter, is 0.415 mm (0.016"), measured from an image of the injector. The entrance length to hydraulic diameter ratio is 67 for the annular passage. The injector has a small bias of 8% of the mean gap width. The post (inner tube) is recessed by  $0.5 D_1$ , 0.25 mm (0.010").

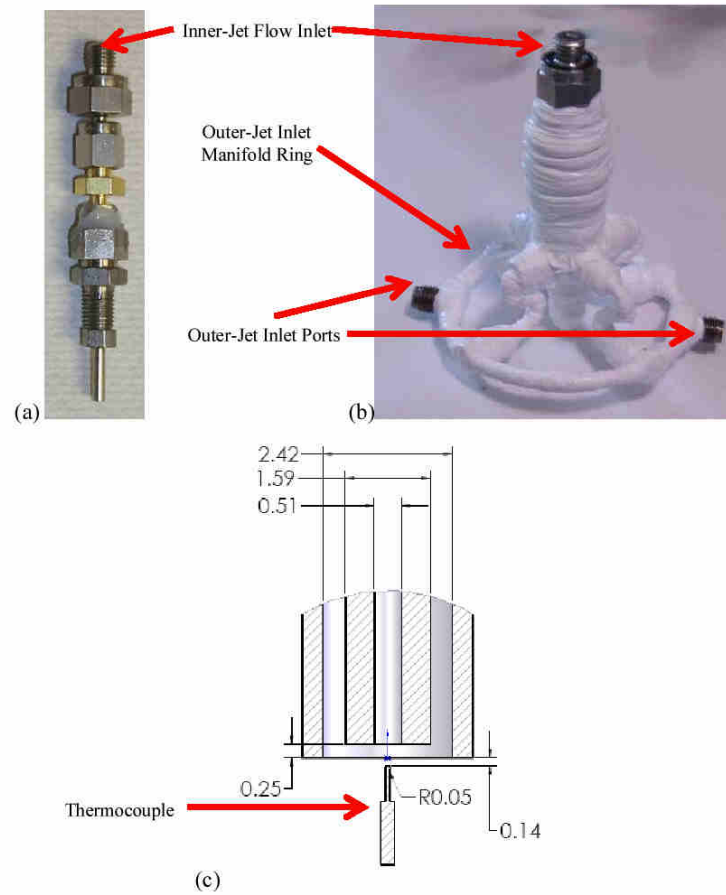


Figure 3.4: Photograph of shear-coaxial injector (a) without gas manifold and insulation, (b) with gas manifold and PTFE insulation. Scale cross-section drawing (c) of injector exit-plane area also indicates relative size and position of thermocouple used for temperature measurement. Dimensions in mm.

### 3.4 Acoustic Driver

The acoustic driver, Piezo-Siren (Fig. 3.5), used in this experiment was developed especially for this apparatus as part of a Small Business Innovative Research (SBIR) contract with the U.S. Air Force and Hersh Acoustical Engineering, Inc. A unique quality of this Piezo-Siren is the ability to produce high-amplitude acoustic waves in a high-pressure static environment. The actuator for the acoustic driver is a piezo-ceramic crystal, contained within an aluminum housing with an aluminum cone on one side to produce the acoustic waves.

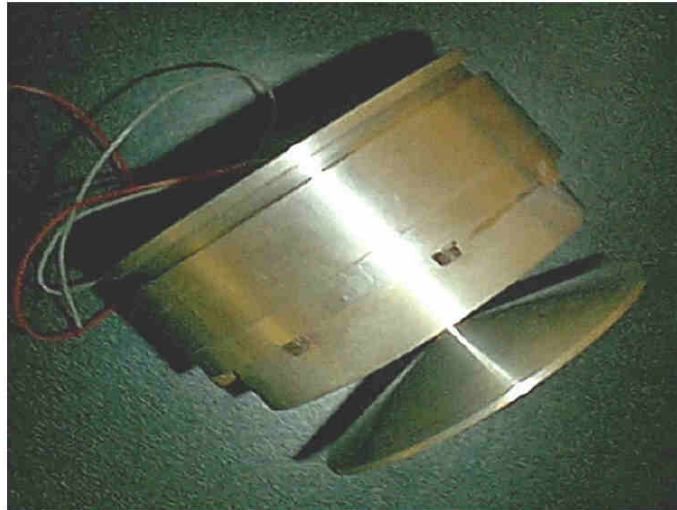


Figure 3.5: Piezo-Siren, high-amplitude high pressure acoustic driver.

The Piezo-Siren along with the wave guide (discussed below) that directs the acoustic waves to the inner-chamber are housed inside a high-pressure adaptor, externally connected to the main chamber (Fig. 3.6). The Piezo-Siren housing and the adaptor as a unit is bolted to the main chamber (see Fig. 3.1) at the location of the oblong window opening (see Fig. 3.2) and is sealed to the main chamber with o-ring face seals.

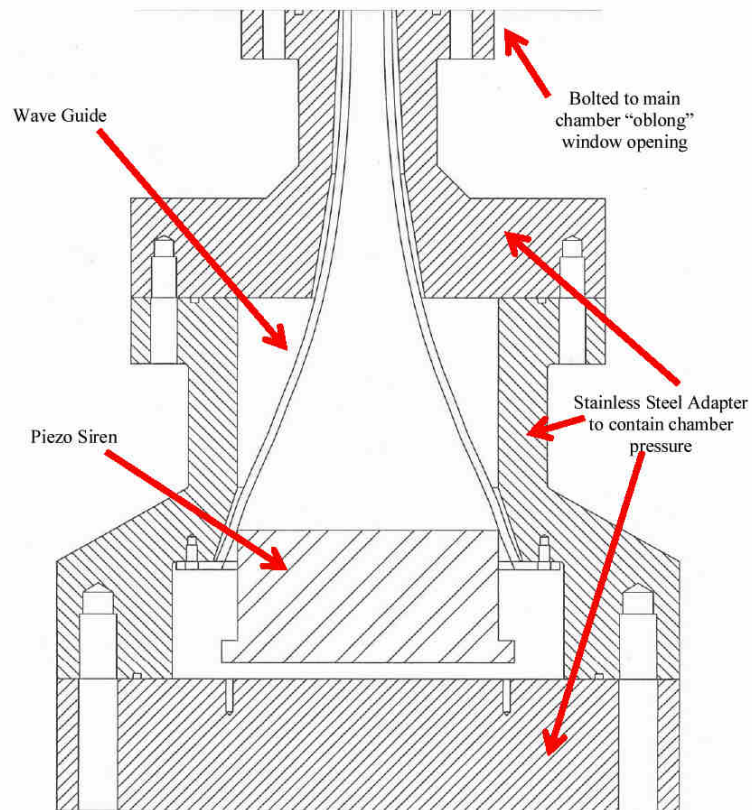


Figure 3.6: Plan view cross-section drawing of acoustic driver housing, wave guide, and assembly for attachment to main chamber.

In order to maintain the amplitude of the acoustic waves at a high level near the jet, a smaller inner-chamber, see Fig. 3.7, is housed within the main high-pressure chamber. The inner-chamber support structure is made of stainless steel, and has acrylic windows for jet visualizations. The width of the rectangular cross-section of the inner-chamber is 13 mm (0.5"). Because of the rectangular cross-section of the inner-chamber and the circular cross-section of the acoustic driver, a transition wave guide shown in Fig. 3.8 was necessary to minimize losses from the acoustic driver. The wave guide is made of copper and has a catenary contour which was designed also by Hersh Acoustical Engineering, Inc. The diaphragm of the acoustic driver has a diameter larger than the height of the inner-chamber. The rectangular cross-section of the wave guide is oriented with the longest side being parallel to the axis of the jet.

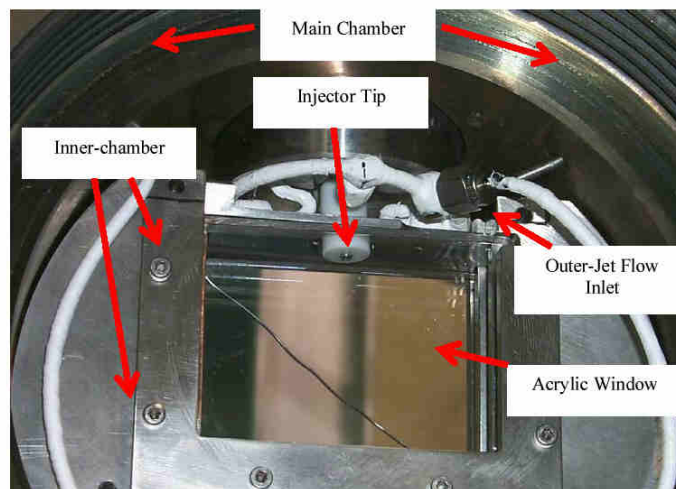


Figure 3.7: Photograph of Inner-chamber.



Figure 3.8: Acoustic Wave Guide

### 3.5 Instrumentation

The data acquisition system used for the collection of temperature, chamber pressure, and mass flow rate measurements was a Campbell Scientific CR5000 data logger. The data logger has 20 differential analog input channels, capable of acquiring data at an aggregate rate of 1000 Hz (50 Hz per channel) at 16 bits. The input channels recorded the temperature, chamber pressure, and various mass flow rate measurements.

The chamber pressure was measured by a Stellar ST 1500 pressure transducer, with a full scale range of 70 bar (1000 psi). The transducer used in the system was ordered with special manufacturer's limits of error of  $\pm 0.05\%$  of full scale (FS), which

is approximately  $\pm 3.5$  kPa (0.5 psi). However, the transducer was calibrated with a precision pressure measurement and calibration system, Ruska Model 7310, which has an accuracy of  $\pm 0.01\%$  of full scale (1.4 kPa, 0.2 psi). The calibration outcome is a plot of transducer voltage versus the reference set pressure. A linear fit to the data was then used to relate voltage to the reference pressure. Figure 3.9 shows the difference between the measured pressure (using the linear fit) and the set pressure on the Ruska precision calibrator. The calibration procedure was to first increase the pressure from the atmospheric value to 90% of the full scale. Next, the pressure was decreased from 90% FS to atmospheric, finally increasing the pressure again to 90% of the FS range a second time. The accuracy over the range of the transducer is actually about double of that reported by the manufacture (i.e.,  $\pm 0.1\%$  FS), which is approximately  $\pm 7$  kPa (1 psi). This was determined to be sufficient accuracy for this work, despite being twice the value reported by the manufacturer.

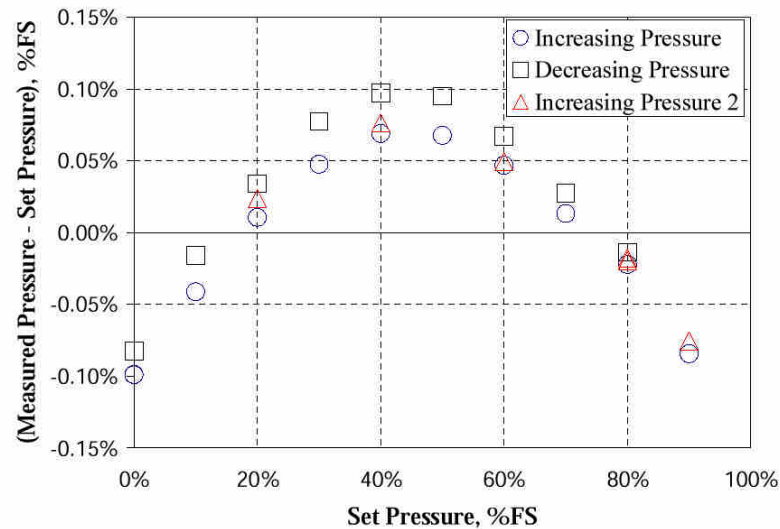


Figure 3.9: Calibration of the chamber pressure transducer. Difference between the measured pressure (using the linear fit) and the set pressure of the precision calibration device. The circle symbols indicate the increasing pressure, followed by decreasing the pressure (square symbols), finally increasing the pressure a second time (triangle symbols).

The acoustic pressure in the inner-chamber was only measured under warm chamber conditions without any fluids flowing through the injector. The pressure transducer used to measure the acoustic pressure was a Kistler model 601B1, connected to a dual mode charge amplifier Kistler Type 5010. The data acquisition system used to collect data from the Kistler transducer was a Lab Master DMA from Scientific Solutions with a maximum aggregate data rate of 100 kHz (with a 12bit A/D converter). The Kistler transducer was mounted on a traversing stage, a drawing of which is shown in Fig. 3.10. The traversing stage mounts into one of the openings for the oblong windows

of the main chamber (Fig. 3.2) using a stainless steel window blank (instead of the window) with a 13 mm diameter hole bored through to permit the traversing rod to pass into the pressure chamber. The position of the transducer is determined using a micrometer handle, Model BM32.80 from Newport Corp. The precision of the micrometer is 0.01 mm.

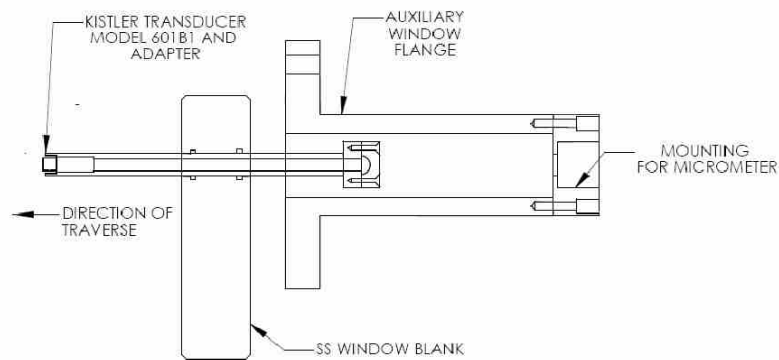


Figure 3.10: Traversing stage for Kistler transducer

Temperature measurements in the entire facility are made with Type E (chromel – constantan) thermocouples (TC). Type E thermocouples have the largest Seebeck coefficient ( $dV/dT$ ), which permits the greatest sensitivity amongst thermocouples. Accurate cryogenic temperature measurement with thermocouples is difficult. The only thermocouple type with ANSI limits of error at cryogenic temperatures is Type T (copper – constantan), but the Seebeck coefficient is about 30% smaller than a Type E [73]. Very accurate measurements were not necessary for most of the temperature measurements in this work. However, at the injector exit-plane high accuracy is required due to the need to

compute density ( $\rho$ ) from the temperature and chamber pressure measurements. These measurements are then used for the calculations of the injector exit velocities. At high chamber pressures, especially near the critical pressure of the fluid, small uncertainties in temperature can produce large uncertainties in density.

Resistance temperature detectors (RTD) are usually the thermometer of choice at cryogenic temperatures. However, due to the small probe sizes required to make high-resolution spatially-resolved measurements near the injector exit-plane area, an exposed-junction thermocouple with a bead size of 0.1 mm (0.004") in diameter was selected. Upon comparison between values obtained from the thermocouple and a precision RTD probe in saturated liquid nitrogen, it was noted that a difference of about 5 K exists between the thermocouple and the RTD data. Over the conditions of interest, errors of 5 K could produce errors in density as great as  $600 \text{ kg/m}^3$ . Clearly, the high errors in density calculations from the associated uncertainties in temperature at the 5 K level are large and need to be reduced if meaningful results are to be obtained. Therefore, it was necessary to individually calibrate each thermocouple, along with its the extension wire and the data acquisition system as a system against a precision Pt-RTD.

The precision RTD probe was from the Hart Scientific company, model number 5622-05, precision calibrated with an accuracy of  $\pm 0.04 \text{ K}$ . Several constant-temperature baths were selected to perform the calibration. The constant temperature baths used were, saturated  $\text{LN}_2$ ,  $\text{LN}_2$ /isopentane,  $\text{LN}_2$ /methylocyclopentane, ice/water, and room temperature air. At each temperature, 500 points were collected over two minutes and averaged. The resulting calibration curve in Fig. 3.11 shows a high degree of linearity in the curve fit as indicated by the correlation coefficient of nearly one. The maximum

deviation from the data to the curve fit was 0.7 K. A reasonably conservative estimate of the uncertainty using the maximum deviation and Student's t-distribution, resulted in the associated uncertainty of the thermocouple measurement of  $\pm 0.8$  K.

The calibrated thermocouple was then traversed through the jet near the exit-plane using a modified form of traversing stage described earlier for the acoustic pressure measurements (Fig. 3.10). The relative size and axial position of the thermocouple used for exit-plane measurements is shown in Fig. 3.4(c).

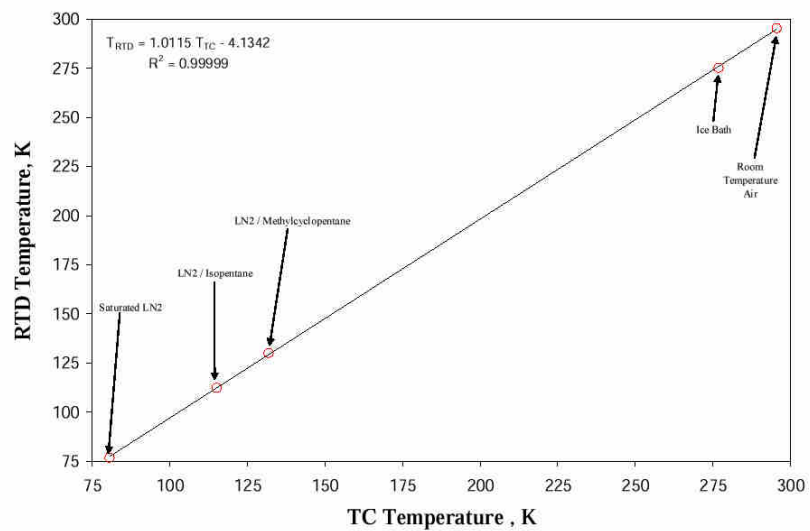


Figure 3.11: Thermocouple Calibration Curve

Mass flow rates of the gaseous streams were measured with Porter Instrument Company, Inc mass flow meters. The flow to the inner-jet was measured with a Type 122 mass flow meter calibrated for nitrogen, with a range of 0 to 50 standard liters per

minute (SLPM) (967 mg/s). The mass flow meter used to measure the flow rate of the outer-jet was a Type 123 with 0 to 200 SLPM (3868 mg/s) range, which was used for all flows less than 200 SLPM or a Type 123 with a range of 0 to 500 SLPM (9670 mg/s) for high values. The factory calibrated accuracy for all mass flow meters was  $\pm 1\%$  of FS, this accuracy was doubled for the uncertainty calculations.

### 3.6 Imaging Set-up

Most of the information about the behavior of the jet in this work comes from the flow visualizations. The jets were imaged using a back-lit arrangement with various lenses on digital cameras. One of the cameras used to capture images was a PixelFly HiRes CCD camera made by the Cooke Corporation. The resolution of the camera is 1360 by 1024 pixels with a 12 bit (A/D) dynamic range. The PixelFly was fitted with a Sigma macro zoom 28 – 200 mm lens and a c-mount-to-f-mount adapter. The framing rate of the camera was 10 Hz. The shutter speed was set at 30  $\mu$ s. A digital delay pulse generator was used to synchronize the camera with the strobe for backlighting the jets. The digital delay pulse generator was a Stanford Research Systems, Inc. model DG535. The strobe was a General Radio Stroboslave Type 1539-A, with approximately a 0.6  $\mu$ s flash time. A light diffuser was placed in between the strobe and the chamber which provided better quality images. Since the amount of the stray light from the room picked up by the camera was small, the images were primarily defined by the strobe flash.

High-speed framing cameras used in this work was a Phantom version 5.1 CMOS high-speed framing digital camera from Vision Research, Inc. with a maximum framing

rate of 95 kHz. However, the highest framing rate used here was 18.0 kHz, which provided the best trade-off between resolution (128 by 256) and framing rate. The Phantom ver. 5.1 has a dynamic range of 10 bits. Another high-speed camera used was a Phantom version 7.1 CMOS camera. The Phantom ver. 7.1 has a 12 bit dynamic range, and is capable of framing at even faster rates than the Phantom 5.1. The lens for the high-speed cameras were a 105-mm Micro Nikkor f/2.8, and a 200-mm macro Micro Nikkor f/4. Various extension tubes were also used to optimize the field of view. The high-speed images were illuminated with one of two continuous light sources available for these studies. One was a Cuda Product Corp. continuous fiber optic light source model I-150 using a 150 W Quartz halogen lamp. The other source was a 200 to 500 W mercury-xenon (Hg-Xe) arc-lamp from Oriel Instrument Corp. model number 66905. The arc-lamp was fitted with the Asperab<sup>®</sup> condenser lens to collimate the light. The shutter speed of Phantom V5.1 was set at 2  $\mu$ s, and thus the images were defined by this speed because of the continuous light source used for back illumination. The Phantom V7.1 had a 1  $\mu$ s shutter speed option.

For one particular set of tests, the two Phantom cameras were used synchronously and arranged as shown in Fig. 3.12. Synchronization of multiple Phantom cameras is accomplished by connecting the two via a communication cable and choosing one to be the master clock. Because of the available windows, it was necessary to have one of the cameras (V.5) front-lit rather than in a shadowgraph-type configuration.

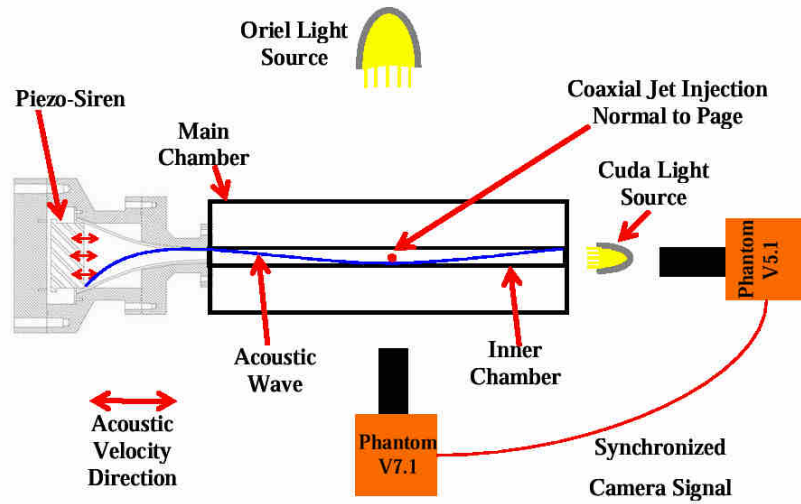


Figure 3.12: Optical layout for the two Phantom camera arrangements.

## Chapter 4

### Results and Discussion

For a given injector design, there are several major operating parameters one can vary such as the outer-jet exit temperature, outer-to-inner jet velocity ratio, and chamber pressure. Ideally, one would like to change only one of these parameters, keeping the others constant. However, in practice, this is an exceedingly difficult task. On this basis, the experimental setup was designed in such a way as to facilitate near-independent variation of these parameters. For example, changes in the outer-jet exit temperature alone affect the fluid density and therefore velocity ratio at a given fixed flow rate. Hence, to maintain a near-constant velocity ratio, the outer-jet flow rate is adjusted accordingly when its temperature is changed. The experimental matrix was organized to enable comparisons between the results at different outer-to-inner jet velocity (and momentum) ratios. Thermodynamic conditions of the jets at the exit of the injector, calculated from temperature and pressure measurements, are shown in Fig. 4.1. The vertical bars represent the uncertainty of the density values, the details of which are discussed below. The number near each data point in Fig. 4.1 corresponds to the case number listed in Table 4.1. In order to simulate and understand the effect of temperature ramping as performed in a stability rating of a liquid rocket engine, two nominal outer-jet temperatures (around 135–140 K (low) and around 185–200 K (high)) were selected, and then the mass flow rate of the outer-jet was varied to obtain a desired outer-to-inner jet velocity ratio. Some minor adjustments on the inner-jet were also required. References

to these cases in the text are made as “low” and “high” outer-jet temperatures and should be clear in the context of the discussion. The flow issuing from the center-post of the injector is referred to as the inner-jet, and that issuing from the annular coaxial region of the injector is the outer-jet. The shear-coaxial jet was excited at the first two resonance modes of the inner-chamber, which are listed in Table 4.1. The resonant modes vary slightly in frequency because of changes in the chamber temperature and pressure, ultimately affecting the speed of sound in the chamber fluid. The outer-jet temperature reported in Table 4.1 computed from by integrating the temperature profile over the region of space defining the outer-jet. The inner-jet temperature reported in Table 4.1 was taken as the centerline temperature.

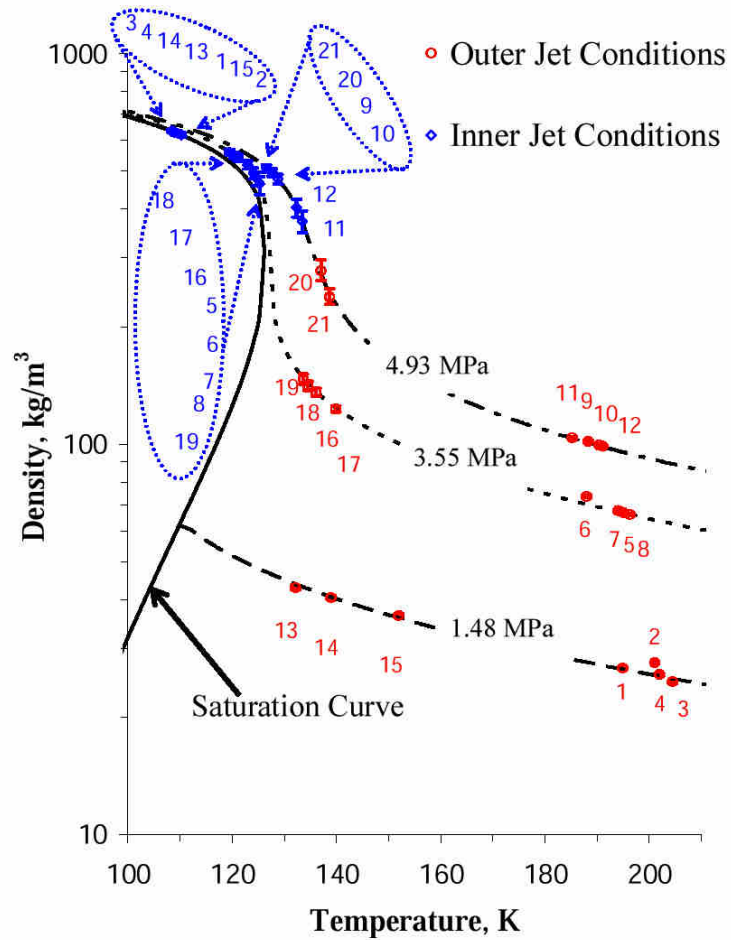


Figure 4.1: Density – Temperature ( $\rho - T$ ) diagram displaying the conditions of the inner- and outer-jets of the shear-coaxial jet. The red circles are the outer-jet conditions, and the blue diamonds are the inner-jet conditions. The numbers listed near the points correspond to the case number listed in Table 4.1.

Table 4.1: Summary of conditions measurement for coaxial jet.

Case	Chamber		Outer Jet		Inner Jet		Chamber		Outer Jet		Inner Jet		Outer Jet		Inner Jet		Outer Jet		Inner Jet		M	Acoustic Freq.		
	P (MPa)	mdot (mg/s)	T (K)	mdot (mg/s)	T (K)	T (K)	Density (kg/m <sup>3</sup> )	Density (kg/m <sup>3</sup> )	U (m/s)	Re (x10 <sup>3</sup> )	U (m/s)	Re (x10 <sup>3</sup> )	U (m/s)	U (m/s)	Re (x10 <sup>3</sup> )	Re (x10 <sup>3</sup> )	U (m/s)	U (m/s)	Re (x10 <sup>3</sup> )	Re (x10 <sup>3</sup> )		of	of	1 <sup>st</sup> Mode (kHz)
1	1.49	316	238	276	195	109	21.4	26.7	627.9	4.5	2.2	0.77	1.21	2.1	0.2	2.96	5.20							
2	1.59	767	248	280	201	110	21.9	27.6	620.8	10.9	2.2	1.87	1.27	4.9	1.1	2.89	5.16							
3	1.45	1271	249	281	204	108	19.9	24.6	634.5	19.8	2.2	2.99	1.20	9.1	3.2	2.88	5.16							
4	1.49	1602	237	280	202	108	21.6	25.7	634.6	23.9	2.2	3.81	1.19	11.0	4.9	2.98	5.18							
5	3.56	801	238	287	195	121	51.9	66.9	541.1	4.6	2.6	1.86	1.76	1.8	0.4	2.99	5.23							
6	3.70	2001	233	287	188	123	55.4	73.4	520.0	10.4	2.7	4.73	1.90	3.8	2.1	2.99	5.28							
7	3.57	3132	235	288	194	124	53.1	67.5	495.9	17.8	2.9	7.28	2.08	6.2	5.2	2.95	5.20							
8	3.55	3899	235	290	196	125	52.6	66.0	481.1	22.6	3.0	9.00	2.20	7.6	8.0	2.96	5.20							
9	4.97	1156	240	294	188	128	72.6	101.8	495.9	4.4	2.9	2.61	2.11	1.5	0.5	3.06	5.24							
10	4.95	2821	237	293	190	129	73.4	99.5	478.3	10.9	3.0	6.34	2.24	3.6	2.7	2.99	5.34							
11	4.94	4558	228	296	185	133	77.1	103.8	372.5	16.8	3.9	10.39	3.20	4.3	5.1	2.98	5.25							
12	4.94	5812	233	295	191	132	75.0	98.8	404.0	22.5	3.6	13.05	2.88	6.3	9.6	2.95	5.24							
13	1.45	1159	231	280	231	132	109	21.5	42.9	630.8	10.3	2.2	3.82	1.21	4.7	1.5	2.94	5.19						
14	1.47	1858	224	281	224	139	109	22.6	40.4	630.0	17.6	2.2	5.90	1.22	8.0	4.1	2.94	5.19						
15	1.50	2328	219	280	219	152	109	23.6	36.4	627.9	24.5	2.2	6.90	1.23	11.1	7.2	2.91	5.19						
16	3.54	1436	228	291	228	136	121	54.6	135.8	542.4	4.1	2.6	3.84	1.78	1.5	0.6	3.06	5.19						
17	3.53	3521	202	291	202	140	120	63.2	123.1	549.9	11.0	2.6	9.49	1.73	4.2	3.9	3.05	5.19						
18	3.52	5731	197	289	197	135	119	65.2	141.0	560.4	15.6	2.5	15.26	1.65	6.1	9.4	3.06	5.28						
19	3.54	7076	197	293	197	134	125	65.7	146.8	464.5	18.5	3.1	18.66	2.35	5.9	11.2	3.01	5.23						
20	4.97	2603	218	293	218	128	82.2	278.1	497.7	3.6	2.9	4.75	2.09	1.2	0.8	2.95	5.23							
21	4.88	6547	203	296	203	139	127	88.8	238.4	508.8	10.5	2.9	13.31	2.03	3.7	6.3	2.99	5.25						

#### 4.1 Uncertainty Analysis

In order to determine the measurement uncertainty, it is necessary to have both the measured value and the true value of a particular physical quantity. However, the true value is almost never known, with possible exceptions of calibration experiments when a reference point is defined by a physical state of matter, such as triple point of water. Conducting an uncertainty analysis early in the planning stages usually aids the analysis of the data after completion of the experiments. The purpose of estimating the uncertainties in an experiment is not only to determine “how good the data are”, but, more importantly, to decide whether differences between various experimental points in a given plot have a significance and lead to a proper conclusion of the trend. For example, it is known that density is very sensitive to temperature in regions near the critical point of a fluid. Therefore, great care was taken with those measurements, particularly in the calibration of the thermocouples as described in Chapter 3.

Measured quantities have uncertainties associated with them based on the accuracy of the instrument, the calibration, and the usage of the instrument. When calculating parameters from these measured independent variables, the uncertainty of a derived quantity increases based on the uncertainties of the individual terms and it varies according to the root-sum square rule. Moffat [74] describes the estimation of the derived-quantity uncertainty as:

$$\delta Q_{derived} = \sqrt{\sum_{i=1}^n \left( \frac{\partial Q_{derived}}{\partial x_i} \delta x_i \right)^2} \quad (4.1)$$

Where,

$Q_{derived}$  is the derived quantity,

$x_i$  are the independent variables used to calculate  $Q_{derived}$ ,

$\delta x_i$  is the individual uncertainty of the independent variables, and

$n$  is the number of parameters in the equation used to compute  $Q_{derived}$ .

To use Eq. 4.1 correctly, the individual uncertainties of the independent variables ( $\delta x_i$ ) must be known. Often the manufacture of an instrument will report the accuracy of an instrument as a fraction of the full scale reading. To use this information it must be converted to a standard deviation, in some manner. According to Moffat [74], this is a choice that is somewhat subjective, and the experience of the user should be relied upon. For example, in this work, the pressure transducers described in Chapter 3 have a manufacturer's reported accuracy of  $\pm 0.05\%$  of full scale reading. To gain an appreciation of what that accuracy represented, the pressure transducers were calibrated using the data acquisition system, which accounts for possible fixed errors in the measuring system and enables an interpretation of the accuracy reported by the manufacture. Fortunately, a precision pressure calibration device (Ruska, as described in Chapter 3), which has a precision of 0.01% of full scale, was available to test the reported accuracy of the pressure transducers, and offer an interpretation of the results. The value used in the uncertainty analysis was not the  $\pm 0.05\%$  of full scale output from the transducer reported by the manufacturer, but rather  $\pm 0.1\%$  (see Fig. 3.9). Part of the increase was most likely a contribution of the data acquisition system. However, an additional part was due to the manufacturer, only reporting the accuracy for the increasing pressure calibration and not accounting for the hysteresis of the transducer

upon decreasing pressure. Individual calibration of each instrument in conjunction with the data acquisition system was not possible with all the available equipment, as was the case with the mass flow meters in this work. The reported calibration sheet from the manufacture of the mass flow meters was  $\pm 1\%$  of full scale output, and a precision calibration device for the mass flow measurement was not available for this work. The manufacturer's calibration was judged to represent one half of the standard deviation. Thus the uncertainty in the mass flow measurements was doubled and then combined with the uncertainties of the data acquisition system according to the root-sum-square procedure. The temperature measurements at the exit-plane of the injector required great care. The thermocouples were individually calibrated against a precision Pt-RTD as described in Chapter 3. However, to compute the uncertainty of the temperature measurements, it was necessary to include random errors in the measurements, and then combine these using the root-sum-square process, resulting in the  $n^{th}$  order uncertainty of the measurement. Once one has the uncertainties of the individual measurements (i.e.,  $\delta x_i$ ) and an equation that relates the independent variables to the dependent variables, then Eq. 4.1 may be applied.

However, there are instances where a simple equation relating the independent variables to the dependent variables does not exist, as in the present case with the density calculations using the NIST REFPROP [14] equations of state. Moffat [74] suggests that for difficult-to-differentiate quantities, one should compute the uncertainties based upon the evaluation of  $Q_{derived}$  at  $x_i \pm \delta x_i$ , and then compute the root-sum-square deviation of the finite differences in  $Q_{derived}$  for the positive and negative variation in  $x_i$  as shown in Eq. 4.2. Caution should be exercised as to the direction of the deviation, for example

with density, a positive deviation in temperature causes a negative deviation in density. Therefore it is necessary to consider the negative deviation of temperature and the positive deviation in pressure to compute the positive deviation in density, and the opposite temperature and pressure deviations for the negative deviation in density. Moffat [74] recommends averaging the positive and negative deviations, but suggests this with caution, because a definitive analysis has not been performed as to the consequences of this averaging process. Because of the non-linear behavior of density in the regions of interest in this work, a more conservative approach to capturing the uncertainty in the variation of density was used by retaining both positive and negative deviations rather than averaging the two. Thus, occasionally producing asymmetric error bars.

$$\delta Q_{derived\pm} = \sqrt{\sum_{i=1}^n (Q_{derived}(x_i \pm \delta x_i) - Q_{derived}(x_i))^2} \quad (4.2)$$

Unless otherwise noted, all error bars on the figures in this work were computed in the fashion outlined above.

## 4.2 Exit-Plane Temperature Measurements

Owing to sensitivities of density to temperature changes, careful measurements of the temperature at the exit-plane of the jet were necessary. As previously mentioned, the thermocouple used to measure the exit-plane temperature was calibrated using a precision Pt-RTD. Because of the small size of the injector ( $D_I = 0.508$  mm), a probe of small size was necessary and a Pt-RTD was not available in the required dimensions. Therefore, the smallest thermocouple commercially available was selected, with a bead diameter of 0.10 mm. The thermocouple, attached to a support structure shown in Fig. 4.2, traversed through the jet at an axial location of about  $0.28 D_I$  downstream of the injector exit-plane (i.e., the exit edge of the outer tube, and note that the inner tube is recessed). At each radial location, 1500 measurements were taken over 30 seconds and averaged. It is also important to note that during the initial chill-down phase, this thermocouple was positioned in the outer-jet so the temperature could be monitored to achieve the desired operating conditions. However, only a coarse control over this temperature was achievable by adjusting the liquid nitrogen flow rate to the heat exchanger (see Fig. 3.3, HE-0209).

Figure 4.3 shows the measured temperature and the associated radial profiles of density computed using the NIST REFPROP [14] program with the measured temperature and chamber pressure as input data. The data in Fig. 4.3 are presented in tabular format in Table B.1 in Appendix B. The horizontal axis is the radial distance from the jet centerline and is normalized by the inner-tube inside radius ( $R_I$ ). The top, middle,

and bottom rows in Fig. 4.3, are at the nominal chamber pressures of 1.5 (subcritical), 3.5 (near-critical), and 4.9 (supercritical) MPa, respectively. The scale for the temperature profiles is read from the left axis and density on the right axis. The left and right columns in Fig. 4.3 are at the low (135 – 140 K) and high (185 – 200 K) outer-jet temperatures, respectively. The solid lines and symbols represent measured temperature profiles, and the dashed lines and hollow symbols show computed densities. Although low in resolution, temperature profiles for different conditions are shown on one page in order to facilitate comparisons of the global effects of different operating conditions as shown in Figs. 4.3 (a) – (f). However, the small-size format may not permit viewing the details, thus the individual figures are presented in full-page format as well.

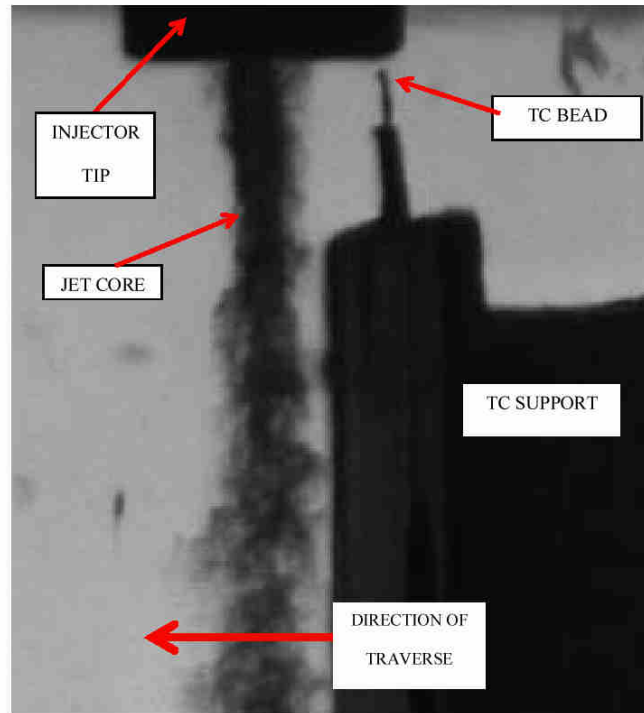


Figure 4.2: Thermocouple (TC) and the support mechanism used to perform radial temperature measurements in the coaxial jet. The thermocouple bead diameter is 0.10 mm. The resolution of the radial distance is 0.01 mm. The distance from the injector exit-plane to the thermocouple bead is 0.14 mm or  $0.28 D_j$ .

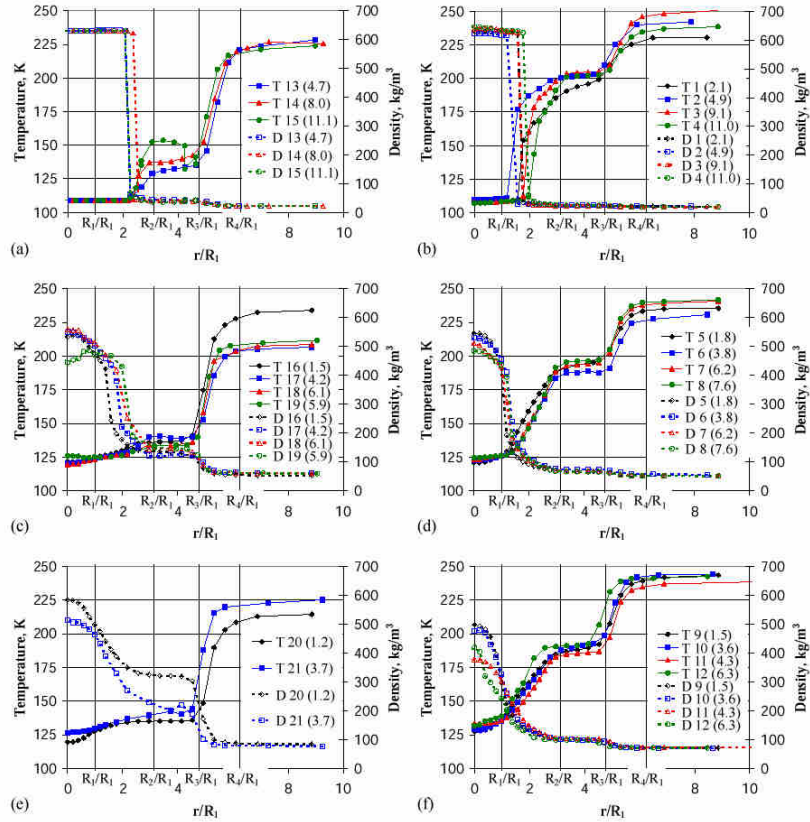


Figure 4.3: Radial profiles of the measured average temperature and calculated density. Conditions of cases are listed in Table 4.1. The chamber nominal pressure in the top row is 1.5 MPa, in the middle row is 3.5 MPa, and in the bottom row is 4.9 MPa. The nominal outer-jet temperatures in the left and right columns are about 140 K and 190 K, respectively, see Table 4.1 for exact values. The letters “T” or “D” in the inset of the figures refers to temperature or density, respectively, the next number indicates the particular case number for the data corresponding to the case listed in Table 1, and the number in parenthesis is the corresponding outer-to-inner jet velocity ratio.  $R_1$ ,  $R_2$ ,  $R_3$ ,  $R_4$  are the radii of the surfaces of the coaxial injector. For example,  $R_1$  is the inner-diameter of the inner-tube, and  $R_2$  is the outer-diameter of the inner-tube.

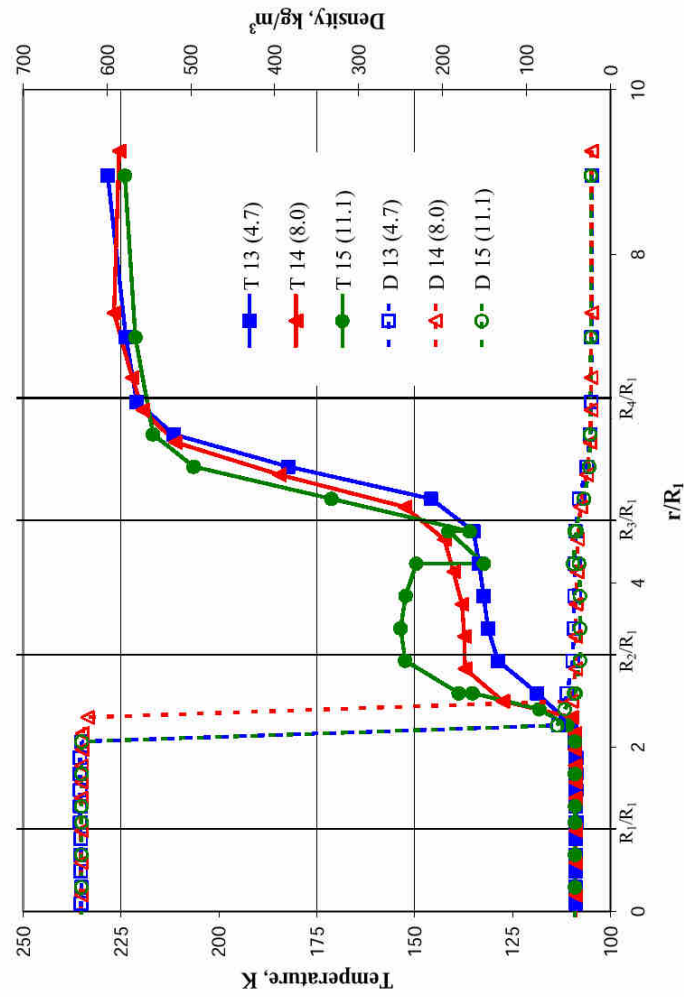


Figure 4.3(a). Radial temperature and density profiles of subcritical pressure and low outer-jet temperature.

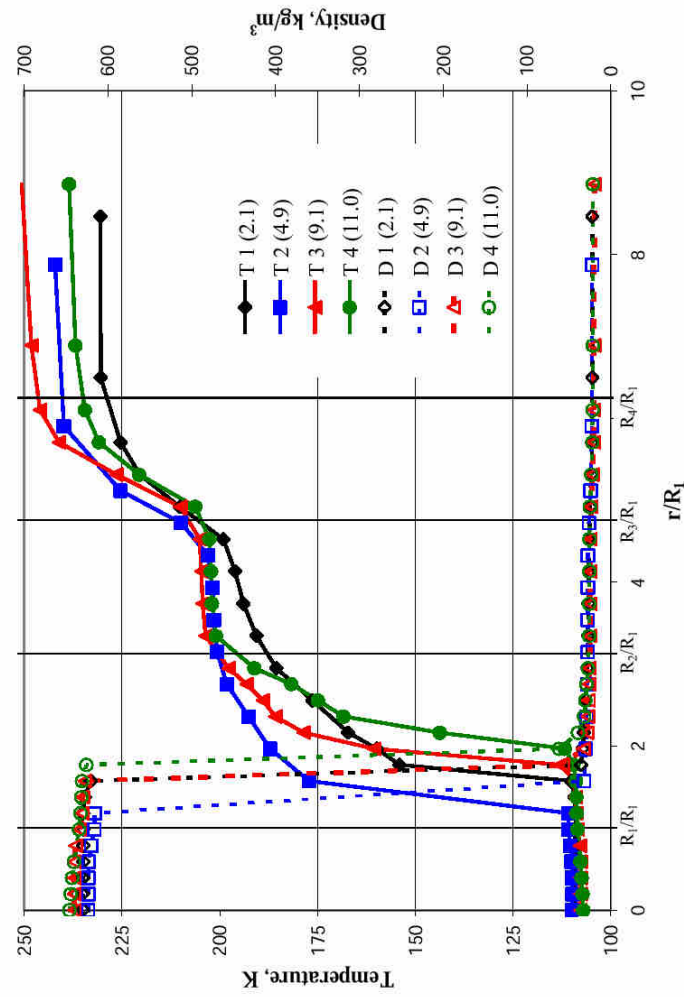


Figure 4.3(b) Radial temperature and density profiles of subcritical pressure and high outer-jet temperature.

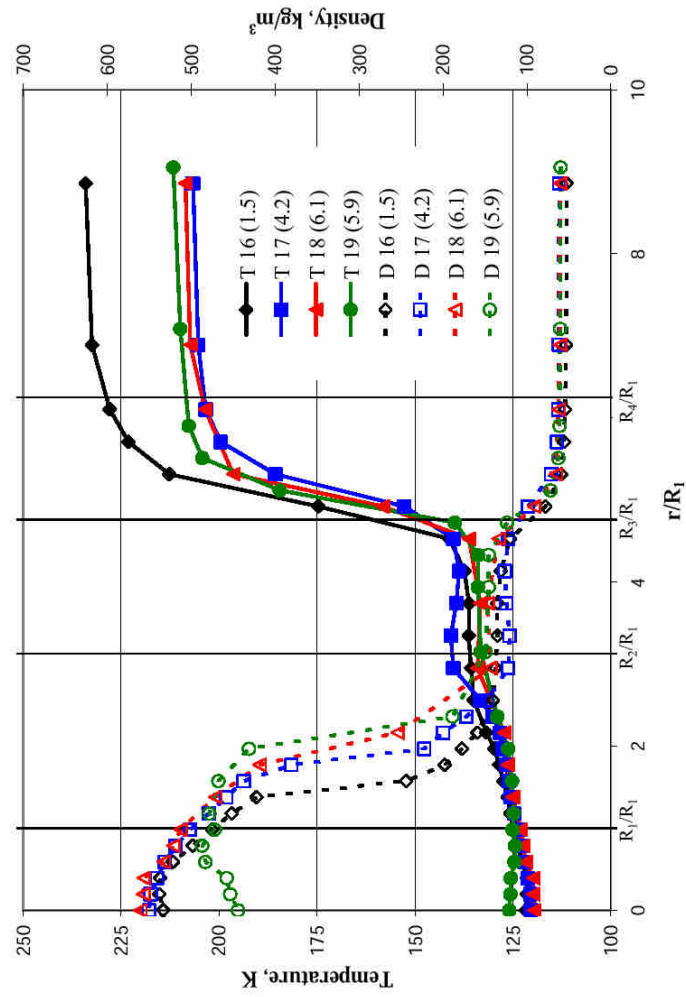


Figure 4.3 (c). Radial temperature and density profiles of nearcritical pressure and low outer-jet temperature.

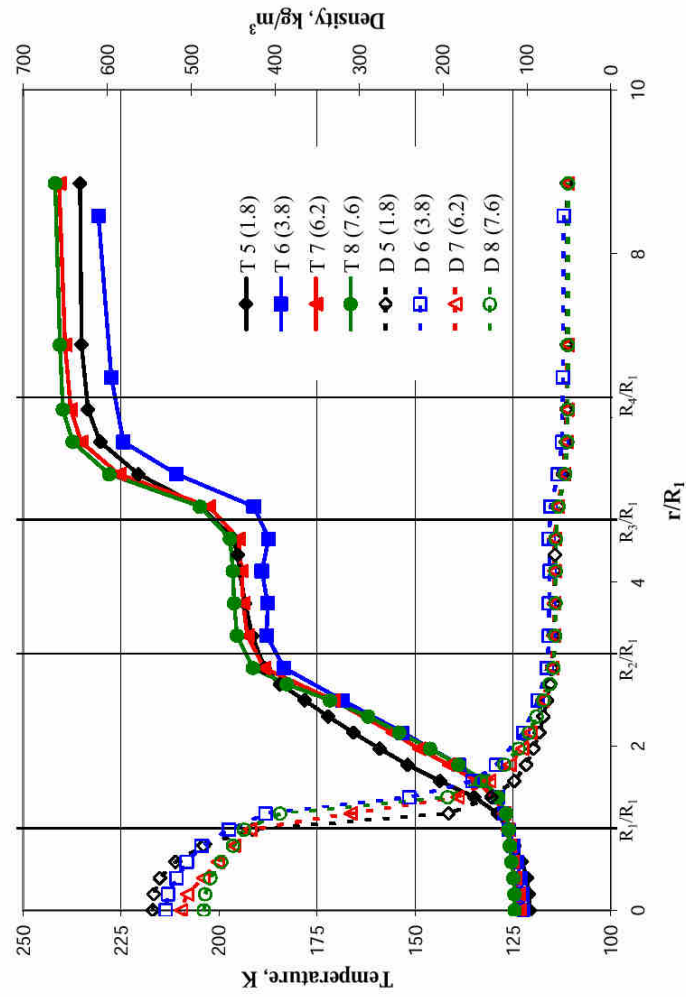


Figure 4.3 (d) Radial temperature and density profiles of nearcritical pressure and high outer-jet temperature.

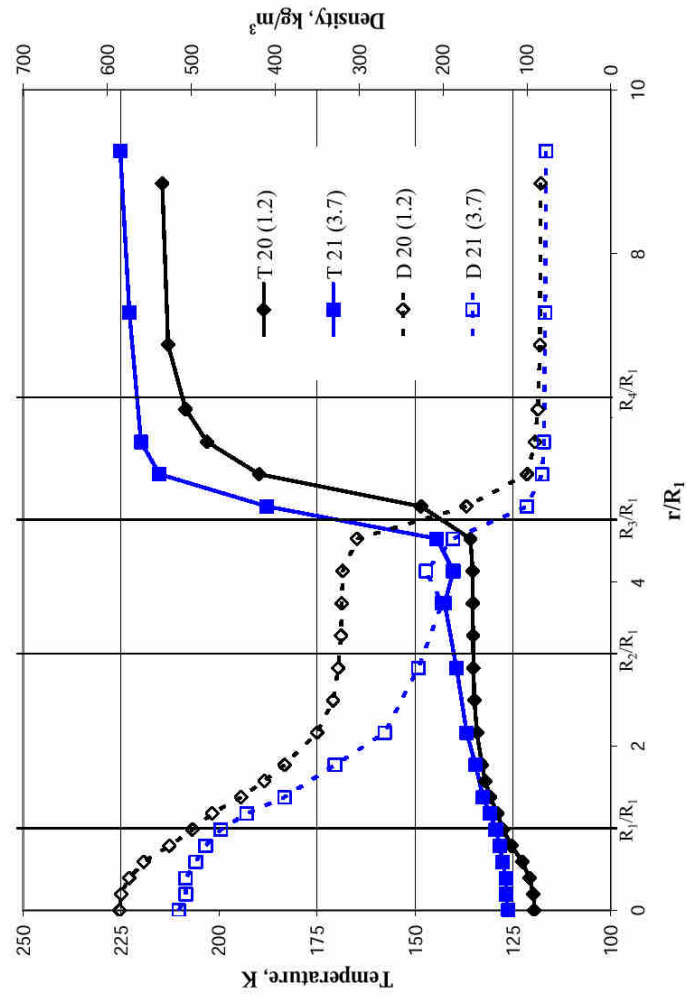


Figure 4.3 (e) Radial temperature and density profiles of supercritical pressure and low outer-jet temperature.

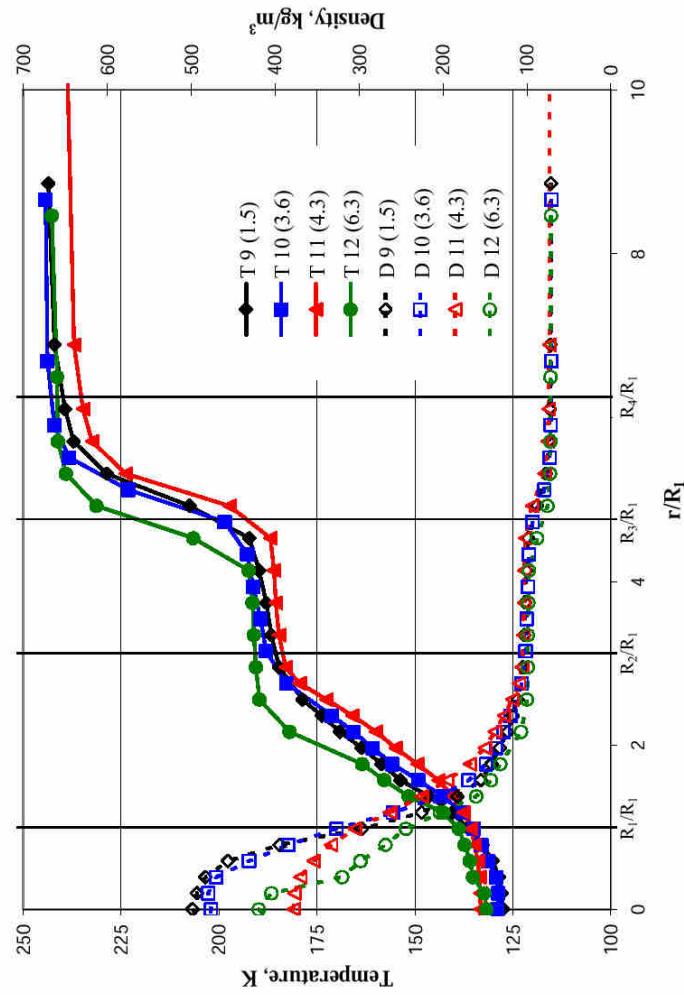


Figure 4.3 (f) Radial temperature and density profiles of supercritical pressure and low outer-jet temperature.

An attribute that the temperature profiles in Fig. 4.3 possess is that there are three distinct zones where the temperature gradient is fairly small: the core or region near the centerline of the jet, the region that defines the flow of the outer-jet, and the far-field inner-chamber environment. The temperatures in these three regions were used to compute physical properties such as densities and viscosities, which in turn were used to compute quantities such as velocity, momentum, and their appropriate ratios.

At a given subcritical chamber pressure (i.e., nominally 1.5 MPa, the top row in Figs. 4.3 (a) and (b)), both the temperature and density profiles representing the core region of the inner-jet at the injector exit area are flat in shape, producing “top-hat” density profiles. The profiles then sharply change to quite different values, typical of a transition from a liquid to a gas phase, as chamber pressure is raised. Note that for the low outer-jet temperature case (i.e., Fig. 4.3 (a)), and at the measured axial location, this constant core temperature value penetrates well beyond the inner-tube radius, up to about  $r/R_I$  of 2.5, independent of the velocity ratios used. Under this condition, variations of the velocity ratio have little impact on the radial extent of the inner-jet as defined by either the temperature or density profiles. Also, small variations in the outer-jet temperature have little effect on the calculated values for densities. However, at the higher outer-jet temperature in Fig. 4.3 (b), the radial extent or penetration of the inner-jet is strongly affected by the value of the outer-to-inner velocity ratio, primarily due to the increased heat transfer to the inner-jet from the outer-jet, both inside and immediately outside the injector. Note that the outer-jet temperature is controlled manually by changes in the liquid nitrogen flow rate to the secondary heat exchanger used to cool the outer-jet flow, see Fig. 3.3. The control over this temperature is somewhat coarse and it

is a manual adjustment, which accounts for the variations seen in the outer-jet temperatures shown in Fig. 4.3 (a). The variability of the inner-chamber temperature at the far field is related to changes in several factors, including mass flow rates of all nitrogen streams into the inner-chamber, their respective temperatures, and the length of time spent running the experiment, see Fig. 4.3 (b). Under the higher outer-jet temperature shown in Fig. 4.3 (b), the heat exchanger control system was able to maintain this temperature at a reasonably constant value and, again, small changes in temperature has only a small impact on the calculated densities at this pressure.

As the chamber pressure is elevated to a near-critical value (i.e., nominally 3.5 MPa, the middle row of Fig. 4.3, Figs. 4.3 (c) and (d)), the “top-hat” nature of the radial density profiles is lost and more rounded shapes are observed, perhaps due to the changes in the heat transfer characteristics inside the tube under elevated pressures, especially at near-critical pressures. Additionally, the temperature of the core (of the jet) at the centerline is greater than the corresponding temperatures at the subcritical pressure discussed above. The density increase within the outer-jet zone from that of the far-field chamber value, especially at lower outer-jet temperature, is larger ( $\sim 15 - 20 \text{ kg/m}^3$ ) and more noticeable than that observed under subcritical pressures (see Figs. 4.3 (a) and (b)). It is also noted that for the case “T 19” on the plot Fig. 4.3 (c), the temperature at the centerline is slightly higher (by approximately 5 K) than all the other cases, causing the density profile to exhibit its maximum value at a slightly off-axis radial location. It is believed that the thermocouple traverse plane may have moved off the axis of symmetry of the jet.

A further increase in chamber pressure to a supercritical condition (i.e., ~4.9 MPa, the bottom row of Figs. 4.3 (e) and (f)) leads to an insignificant change in the qualitative behavior of the profiles as compared to the 3.5 MPa near-critical pressure data. Again, a strong contrast is seen between the far-field chamber and outer-jet densities, indicating the sensitivity of the density to small changes in temperature under this condition. It is also noticed that at all velocity ratios, the value of the centerline temperature at the higher outer-jet temperature (Fig. 4.3 (f)) is supercritical (i.e.  $> 126.2$  K), whereas it is subcritical for all other cases in Fig. 4.3. For the lower outer-jet temperature cases, the difference in density between the outer-jet region and the far-field value is in excess of  $200 \text{ kg/m}^3$ , which makes this feature easily observable in images of the jet, but does not permit easy and clear distinction of the inner-jet dark-core area.

### 4.3 Flow Visualizations

Flow visualization of fluid flows allows for both qualitative and sometimes quantitative measurements from images. The discussion in this section will be limited to qualitative descriptions of the phenomena observed in the images of the jets.

#### 4.3.1 Qualitative Behavior of Single Round Jets

Full characterization of the behavior of single round jets is beyond the scope of this work and was done by Chehroudi et al. [24-30]. However, during validation experiments of the apparatus, interesting results were obtained from the high-speed movies. As the same injector assembly as the one described in Chapter 3 was used to produce all jet flows in this work, a single round jet was produced by turning off the outer-jet flow through the coaxial injector.

Nine sequential frames from the movie of the subcritical single round jet with a fixed inter-frame duration of 222  $\mu\text{s}$  and at a subcritical pressure (1.50 MPa) are shown in Fig. 4.4. Visible droplets on the order of 100 to 500  $\mu\text{m}$  are being ejected from the jet. Recall that the inner diameter of the inner tube ( $D_1$ ) for this injector is 0.508 mm, and the center post (or inner tube) is recessed by  $0.5 D_1$ . The apparent width of the jet at the exit-plane of the injector is about 0.85 mm, which is larger than the  $D_1$ . The increase in exit diameter of the jet is attributed to the post recess, which allows the jet to spread before being visible downstream of the recessed injector post.

The average exit velocity of the jet is 2.2 m/s ( $Re \approx 1.2 \times 10^4$ ), determined by the mass flow rate and the density calculations. From the movies, the estimated velocity of the droplets in the direction of their motion, leaving the liquid core, ranges from about 0.75 to 2.2 m/s. Once a droplet leaves the jet, the drag acting on it slows the droplet to an extent that sometimes the droplet appears to stop entirely in the chamber fluid. Because of the large temperature differences of about 175 K between the chamber fluid and the injected liquid, strong droplet vaporization is expected. The droplets that appear to come to a stop eventually evaporate completely and disappear into the chamber fluid. The combination of the motion of the droplet and the evaporation results in a visible wake behind the droplets because of the higher density of the wake relative to the chamber fluid. The combination of the droplet and the wake appear to look like a comet (see Fig. 4.4). The estimated droplet ejection angles formed between the jet's axis of symmetry and droplet trajectories vary between  $20^\circ$  and  $60^\circ$ , with an averaged angle of about  $30^\circ$ . Also, occasionally some droplets are ejected from the dark core, which are later entrained back into the jet farther downstream.

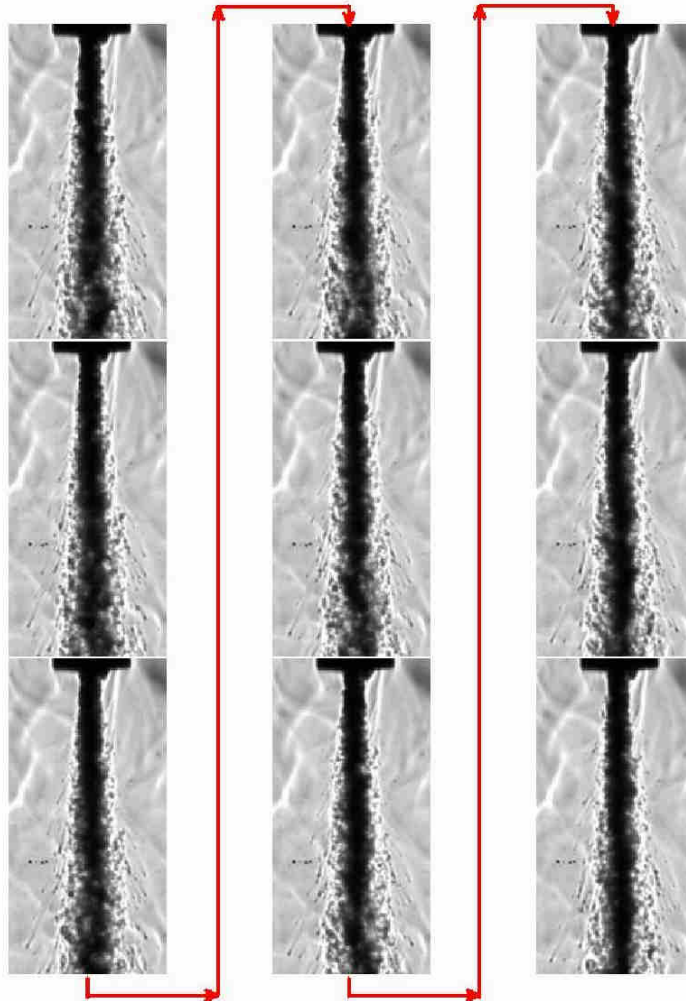


Figure 4.4: Subcritical liquid nitrogen single round jet injected into gaseous nitrogen. Nine sequential frames, starting at the top left, with a time interval between frames of  $222\ \mu\text{s}$  are shown. Time increases down the column of images. The chamber pressure was 1.50 MPa, and the velocity of the jet was 2.2 m/s. The acoustic driver is off. The scale can be determined from the injector tip outer diameter of 3.18 mm.

The vaporizing character of the dark-core of the jet along with the variable-density shear layer in the same region of space obscures high-contrast visualization of the droplet formation details in the periphery of the liquid jet. However, in the vicinity of the injector exit, where the shear layer and the vaporizing region are thin, some information on the droplet ejection mechanism is revealed. Figure 4.5 shows the formation and ejection of a droplet from the dark-core liquid surface. A bulge on the liquid surface in the first image (top left) turns into a ligament, protruding from the liquid surface, which subsequently shears off forming a droplet. As the droplet passes through the shear layer (or, vaporizing peripheral region of the jet), it becomes more difficult to discern the drop until it emerges from the layer. The wake of the vaporizing droplet is evident, particularly in the last row of images in Fig. 4.5.

The visual appearance of the drop formation is consistent with the phenomenological mechanism proposed by Wu et al. [75]. The initial ligament on the surface of the liquid jet is formed by a turbulent eddy of the size on the order of the integral length scale within the liquid jet that breaks through the surface and is subsequently sheared off from the core of the jet.

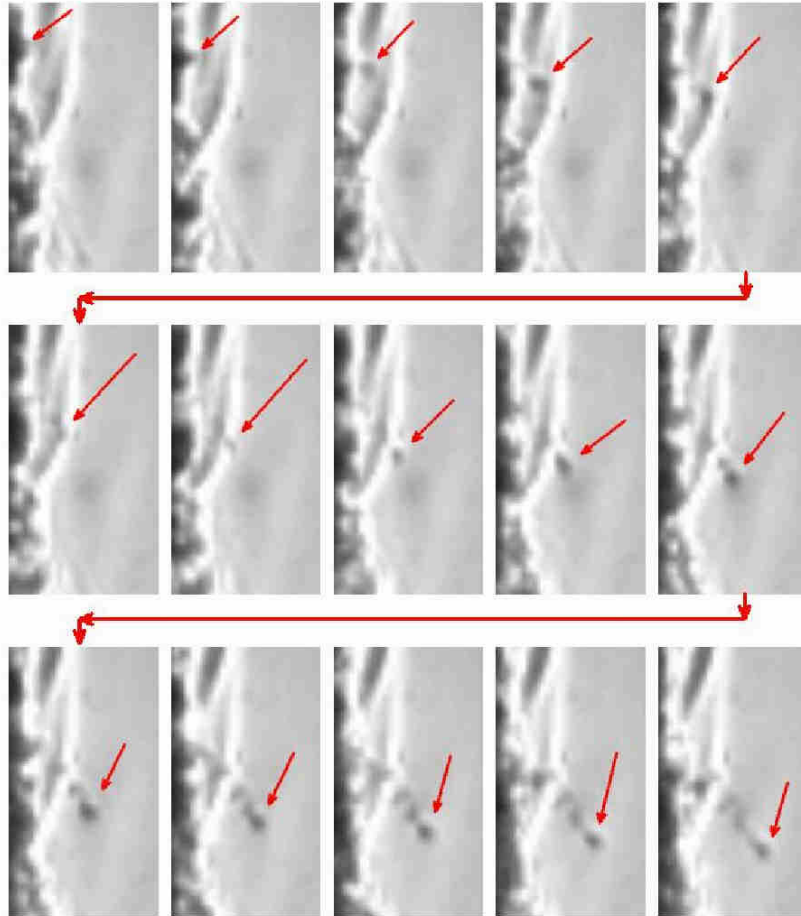


Figure 4.5: Droplet formation and ejection from liquid jet surface. Fifteen sequential frames are shown starting at the top left, with a time interval between frames of  $56 \mu\text{s}$ . Time increases across a row. The pressure was 1.50 MPa, and the velocity of the jet was 2.2 m/s. The acoustic driver is off.

Acoustic excitation of the single jet under subcritical pressures produced interesting behavior of the droplets. Figure 4.6 (a) shows an image of the jet impacted by a transverse acoustic field. The upper edge of the frame is located at about  $10 D_1$  downstream, and two expanded views of droplets are also shown in Fig. 4.6 (b) and (c). As droplets travel away from the jet, a transverse acoustic (fluctuating) velocity is imposed on the droplet motion. Evident in Figs. 4.6 (b) and (c) is a sinusoidal structure in the wake of the droplets. As time passes, droplets are completely vaporized and subsequently this wake structure disappears. In short, consider a droplet moving with some mean velocity, as it evaporates it leaves behind a wake that has a greater density than that of the chamber fluid, thus making it visible in the images. When the acoustic velocity field exists in the chamber, the observed wake indicates an approximate trajectory a given droplet has taken. Once, the droplet slows down and its mean penetration velocity approaches zero, it begins to oscillate with the chamber fluid. However, because the mean velocity of the drop is very small (or, approaching zero) at that time, the high-density wake is not visible, rather the droplet continues to vaporize until the fluid becomes indistinguishable from the chamber fluid.

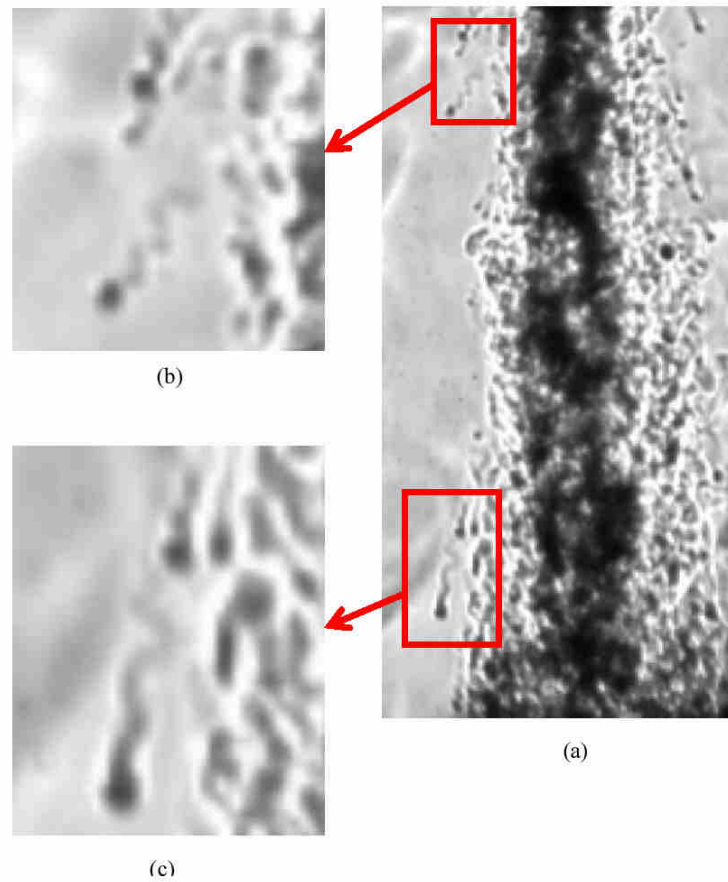


Figure 4.6: Acoustic wave interaction with subcritical liquid nitrogen single round jet injected into gaseous nitrogen. The pressure was 1.50 MPa, and the velocity of the jet was 2.2 m/s. The acoustic driver is on at 3.03 kHz, amplitude is about 170 dB. The top of the frame is about  $10 D_1$  down stream of the injector exit-plane..

Upon an increase in chamber pressure to a near, but slightly supercritical condition, substantial differences in the behavior of the single round jet are observed. Figure 4.7 shows fifteen sequential frames of the single round jet at a pressure of 3.47 MPa, which is slightly supercritical ( $P_c$  of  $N_2$  is 3.40 MPa). Droplets are not observed at this pressure, as expected. Occasionally, a fluid parcel forming from a ligament on the surface of the jet would become separated from the core similar to the droplet formation scenario observed at subcritical pressures. However, in contrast to the subcritical-pressure droplet formation, the fluid parcel remained at approximately the same location until it warms and subsequently disappeared into the chamber fluid, or was entrained back into the jet.

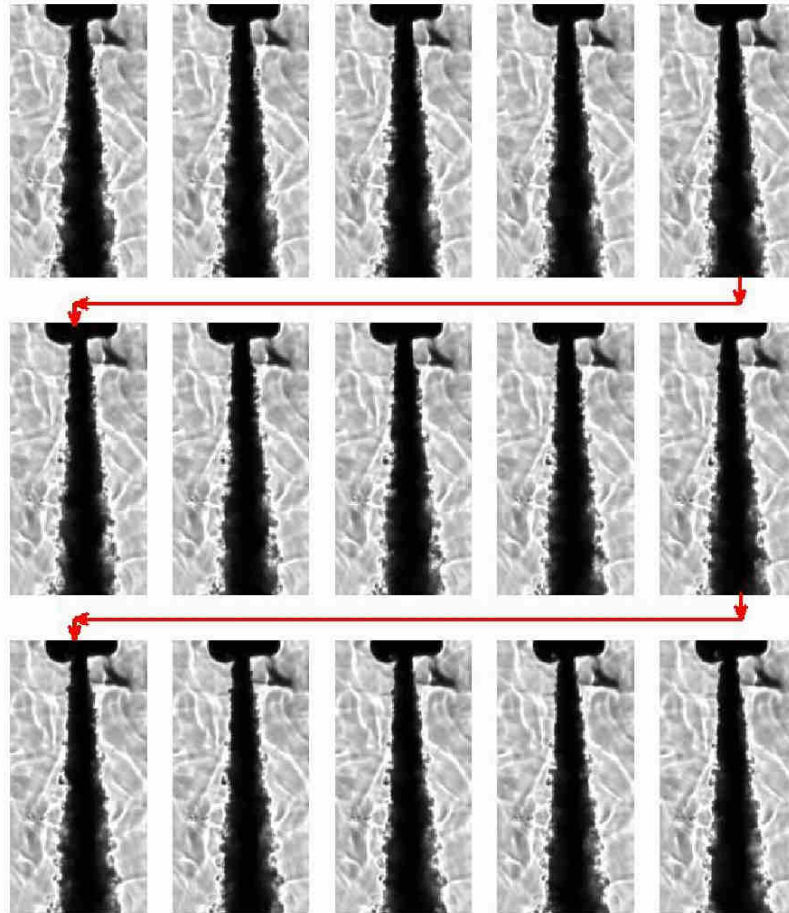


Figure 4.7: Near-critical cryogenic nitrogen single round jet injected into gaseous nitrogen. Fifteen sequential frames, starting at the top left, with a frame-to-frame time interval of  $222\ \mu\text{s}$ . Time increases across a row. The pressure was  $3.47\ \text{MPa}$ , and the velocity of the jet was  $2.2\ \text{m/s}$ . The acoustic driver is off. The scale can be determined from the injector width of  $3.18\ \text{mm}$ .

### 4.3.2 Qualitative behavior of Shear-Coaxial Jets

Flow visualization of the shear-coaxial jet provides detailed information on the flow structure, in particular, it could provide information about the atomization or breakup processes under different operating conditions (spanning sub- to supercritical chamber pressures) and on the interaction of the acoustic field with the jet. For this reason, this section is dedicated to cataloguing some of the shear-coaxial jet behavior both with and without acoustical excitation.

Figures 4.8 – 4.10 are sample images of the coaxial jet under different conditions discussed in the ensuing paragraphs. The scale presented in Fig. 4.9 is the same as those for Figs. 4.8 and 4.10. One prominent feature of these images is the so-called “dark core”, which represents the high-density region of the inner-jet. In these images, the inner-jet has a much higher density than anywhere else in the field, thus the light rays passing through this region experience large deflections causing the light rays to not be collected by the camera lens, and hence the reason for the dark, black appearance of the high-density regions. Details of this process are presented in Davis [76]. In many of the conditions, identification of the outer-jet is made difficult because of the low density and low density gradient between the outer-jet and the inner-chamber environment. However, under some conditions (see Figs. 4.3 (c) and (e) at the low temperature for near- and super-critical conditions), the density and the density gradient are large enough to easily distinguish the periphery of the outer-jet. This periphery is made visible in the high-speed images presented later in this chapter due to the choice of a new high-performance camera and improved illumination system.

Figure 4.8 shows the visualization of the coaxial jet under a subcritical chamber pressure and low outer-jet temperature. From left to right, in both rows, they correspond to cases 1 to 4 in Table 1. For the top row, Figs. 4.8 (a) to (d), the acoustic driver is off and the bottom row, Fig. 4.8 (e) to (h), shows the images corresponding to the same flow conditions as the top row but the acoustic driver is turned on. Images in the same column correspond to the same operating conditions and were taken in the same test run. The outer-to-inner jet velocity ratio increases from left to right in Fig. 4.8, while the inner-jet velocity is approximately constant. At the lowest velocity ratio (Fig. 4.8 (a)), the breakup of the jets appears to fall into the non-axisymmetric Rayleigh category, and the next higher velocity ratio (Fig. 4.8 (b)) is of the membrane-breakup type, even though the aerodynamic Weber number is much greater than that observed for water-into-air injection by Faragó and Chigier [61]. At the next two higher velocity ratios (Fig. 4.8 (c) and (d)), a fiber-type breakup is observed with a pulsating or superpulsating mode. Faragó and Chigier [61] describe the pulsating and superpulsating sub-modes of atomization as the periodic change in the axial flow direction of the liquid volume fraction, which is evident in images by the periodic appearance of dark regions downstream of the end of the core. The exit diameter of the dark core at the injector exit-plane for case 2 (Fig. 4.8 (b)) is noticeably smaller than the others. Comparison between the diameters of the high-density region defined through temperature measurements in Fig. 4.3 (b) and those of the dark core seen in the images at the exit-plane of the injector, reveals very similar trends. Upon an increase in the velocity ratio, the atomization process is enhanced, which is qualitatively visible, particularly when viewed in high-magnification images, from the decrease in the droplet sizes.

Comparing the top and bottom rows of images, a clear effect of the acoustic field is noticed for all four conditions in Fig. 4.8. The breakup of the dark core of the inner-jet is accelerated and large-amplitude wave structures are formed. From these visualizations and the high-speed movies, it appears that, near the injector exit area, the dark core of the inner-jet is “pushed out” into the path of the outer-jet flow and is then convected downstream away from the injector. The dark core develops a cusp-like structure at a distance from the injector which subsequently separates from the attached region of the jet and ultimately disappears, becoming fully mixed with the outer-jet fluid. A more detailed description of the mechanism of interaction of the acoustic wave and the jet is given later in this chapter.

Figure 4.9 shows the impact of the velocity ratio and acoustic field on the coaxial jet under the low outer-jet temperature condition. The relatively low velocity ratio condition, which would correspond to Figs. 4.8(a) and (e), is absent from the images shown in Fig. 4.9, because that particular condition was unattainable with the experimental apparatus used in this study. As seen in the temperature measurements (see Fig. 4.3), the core of the jet also appears thicker under the low outer-jet temperature case. The breakup seems to be of the fiber type with a pulsating or superpulsating sub-mode, evident from the periodic high-density structures visible in Figs. 4.9 (b) to (d). The jet responds to the acoustic field at all conditions with increasingly dramatic effects at higher velocity ratios. Comparing the linear extent of the dark core for the acoustically-excited jets of Figs. 4.9 (f) to (h) with those of Figs. 4.8 (f) to (h) show that it is somewhat longer for the former (i.e., the low outer-jet temperature case).

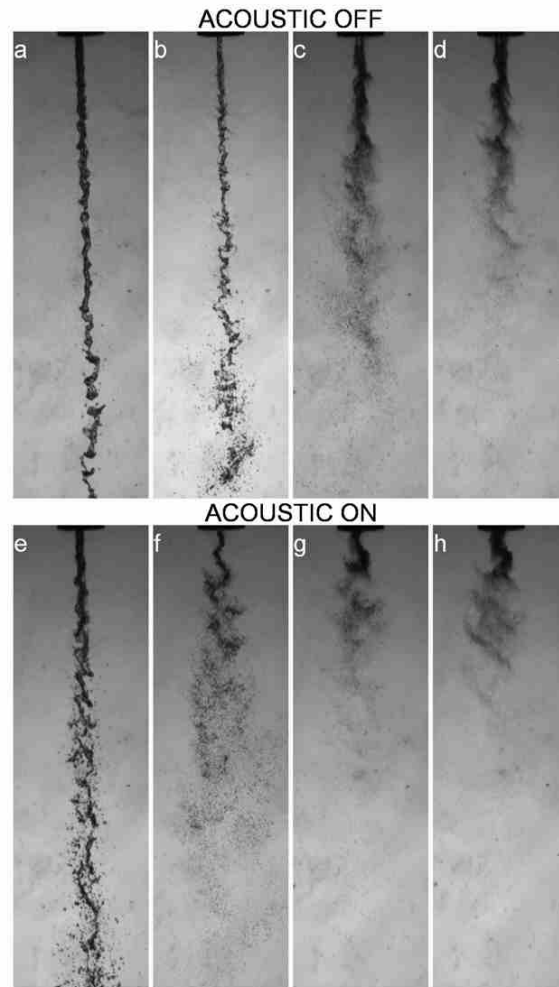


Figure 4.8: Shadowgraph images of coaxial jet at subcritical chamber pressure ( $\sim 1.5$ MPa) and at the *high outer-jet temperature* ( $\sim 190$  K) corresponding to cases 1 – 4 listed in Table 4.1 from left to right. The acoustic driver is off for images in the top row and on for the bottom row at  $\sim 3$  KHz. The velocity ratio is the same for each column and increases from left to right.

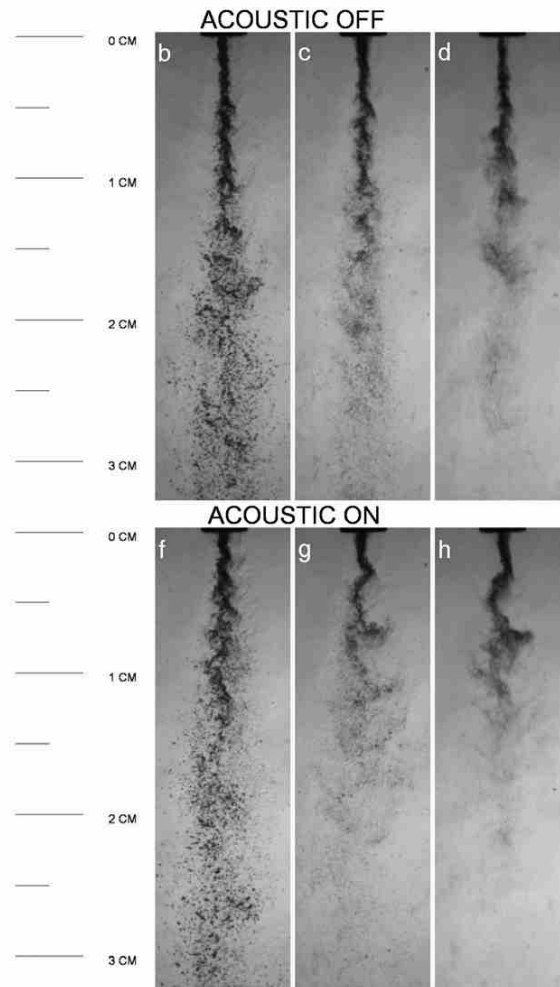


Figure 4.9: Shadowgraph images of coaxial jet at subcritical chamber pressure ( $\sim 1.5\text{MPa}$ ) and *low outer-jet temperature* ( $\sim 140\text{K}$ ) corresponding to cases 13 – 15 listed in Table 4.1 from left to right. The acoustic driver is off for images in the top row and on for the bottom row at  $\sim 3\text{KHz}$ . The velocity ratio is the same for each column and increases from left to right. The lowest flow rate condition was unattainable experimentally.

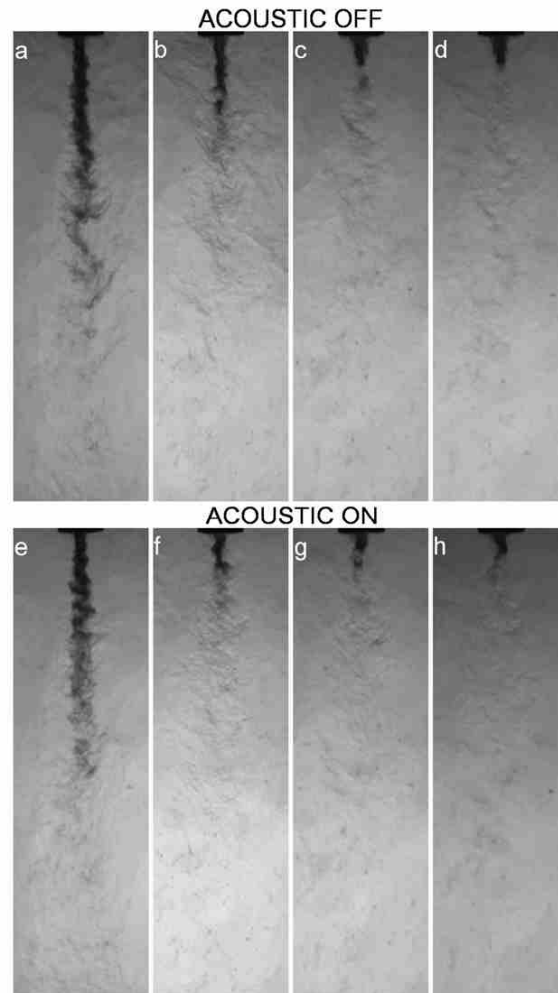


Figure 4.10: Shadowgraph images of a coaxial jet at nearcritical chamber pressure ( $\sim 3.5$  MPa) and at a *high outer-jet temperature* ( $\sim 190$  K) corresponding to cases 5-8 listed in Table 4.1 from left to right. Images in the top row the acoustic driver is off, and the bottom row the acoustic driver is on at  $\sim 3$  KHz. The velocity ratio increases from left to right.

Shadowgraph images of the coaxial jet at a near-critical (but slightly supercritical) chamber pressure ( $\sim 3.5$  MPa) are shown in Fig. 4.10, and are arranged with the same format and scale as those in Figs. 4.8 and 4.9. Droplets that were clearly detected under the subcritical chamber pressure are not present as expected (see Chehroudi et al. [27]). The length of the dark-core decreases significantly as the momentum flux ratio is increased from less than unity (Fig. 4.10 (a)) to greater than one (Figs. 4.10 (b) to (d)). For the higher momentum flux ratio (and velocity ratio) the shape of the dark core changes from cylindrical to conical. The conical shape of the core was observed only for shear-coaxial jets that were at supercritical chamber pressures.

Judging solely from the dark region of the jet, the effects of the acoustic field are less pronounced. However, from the high-speed movies taken with the Phantom camera and shown in the fourth row from the top of Fig. 4.11, the oscillation of the jet is quite visible due to the increased framing rate and the improved illumination arrangement, which allowed the outer-jet boundaries to be visualized. Figure 4.11 is composed of ten consecutive frames acquired from high-speed movie of the jet. The first and second, the third and fourth, and the fifth and sixth pair of rows are at sub-, near-, and supercritical chamber pressures, respectively. In the first, third, and fifth rows the acoustic driver is off, and in the second, fourth, and sixth rows it is on at approximately 3 kHz. The framing rate was 18 kHz, producing a time interval of  $55.6 \mu\text{s}$  between the frames. Previously reported observations by Davis and Chehroudi [32] that the effect of the acoustic field was less under near- and supercritical pressures are still valid. However, the jet oscillations in the acoustic field under near- and supercritical conditions seen in

Fig. 4.11 (using high-framing-rate camera) were not previously detected because of the low-framing-rate camera used in the early report [32].

Not immediately obvious in Fig. 4.11, but seen when played as a movie, the structures in the far-field background of the frame begin to oscillate laterally at the same frequency of the acoustic driver. One can measure the magnitude of these velocity fluctuations from the movies. Assuming that the acoustic wave in the chamber is a plane wave, the estimated pressure fluctuations from these measurements agreed with previously-measured pressure fluctuations. Details of the quantitative velocity measurements are discussed later in this chapter.

Surprisingly, at the subcritical pressures, the top two rows of Fig. 4.11, droplets are not visible, something one might expect to see under subcritical pressures. The inability to visualize droplets can be attributed to several factors. First, the resolution of the images is low, and only the largest droplets would be visible. However, because of the high velocity ratio, about 9.1, atomization is expected to be quite good and only small droplets would be produced. Also, the temperature of the outer-jet is about 96 K warmer than the inner-jet, which produces rapid vaporization of these small droplets.

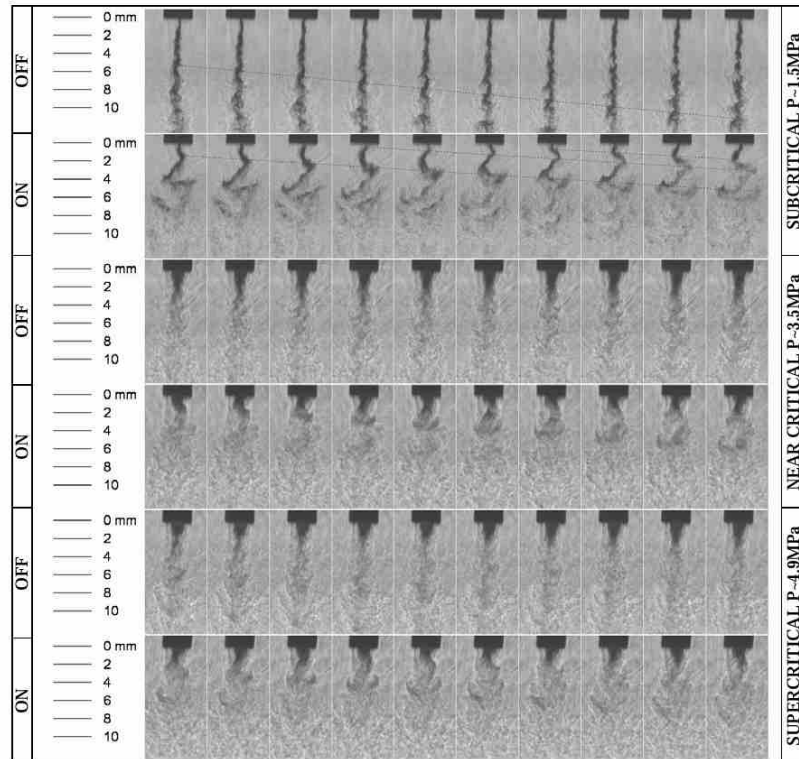


Figure 4.11: Consecutive frames from high-speed shadowgraph images of case 3, 7, and 11 (from Table 4.1) with the acoustic driver turned on and off. Time increases from left to right with an interval of  $55.6 \mu\text{s}$  between frames. The first two rows are at a subcritical chamber pressure ( $\sim 1.5 \text{ MPa}$ , case 19 of Table 4.1), the third and fourth rows are at a near-critical chamber pressure ( $\sim 3.5 \text{ MPa}$ ), and the fifth and sixth rows are at a supercritical chamber pressure ( $\sim 4.9 \text{ MPa}$ ). The acoustic driver is off for the first, third, and fifth rows and on for the second, fourth, and sixth at  $\sim 3 \text{ kHz}$ .

#### 4.4 Characterization of Acoustic Wave – Jet Interaction Mechanism

As seen from the images in the previous section, the acoustic waves can have a profound effect on the behavior of the jet. The intent of this section is to document and characterize this interaction.

##### 4.4.1 Acoustic Pressure Measurement

Pressure measurements were made under warm, ambient temperature conditions in the inner-chamber with a piezoelectric pressure transducer described in Chapter 3. The pressure transducer was traversed through the inner-chamber in order to map the variations of the acoustic pressure in the chamber at the first resonance frequency of 2.80 kHz under these conditions. Figure 4.12 is a plot of the root-mean-square (RMS) amplitude of the acoustic pressure variations in kPa on the left axis, and in dB using the standard reference pressure of 20  $\mu$ Pa on the right axis, versus the transverse distance measured from the centerline of the jet at the static chamber pressure of 1.49 MPa. The acoustic driver is located on the left side of the jet in this figure. Because of the limited range of the micrometer used for traversing the pressure transducer, and in order to be able to map the entire range of the inner-chamber, it was necessary to use a spacer bar. The right and left edges of the inner-chamber window are indicated by the dashed vertical lines, and for visual aid, the outer diameter of the injector's outer tube is indicated by the dotted vertical lines.

The mode shape suggested by the RMS of the acoustic pressure is not a pure standing wave arising from a sinusoidal source. The acoustic field shows some

asymmetry which can be seen through differences in the peak values. The amplitude of the acoustic pressure is large and finite everywhere that it was measured ranging from 2% to 7% of the chamber pressure, suggesting a potential for nonlinear wave effects. The injector is located at the minimum amplitude of the acoustic pressure field of about 183 dB. There is a step in the internal chamber where the inner-chamber window is attached to the mounting hardware. Kinsler et al. [77] state that the normal modes of an enclosure, which were based on the linear acoustic theory, can be altered significantly by changing the shape of the enclosure. The wavelength ( $\lambda$ ) measured as the distance between the local maxima on either side of the injector is 69 mm, which is much larger than the characteristic length of the injector ( $\lambda / D_1 \approx 135$ ), placing this in the long-wavelength limit.

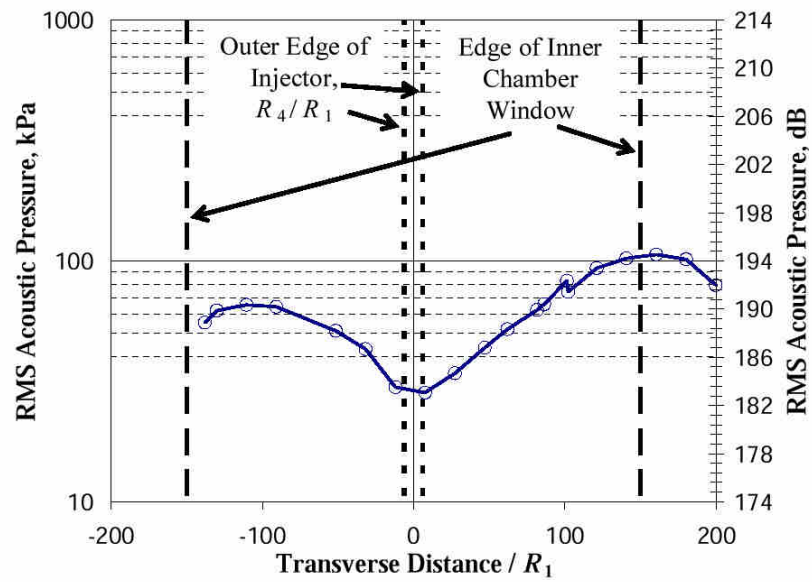


Figure 4.12: Variations of the RMS of acoustic pressure oscillations (in kPa on the left axis, and in dB on the right axis) along the length of the inner-chamber. The static chamber pressure was 1.49 MPa, and the temperature was ambient  $\sim 300\text{K}$ . The acoustic driver is located at the far left position.

It was found that if the acoustic driver operated at power levels below the maximum available with the equipment used in this work, the effects of the acoustic field on the jet were greatly reduced or not discernable. A plot of the RMS amplitude of the acoustic pressure oscillations at the first resonance frequency of the inner-chamber with chamber pressure is shown in Fig. 4.13. The acoustic driver was operated at its maximum power setting for the data in this figure as well as all data acquired in this work. In Fig. 4.13, the transverse position of the piezoelectric pressure transducer was 1.75 mm away from the jet centerline on the right side of the injector (using Fig. 4.12 as the reference for right and left sides). The reduction in the RMS of the acoustic pressure oscillations with an increase in chamber pressure was due to increased density of the chamber fluid considering that a constant input power was supplied to the driver. Details of this statement are discussed in section 4.4.3 below.

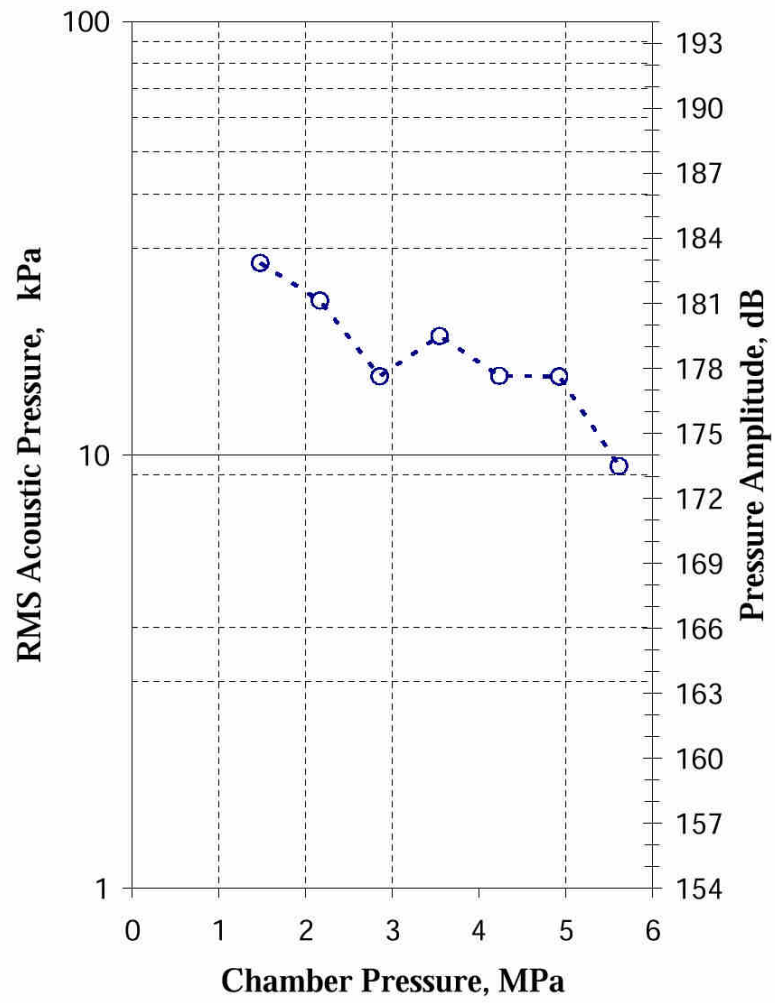


Figure 4.13: Variation of the RMS of the acoustic pressure with the chamber pressure, measured 1.75 mm to the right of the injector centerline in the direction away from the acoustic driver.

#### 4.4.2 Acoustically-Driven Mode of the Shear-Coaxial Jet

The oscillatory mode of the jet was expected to be three dimensional and possibly helical by inspection of the movies of the type used to construct Fig. 4.11. Many phenomena in nature are three dimensional, and a natural instability mode of a jet can be helical. Particularly in this case, the “cusp-shaped” structures, formed from the dense dark-core fluid when approaching the shear layer between the outer-jet and the chamber fluid, suggested that the mode may be helical. Movies of the acoustically-excited jet, viewed perpendicular to the acoustic velocity direction, can only capture a portion of the information. An analogy, albeit crude, can be made to that of a spinning string. If one holds a given length of a string at one end and spins it (helically), while looking only perpendicular to the length of the string with one eye closed (to eliminate depth perception), then the string would appear to have a “cusp-like” structure. However, upon oscillating the end of the string with a “back and forth” motion (as opposed to spinning) and viewing the string in the same manner, the “cusp-like” structure is not observed. Only by looking at the string with both eyes open is that the true behavior of the string is revealed. Therefore, it was necessary to view the jet with two synchronized high-speed cameras to reveal the true modal behavior of the jet.

The two phantom cameras were synchronized, oriented orthogonal to one another as described in Chapter 3, and then images of the jet were taken. One camera viewed the jet perpendicular to the acoustic velocity fluctuations and the other parallel, or pointed into the acoustic velocity direction. Figure 4.14 consists of twelve sequential images in

each column, with direction of increasing time indicated by the arrows. The images in columns one and two show results for when the acoustic driver is off, and columns three and four indicate results when the acoustic driver is turned on at 3.03 kHz. In each row, the images in columns one and two are taken at the same time. Similarly, the images within the same row in columns three and four are taken simultaneously. The images in columns one and three view the jet perpendicular to the acoustic velocity fluctuations, and columns two and four see the jet parallel to it. The images taken perpendicular to the acoustic velocity fluctuations (columns one and three) are shadowgraphs, but images viewed in the parallel direction are forward-illuminated. A different light configuration for the parallel case was required because of the location of the acoustic driver which was blocking the optical access for back-illumination. This accounts for the differences in the background and the outer-jet region of the flow seen between the two cases in Fig. 4.14. The chamber pressure of the jet in Fig. 4.14 was 1.57 MPa (subcritical). In these tests, it was necessary to reconfigure the chamber by replacing the traversing thermocouple assembly with a window in its opening to view the jet in the direction parallel to the acoustic velocity. Therefore, no exit-plane temperature measurements were made and consequently the values for density, velocity ratio, and momentum flux ratio are not as accurate as the other measurements reported in this work. The outer-to-inner-jet velocity ratio and momentum-flux ratio are estimated to be 10.4 and 4.6, respectively.

Comparing the jets in the first two columns of Fig. 4.14, with the acoustic driver off, periodic structures in the jet are visible, which are associated with the pulsating or superpulsating sub-mode of atomization in both viewing directions. However, upon exciting the jet, a large-scale sinusoidal structure of the dark core was observed only

when viewed perpendicular to the acoustic velocity direction. Viewing the jet in the parallel direction does not reveal the same large-scale oscillations of the core. This suggests that oscillatory motion of the jet is predominantly in the direction of the acoustic velocity direction and no helical mode exists. Some three-dimensional movement of the core does occur, but these motions do not take place in the same periodic manner as do the jet oscillations in the direction of the acoustic velocity. The large-scale oscillations of the dark core seen in the third column of Fig. 4.14 are periodic and correspond to the acoustic driving frequency.

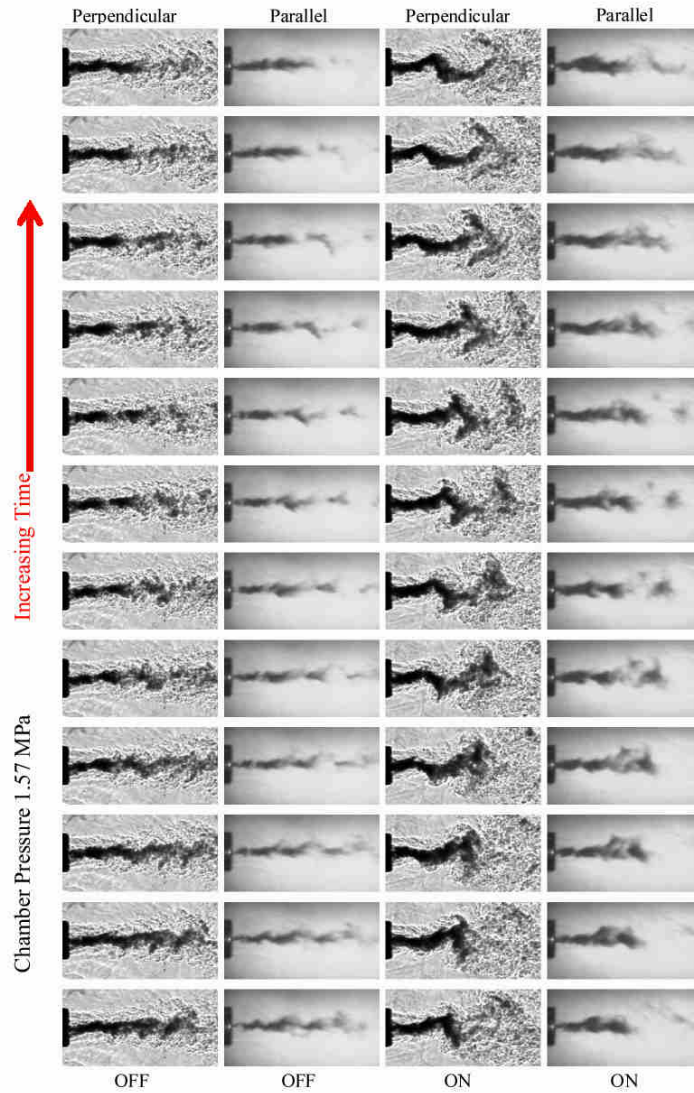


Figure 4.14: Synchronized images viewed both perpendicular and parallel to acoustic velocity direction. Columns 1 and 2 acoustic driver is off, 3 and 4 on at 3.03 kHz.

By changing the driving frequency to the second resonance frequency of the inner-chamber a decrease in the wavelength defined by the core of the jet is observed. Figure 4.15 is composed of six sequential frames taken at 18 kHz of the shear-coaxial jet at the same conditions with the acoustic driver turned off in the first column, on at 2.98 kHz in the second column, and on at 5.16 kHz in the third column. A wavelength,  $\lambda$ , can be defined as the distance between the peaks of the sinusoidal structure formed by the dark core of the jet. When the frequency of the acoustic driver was increased to the second resonance mode, the wavelength,  $\lambda$ , of the dark core decreased. For the images a wavelength could be identified from the core of the jet, the mean wavelength was always shorter for the higher frequency mode than the lower one.

The characteristic time for a fluid particle to move from one peak to the next peak,  $\tau_\lambda$ , should be given by the distance traveled, which is approximately,  $\lambda$ , divided by some characteristic velocity,  $u$ . The acoustic time scale is given by the time period for one cycle,  $f^{-1}$ , or inverse frequency. If indeed the acoustic driving force is the cause for the oscillation of the core, the ratio of these two time scales, a Strouhal number,  $St = \lambda f / u$ , should be unity. A difficulty with this relationship is the determination of an appropriate velocity scale,  $u$ . In the absence of such a velocity scale, a ratio of  $St$  evaluated at two frequencies at the same velocity conditions of the jet, should be constant. Measuring  $\lambda$  from the images is not always easy to perform, particularly at near- and supercritical chamber pressures. Therefore, measurements were made from the subcritical pressure jets from 30 images where the wavelength could be measured on most images to within  $\pm 10$  pixels accuracy.

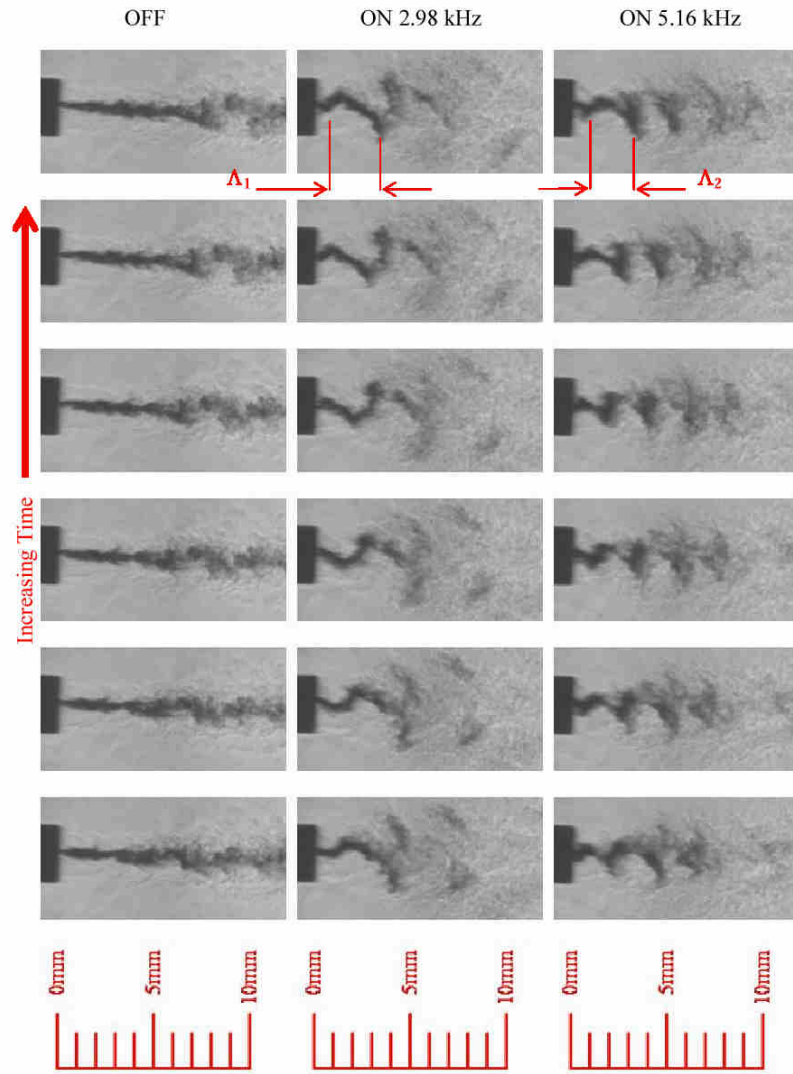


Figure 4.15: Consecutive images framed at 18kHz of case 3 of Table 4.1. Column 1 acoustics off, column 2 acoustics on at 2.98 kHz, column 3 acoustics on at 5.16 kHz.

Figure 4.16 is a ratio of the  $St$  for the jet at the same flow conditions, evaluated at the second resonance frequency to that of the first resonance frequency. As described above, this ratio should be a constant if the acoustic driver is controlling the oscillation of the core. The error bars on the figure represent the  $n^{th}$  order uncertainty analysis (as described in the beginning of this chapter) for 30 images taken at a 10 Hz sampling rate while the jet was excited at the two resonance frequencies of the inner-chamber. Although this only represents two frequencies and results carry large error bars, with the exception of one point, the ratio of the averaged  $St$  evaluated at the two frequencies is constant (mean value of  $\sim 1.4$ ) at various velocities of the jet to within  $\pm 25\%$ .

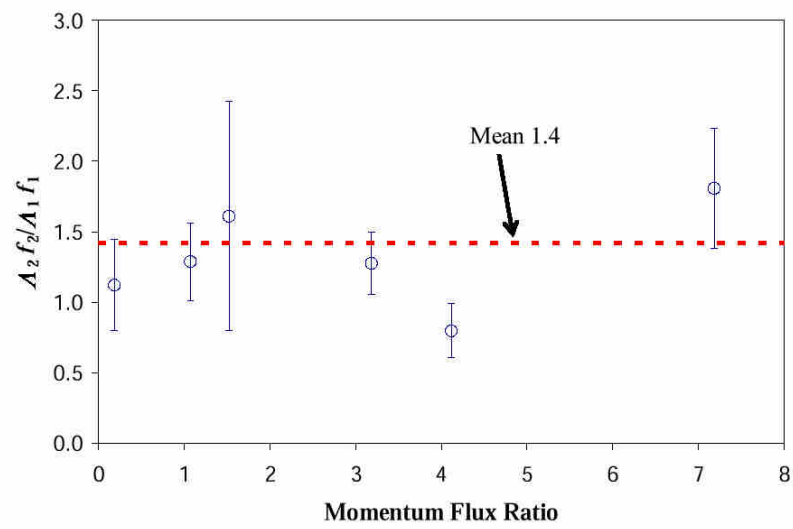


Figure 4.16: Ratio of the wavelength measured from the dark core of the jet multiplied by the frequency of the acoustic driver for the second resonance frequency (subscript 2) to the first resonance frequency (subscript 1) as a function of momentum flux ratio.

#### 4.4.3 Acoustic Velocity Measurements

When viewing the movies of the jet, one can visually track fluid structures, possibly suggesting that velocity can be measured from these consecutive images. These structures in the fluid could be treated as though they were seed particles such as usually done with particle imaging velocimetry (PIV) or molecular tagging velocimetry (MTV). Velocity from unseeded flows has been attempted previously by Okamoto et al. [72] using a spatial cross-correlation between shadowgraph frames to determine motion, and ultimately velocity.

To compute velocity, the displacement of a fluid structure (i.e.,  $\Delta x$  or  $\Delta y$ ) and a time interval ( $\Delta t$ ) between frames are required. Velocity is then simply approximated by  $\Delta x / \Delta t$ . A difficulty arises in obtaining the displacement of the fluid for an unseeded flow. From the movies taken in this work, structures are visible in the background and in the jet. Using a spatial cross-correlation (Eq. 4.3) between consecutive frames, these structures, which may or may not be identifiable to the human eye, can serve as particles from which displacements can be measured. However, the difficulty is that, unlike solid particles, fluid particles have the ability to dilate in addition to translation and rotation. Additionally, the shadowgraph is a line integral technique. Thus it not only obtains information from a very narrow slice of the flow field similar to PIV, but also collects data from the entire depth of field.

$$R_{p,q} = \frac{\sum_{i=0}^n \sum_{j=0}^m f_{i,j} g_{(i+p,j+q)}}{\sqrt{\left( \sum_{i=0}^n \sum_{j=0}^m f_{i,j}^2 \right) \left( \sum_{i=0}^n \sum_{j=0}^m g_{(i+p,j+q)}^2 \right)}} \quad (4.3)$$

Where,

$f$  is the region of interest in the first image of size  $n \times m$  pixels,  
 $g$  is the region of interest in the second image of size  $n \times m$  pixels,  
 $p$  and  $q$  are the displacement of the  $n \times m$  window in the second image in the  $x$   
and  $y$  directions, and  
 $R$  is the value of the spatial cross-correlation.

The method for determining the displacement at a given location starts with selecting an  $n$  by  $m$  region of interest (ROI) in an image (named, source window) centered at that location. Next, a region of interest of the same size in an image taken at a later time, but displaced from the first image ROI (or, source window) by  $(p,q)$  (named, search window) is selected, and a correlation coefficient,  $R_{p,q}$ , is computed. This process is repeated for various  $p,q$  combinations, moving the search window, creating a spatial cross-correlation for each  $p,q$  pair. The location of the maximum of the spatial cross-correlation  $(p_I, q_I)$  for the interrogation domain, is assumed to correspond to the displacement of the fluid particle (i.e.,  $\Delta x = p_I$  and  $\Delta y = q_I$ ). The attainable maximum resolution is  $\pm 1$  pixel, although some authors [78] performing similar MTV measurements have reported subpixel accuracy by fitting high-order polynomials to the spatial cross-correlation space. However, in this work no physical reason presents itself to justify that the spatial cross-correlation space should vary as a high-order polynomial for improvement of the measurement accuracy.

Initially, the movies used to measure velocities were of low resolution (128 x 256 pixels) images because of the high-framing rate (18 kHz) and the limitations of the Phantom v.5 camera. Also, the available camera lenses used with this camera produced a scale for the image that was equal to 19.2 pixels per mm. The cross-correlation technique, described above, was applied to the acquired movies, a frame of which is represented by the image in Fig. 4.17 (a). Small boxes drawn on this image, each indicates a source box at which frame-to-frame fluid displacement was measured by calculation of the cross-correlations. The spatial cross-correlation space for the fifth source window from the left in Fig. 4.17 (a) is shown in Fig. 4.17 (b). To obtain reliable estimates of the displacements, it is necessary to have a strong gradient in cross-correlation space in two orthogonal directions. The spatial cross-correlation space shown in Fig. 4.17 (b) possesses the strongest gradients of all the source windows shown in Fig. 4.17. The shape of the spatial cross-correlation space indicates that only the transverse direction, the direction of the acoustic velocity, possesses a strong gradient, and thus the displacement measurements in that direction is reliable. It should also be mentioned that in PIV and MTV work, the spatial cross-correlation values are lower than what is obtained here. Nearly all values of the spatial cross-correlations for reasonable search distances is greater than 0.9. Generally, in a PIV approach, the field is illuminated with a laser sheet, producing images by elastic scattering from the particles. The resulting images are mostly black (low gray scale values), with some white particles (high gray scale values) producing typically lower values of the spatial cross-correlations. The images here, however, have intensities spanning the entire dynamic range, and correlating gray with gray yields higher spatial cross-correlation values.

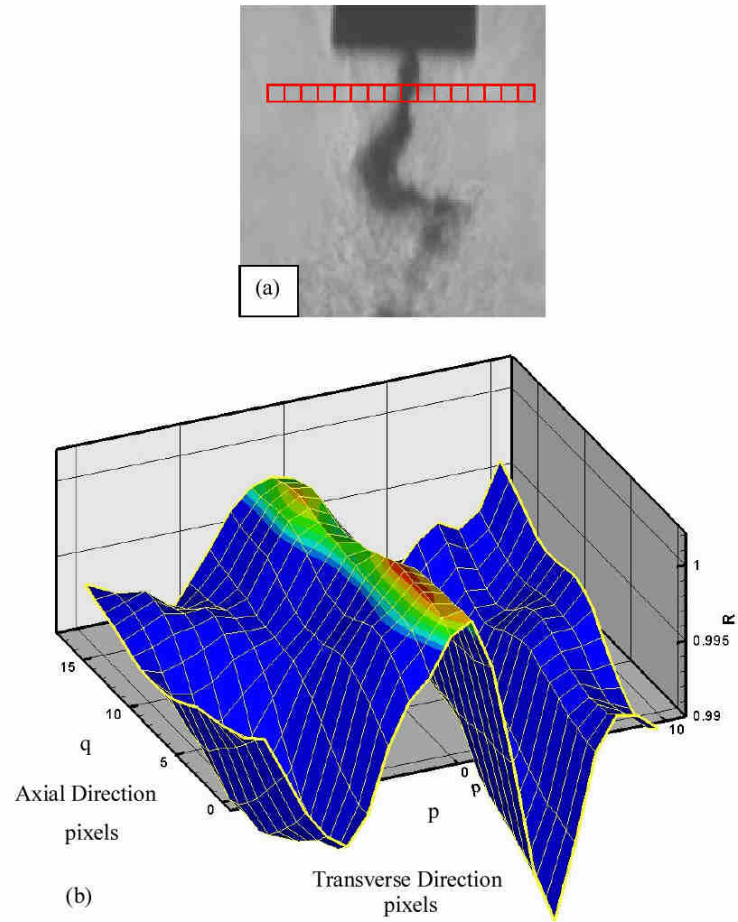


Figure 4.17: An image frame from a movie with boxes indicating the locations of the source windows for the spatial cross-correlation calculations (a), and (b) shows the spatial cross-correlation space for the fifth source window from the left in (a).

The transverse velocity measurements obtained from a sequence of images in a high-speed movie like that shown in Fig. 4.17 resulted in displacements with a very limited range, that is, -1 to 1 pixel. This is due to the resolution, field of view, and sampling time of the image frames. A balance between this range of motion and the sampling frequency needs to be made. On one hand, large displacements from longer times between frames enhances the dynamic range of the velocity measurement, but, on the other, it increases detection noise due to more distortion of fluid structures. Alternately, decreasing the sample time decreases the noise in velocity measurements, but can severely limit its dynamic range.

Despite the low dynamic range of the transverse velocity, a Fourier transform (128-point fast-Fourier transform (FFT) of the transverse velocity signal) was performed on the velocity. A power spectrum normalized by the dc component is shown in Fig. 4.18 for the first two resonance modes of the chamber at (a) 3.06 kHz and (b) 5.16 kHz, respectively. Evident from the large peak of the power spectrum is that the transverse velocity in the chamber responds to the acoustic driver at the same frequency, see Fig. 4.18 (a). At the higher resonance mode (Fig. 4.18 (b)), a measurable peak is observed at the driving frequency of 5.16 kHz. The sampling frequency (i.e., the image framing rate) was 18 kHz, resulting in only about 3.5 samples per cycle at 5.16 kHz. Consequently, a small peak due to aliasing appears at half the driver frequency.

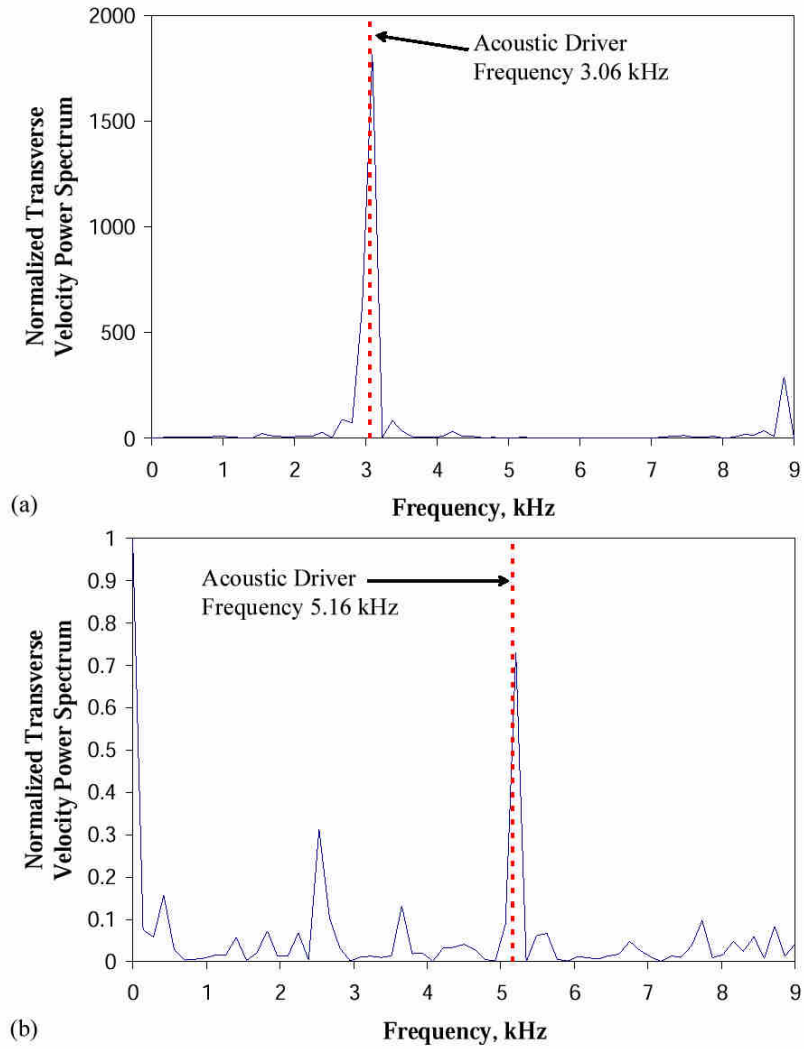


Figure 4.18: Power spectrum of the transverse velocity signal normalized by the dc component. The acoustic driver frequency was (a) 3.06 kHz and (b) 5.16 kHz, respectively.

Upon obtaining a Phantom v.7 camera, which has enhanced resolution at higher framing rates and a lens capable of increasing the magnification, the dynamic range of the velocity measurements was increased without suffering increased detection noise in the velocity signal. Additionally, the spatial cross-correlation space improved by showing a stronger gradient in two orthogonal directions. Figure 4.19 is the spatial cross-correlation space of the increased magnification and resolution image. This configuration gives an image scale of 62.4 pixels per mm, an increase of more than three times over the image shown in Fig. 4.17 (a). Improvements in the dynamic range of the transverse velocity measurements resulted in increased range of displacement to  $\pm 4$  pixels, at the same 18 kHz sample rate for subcritical jet, at the expense of a decreased field of view. From these improved velocity measurements, it was estimated that the fluid element displacements can be measured to within  $\pm 1$  pixel. The source window was selected to be square in shape and its size for the rest of the velocity measurements was 21 by 21 pixels. A study of the size of the square source window was done by varying its dimension from 3 by 3 pixels to 33 by 33 pixels. Once the size of the square was greater than 15 by 15 pixels, the velocity signal, in the form of displacements, did not change by more than the  $\pm 1$  pixel. The source window size for the rest of the velocity measurements was then set at 21 by 21 pixels. Rectangular pixel windows were not investigated.

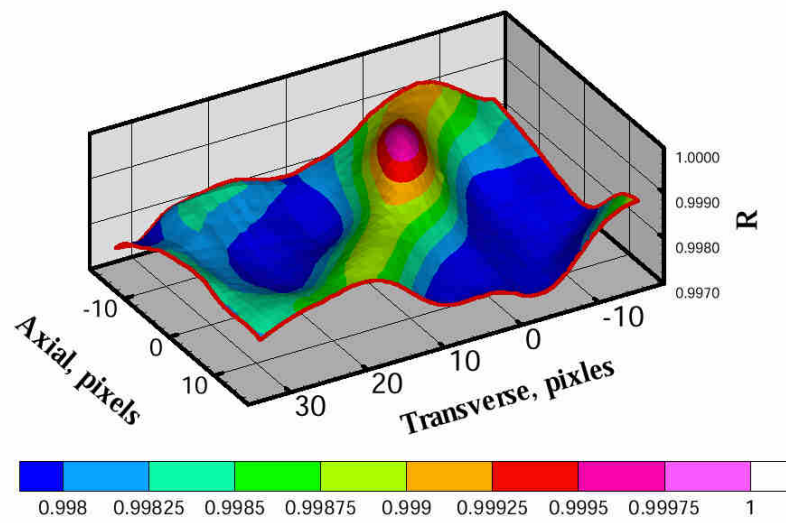


Figure 4.19: Spatial cross-correlation space for image resolution of 512 x 256.

From displacement measurements of chamber fluid elements, the transient start-up phase of the acoustic driver was captured. Figure 4.20 shows the start-up transient of the transverse velocity fluctuations of the chamber fluid for, (a) a subcritical chamber pressure of 1.49 MPa and, (b) for a near-critical chamber pressure of 5.36 MPa. The positive velocity points in the direction of the push stroke of the acoustic driver (i.e., left to right in Fig. 4.12), and the negative velocity direction is in the pull stroke. At the subcritical pressure (Fig. 4.20 (a)), the behavior of the acoustic velocity resembles that of a transient pressure trace for the onset of a combustion instability, resulting in a limit-cycle. A bias in the maximum amplitude exists in the positive direction by equivalent of one more pixel of motion in the images. Because the uncertainty of the measurement is  $\pm 1$  pixel, the conclusion from this observation is not certain. However, at times greater than about 23 ms after the start of the acoustic driver, the measured amplitude does not change. At the near-critical chamber pressure (Fig. 4.20 (b)), the transverse velocity range is reduced to the equivalent of  $\pm 1$  pixel. Although the same optical arrangement was used at both pressures, most likely the amplitude of the acoustic wave was reduced at higher pressures, a subject further discussed in the next section. The first observable motion at both pressures, however, occurs within one frame of each other, at approximately 2.17 ms after the start of the acoustic driver.

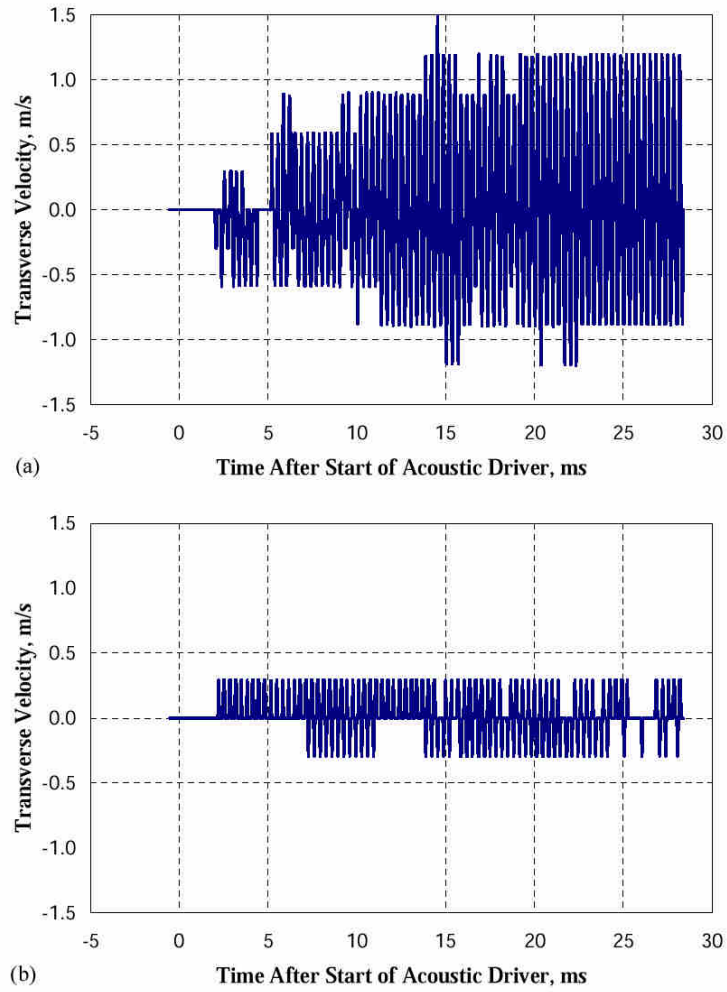


Figure 4.20: Transient transverse velocity after start of the acoustic driver, at chamber pressures of (a) 1.49 MPa and (b) 3.56 MPa, respectively. The acoustic driver frequency was (a) 3.01 kHz and (b) 3.04 kHz, respectively.

Because of the limited dynamic range of the system at the higher pressure conditions, the analysis of the velocity was restricted to a subcritical pressure. Figure 4.21 is the transverse velocity signal measured at an axial distance of  $1.4 D_1$  downstream of the injector exit-plane and at transverse distances measured from the jet centerline of  $4.86 D_1$  (in the chamber fluid),  $2.24 D_1$  (at the edge of the outer-jet), and  $0.73 D_1$  (at the edge of the inner-jet), moving toward the acoustic driver. These measurements were made from the same movie used to make the measurements in Fig. 4.20 (a), except about 100 ms after the limit cycle behavior was established. The transverse velocity measured in the chamber fluid (Fig. 4.21(a)), far from the influence of the jet, appears to be sinusoidal in nature. However, the velocities measured at the edge of the outer- and inner-jets, Figs. 4.21 (b) and (c), respectively, have a certain level noise superimposed on the sinusoidal variations, which is possibly due to the jet turbulence.

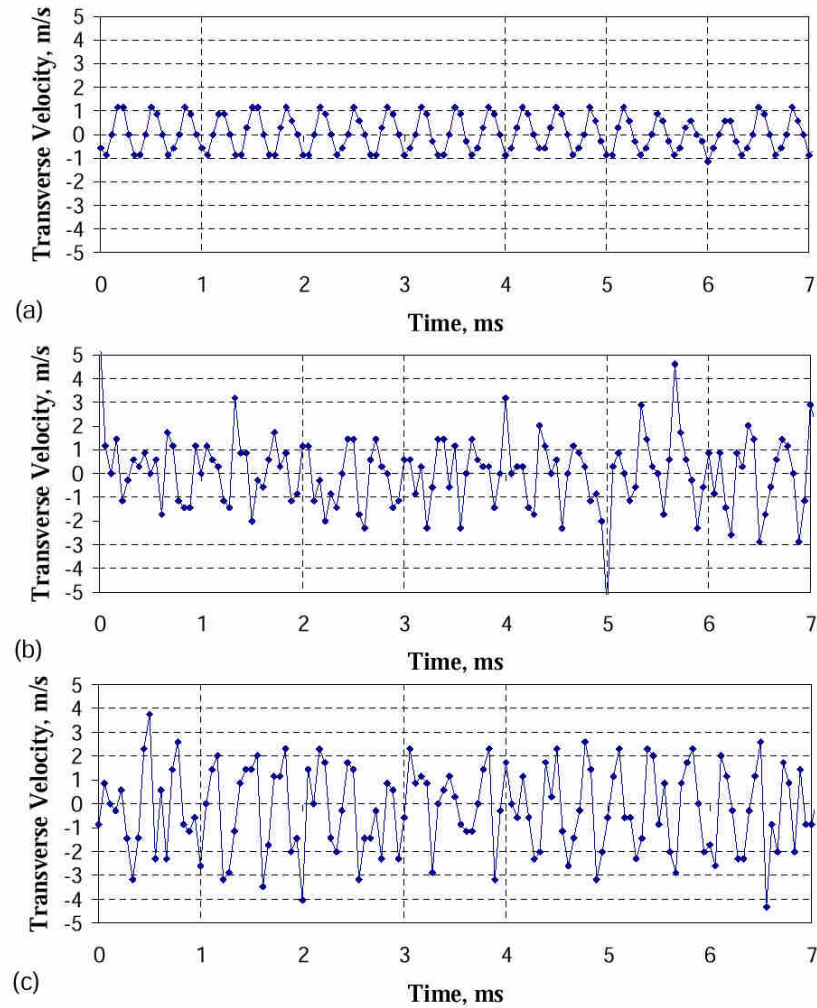


Figure 4.21: The instantaneous transverse velocity measured at  $1.4 D_1$  downstream of injector exit-plane, at progressively closer radial distances to the injector centerline: (a)  $4.86 D_1$  from the centerline of the jet in the chamber fluid, (b)  $2.24 D_1$  from the centerline at the edge of the outer-jet, and (c)  $0.73 D_1$  from the centerline at the edge of the inner-jet. The chamber pressure was 1.49 MPa.

Within the uncertainty of the measurements, the mean of the three transverse velocity signals shown in Fig. 4.21 is zero. The root mean square (RMS) of the transverse velocity ( $V_{RMS}$ ) variations plotted versus the transverse position ( $x$ ) is shown in Fig. 4.22. The RMS transverse velocity in the chamber fluid is lower than what is measured at the edge of either the outer-jet or inner-jet. It appears that  $V_{RMS}$  at the edge of the inner-jet is the largest, but, to within the uncertainty of the measurement, it can not be reliably determined to be different from the  $V_{RMS}$  at the edge of the outer-jet.

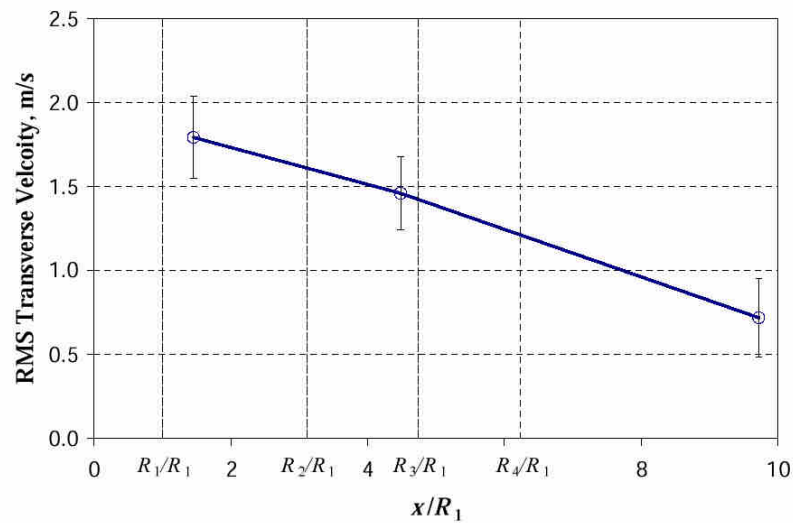


Figure 4.22: RMS of the velocity signal variations with transverse direction ( $x$ ). The error bars on the figure correspond to the  $n^{\text{th}}$  order uncertainty as described in the beginning of chapter 4. The vertical gridlines are the four important radii of the shear-coaxial injector. The chamber pressure was 1.49 MPa.

The power spectra of the three velocity signals in Fig. 4.21, computed from a 128 point FFT, are shown in Fig. 4.23. All of the power spectra in Fig. 4.23 are normalized by the value at the peak value of the power spectrum of the velocity signal measured in the chamber fluid (Fig. 4.23(a)), located at the acoustic driver frequency. Evident in the power spectra is the fact that the maximum energy is contained at the frequency of the acoustic driver. The magnitude of the peak at the acoustic driver frequency increases at both the edge of the outer-jet and the edge of the inner-jet by about 1.75 and 2.8 times greater than that of the chamber fluid, respectively. A second harmonic peak is observed also in the power spectrum of the velocity signal measured at the edge of the outer-jet (Fig. 4.23 (b)), which is believed to be due to the noise and is not seen in the other spectra.

Analysis of the complex portion of the FFT allowed for phase angle determination between the velocity signals. At the axial distance of  $1.4 D_1$  downstream of the injector exit-plane, the phase angle difference calculated between velocity signals at the frequency of maximum peak in the power spectra (i.e., the acoustic driver frequency) in the chamber fluid ( $x/D_1 = 4.86$ ) and at the edge of outer-jet ( $x/D_1 = 2.24$ ) was  $155^\circ$ , and the phase angle difference between the velocity measured in the chamber fluid and at the edge of the inner-jet was  $70^\circ$ . At this axial location, this indicates that the transverse velocities measured within the chamber fluid and at the edge of the outer-jet are almost completely out of phase.

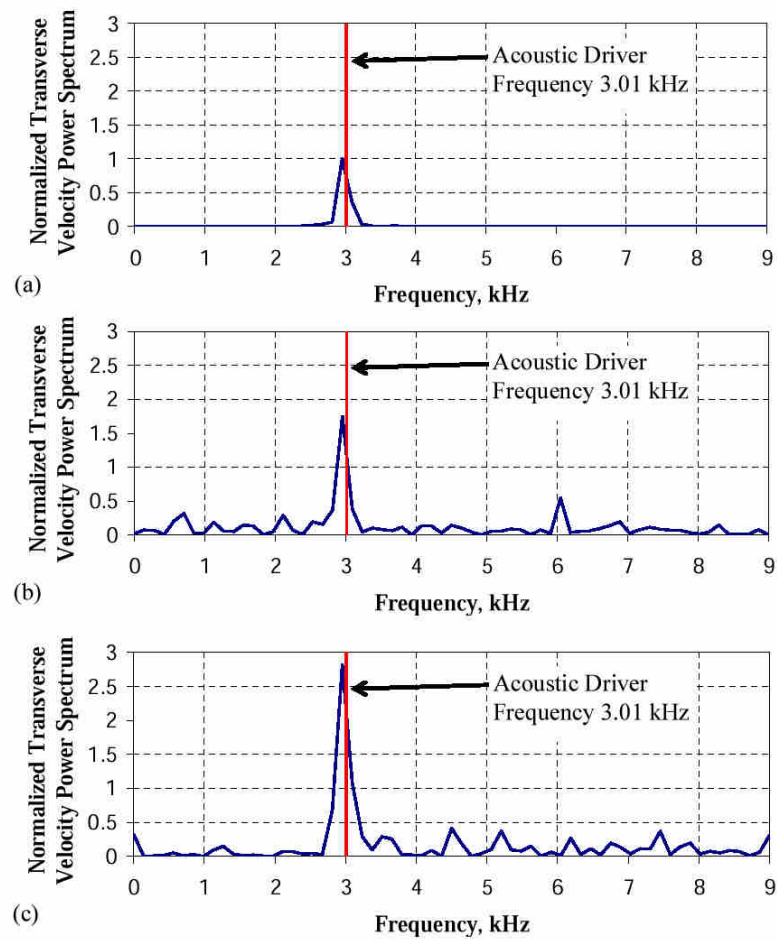


Figure 4.23: Power spectra of the acoustic velocity signals shown in Fig. 4.21 at distances from the centerline of the jet of: (a),  $4.86 D_1$  in the chamber fluid; (b),  $2.24 D_1$  at the edge of the outer-jet; and (c),  $0.73 D_1$  at the edge of the inner-jet. The chamber pressure was 1.49 MPa.

Using the information from the measured variations of the acoustic pressure with chamber pressure shown in Fig. 4.13, the acoustically-induced velocity amplitude was computed by taking advantage of the simple relationship from linear acoustic theory for plane waves as shown in Eq. 4.4, using the characteristic acoustic impedance ( $\rho c$ ). In complicated geometries, where the wave may not be planar and with nonlinear acoustics, there is no guarantee that the relationship in Eq. 4.4 will be valid [77]. However, continuing along with this assumption, and using a relationship, derived in Kinsler et al. [77], between the averaged (integrated over one time period) energy density ( $\bar{\mathcal{E}}$ , energy per unit volume) and the acoustic velocity amplitude shown in Eq. 4.5, one arrives at a possible explanation for the decay in amplitude of the acoustic pressure with increases in chamber pressure. Note the volume of the chamber and the supplied power to the acoustic driver were constant in this work. Therefore, from Eq. 4.5, one expects that the amplitude of the acoustic velocity to decrease with  $\rho^{-0.5}$ .

$$\mathcal{P} = \rho c \mathcal{U} \quad (4.4)$$

$$\bar{\mathcal{E}} = \rho \mathcal{U}^2 / 2 \quad (4.5)$$

Where,

$\mathcal{P}$  is the amplitude of the acoustic pressure,

$\mathcal{U}$  is the amplitude of the acoustic velocity,

$\rho$  is density,

$c$  is the speed of sound, and

$\bar{\mathcal{E}}$  is the integrated energy density over one time period.

Figure 4.24 presents the acoustic velocity computed from two different methods: first, the pressure measurements (the circle symbols) and using Eq. 4.4, and second, the velocity measurement approach described earlier using images (the square symbols) with examples shown in Fig. 4.20. The solid line is a curve fit to velocity amplitude, which is Eq. 4.5 with the addition of a constant ( $\kappa$ ) to account for the nonlinear and non-plane-wave effects and using the energy and the constant  $\kappa$  as the parameters. The dashed line is the curve fit to the same equation, but with a different energy and constant term for the velocity amplitudes measured from images.

It appears that the proposed functional form describes the decay of the velocity amplitude with increased chamber density as estimated through pressure measurements, see Fig. 4.24. However, the velocities measured from the images are somewhat lower. This is considered not a surprising effect because estimated velocities from the pressure measurements were performed under room temperature and computed using a linear theory. Because of the low dynamic range and the displacement uncertainty of  $\pm 1$  pixel, the higher-density point in Fig. 4.24, calculated using the velocity information in Fig. 4.20 (b), has a rather large uncertainty. Considering the velocity measurements from the images as a closer representation of the true values, estimates of the momentum of the acoustic wave can now be made, with  $\bar{\mathcal{E}}$  and  $\kappa$  being  $33 \text{ J/m}^3$  and  $-0.85 \text{ m/s}$ , respectively. The estimation of the acoustic velocity should not be extrapolated to chamber densities outside the range measured here.

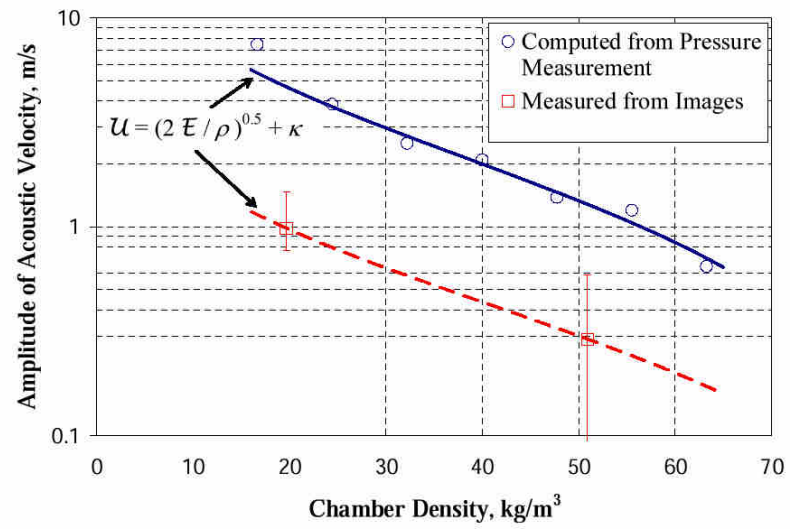


Figure 4.24: Amplitude of the transverse acoustic velocity fluctuations from the chamber pressure measurements (circle symbols) and directly measured from the images (square symbols). The solid and dashed lines represent curve fits using the equation indicated in the figure.

The estimates of the acoustic wave momentum flux ( $\rho \mathcal{U}^2$ ), based on the chamber density and the computed amplitude of the acoustic velocity from images are shown in Fig. 4.25, plotted against the outer-to-inner jet momentum flux ratio. Also, the ratio of the acoustic momentum flux to that of the inner-jet and the outer-jet are shown in Fig. 4.26 and Fig. 4.27, respectively. The momentum flux of the inner-jet is essentially constant at a given pressure for the conditions tested in this work, hence explaining the similar appearance of Figs. 4.25 and 4.26. A decreasing trend seen in the acoustic-to-outer-jet momentum flux ratio with increases in the outer-to-inner momentum flux ratio is primarily due to increase in the outer-jet momentum flux. This plot is shown for ease of comparison between the momentum flux of the acoustic wave and that of the outer-jet. It is evident from these figures that the amplitude of the acoustic velocity fluctuations is highest at the lowest pressure conditions (i.e., low chamber density). This is consistent with the observed qualitative effect of the acoustic waves on the jet. The acoustic momentum flux is about an order of magnitude larger at the subcritical pressures than that under the supercritical pressure (see Fig. 4.25)

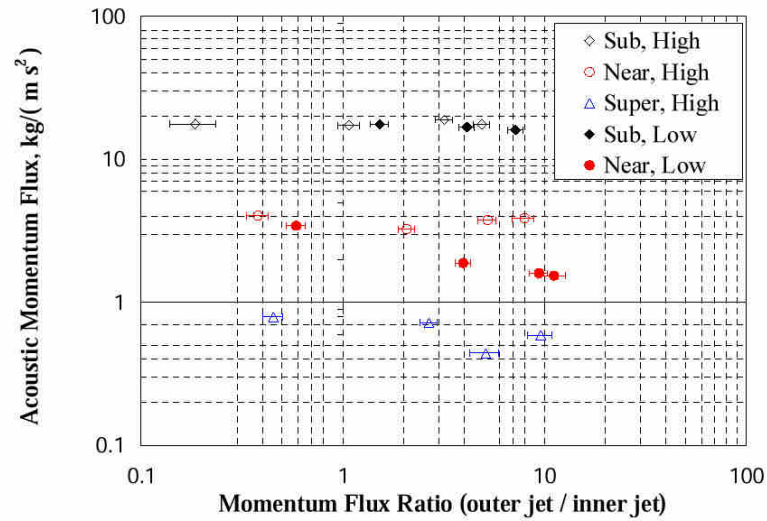


Figure 4.25: Variation of acoustic momentum flux ( $\rho U^2$ ) with the outer-to-inner jet momentum flux ratio. The words sub, near, and super in the figure inset correspond to subcritical, near-critical, and supercritical chamber pressure, respectively. The words “high” and “low” in the figure inset are for the nominal high and low outer-jet temperature cases. The hollow diamond symbols (“Sub, High”) are cases 1-4; the hollow circles (“Near, High”) are case 5-8; the hollow triangle symbols (“Super, High”) are cases 9-12; the solid diamond symbols (“Sub, Low”) are case 13-15; the solid circle symbols (“Near, Low”) are cases 16-19. The case numbers correspond to Table 4.1.

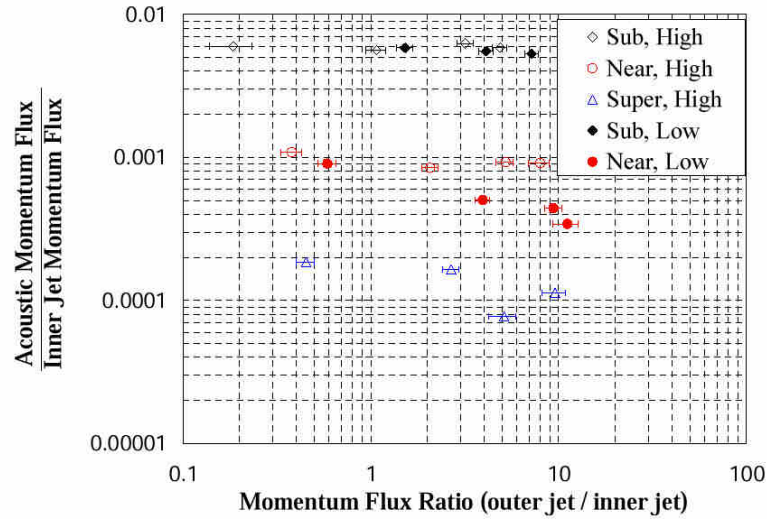


Figure 4.26: Variation of the ratio of acoustic momentum flux ( $\rho U^2$ ) to the momentum flux of the inner-jet with the outer-to-inner jet momentum flux ratio. The words sub, near, and super in the figure inset correspond to subcritical, near-critical, and supercritical, respectively. The words “high” and “low” in the figure inset are for the nominal high and low outer-jet temperature cases. The hollow diamond symbols (“Sub, High”) are cases 1-4; the hollow circles (“Near, High”) are case 5-8; the hollow triangle symbols (“Super, High”) are cases 9-12; the solid diamond symbols (“Sub, Low”) are case 13-15; the solid circle symbols (“Near, Low”) are cases 16-19. The case numbers correspond to Table 4.1.

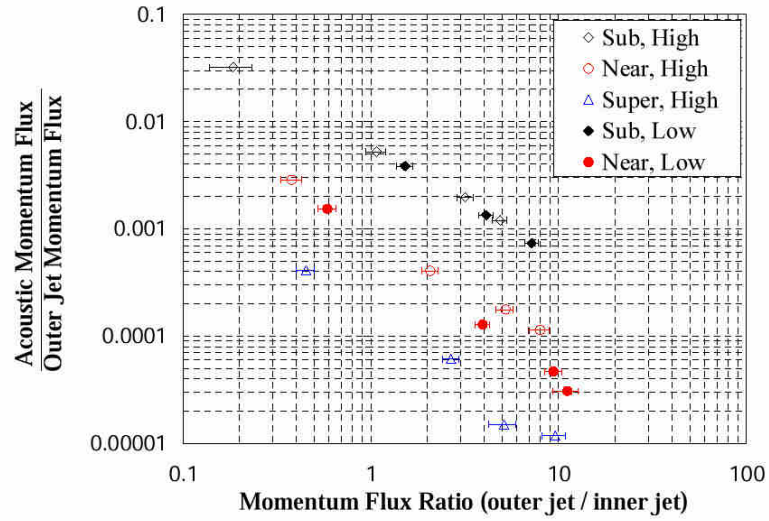


Figure 4.27: Variation of the ratio of acoustic momentum flux ( $\rho U^2$ ) to the momentum flux of the outer-jet with the outer-to-inner jet momentum flux ratio. The words sub, near, and super in the figure inset correspond to subcritical, near-critical, and supercritical, respectively. The words “high” and “low” in the figure inset are for the nominal high and low outer-jet temperature cases. The hollow diamond symbols (“Sub, High”) are cases 1-4; the hollow circles (“Near, High”) are case 5-8; the hollow triangle symbols (“Super, High”) are cases 9-12; the solid diamond symbols (“Sub, Low”) are case 13-15; the solid circle symbols (“Near, Low”) are cases 16-19. The case numbers correspond to Table 4.1.

#### 4.4.4 Acoustic Wave Jet Interaction Mechanism

Using the data and observations presented in the previous sections, a picture of the interaction mechanism between the jet and the acoustic wave can now be presented. Figure 4.28 presents 13 consecutive images of the shear-coaxial jet framed at 18 kHz. These images were taken from the same movie and test run used to construct the third column of Fig. 4.14. The chamber pressure was 1.57 MPa, and the acoustic driver frequency was set at 3.03 kHz. The velocity ratio and momentum flux ratio were 10.4 and 4.6, respectively. The eight horizontal arrows in each image represent the direction and magnitude of the acoustic velocity estimated by visual inspection from the movie. The arrows were not computed by the spatial cross-correlation technique, because of the lower resolution of these images, which was necessary in order to have a larger field of view. As a visual aid, the two vertical lines near the center of each frame indicate the extent of the inner diameter of the inner tube,  $D_1$ . The curves starting at the edge of the outer-jet represent the averaged boundary, delineating the extent of the outer-jet with no acoustical excitation. These lines were determined by applying a variance filter, which uses a 7x7 region of interest (ROI) which computes the variance of the ROI then replaces the center pixel with the variance for that particular ROI. The texture of the outer-jet fluid is different from the chamber fluid and the inner-jet. The variance filter converts what the human eye perceives as texture (vaguely defined) and converts it to intensity variations. The reader is referred to Russ [79] for more details on image textures. Two hundred variance images of the jet without acoustic excitation were averaged from which a line denoting the boundary can be easily distinguished. These averaged outer-jet

boundaries were then superimposed in the form of the curves drawn at the edge of the outer-jet starting from the injector tip.

Qualitatively speaking, fluid structures may be tracked sequentially in time. Starting in the first frame of Fig. 4.28, a bold circle is drawn around a fluid structure at the interface between the inner and outer-jets near the injector tip. In the second frame, the bold circle from the first frame is redrawn at the same position, but not in bold, and a bold circle is then drawn around the updated location of the same fluid structure, initially identified in frame number one, with a bold arrow connecting the centers of the two circles. This process is then repeated for consecutive frames with the bold circle and arrow denoting the movement from the last frame for the same fluid structure, until the structure is no longer distinguishable, which in this case occurs after about the tenth frame. In the fifth frame, a second fluid structure on the left side of the core is identified and tracked in the same manner.

By tracking a given fluid structure, identified by the circles in Fig. 4.28, a trajectory can be constructed. Despite reversal of the acoustic velocity in the chamber fluid several times, indicated by the direction of the horizontal arrows, the trajectory of a fluid feature on the dark core of the jet shown in Fig. 4.28 does not exhibit a periodic pattern. Recall from section 4.4.3 that there is a phase difference between the transverse velocity measured in the chamber fluid (sufficiently away from the jet) and that at the edge of the core of about  $70^\circ$  at an axial location of  $1.4D_1$  downstream from the injector tip. This phase difference is due to the inertia that the dense core possesses. From the first two frames in Fig. 4.28, the horizontal arrows suggest that the acoustic velocity in the chamber fluid, and consequently its momentum, is at a maximum value in the

direction towards the left side of the jet. However, the direction of the transverse momentum at the edge of the core is in the direction of the left-right-oscillatory motion of the core. Because of the phase differences between the transverse velocity in the chamber fluid and that at the core of the jet, this is opposite to the direction of the transverse momentum of the chamber fluid. The momentum of the transverse wave at the edge of the core causes the portion of the core near the injector tip to be displaced in the same direction at this location, which is most likely due the force created by the drag on the core of the jet. Buffum and Williams [68] observed an order of magnitude increase in drag coefficient for the single jet in an acoustic field compared to that of a solid cylinder of an equal diameter. One may hypothesize that the transverse motion of the core is a result of the vibration of the inner tube of the injector excited by the acoustic vibrations. However, the wavelength of the acoustic wave is much longer than the annular gap width of the injector,  $(D_3-D_2)/2$ , as indicated by Fig. 4.12. Even if one accounts for the radial variation in sound speed using temperature profiles shown in Fig. 4.3, the computed wavelength is still two orders of magnitude larger than the annular gap width of the injector. This suggests that the acoustic driver is not resonating the annular cavity in the injector formed between the inner- and outer-injector tubes in a transverse mode. Additionally, although the inner tube is recessed and is not visible in the images or movies, the outer tube of the injector is. Meticulous examination of the movies showed that the outer tube remains vibration free, suggesting that mechanical vibrations of the injector are not a probable cause of the jet behavior.

The ensuing sinusoidal shape of the dense core results directly from the fluid in the core being displaced near the injector tip and subsequently convected downstream.

The transverse momentum reverses its direction at the frequency of the acoustic driver (see Figs. 4.16, 4.18, 4.20, 4.21, and 4.23), and as fluid elements continually leave the injector, they are eventually displaced in accordance with the local momentum direction at that time near the injector tip. Then, within a short axial distance from the injector tip, the fluid elements of the dark core largely become insensitive to the existence of the transverse momentum, and follow nearly linear trajectories. A consistency check of this scenario was performed by fitting a line to the transverse position ( $x$ ) versus time data from the identified fluid parcels of Fig. 4.28 producing lines with an  $R^2$  correlation coefficient of 0.97. The trajectory of the fluid particle was judged visually, and therefore is somewhat subjective and errors are unknown. Therefore, the curve fit to the trajectory does not provide definitive proof that the transverse velocity (i.e., the time derivative of the curve fit) is constant, but it is consistent with the observations. The consequence of this linear variation of the fluid parcel transverse displacement is that if it were to continually be affected by the forces resulting from the transverse acoustic momentum while being convected downstream, then it would not exhibit this linear behavior. However, if one looks at images 7 to 13 in Fig. 4.28, approximately one cycle later from the image 1, and follows the portion of the core in time that grows into a large displacement peak, nearly the same trajectory of a similar nature to the previous cycle is traced.

The motion of the core appears to dominate the behavior of the jet. The displacement of the outer-jet seems to be governed by the displacement of the dense core. Looking at Fig. 4.28, the displacement of the outer edge of the jet is relatively small compared to the averaged outer edge boundary of the unexcited coaxial jet at the same

conditions, until farther downstream where the core begins to break up and becomes well mixed with the chamber fluid. However, in the near-field region of the jet, when a transverse displacement of the edge of the outer-jet occurs, it correlates well with a large lateral displacement of the core. The relatively large displacement of the dark and dense core compared to that of the chamber fluid suggests a possible amplification of the transverse velocity (see Figs. 4.22 and 4.23 ) caused in some way by the existence of the outer-jet. An examination of a single jet, produced by merely turning off the outer-jet flow and maintaining the other conditions constant, does not show an imposed large-scale sinusoidal structure on the core of the jet, see Chehrودي [29]. A possible reason for this amplification, at least in part, is due to the existence of the high-speed outer-jet. Once fluid from the core is displaced into the higher-speed outer-jet, the momentum of the outer-jet is much greater than that of the acoustic waves which controls the forces acting on the core, accelerating the fluid elements from the core very quickly in the axial direction within a short distance from the injector tip.

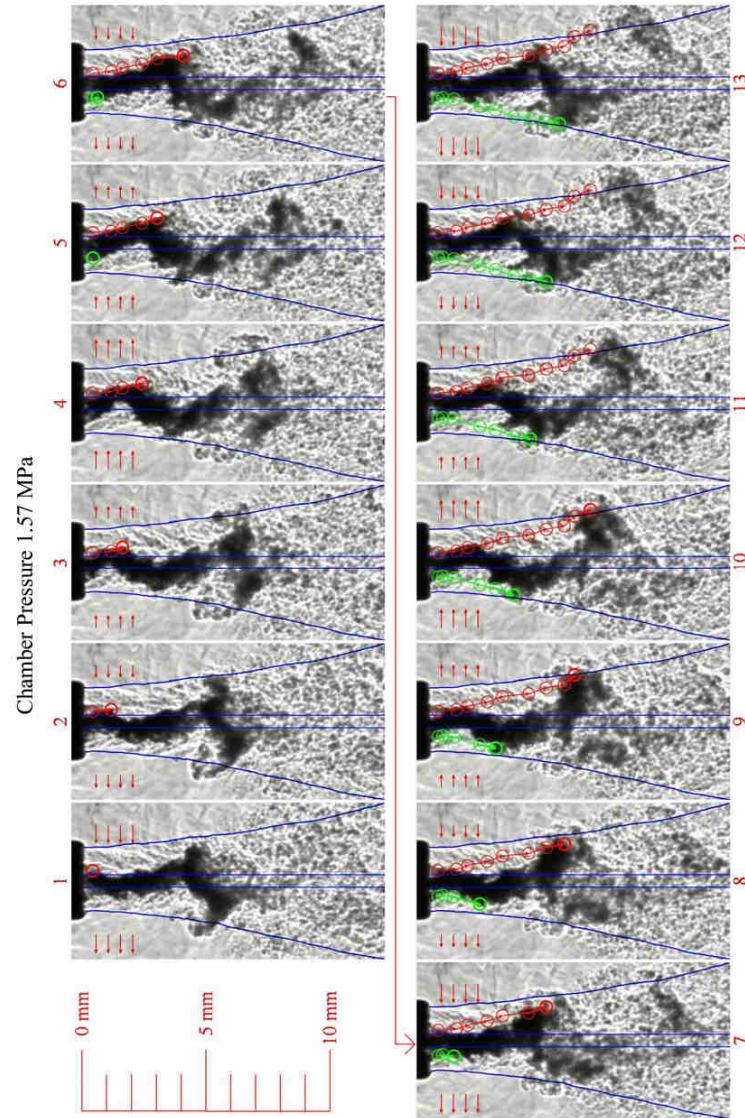


Figure 4.28: Annotated consecutive images of a subcritical pressure shear-coaxial jet.

Figure 4.29 presents 18 sequential images taken at an 18 kHz framing rate from the near-injector region at a subcritical chamber pressure. The images were from the same movie (test run) used to compute the velocities in Fig. 4.21. The chamber pressure was 1.49 MPa (subcritical) and the acoustic driver frequency was tuned at 3.01 kHz. Because of the arrangement of the images, the sampling frequency, and the acoustic driver frequency, the images in each row are approximately  $180^\circ$  out of phase (for example, frames 1 and 10). The velocity ratio and momentum flux ratio were 11.3 and 5.5, respectively. The length of the horizontal arrows drawn in each frame of Fig. 4.29 is the displacement, in pixels, extracted from the velocity measurements reported in Fig. 4.21 (a), scaled up by a factor of ten for clarity of presentation. Although four arrows are drawn indicating the direction of the acoustic velocity in the chamber fluid, only one axial measurement was made, being at a position  $1.4 D_1$  downstream of the injector exit-plane (between the second and third arrow from the top of each frame). Because the time interval between the frames is constant, the length of the arrows is directly proportional to the velocity. The two vertical lines drawn near the center of the injector represent the extent of the inner diameter of the inner tube ( $D_1$ ). The two curves originating from the tip of the injector represent the averaged edge of the outer-jet without acoustical excitation, which were determined from the averaged unexcited jet images in the same manner as in Fig. 4.28.

One structure that can be observed in the magnified images of Fig. 4.29 is the recirculation region attached to the lip of the inner tube. A magnified image of the frame number 10 in Fig. 4.29 is shown in Fig. 4.30. A similar recirculation zone was also predicted by Zong and Yang [80] in a coaxial injector attached to the lip of the inner tube

in an unexcited jet. The darker appearance of this region (compared with that of the outer-jet fluid) is due to an increase in density above that of the outer-jet, which results from the mixing of fluid elements from the high-density inner core region which was also predicted by Zong and Yang [80]. In some instances, the recirculation zone entrains enough of the inner-jet fluid leading to a decrease in the inner diameter of the core (identified by a very dark core). It is speculated that this recirculation region and the interaction with the acoustic wave is what causes the large-scale motions of the dark-core. Recall that the fluid from the dense dark-core appears to be strongly effected by the acoustic wave in the vicinity of the injector tip. The conjecture is that the acoustic wave momentum causes a collapse of the recirculation zone. For example, if the acoustic velocity direction is pointing to the right, then the left recirculation zone collapses, and vice-versa. At the same time, on the opposite side of the core, the low pressure recirculation zone pulls the core in the direction of low pressure which is the same direction as the momentum of the acoustic wave is pointing. This speculation would also account for the increased displacements of the core observed for shear-coaxial jets over that of a single round jet (no coaxial flow), because the recirculation is not present there. This cannot be definitively proven given the available data in this work.

An interesting vortex structure forms on the lip of the outer tube of the injector. This region and the vortex are denoted by the arrows pointing to the outer edge of the injector tip in Fig. 4.30, and are also visible to a lesser extent in Fig. 4.29 because of the reduced magnification. The vortex appears toroidal in shape from the examination of the movies, and continues to form during the push stroke of the acoustic driver. Once the acoustic velocity field reverses its direction, the vortex is formed and then broken up by

another change in velocity field direction, which is then entrained into the outer-jet or is mixed into the chamber fluid. This vortex appears to have little or no effect on the behavior of the jet with acoustic excitation

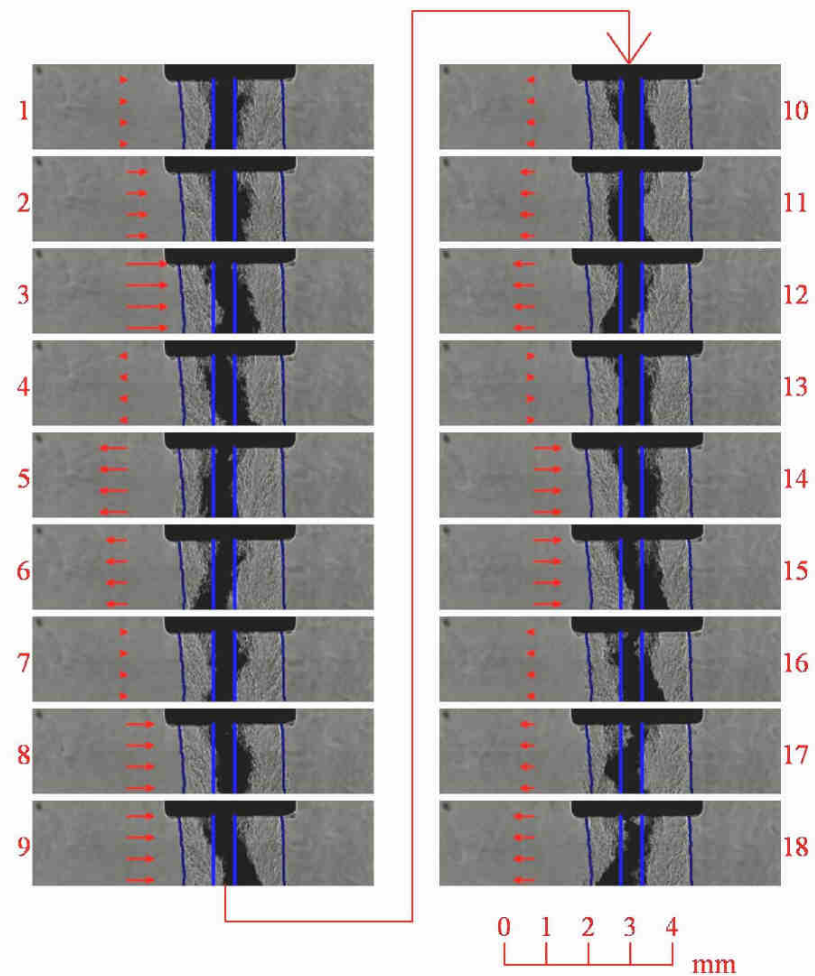


Figure 4.29: Annotated consecutive images of the shear-coaxial jet at subcritical chamber pressure. Images show magnified views of the near-injector region. Horizontal arrow length is quantitative and proportional (amplified by 10 for clarity) to velocity measured in Fig. 4.21 (a). Two parallel vertical lines in the center show the inside diameter of the inner tube. The chamber pressure was 1.49 MPa (subcritical), and the acoustic driver frequency was at 3.01 kHz.

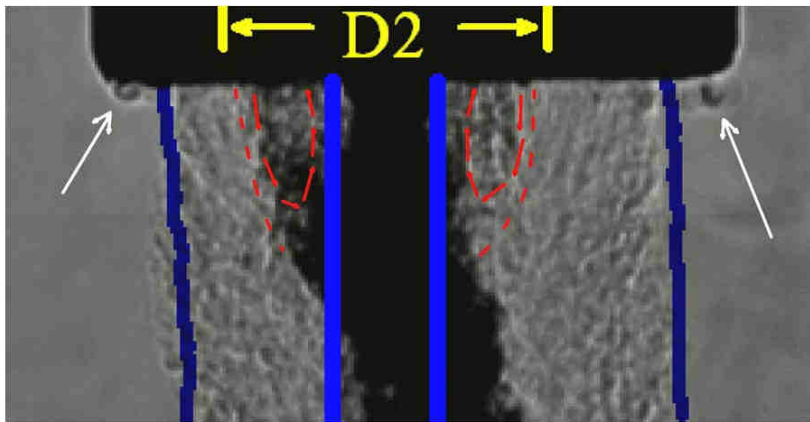


Figure 4.30 Magnified view of frame number 10 from Fig. 4.29. The dashed curves denote the approximate boundary of the recirculation zone, and the arrows within the recirculation region indicate the direction of the rotation. The vortex structures that form on the outer rim of the injector are identified by the arrows pointing to the outer edge of the injector tip. The two vertical lines with the dimension  $D_2$  denote the extent of the outer diameter of the inner tube,  $D_2 = 1.59\text{mm}$ .

#### 4.5 Dark-Core Length

Many researchers measured core length of different shear-coaxial jets in the past, and Table 4.2 presents a summary of all the works reported in the open literature. The core length was either measured or an equation correlating core length was reported. The intent of Table 4.2 is to provide detailed information on all relevant works, including the operating conditions, geometries, measurement techniques, and proposed equations correlating core lengths in one convenient location. Often, the terms potential-core, potential cone, intact liquid length, and breakup length are used interchangeably, and vaguely defined (see references in Table 4.2). The potential-core does exist for all coaxial jets, but is usually only reported for single-phase coaxial jets, and liquid intact length or breakup length is generally reported for “two-phase” coaxial jets. By “single-phase” coaxial jet, it is meant a shear-coaxial jet where all three fluid components (i.e., the inner-jet, the outer-jet, and the chamber or ambient fluid) are the same phase, either all gas, all liquid, or all supercritical fluid. The term “two-phase” coaxial jet here means a shear-coaxial jet where the inner-jet is liquid phase, and the outer-jet and the chamber (or ambient fluid) are gas phases.

Different techniques are used to measure core length (see Table 4.2) ranging from Pitot tube pressure measurements to analysis of photographs. It seems that images were used in most measurements of the core for two-phase jets. With a few exceptions, notably Woodward [62], often the measurement methods from images are not discussed with sufficient details. Therefore, in order to produce repeatable measurements, to

account for the variability in the light source intensity, and to be able to process a large number of images in a repeatable fashion, an accurate computer algorithm is necessary. When a region of an image is referred to as a “dark core”, this is simply referring to a contiguous area of the jet, always defined by the inner-jet, which clearly stands out in darkness level with respect to the remaining areas. This will be explained further in a quantitative manner below.

All of the dark core length data of the present study in figures in Section 4.5 is also presented in Table B.2 in Appendix B.

Table 4.2: Summary of published operating conditions, geometries, measurement techniques, and proposed equations from the literature, measuring or correlating core length for shear-coaxial jets.

REF	Author	Date	Fluid Inner Jet	Fluid Outer Jet	Fluid Ambient	Pressure (MPa)	$T_j$ (K)	$T_o$ (K)	$T_c$ (K)
[44]	Forstall & Shapiro	1950	Air+10%He	Air	Air	0.1*	Amb. <sup>a</sup>	Amb.	Amb.
[45]	Chigier & Beer	1964	Air	Air	Air	0.1*	Amb.	Amb.	Amb.
[46]	Champagne & Wygnanski	1971	Air	Air	Air	0.1	Amb.	Amb.	Amb.
[48]	Au and Ko	1987	Air	Air	Air*	0.1*	Amb.	Amb.	Amb.
[8]	Eroglu et al.	1991	Water	Air	Air	0.1*	Amb.	Amb.	Amb.
[62]	Woodward	1993	KI (aq.)	N2, He	N2, He	0.1 – 2.17	Amb.	Amb.	Amb.
[50]	Villermaux et al. <sup>g</sup>	1994	Water	Water	Water	0.1*	Amb.	Amb.	Amb.
[63]	Englebert et al.	1995	Water	Air	Air	0.1	293	293 – 636	293
[64]	Carreau et al.	1997	LOX	He, N2, Ar	NC <sup>c</sup>	0.1	82 <sup>d</sup>	245 – 272 <sup>d</sup>	NC
[51]	Rehab et al. <sup>g</sup>	1997	Water	Water	Water	0.1*	Amb.	Amb.	Amb.
[52]	Rehab et al. <sup>g</sup>	1998	Water	Water	Water	0.1*	Amb.	Amb.	Amb.
[53]	Villermaux <sup>g,h</sup>	1998	Water	Water	Water	NR	NR	NR	NR
[58]	Lasheras et al. <sup>g</sup>	1998	Water	Air	Air	0.1	Amb.	Amb.	Amb.
[54]	Lasheras & Hopfinger <sup>g,i</sup>	2000	NR	NR	NR	NR	NR	NR	NR
[60]	Favre-Marinet & Schettini	2001	Air, SF6	Air, He	Air, He	0.1	Amb.	Amb.	Amb.
[65]	Porcheron et al.	2002	LOX, Water	He, N2, Ar, Air	Air	0.1	82, 293	245 – 293	293
This work	Davis	2005	N2	N2	N2	1.4 – 4.9	108 – 133	132 – 204	197 – 249

Table 4.2: Summary of published operating conditions, geometries, measurement techniques, and proposed equations from the literature, measuring or correlating core length for shear-coaxial jets. (continued)

REF	Author	Density Ratio Outer / Inner	Velocity Ratio Outer / Inner	M Outer / Inner	Re Inner ( $\times 10^4$ )	Re Outer ( $\times 10^4$ )	We
[44]	Forstall & Shapiro	1.09	0.2 - 0.75	0.04 - 0.61	NR	NR	NA
[45]	Chigier & Beer	1*	0.024 - 9.22	$5.8 \times 10^{-4}$ - 85.0	$\sim 10^b$	$\sim 10^b$	NA
[46]	Champagne & Wygnanski	1*	0 - 10	0 - 100	1.01 - 10.15	0 - 9.6	NA
[48]	Au and Ko	1*	1.25 - 6.67	1.5 - 44	NR	NR	NA
[8]	Eroglu et al.	0.001	4.5 - 131.2	0.02 - 17.2	0.15 - 0.93	2.0 - 11.6	15 - 530
[62]	Woodward	0.0006 - 0.018	0 - 30	0 - 1.7	7.86 - 18.9	NR	$12 - 3.6 \times 10^4$
[50]	Villermaux et al. <sup>g</sup>	1	1 - 6	1 - 36	>5000	>5000	NA
[63]	Englebert et al.	0.0008 - 0.0012	10.25 - 66.75	0.12 - 4.3	0.54 - 3.4	4.8 - 16.5	76 - 2610
[64]	Carreau et al.	NR	NR	3 - 21.5	5.32 - 8.11	NR	$9.19 \times 10^3$ - $3.48 \times 10^4$
[51]	Rehab et al. <sup>g</sup>	1	2 - 5	4 - 25	NR <sup>f</sup>	NR <sup>f</sup>	NA
[52]	Rehab et al. <sup>g</sup>	1	2.2 - 5.6	4.9 - 31	1 - 10	1 - 10	NA
[53]	Villermaux <sup>g,h</sup>	1*	NR	NR	NR	NR	NR
[58]	Lasheras et al. <sup>g</sup>	0.001	NR	NR	NR	NR	NR
[54]	Lasheras & Hopfinger <sup>g,i</sup>	NR	NR	NR	NR	NR	NR
[60]	Favre-Marinet & Schettini	0.028 - 1	3.0 - 70	1 - 200	NR	3.2, 11.0	NA
[65]	Porcheron et al.	$1.6 \times 10^{-3}$ - $2.3 \times 10^{-3}$	NR	2 - 21.6	NR	NR	0 - 14000
This work	Davis	0.04 - 0.56	1.2 - 11.1	0.19 - 11.2	1.2 - 3.2	0.8 - 19	32 - $\infty$

Table 4.2: Summary of published operating conditions, geometries, measurement techniques, and proposed equations from the literature, measuring or correlating core length for shear-coaxial jets. (continued)

REF	Author	$D_1$ (mm)	$D_2$ (mm)	$D_3$ (mm)	$(D_3-D_2)/2$ (mm)	Area Ratio Outer / Inner	Post Recess (mm)	Injector $L_{post}/D_1$
[44]	Forstall & Shapiro	6.4, 25	NR	102	NR	NR	NR	NR
[45]	Chigier & Beer	25	64	97	16.5	8.50	0*	NR
[46]	Champagne & Wygnanski	25	NR	NR	NR	1.28, 2.94	0*	NR
[48]	Au and Ko	2	2.2	4	0.9	2.79	0*	NR
[8]	Eroglu et al.	0.971	1.262	10.36	4.549	112.15	-0.6	57
[62]	Woodward	4.76	6.35	9.86	1.76	2.51	0.0	85
[50]	Villermaux et al. <sup>g</sup>	40	51	55	0.2	0.27	0*	"long"
[63]	Englebert et al.	2.3	2.95	14.95	6.00	40.60	0	22
[64]	Carreau et al.	5 <sup>d</sup>	5.57 <sup>d</sup>	16 <sup>d</sup>	5.2 <sup>d</sup>	9	0	NR
[51]	Rehab et al. <sup>e</sup>	20	21	27	3	1.82	0	NR
[52]	Rehab et al. <sup>e</sup>	NR	NR	NR	NR	1.82, 1.87, 5.24 <sup>e</sup>	0 - 2 $D_1$	NR
[53]	Villermaux <sup>g,h</sup>	NR	NR	NR	NR	NR	NR	NR
[58]	Lasheras et al. <sup>g</sup>	3.8	4.2	5.6	0.7	0.95	0	29
[54]	Lasheras & Hopfinger <sup>g,i</sup>	NR	NR	NR	NR	NR	NR	NR
[60]	Favre-Marinet & Schettini	20	20.4	27	3.3	0.78	0	6.75
[65]	Porcheron et al.	5, 2.1	5.57, 2.5	16, 7	2.25	9, 9.69	0*	NR
This work	Davis	0.51	1.59	2.42	0.415	12.80	0.25	100

Table 4.2: Summary of published operating conditions, geometries, measurement techniques, and proposed equations from the literature, measuring or correlating core length for shear-coaxial jets. (continued)

REF	Author	Diagnostic	Quantity Measured	Equation
[44]	Forstall & Shapiro	Pitot tube, Sampling Tube	Potential Core	$L/D_1 = 4 + 12V_r$
[45]	Chigier & Beer	Pitot tube	Potential Core	NR
[46]	Champagne & Wagnanski	Hot wire anemometer	Inner Core	NR
[48]	Au and Ko	Hot wire anemometer	Potential Core	$L/D_1 = 9.9/V_r$
[8]	Eroglu et al.	Back-lit still	Liquid Intact Length	$L/D_1 = 0.66 We^{-0.4} Re^{0.6}$
[62]	Woodward	x-ray Radiography	Intact Liquid Core Length	$L/D_1 = 0.0095 \left( \frac{\rho_a}{\rho_i} \right)^{-0.26} We^{-0.22/H} Re^{0.68}$
[50]	Villermaux et al. <sup>g</sup>	Hot film anemometer	Potential Core / Cone	$L/D_1 = 7/V_r$
[63]	Englebert et al.	Back-lit high-speed 16mm film	Breakup Length	$L/D_1 = 40 We^{-0.27}$ $\frac{2L}{D_3 - D_2} = 10.6 M_R^{-0.3} = 13.7 E_R^{-0.2}$
[64]	Carreau et al.	Fiber optic Probe	Breakup Length, Potential Cone Length	$L/D_1 = 0.0012 \left( \frac{\rho_a}{\rho_i} \right)^{-0.32} We^{-0.33} Re^{0.55}$
[51]	Rehab et al. <sup>g</sup>	Hot film anemometer, Pitot tube, LIF image	Potential Core	$L/D_1 = 6/V_r$ ; $L/D_1 = 8/V$ $L/D_1 = 0.5 \left( \frac{1}{(C\alpha V_r)^2} - 1 \right)^{1/2} \approx \frac{1}{2C\alpha V_r}$
[52]	Rehab et al. <sup>g</sup>	Hot-film anemometer	Potential Cone	$L/D_1 = c/V_r$ ; $6 < c < 8$
[53]	Villermaux <sup>g,h</sup>	<sup>h</sup>	Potential Cone, Liquid intact length	$L/D_1 = 6/M^{1/2}$

Table 4.2: Summary of published operating conditions, geometries, measurement techniques, and proposed equations from the literature, measuring or correlating core length for shear-coaxial jets. (continued)

REF	Author	Diagnostic	Quantity Measured	Equation
[58]	Lasheras et al. <sup>g</sup>	Photograph	Liquid intact length	$L/D_1 = \left( \frac{1}{4(C\alpha)^2 M} - \frac{1}{4} \right)^{1/2} \approx \frac{6}{M^{1/2}}$
[54]	Lasheras & Hopfinger <sup>g,i</sup>	i	i	$L/D_1 = \frac{1}{2cM^{2/3}} \left( \frac{\sigma}{\mu_i U_i} \right)^{1/3}$ $L/D_1 \approx \frac{6}{M^{1/2}} \left( 1 - \frac{U_i}{U_o} \right)^{-1}$ $L/D_1 \approx \frac{6}{M^{1/2}} \frac{1}{\left( 1 - \frac{B\sigma}{\mu_o U_o} \right)^{0.5}}$
[60]	Favre-Marinet & Schettini	Aspirating Probe w/ hot-wire	Potential Core	$L/D_1 \propto M^{-0.5}$
[65]	Porcheron et al.	Fiber optic Probe	Liquid Core	$L/D_1 = 2.85 \left( \frac{\rho_o}{\rho_i} \right)^{-0.38} Z^{0.34} M^{-0.13}$
This work	Davis	Shadow-graph	Dark Core	$L/D_1 \approx \frac{12}{M^{1/2}}$ $L/D_1 \approx \frac{25}{M^{0.2}}$

**Table 4.2 Notes**

NR = not reported

NA = not applicable

NC = not clear from report

Amb. = ambient

\* assumed from the context, but not directly reported

<sup>a</sup> Ambient temperature assumed from the context of discussion, but not specifically stated in report.

<sup>b</sup> reported as approximately  $10^5$

<sup>d</sup> The dimensions of the injector and the temperatures were not given in the paper, but were given in the paper by Porcheron et al.[65]

<sup>e</sup> This number is the diameter ratio squared, which is approximately the area ratio for a very thin lip injector. The only dimensional information given was the diameter ratios (1.35, 1.37, and 2.29 mm) and the lip thickness  $(D_2-D_1)/2$  of 0.3 mm.

<sup>f</sup> A  $Re$  based on momentum conservation reported and defined as  $Re = \rho_o U_o D_2 / \mu * (1 - (D_1/D_2))^{0.5}$  ranged from  $10^4 - 10^5$ .

<sup>g</sup> These papers are from the same collaboration / research group over several years.

<sup>h</sup> This paper was an analysis paper that presented a different equation based on the data from the same group of researchers [50]-[52]

<sup>i</sup> This paper was a review paper encompassing the work from this same collaboration of researchers, as well as others.

<sup>j</sup> Unable to make measurements from images, and therefore not compared quantitatively to theory for core length.

#### 4.5.1 Adaptive Thresholding Measurement of Dark-Core Length

There are many difficulties in performing quantitative measurements from a large number of images of a jet. Typically, a thresholding technique is used for making measurements from digital images. A threshold technique is applied to convert a gray-scale image to a binary image (only black and white). This is done by determining a gray-scale level (or a threshold level) and assigning all pixels that have gray-scale intensities greater than that number to a white color, and the pixels with gray-scale intensities below that particular gray-scale number to a black color. Other variations of this method exist, such as dual thresholding, which selects a range of gray level intensities to be white, and the intensities outside of this range to be black. The purpose of applying a threshold is to make a region of the image easily identifiable to either a human or computer, or both. The difficulty with applying this technique is determining the gray-scale level that should be defined as a threshold. For example, if using a strobe light for illumination purposes, the intensity of the background of the image will most likely vary from shot to shot. Additionally, if the chamber pressure or temperature field varies significantly, then the refractive index field can change the appearance of the background. Another difficulty is the selection of a criterion to assess the location where the core is broken up into separated pieces. It is then possible for two people to make different measurement judgments as to the core length. Also, with the use of digital cameras, capable of collecting a large number of images, a manual measurement becomes an extremely tedious and time consuming task.

A judicious choice of a threshold level on the gray-scale intensity level of each image is necessary, primarily because a single fixed value is not sufficient for all images to consistently determine the end or break point of the dark core. Figure 4.31 is a sample image illustrating an automated thresholding procedure for the determination of the length of the dark core. Figures 4.31 a, b, and c are, respectively, the untouched original photograph, the image threshold applied between 0-128 to indicate the injector, and the image threshold applied between 128-929 to represent the dark core. Figure 4.32 is the image histogram corresponding to Fig. 4.31 indicating the number of pixels versus a 12-bit gray-scale level. The ability of an algorithm to successfully predict the proper threshold level is based on the physical meaning of different gray level zones in an image as shown in Fig. 4.32. For example, the peak to the left of the dashed line in this figure indicates the metal surface of the injector. With the object (i.e., injector) being backlit and the injector being absolutely opaque, one would expect that the zero-level intensity should all represent the injector itself. However, the slight shift of the peak to a higher value is due to stray light being reflected by the chamber windows and other surfaces towards the injector which is then reflected back into the camera. The low number of pixels at gray level values between the dashed and dotted lines in Fig. 4.32 physically represents the dark core of interest, and the broad noisy peak at gray levels to the right of the dotted line in this figure defines the background. A difficulty with the adaptive thresholding is selecting the proper gray level denoting the difference between the dark core and the background.



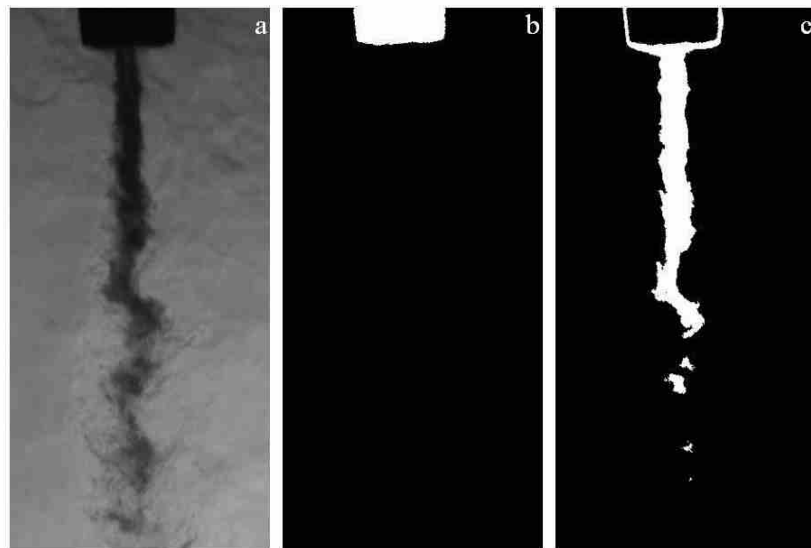


Figure 4.31: The image of (a) coaxial jet as captured, (b) threshold applied for injector, (c) threshold applied for dark core.

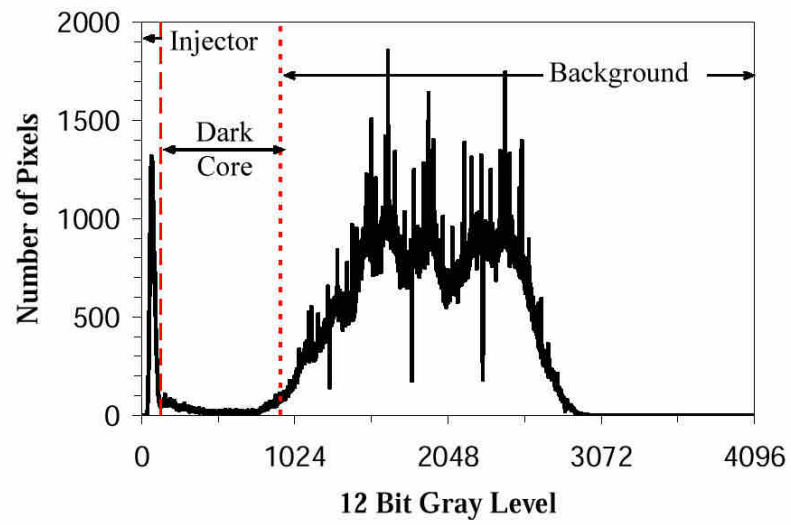


Figure 4.32: Histogram of image in Fig. 4.31 (a).

As mentioned previously, variations of the light intensity from shot to shot are usually significant and a matter of concern. For example, in the case of Fig. 4.32, the threshold level distinguishing the end of the dark core and the beginning of the background is at a gray level of 929. However, this value varies from shot to shot in a sequence of images taken at the same operating conditions. Also, it varies more widely when the chamber conditions are changed due to differences in the refractive index field. Therefore, it was necessary to devise a methodology for an accurate and repeatable determination of the rise of the portion of the curve representing the contribution of the background in these images. More importantly, the outcome should conform to what the human eye visually determines to be the end of the dark core. To select the threshold level identifying the rise of the background, data from the histogram in this region was curve-fitted, using a non-linear Levenberg – Marquardt least squares algorithm [81], to a piece of a Gaussian function (Eq. 4.6). This function is then differentiated and the point where the derivative of this curve is equal to  $e^{-1}$  was assigned to be the threshold level corresponding to the dotted line shown in Fig. 4.32 and the image of Fig. 4.31 (c). Once the proper threshold levels are determined, the program then searches for the first break in the core, and the difference between the location of the end of the injector tip and the first break in the core is taken as the dark core length ( $L$ ).

$$f(I) = A \exp\left(-\frac{(B-I)^2}{C}\right) + D \quad (4.6)$$

Where,

$I$  is the gray level intensity, and  
 $A$ ,  $B$ ,  $C$ , and  $D$  are constants.

Completion of an algorithm is only the first step in the analysis. A more important step is the verification that the adaptive thresholding algorithm gives results corresponding to the visual perception of the image. Evidence of the soundness and consistency of this algorithm is presented in Fig. 4.33. This figure is a plot of the dark-core length ( $L$ ) in number of pixels and presents a comparison between a careful manual measurement by visual inspection and the previously-described algorithm using an averaged image of those taken at a fixed operating condition. The averaged image was used for the comparison and evaluation between the results of the algorithm and the visual measurements. An averaged image is formed by first computing the mean intensity at a given pixel location from a set of images, then repeating this process for all the pixels. In the next step, the maximum and the minimum intensity values are found for the averaged-image. Lastly, this image is rescaled by mapping the minimum and maximum intensity values (and all others in between) to a 12-bit gray-scale ranging from 0 to 4095. The error bars in Fig. 4.33 represent the sensitivity of the measurements to the variations of the automatically-selected threshold level when changed by  $\pm 10\%$ . The large error bars on several points indicate that a proper selection of this threshold is essential in achieving a reliable result and a good agreement with manual measurements. A large positive error bar indicates a truly-disconnected fluid ligament (judged visually) misinterpreted as being connected and a large negative error bar indicates a truly-connected fluid ligament which is misjudged as disconnected.

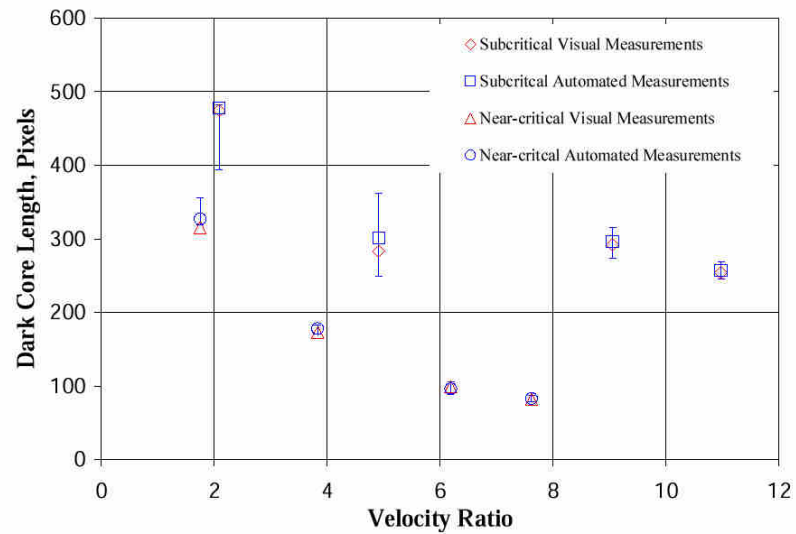


Figure 4.33: Dark core length (in pixels) versus velocity ratio (outer-to-inner jet) comparing the visual measurement with that of the algorithm programmed for automated measurement of this length using an average image representative for each of the conditions. The error bars represent a sensitivity analysis, varying the automatically-selected threshold level by  $\pm 10\%$ . The diamonds and the up-triangles are for manual visual measurements under sub- and nearcritical chamber pressures and the squares and circles are for corresponding pressures using automated computer measurements.

According to Eroglu et al.[8], the average of the length measured from individual images of a set can be regarded as the time-averaged length. It should be noted that, for each operating condition in this work, length measurements were also made from an averaged image from the set. A comparison between the averaged dark-core length measured from a set of 30 individual images and the dark-core length from the averaged-image from the same set of images is presented in Fig. 4.34, with the 45° line ( $y = x$ ) drawn for ease of comparison. The length measured from the averaged image is somewhat shorter than the average of the individual dark core values calculated in a given set. This decreased length in the averaged image is due to the fluctuations of the dark core, causing occasional appearance of the core at a give position around the end of the core, while leading to its disappearance in other images of a set. Recall that the averaged image is calculated by computing the mean intensity at any pixel location from a set of images, then rescaling this mean value to integers between a gray-scale range (in this case, 0 and 4095, for a 12-bit resolution). The net result of the averaging process is that, for example, a black pixel (or, low gray-scale intensities) with a corresponding white pixel (or, higher gray-scale intensities) in a different image of a set of two images result in gray-scale level in the averaged image that is shifted to a higher intensity value (i.e., 0.5). This effect, particularly in the region of space near the end of the dark core, causes a length measured by the averaged image to be shorter than the average of the individual images of a set. It was found that the difference between the averaged dark-core length from a set of individual images and the dark-core length measured from the averaged image increases as the root-mean-square length fluctuations increases. For the remainder

of this work the averaged dark core length measured from 30 individual images is reported.

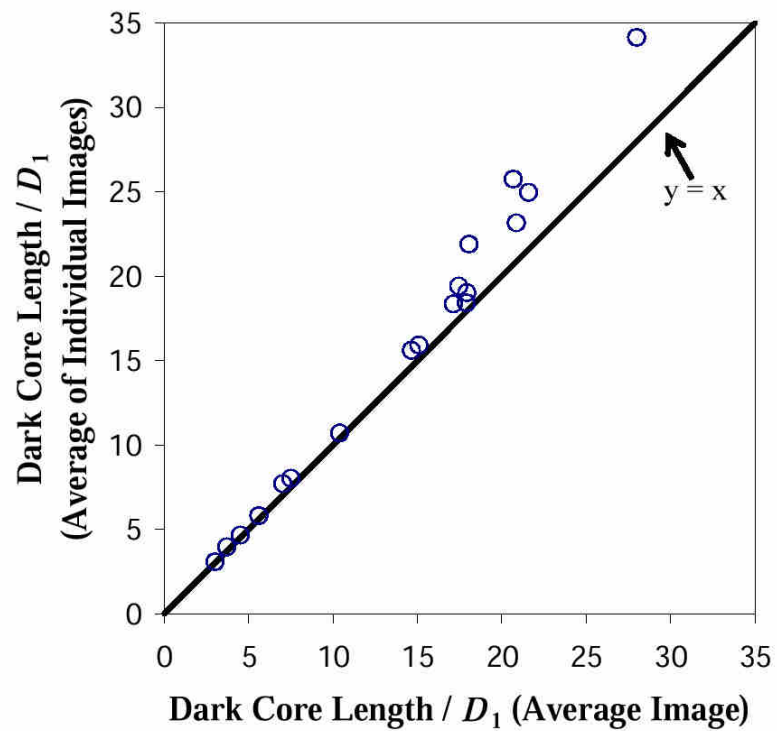


Figure 4.34: Comparison of the average dark-core length measured from of set of individual images versus the dark-core length measured from the average image of the same set.

#### 4.5.2 Influence of Velocity Ratio on the Dark-Core Length

Velocity ratio (outer-to-inner jet) has been a design parameter for shear-coaxial injectors, particularly, as a criterion to ensure the stable operation of liquid rocket engines (LRE). For liquid oxygen (LOX) / hydrogen ( $H_2$ ) engines, the design rule-of-thumb has been to keep the velocity ratio greater than about ten to prevent or minimize the occurrence of combustion instabilities (see Hulka and Hutt [3]). Although experimental data suggested this criterion, no physical explanation has been provided. One method to rate a liquid rocket engine (LRE) for combustion instability is the so-called “temperature ramping”, which is accomplished by lowering the temperature of the  $H_2$  while maintaining  $H_2$  mass flow rate at a constant value. The lower the  $H_2$  temperature is at the onset of the measured combustion instability, the greater the stability margin of that particular LRE. Note that as the  $H_2$  temperature is lowered at a constant mass flow rate, the actual velocity ratio is also lowered.

The dark-core lengths normalized by the inner-jet diameter are shown in Fig. 4.35 (a) and Fig. 4.36 (a) as a function of velocity ratio ( $V_r$ ). The root-mean-square (RMS) of the variations of this physical quantity is also shown in Fig. 4.35 (b) and Fig. 4.36 (b). Figures 4.35 and 4.36 present results for both high and low outer-jet temperatures of  $\sim 190$  K and  $\sim 140$  K, respectively. The error bars on the plots represent the  $n^{\text{th}}$  order uncertainty as described at the beginning of this chapter.

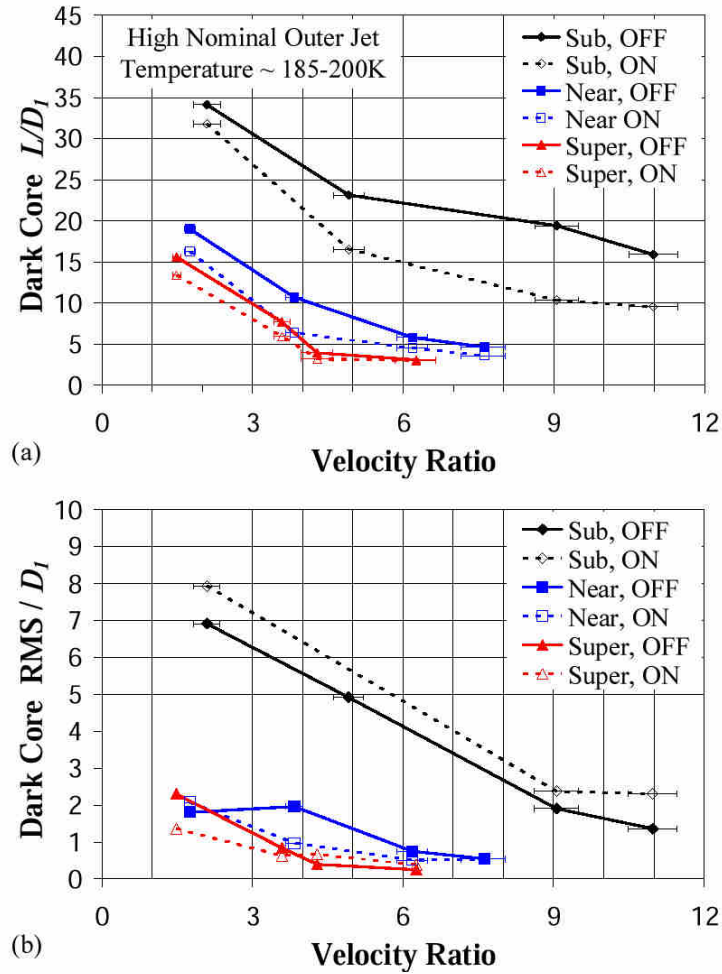


Figure 4.35: Plot of the averaged dark-core length (a) and the RMS of the length variations (b) normalized by the inner diameter. The solid symbols and lines represent the data for when the acoustic driver is OFF, and the hollow symbols and dotted lines show the data when the acoustic driver was operated at  $\sim 3\text{kHz}$  (ON). The diamond, square, and up-triangle symbols are sub-, near and supercritical chamber pressures, respectively. All cases are for the high nominal outer-jet temperature of  $\sim 190\text{ K}$ .

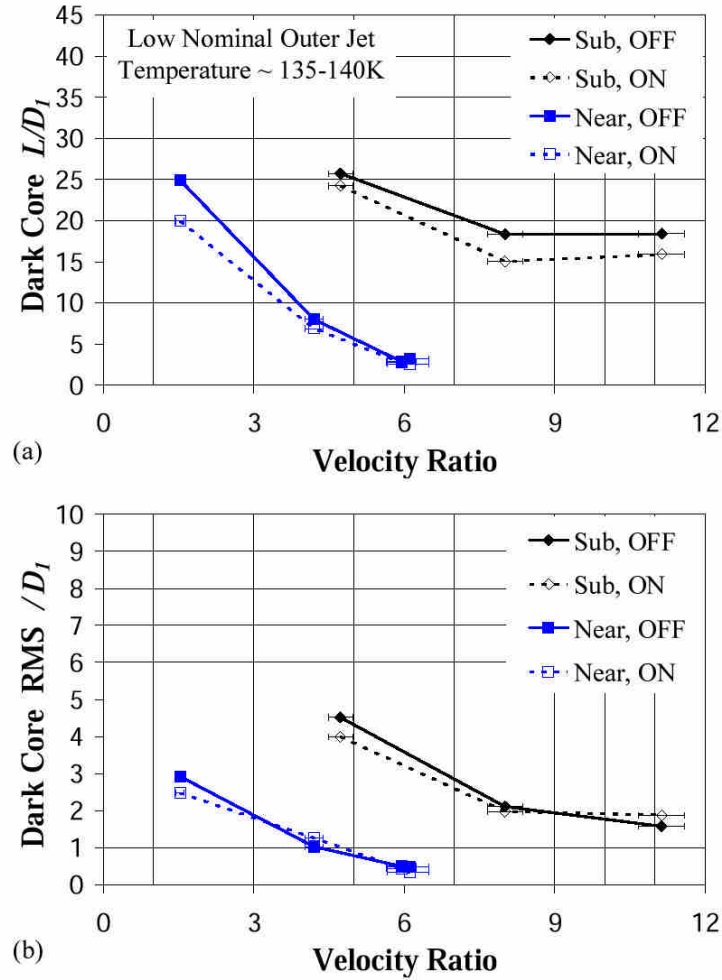


Figure 4.36: Plot of the averaged dark-core length (a) and the RMS of the length variations (b) normalized by the inner diameter. The solid symbols and lines represent data for when the acoustic driver off, and the hollow symbols and dotted lines show results when the acoustic driver is operated at  $\sim 3\text{kHz}$  (ON). The diamond and square symbols are for sub- and near-critical chamber pressures, respectively. All cases are for the lower nominal outer-jet temperature of  $\sim 140\text{ K}$ .

Evident in Figs. 4.35 (a) and 4.36 (a) is that the mean length of the dark core, which provides an indication of high-density regions of the flow, decreases as the chamber pressure is increased. A possible explanation of this effect is that as the chamber pressure increases in the present system, the temperature of the inner-jet also increases. The net effect causes the density of the inner-jet to decrease (as seen in Figs. 4.3 (a)-(f)), which leads to a shortened length of the dark core. Since the jet begins with a lower density, less time is then required to fully mix the dark inner-jet with the background. Work that is relevant to the present study was performed by Glogowski et al. [82] and Vingert et al. [83], in which a shear-coaxial injector was utilized with a design derived from a prototype SSME fuel preburner element using liquid nitrogen (LN<sub>2</sub>) and gaseous nitrogen (GN<sub>2</sub>). They stated that the length of the dark core in the acquired images increased significantly upon elevation of the chamber pressure from sub- to supercritical, at constant mass flow rates. They attributed this to the drop in the relative velocity between the inner and outer (annular) streams. Although temperature measurements were made somewhere downstream of the critical flow venturi location in the feed system, it was not clear how far upstream of the injector exit area this temperature measurement was made. It is known that small changes in temperature in this thermodynamic region can bring about large changes in density, affecting the parameters, especially outer-to-inner velocity ratio, used to characterize the injector exit conditions. Close examination of the figures presented by Vingert et al. [83] suggests that the dark core (that is, the flow issuing from the inner tube) of the jet actually appears to contract in length, while the visual impression of the outer annular flow is that it grows in length.

At a constant chamber pressure, as the velocity ratio ( $V_r$ ) is increased, the mean length of the dark core decreases and approaches a somewhat constant region. In a mean sense, when the dark core feels the imposed external acoustic field, the length of the core is shorter than or equal to the length when the acoustic driver is turned off. Miesse [66] also observed a contraction, but for single round jets excited by an external acoustic field. Under the near- and supercritical chamber pressures, as the  $V_r$  parameter increases, the difference between the lengths of the dark core, measured with and without the acoustic field, diminishes.

The RMS values of the dark-core length fluctuations, shown in Figs. 4.35(b) and 4.36(b), exhibit somewhat similar trends to those seen with their mean values. It is known that for a liquid-fueled rocket, atomization and breakup processes, interactions between the propellant jets, droplet formation, and vaporization are all affected by the pressure and, particularly, velocity fluctuations. Also, for any chemically-reacting system, the rate at which energy is released is sensitive to the rate of change of temperature, density, pressure, and, of course, mixture ratio. It is then quite intuitive to relate, in some form, the RMS values of the dark-core length fluctuations to mixture ratio variations. On the other hand, a low RMS value can be interpreted as the jet's inherent steadiness and vice versa. Examination of Figs. 4.35(b) and Fig. 4.36(b) clearly shows that this property is reduced significantly as the velocity ratio is increased when the chamber pressure is subcritical. Although these results are for a single injector design, it is then quite possible that the observed improvement in combustion stability for liquid rocket engines at higher values of velocity ratio is a result of the jet's inability to generate large mass flow rate fluctuations under these conditions, weakening a key feedback line

for the self-excitation process. In temperature ramping exercises for stability rating of LOX/H<sub>2</sub> engines, the mass flow rate is usually maintained at a constant value [3]. Therefore, as the temperature of the H<sub>2</sub> is decreased during a ramping episode, the H<sub>2</sub> becomes more dense, which decreases the injector velocity ratio ( $V_r$ ). Hence, the decrease in  $V_r$  causes a shift in the operating condition to those providing higher RMS fluctuations of the core. Additionally, considering that a liquid rocket engine may have regions, particularly near the LOX core, where they exist under subcritical condition even if both propellants are individually injected at supercritical conditions (described in Chapter 2), these RMS plots suggest that such a decline in the velocity ratio amplifies the jet's inherent unsteadiness. This provides a possible explanation for the engine's eventual arrival into an unstable zone as a temperature ramping test proceeds. Also, the observation reported by Wanhainen et al. [84], who found that a decline in LOX density was de-stabilizing, can be explained in a similar manner. Ultimately, this initial finding requires testing under multi-element injector combustion conditions for verification, which is considered beyond the scope of this work.

As indicated in Table 4.2  $V_r$  has been used as a correlating parameter for core length by many investigators. Figure 4.37 is a comparison between the data taken from all of the available and relevant core length measurements reported in the literature. The hatched region in Fig. 4.37 represents the region of separation between single-phase and two-phase shear-coaxial jet results. All points below the hatched region are for single-phase coaxial jet cases, and the remaining points located above the hatched region are for two-phase coaxial jets. The important observation here is that the mean dark-core lengths for the near-critical and supercritical pressure conditions from this work, which were

measured from images and are in fact single-phase, fall on the single-phase side of the hatched region. Although the spatial discrimination between the single- and two-phase cases is interesting in Fig. 4.37, and will be discussed later, the large level of scatter might be explained by one or any combination of three reasons. Initially, one might suppose a reason for this observation to be related to the measurement technique. For example, all of the two-phase core lengths presented in Fig. 4.37 were measured from images of one type or another and the core-length measurements for the single-phase cases were acquired from some type of velocity measurement, estimating the potential-core (see Table 4.2). Another reason emerges from different definitions of these terms. For example, there is truly a difference between potential-core length and other names used referring to liquid-intact lengths. Thus, caution should be exercised when using these terms interchangeably, because physically they represent different quantities. Additionally, the velocity ratio may not be the proper parameter to represent the physical phenomenon. This matter will be discussed further in the next section.

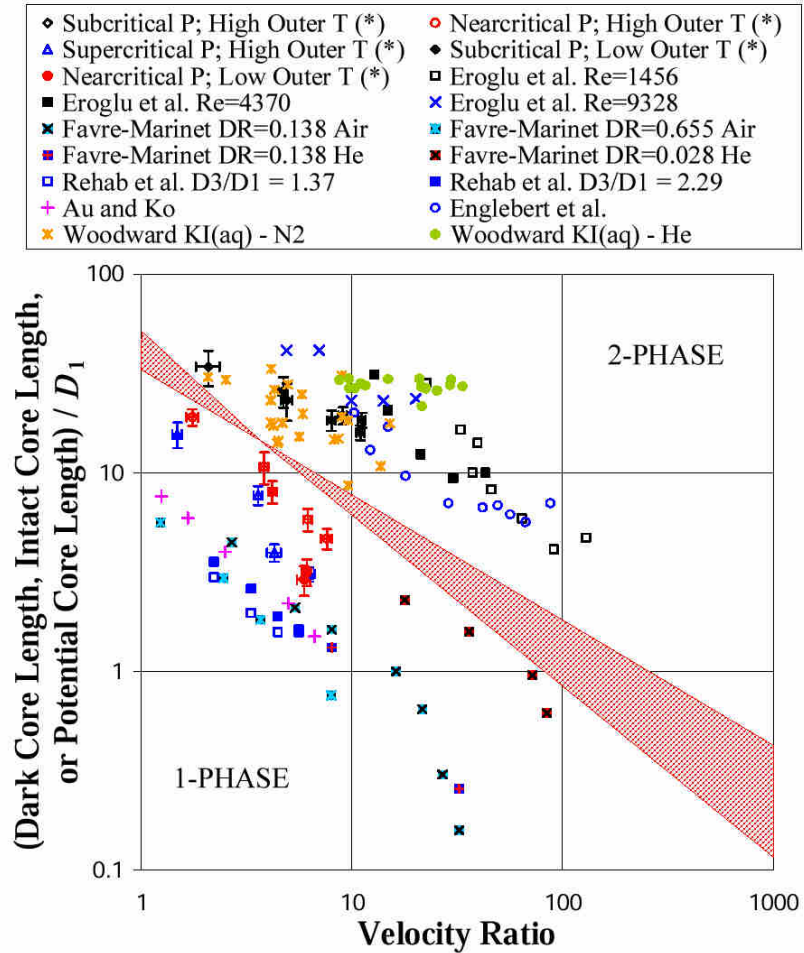


Figure 4.37: Comparison of measured core length data vs. velocity ratio (outer /inner). Data series indicated by (\*) denotes this work. References for the data taken from other work listed in Table 4.2. DR denotes density ratio of the outer-jet to the inner-jet.

### 4.5.3 Scaling of the Dark Core with Momentum Flux Ratio

Scaling of the core length with momentum flux ratio ( $M = (\rho_0 U_0^2)/(\rho_i U_i^2)$ ) has been suggested by several authors with the dependence ranging from  $M^{-0.5}$  to  $M^{-0.13}$  (see Table 4.2). Note that for a uniform-density coaxial jet, the velocity ratio is equal to the square root of the momentum flux ratio. A plot of the measured dark-core length values in this work versus the momentum flux ratio is shown in Fig. 4.38. The dashed line in Fig. 4.38, corresponding to Eq. 4.7, is a least-square curve fit to the subcritical data, and the dotted line, corresponding to Eq. 4.8, is a least squares curve fit to the near- and supercritical data. A clear distinction exists between the dark-core length for the subcritical case (diamond symbols) and that for the near- and supercritical chamber pressures, with the subcritical dark-core length being longer for a given  $M$ . This is similar to the observation made with the velocity ratio in Fig. 4.37. It should be noted that the near-critical pressure data is slightly supercritical, and both the near- and supercritical pressure conditions produce a single-phase coaxial jet.

As indicated by Eq. 4.8 and the data in Fig. 4.38, the single-phase data (i.e., near- and supercritical pressures), have the same  $M^{-0.5}$  dependence form, which were also reported by others (see Table 4.2). However, the two-phase subcritical data has a weaker dependence,  $M^{-0.2}$ , than the single-phase dark-core length. Other quantitative differences between jet flows at subcritical and supercritical pressures have been reported before. For single round jets, Chehroudi and co-workers [27, 28, and 30] found that at supercritical pressures the spreading rate and fractal dimension values were the same as those for a gaseous jet injected into a gaseous ambient with different densities (i.e.,

variable-density, single-phase, gaseous jet). This is considered a similar observation, but for the dark-core length. Under supercritical pressures, our coaxial jet results scales with  $M^{-0.5}$ . From Table 4.2 and the data presented in Fig. 4.38, it appears that the inverse square root of the momentum flux ratio, originally found from the equal-density water-water work of Rehab et al. [51], [52], and later extended to gas-gas coaxial jet with different densities by Favre-Marinet and Camano-Schettini [60], also applies as well to the dark-core length for supercritical shear-coaxial jets. The similarity between the dark-core length at supercritical pressures and single-phase shear-coaxial jets is possibly due to a lack of surface tension under near- and supercritical conditions. However, caution should be exercised when extrapolating these results to systems containing multiple chemical species. A system containing a mixture of different chemical species at a pressure greater than the critical pressure of any of the individual components, may in fact still be below the critical pressure of the mixture at various locations of the jet, as previously discussed in Chapter 2.

$$\frac{L}{D_1} = \frac{25}{M^{0.2}} \quad (4.7)$$

$$\frac{L}{D_1} = \frac{12}{M^{0.5}} \quad (4.8)$$

*Where,*

$L$  is the dark core length,

$D_1$  is the inner diameter of the inner-jet, and

$M$  is the momentum flux ratio outer-jet to inner-jet.

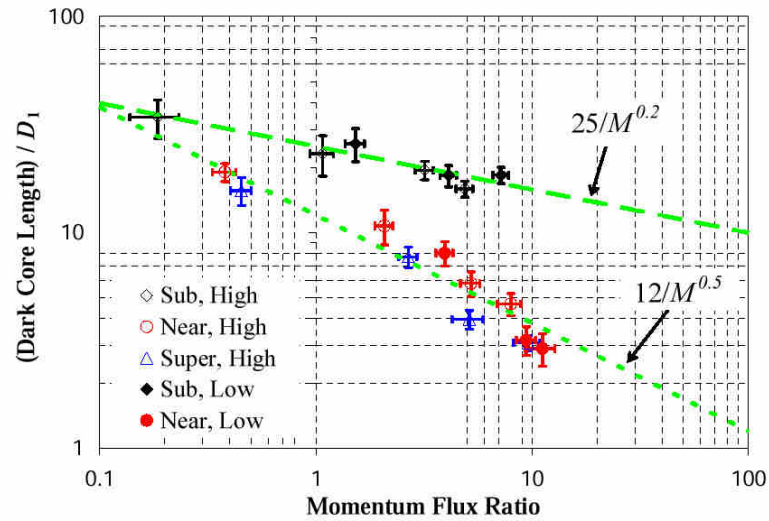


Figure 4.38: Dark core length versus momentum flux ratio. The diamond, circle, and up-triangle symbols represent sub-, near-, and supercritical chamber pressure, respectively. The hollow symbols are at a high outer-jet temperature ( $\sim 190$  K) and solid symbols are at a low outer-jet temperature. The error bars on the data points in Fig. 12 for the dark core length represent one standard deviation from the mean, and the error bars for the momentum flux ratio are the  $n^{\text{th}}$  order uncertainty as described at the beginning of this chapter. The dashed line is  $25/M^{0.2}$  and the dotted line is  $12/M^{0.5}$ .

The near- and supercritical pressure dark-core length data for all of the single-phase cases taken from the references listed in Table 4.2 are plotted against momentum flux ratio in Fig. 4.39. Rehab et al. [51, 52] indicate that injector geometrical effects are attributed to the variation of a constant in the equation of the form given by Eq. 4.8. In addition, this constant was reported to be between 5 and 9 in [51] while to be suggested between 6 and 8 in [52]. Certainly, geometrical differences in injector design can influence the core length, but other differences in the experiment can also change this value.

Figure 4.39 also shows four data points from Favre-Marinet and Camano Schettini [60] (data series denoted by x, +, and \* inscribed within a square) at a momentum flux ratio of about 8.9 for different density ratios and fluids with the same injector and measurement technique. Note that the injector produces shear-coaxial jets with different core lengths. This suggests that even though momentum flux ratio incorporates the effect of density differences between cases in some manner, it may not capture the entire effect.

Regarding the data by Rehab et al. [52], the authors reported reasonably good agreement with the  $M^{-0.5}$  dependency when a semi-empirical theory was used, although a curve fit to their extracted experimental data indicates a somewhat slower fall of  $L/D_1$  with momentum flux ratio, see dashed-dotted line in Fig. 4.39. It appears that the majority of the core-length data can be captured using the inverse square root dependence on momentum flux ratio with the constant varying from the low value of 5, reported by Rehab et al. [51], to a value of 12 for the dark core length data at near and supercritical pressures up to a momentum flux ratio of about 100. Favre-Marinet and Camano

Schettini [60] reported that for their data at the high momentum flux ratios a recirculation bubble forms at the end of the core causing a decrease in length as shown in Fig. 4.39.

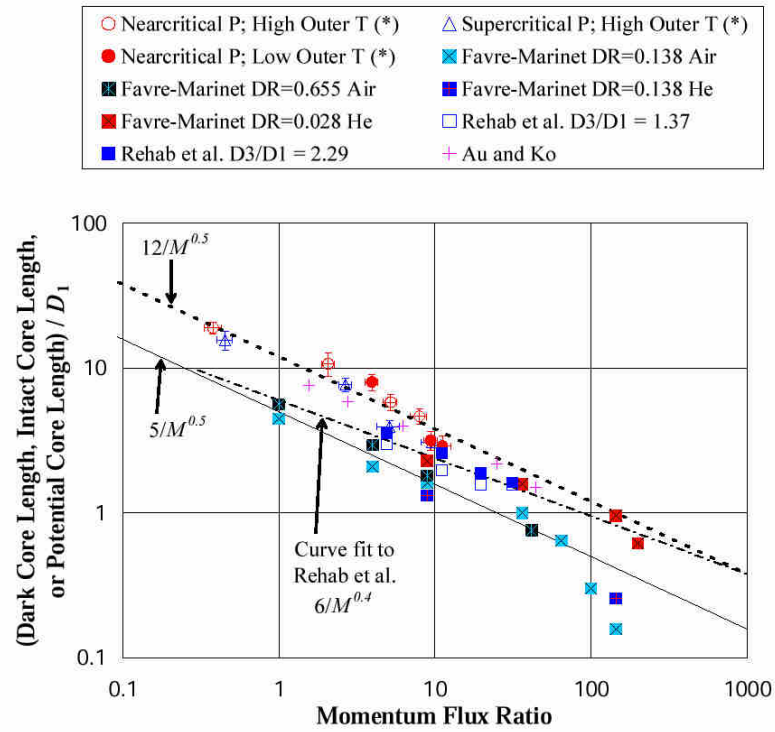


Figure 4.39: Comparison of dark core length, intact core length, or potential-core length for single-phase coaxial jets. This work (denoted by \*), Favre-Marinet and Camano Schettini [60], Rehab et al. [52], Au and Ko [48]. DR denotes density ratio of the outer-jet to inner-jet.

The measured results for the core length in two-phase shear-coaxial jets reported by others listed in Table 4.2 are compared with the subcritical pressure dark-core length measured in this work in Fig. 4.40 plotted as a function of momentum flux ratio. Some information is important to keep in mind when comparing these results as follows. There are only three references in the literature that report measurements of core length for two-phase shear-coaxial jets. Also, only one, Porcheron et al. [65], reports an equation that was developed, in part, for a cryogenic liquid core (see Table 4.2). However, because the measuring technique involved acquisition of a quantity named “liquid-presence probability (LPP)” (see Chapter 2 for details), quite different from all the other techniques, only the computed values from the equation indicated by the dashed-dotted line in Fig. 4.40 can be compared. Englebert et al [63], Eroglu et al. [8], and Woodward [62] all used water or a water solution as the fluid flowing from the inner-jet. In the experiments of Eroglu et al. [8], using the same apparatus as in Farago and Chigier [61], they observed laminar flow for  $Re < 6000$ , and a transition regime to turbulent flow in the range of  $6000 < Re < 10^4$ . Therefore, it is unlikely that any of the measurements made by Eroglu et al. [8] had a fully-developed turbulent velocity profile at the injector exit-plane. The entrance length of the injector used by Englebert et al. [63] was  $22 D_1$ . At the range of  $Re$  reported by Englebert et al. [63] (see Table 4.2 ) the required entrance length, estimated from the equation reported in White [85], ranges from about 18 to  $25 D_1$ . It is possible that some of the data points were not taken under fully-developed condition. This was acknowledged by Englebert et al. [63] and another injector with an entrance length of  $50 D_1$  was reported to not influence the breakup mechanism or the diameter of droplets after breakup. However, the effect on the core length was not reported. In

addition, both injectors used by Eroglu et al. [8] and Engelbert et al. [63] had much larger injector gap widths (i.e., annular outer-jet thickness), compared to the inner-jet diameter (see Table 4.2), than that typically associated with rocket engine shear-coaxial injectors. On the other hand, the injector used by Woodward [62] had a gap-width-to-inner-jet diameter more inline with those of typical rocket injectors. The required entrance length of the injector for the  $Re$  range reported by Woodward [62] was between 29 and 33  $D_1$ , whereas the actual length of the injector was 85  $D_1$ . Therefore, it is likely that the data of Woodward [62] did indeed have a fully-developed turbulent exit velocity profile. However, due to the high density of the aqueous solution of potassium iodide (KI(aq.)) used by Woodward [62], most of the data were for  $M < 1$ , even at velocity ratios as high as 30.

Evident in Fig. 4.40 is the fact that for the  $1 < M < 10$ , the dark-core length at the subcritical condition are longer than the laminar or transition regime jets of Eroglu et al. [8] and Englebert et al. [63] and appears to follow the trend of the aqueous solution of potassium iodide with helium (KI(aq) – He) data of Woodward [62]. The equation from Porcheron et al. [65] (see Table 4.2), indicated by the dashed-dotted line, was evaluated at the average Ohnesorge number ( $Z$ ) and density ratio (outer-to-inner jet) equivalent to the subcritical data of this work, cases 1-4 and 13-15 from Table 4.1. Note that the equation of Porcheron et al. [65], despite having a similar dependence on momentum flux ratio ( $M^{-0.13}$ ) as the subcritical data of this work ( $M^{-0.2}$ ), and the seemingly relevant non-dimensional parameters of Ohnesorge number and density ratio, under-predicts the subcritical dark-core lengths by about 1.5 orders of magnitude. This is most likely due to their definition of core length and the measurement technique mentioned earlier. The

liquid–presence probability (LPP) was measured by a fiber optic method, and correlated with density ratio, Ohnesorge number, momentum flux ratio, and axial distance from the injector. When the LPP dropped to 50%, that axial distance was defined as the core length. By adjusting this LPP to about 2.5%, which results in a change to the constant in their equation, the agreement with the subcritical data of this work is quite good. However, their equation is very sensitive to the choices of the LPP value. For example, changing LPP by 1% causes the equation to over-predict by about one-half order of magnitude, and changing it by 5% causes an under-prediction of the same order. Another observed problem with changing the LPP to 2.5% to fit the data of this work is that the water data of Englebert et al [63], Eroglu et al. [8], and Woodward [62] is then over-predicted by about an order of magnitude. This kind of behavior suggests a lack of generality of this equation despite its appearance, incorporating seemingly-relevant parameters such as Ohnesorge number and density ratio.

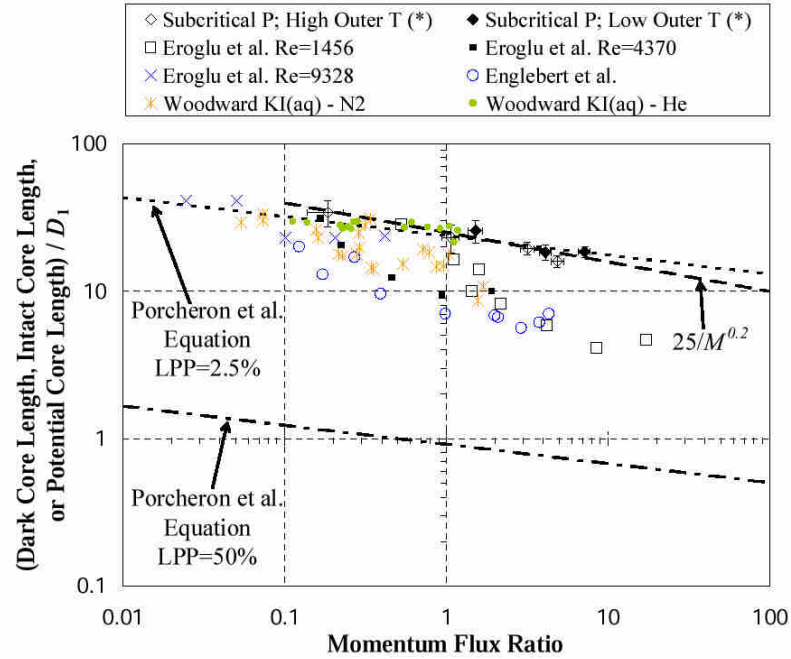


Figure 4.40: Comparison of the dark-core length, intact core length, or potential-core length for two – phase coaxial jets. This work (denoted by \*), Eroglu et al. [8], Engelbert et al. [63], Woodward [62]. Porcheron et al. [65] did not report core length measurements because of the measurement technique of liquid probability presence, but only an equation, see Table 4.2 for a summary of the work, and Chapter 2 for more details. Dashed-dotted line is the equation of Porcheron et al. evaluated at the average conditions of the subcritical data of this work with the LPP = 50%, and the dotted line is their equation evaluated at the same conditions except LPP = 2.5%

Figure 4.41 combines the single-phase core length data in Fig. 4.39 with the two-phase data shown in Fig. 4.40. This plot is unique in the sense that, to the best of the author's knowledge, presents all of the relevant core length data available in the open literature, spanning five orders of magnitude in momentum flux ratio. In the range of  $1 < M < 10$ , which is relevant for cryogenic liquid rocket engines (SSME preburner and main chamber momentum flux ratios are about 3.4 and 1.2, respectively [42], [43]), two distinct regimes in core length exist. The single-phase coaxial jets are shorter and scale differently than the two-phase dark-core lengths of this work. An interesting aspect of these data is that for the momentum flux ratios less than about one, all data points seem to converge to single narrow range. Additionally, in the limit of momentum flux ratio approaching zero (i.e.  $U_o \rightarrow 0$ ), results fall near the upper bound of single round jets (no coaxial jet). More specifically, the data in this limit tends to fall near the upper bound of the intact-core length range expected for single round jets as predicted by the Eq. 4.9 suggested in Chehroudi et al. [86]. This range for the single jet indicated in Fig. 4.41 was calculated using the recommended constant by Chehroudi et al. [86] of 7.15 using the density ratios (outer to inner jet) that spanned this work (see Table 4.1).

$$\frac{L}{D_1} = \frac{C}{\sqrt{\frac{\rho_o}{\rho_i}}} \quad (4.9)$$

Where,

$L$  is the intact core length,

$D_1$  is the inner diameter of the inner-jet, and

$\rho$  is the density, and

$C$  is a constant ranging from 3.3 to 11, with the optimum being 7.15.

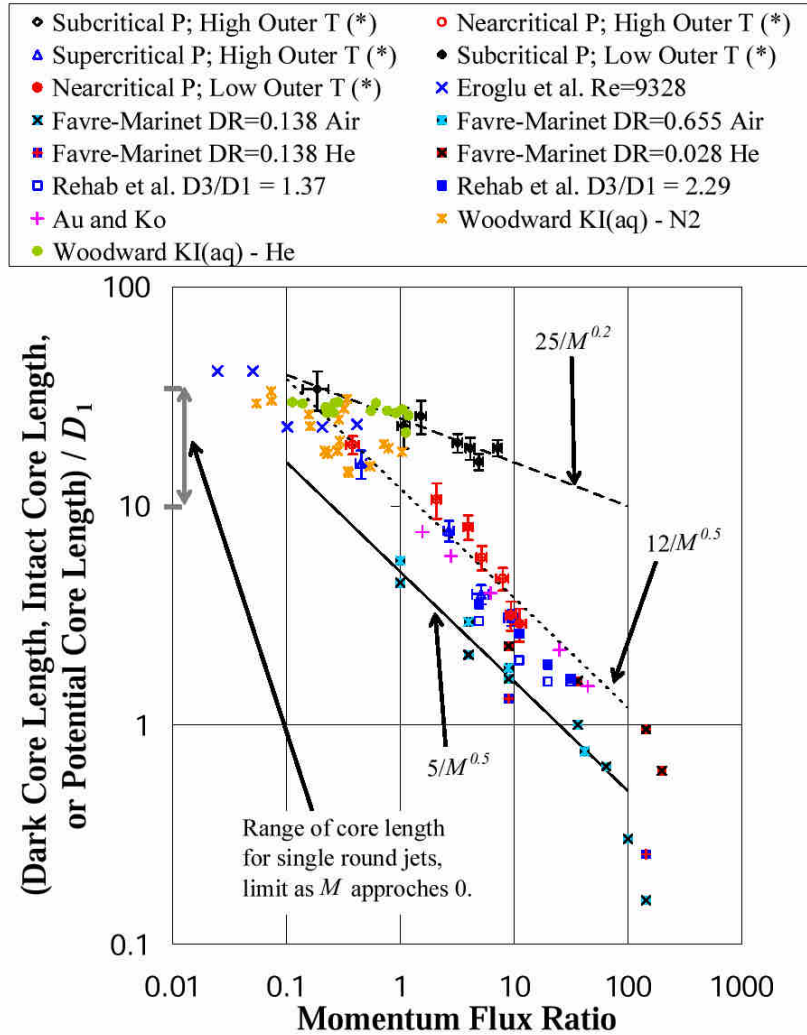


Figure 4.41: Comparison of the dark-core length, intact core length, or potential-core length vs. momentum flux ratio for shear-coaxial injectors, both single-phase and two-phase shear-coaxial jets. The same symbol definitions and references used here as Fig. 4.39 and Fig. 4.40.

The dark-core length data from this work for momentum flux ratios less than one are plotted in Fig. 4.42 against outer-to-inner jet density ratio, and compared with Eq. 4.9 using the optimum value of  $C = 7.15$  suggested by Chehroudi et al. [86]. It is clear from Fig. 4.42 that in the low-momentum-flux-ratio limit, the controlling nature of the high-speed outer-jet is diminished and the core length values are similar to those of single round jets.

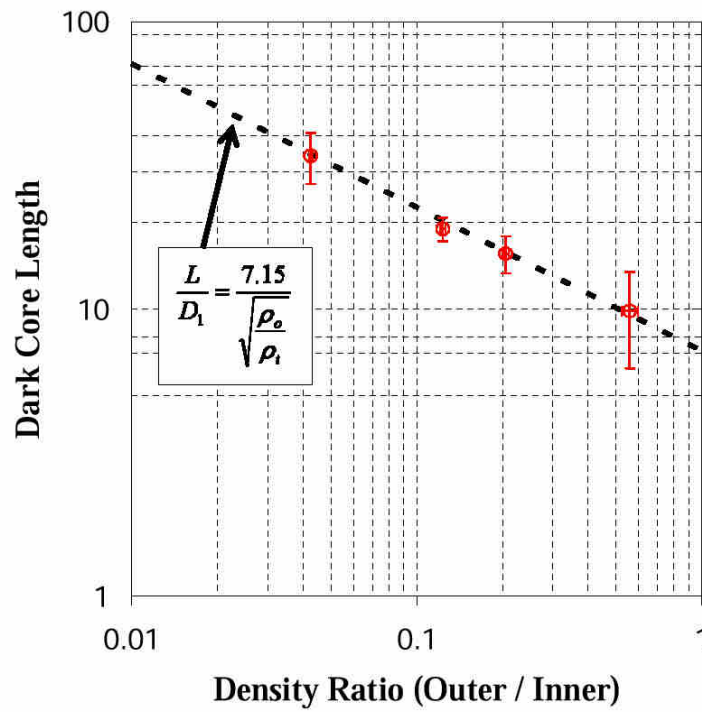


Figure 4.42: Comparison of dark core length, for  $M < 1$ , with Eq. 4.9 developed for single round jets.

## Chapter 5

### Summary, Conclusion, and Recommendations for Future Work

#### 5.1 Summary and Conclusions

A flow study was conducted on a cryogenic shear-coaxial injector at pressures spanning from subcritical to supercritical values, both with and without high-amplitude external acoustic excitation. This injector design was based on the experience gained from a single round jet exposed to similar conditions, see Chehroudi and coworkers [16-22]. The injector was placed in a chamber, near the minimum of the pressure oscillation amplitude of its acoustic mode. The flow from the inner-jet of the coaxial injector was liquid nitrogen (or liquid-like, if at supercritical pressures) and cold gaseous nitrogen flowed from the outer annular jet, both injected into a chamber pressurized with nitrogen at ambient temperature. Radial temperature profiles were measured at the exit-plane of cryogenic shear-coaxial jets using a traversing mechanism holding a very small thermocouple to ensure proper characterization of the boundary conditions. To the best of the author's knowledge, this is the first reported exit-plane temperature profiles of a cryogenic coaxial jet at supercritical chamber pressures. The coaxial jet was imaged with cameras with framing rates up to 18 kHz. Visualizations of the jet were taken both with and without the external transverse acoustic field. The field was initiated by an activation of an acoustic driver at a wavelength two orders of magnitude longer than the

characteristic dimensions of the injector. Both qualitative and quantitative information were obtained from the images.

An algorithm for measuring the dark-core length from an image has been developed. This method, named an adaptive thresholding technique, accounts for the variability of the light source and changes in the refractive index field reflected in images. For this work, the rise of the background light in an image histogram was suitably identified by the slope of the intensity histogram increasing above the  $e^{-1}$  value. There is no guarantee that images of other flows have the same criteria. However, the information from image histograms provided a consistent and repeatable method for identification of the dark-core length of the jet.

Velocity measurements can be made from high-speed shadowgraph movies. Much work must still be done to determine the optimum interrogation source window size and image magnifications to improve overall accuracy of velocity measurements. The velocity measurement relies on the assumption (or approximation) that the motion of shadows of fluid elements in an image from one frame to another represents the motion of the fluid elements. Improvements on this approximation are achieved when the velocity gradient along the direction of light source to the camera is zero, or when the fluid structure is easily identified as a particle. A direct comparison to a proven velocimetry measurement technique, such as laser Doppler velocimetry (LDV), would allow for a better quantification of the technique and prove the validity.

Based on the results of the experiments summarized above the following conclusions are offered:

1. Transient start of the acoustic driver results in a limit cycle behavior, which is evident from the transient velocity measurements, and from the behavior of the jet observed in the high-speed movies. This presents one of the first transient measurements of velocity from shadowgraph images reported in the literature.
2. The amplitude of the acoustic pressure waves and the resulting transverse velocity fluctuations, driven at a resonance frequency of the chamber, decreases as the density of the chamber fluid increases. This is a consequence of operating acoustic driver at a constant maximum power.
3. The wavelength measured from the amplitude of the acoustic pressure measurements (in time or spatially) is two orders of magnitude longer than the characteristic dimensions of the jet. Therefore, the wavelength is too long to excite coherent structures in the shear layer.
4. The acoustic driver governs the behavior of the transverse velocity in the chamber fluid and the jet, which is evident from the peaks in the power spectra of the velocity signals and the movies. The velocity fluctuations measured in the jet are amplified compared to that of the chamber fluid far from the influence of the jet. Also, the most energetic peak in the power spectra of the transverse velocity is at the acoustic driver frequency.
5. The motion of the core dominates the behavior of the jet. The oscillations of the core are predominately in the direction of the acoustic velocity. Some motions of the core do occur in other directions, but are not in the same periodic fashion and are lower in amplitude. The transverse velocity fluctuations impart a force to the core of the jet near the injector tip causing the core to be displaced in the

transverse direction corresponding to the direction of the local momentum at a given time. As a portion of the core is displaced near the injector tip, and convected downstream, it continues to travel in the same transverse direction, despite a reversal of the acoustic velocity field.

6. The mean dark-core length, which is the axial distance from the injector tip to the first break in the core, shortens upon exposure to the acoustic field. However, a clear difference between the acoustically-excited and unexcited jets can be discerned at the highest velocity ratios, high outer-jet temperature, and under subcritical chamber pressure.
7. The dark-core length (for unexcited jet) measured from the averaged image of a set is shorter than the mean of the dark-core length measured from the individual images of the same set. When the fluctuations in the dark-core length are very small, the two quantities are nearly equal. However, when the fluctuations of the dark-core length are large, differences as high as 20% is seen. This is a consequence of the averaging process of the image.
8. As the chamber pressure is increased at a constant velocity ratio, the dark-core length decreases. Because of the variability of the dark-core length, differences in the dark-core length, comparing the near- and supercritical chamber pressures, cannot always be distinguished. However, the dark-core length under subcritical chamber pressure at the same velocity ratio (or momentum flux ratio) is longer than those measured under near- or supercritical pressures.
9. The scaling of the dark-core length with the inverse-square-root of the momentum flux ratio, which was developed from all water shear-coaxial jets [37]-[42], and

later applied to gaseous jets of different densities [43], also applies to supercritical shear-coaxial jets. For this work, the dark-core length at near- and supercritical pressures is approximately given by the equation:  $L/D_1 \approx 12 M^{-0.5}$ . Within the momentum flux ratio range of  $0.1 < M < 100$ , nearly all of the single-phase shear-coaxial jet core length data in the open literature can be contained in a region defined by  $L/D_1 \approx C M^{-0.5}$  when the constant  $C$  is between 5 and 12.

10. At subcritical pressures, the scaling of the dark-core length with momentum flux ratio, for this work, is given by  $L/D_1 \approx 25 M^{-0.2}$ . Limited core length data for two-phase shear-coaxial jets with fully-developed turbulent inner-jet flow exists in the open literature in the range of momentum flux ratios between 1 and 10, considered relevant for liquid rocket engines.
11. When comparing all of the available core length data in the open literature, for a given velocity ratio, the core length of two-phase (i.e., a liquid inner-jet with a gaseous outer-jet and chamber fluid) shear-coaxial jets are longer than those for single-phase shear-coaxial jets, and a clear region of demarcation between the two types can be drawn.
12. In the limit of momentum flux ratio approaching zero (for example, when the velocity of the outer-jet goes to zero), the dark-core length should approach that of a single round jet. For momentum flux ratios less than unity, where the controlling nature of the outer-jet momentum is diminished, the dark-core length scales with the inverse square root of the outer-to-inner density ratio, as predicted by an equation in Chehroudi et al. [52].

13. The root mean square (RMS) variation of the dark-core length decreases with increasing velocity ratio at a given chamber pressure and asymptotically approaches a constant level. The RMS of the dark-core length is greatest at subcritical pressures. To the best of the author's knowledge, this quantity was not previously reported in the literature.
14. From the past works, it was shown that an episode of so-called "temperature ramping", used for stability rating, could lead the engine to an unstable behavior. Also, from other works, it is shown that coaxial injectors with high outer-to-inner jet velocity ratios (greater than  $\sim 10$  for LOX/H<sub>2</sub>) are more stable. In the current work, the observation that the RMS of the dark-core length fluctuations decreased at high velocity ratio under both high and low outer-jet temperatures, is considered as a potential explanation the injector-induced combustion instabilities. It is possible that decreases in the RMS fluctuation levels could weaken a key feedback mechanism for the self-excitation process that is believed to drive the combustion instability in rocket engines. This offers a possible improvement in understanding of the combustion instability in LRE. Ultimately, this hypothesis requires further testing in a multi-element, fired rocket experimental facility, for validation purposes

## 5.2 Recommendations for Future Work

The data in the literature come from a variety of different injectors. A systematic variation of all the important dimensions of the injector geometry should allow for an accurate assessment of the impact the injector has on the length of the dark core. This ought to be combined with measurements from sufficiently large number of images to permit more accurate determination of the variability of the dark-core length. Some relevant dimensions that may produce first-order effects on the behavior of the core are the inner-tube (post) recess and the thickness of the inner-tube lip.

In addition to varying the injector dimensions, systematic changes of the fluids used, particularly with two-phase shear-coaxial jet operation is recommended. By using a single chemical species for both the inner and outer-jets, a clear distinction between subcritical and supercritical can be drawn. However, what may be more relevant to a liquid rocket engine is using a pair of fluids, such as liquid nitrogen and either hydrogen or helium at elevated pressures. The resulting system would have closely related properties to that of a cryogenic liquid rocket engine. Recall that a combusting system, or any system of multiple chemical species, may not be supercritical everywhere because of the highly non-linear behavior of the critical locus dependence on composition. Therefore, it is possible that even though the propellants are injected at pressures greater than the critical pressure, dark-core length may behave similar to a two-phase jet. This is because the region near the core is in fact a two-phase flow. Momentum flux ratio is an important parameter governing core length of a shear-coaxial jet and does a better job at collapsing the data from the open literature than the velocity ratio. However, the

bifurcation that exists between the fully-turbulent two-phase shear-coaxial jets and the single-phase shear-coaxial jets cannot be described with the inverse square root of the momentum flux ratio. There is an inherent difference between the single-phase and two-phase shear-coaxial jets. Perhaps, surface tension is the important quantity explaining the difference. Collapse of the core length data for both single-phase and two-phase jets to a single curve is desirable and has been considered by many researchers, even was claimed by a few. However, preponderance of evidence from this work suggests that a satisfactory collapse to a single curve is not yet achieved, and perhaps may not even exist. However, systematic variations of the viscosity, surface tension, and density of the inner and outer-jets in a given injector is a step in the right direction.

The application of high-speed shadowgraphs for measuring velocity proved to be a promising technique. However, more work is required to determine the accuracy of the approach. This could be accomplished by using some proven velocimetry measurement technique, such as laser Doppler velocimetry (LDV), which would allow examination of this method's limitations.

The acoustic field within the inner-chamber is not completely characterized. The injector in this work was placed at a pressure minimum. A liquid rocket engine experiencing a transverse mode combustion instability will undoubtedly have injectors at many phase angles with respect to the pressure amplitude. By fully characterizing the inner-chamber pressure field and moving the location of the injector, various effects on the jets behavior can be investigated. Additionally, by acoustically driving multiple injectors and analyzing the interaction between the jets, would provide useful information towards better understanding of the rocket combustion instability.

Finally, a computational model that can use the data reported in this dissertation, would provide a wealth of information. The model capable of satisfactory prediction could provide the baseline validation on the fluid mechanics portion of a combustion instability code.

## Bibliography

1. Culick F. E. and Yang, V., "Overview of Combustion Instabilities in Liquid-Propellant Rocket Engines," Liquid Rocket Engine Combustion Instability, edited by V. Yang and W. Anderson, Progress in Astronautics and Aeronautics, AIAA, Washington, DC, 1995, pp. 3-38.
2. Harrje, D. T., and Reardon, F. H. (eds.) "Liquid Propellant Rocket Combustion Instability," NASA SP-194, 1972, pp. 17-19.
3. Hulka, J., and Hutt, J., "Liquid Oxygen / Hydrogen Instability Phenomena," in Liquid Rocket Engine Combustion Instability, edited by V. Yang and W. Anderson, Progress in Astronautics and Aeronautics, AIAA, Washington, DC, 1995, pp. 39-72.
4. DCAPII, ver. 2.1, The Design Institute for Physical Property Data (DIPPR) of The American Institute of Chemical Engineers, 1985.
5. Vingert, L., Gicquel, P., Lourme, D., and Ménoret, L., "Coaxial Injector Atomization," Liquid Rocket Engine Combustion Instability, edited by V. Yang and W. Anderson, Progress in Astronautics and Aeronautics, AIAA, Washington, DC, 1995, pp.145-190.
6. Rayleigh, J. W. S., "On the instability of Jets," Proceedings of London Mathematical Society, Vol. 10, 1878. pp. 4-21.
7. Lefebvre, A. H., *Atomization and Sprays*, Hemisphere, New York, 1989.
8. Eroglu, H., Chigier, N., and Farago, Z., "Coaxial Atomizer Intact Lengths," Physics of Fluids A, Vol. 3, No. 2, Jan. 1991, pp. 303-308.
9. Moran, M. J. and Shapiro, H. N., *Fundamentals of Engineering Thermodynamics*, 3rd ed., J. Wiley and Sons, New York, 1995.
10. Smith, J. M., Van Ness, H. C., and Abbott, M. M., *Introduction to Chemical Engineering Thermodynamics*, 5<sup>th</sup> ed., McGraw-Hill, New York, 1996.
11. van Konynenburg, P. H., and Scott, R. L., "Critical Lines and Phase Equilibria in a Binary van der Waals Mixtures," Phil. Trans. R. Soc. London, Vol. 298, 1980, pp 495.

12. Street, W. B., and Calado, J. C. G., "Liquid Vapor Equilibrium for Hydrogen + Nitrogen at Temperatures from 63 to 110K and Pressures to 57 MPa," *J. Chem. Thermodynamics*, Vol. 10, 1978, pp 1089-1100.
13. Zuo, Y. X., and Stenby, E. H., "A Linear Gradient Theory Model for Calculating Interfacial Tensions of Mixtures," *J. of Colloid and Interface Science*, Vol. 182, 1996, pp. 126-132.
14. REFPROP, Reference Fluid Thermodynamic and Transport Properties, Software Package, Ver. 7.0, NIST, U.S. Department of Commerce, Gaithersburg, MD, 2002.
15. Gielessen, J. and Schmatz, W, *Z. Phys. Chem., Neue Folge*, Vol. 27, 1961.
16. Lee, S. J., The Surface Tension of LOX Droplets at Near-Critical Conditions Using Molecular Dynamics, M.S. Thesis, Aerospace Engineering, The Pennsylvania State University, 2001.
17. Vieille, B., Étude expérimentale de l'atomisation secondaire de gouttes d'oxygène liquide, Thèse par Docteur de L'Université D'Orléans, 1998.
18. Harstad, K. and Bellan, J., "Evaluation of commonly used assumptions for isolated and cluster drops, in nitrogen at all pressures," *Combustion and Flame*, Vol. 127, 2001, pp. 1861.
19. Woodward, R. D., and Talley, D. G., "Raman Imaging of Transcritical Cryogenic Propellants," 34<sup>th</sup> Aerospace Sciences Meeting and Exhibit, AIAA, Washington, DC, 15-18 Jan. 1996.
20. Givler, S. D., and Abraham, J., "Supercritical Droplet Vaporization and Combustion Studies," *Progress in Energy and Combustion Science*, Vol. 22, 1996, pp. 1-28.
21. Yang, V. "Modeling of supercritical vaporization, mixing, and combustion processes in liquid-fueled propulsion systems," *Proc. Combust. Inst.*, Vo. 28, 2000, pp. 925.
22. Bellan, J., "Supercritical (and subcritical) fluid behavior and modeling: drops, streams, shear and mixing layers, jets and sprays," *Progress in Energy and Combustion Science*, Vol. 26, 2000, pp. 329-366.
23. Newman, J. A., and Brzustowski, T. A., "Behavior of a Liquid Jet near the Thermodynamic Critical Region," *AIAA J.*, Vol. 9, No. 8, 1971, pp. 1595-1602.
24. Chehroudi, B., Talley, D., and Coy, E. B., "Initial Growth Rate and Visual Characteristics of a Round Jet into a Sub- to Supercritical Environment of

- Relevance to Rocket, Gas turbine, and Diesel Engines,” 37<sup>th</sup> AIAA Aerospace Science Meeting and Exhibit, AIAA, Washington, DC, 11-14 Jan. 1999.
25. Chehroudi, B., Talley, D. G., and Coy, E. B., “Fractal Geometry and Growth Rate Changes of Cryogenic Jets near the Critical Point,” 35<sup>th</sup> AIAA/ASME/SAE/ASEE Joint Propulsion Conference and Exhibit, AIAA, Washington, DC, 20-24 Jun. 1999.
  26. Chehroudi, B., Cohn, R., Talley, D. G, and Badakhshan, A., “Raman Scattering Measurements in the Initial Region of Sub- and Supercritical Jets,” 36<sup>th</sup> AIAA/ASME/SAE/ASEE Joint Propulsion Conference and Exhibit, AIAA, Washington, DC, 17-19 Jul. 2000.
  27. Chehroudi, B., Talley, D. G., and Coy, E. B. “Visual Characteristics and Initial Growth Rates of Round Cryogenic Jets at Subcritical and Supercritical Pressures,” *Physics of Fluids*, Vol.4, No. 2, Feb. 2002. pp. 850-861.
  28. Chehroudi, B., Cohn, R., and Talley, D. G., “Cryogenic Shear Layers: Experiments and Initial Growth Rates of Round Cryogenic Jets at Subcritical and Supercritical Pressures,” *International Journal of Heat and Fluid Flow*, Vol. 23, 2002, pp. 554-563.
  29. Chehroudi, B., and Talley, D. G., “Interaction of Acoustic Waves with a Cryogenic Nitrogen Jet at Sub- and Supercritical Pressures,” 40<sup>th</sup> AIAA Aerospace Meeting and Exhibit, AIAA, Washington, DC, 14-17 Jan. 2002.
  30. Chehroudi, B. and Talley, D., “Fractal Geometry of a Cryogenic Nitrogen Round Jet Injected into Sub- and Super-critical Conditions”, *Atomization and Sprays*, Vol. 14, 2004, pp. 81-91.
  31. Chehroudi, B., Davis, D. W., and Talley, D. G., “Initial Results from a Cryogenic Coaxial Injector In An Acoustic Field,” 41<sup>st</sup> AIAA Aerospace Sciences Meeting and Exhibit, AIAA, Washington, DC, 6-9 Jan. 2003.
  32. Davis, D. W. and Chehroudi, B., “The Effects of Pressure and Acoustic Field on a Cryogenic Coaxial Jet,” 42nd AIAA Aerospace Sciences Meeting and Exhibit, AIAA, Washington, DC, 5-8 Jan. 2004.
  33. Davis, D. W., Chehroudi, B., and Sorensen, I. “Measurements in an Acoustically Driven Coaxial Jet Under Supercritical Condition,” 43<sup>rd</sup> AIAA Aerospace Sciences Meeting and Exhibit, AIAA, Washington, DC, 10-13 Jan. 2005.
  34. Davis, D. W., and Chehroudi, B., “Measurements of an Acoustically Driven Coaxial Jet under Sub-, Near-, and Supercritical Conditions,” *J. of Propulsion and Power*, 2005 (submitted).

35. Davis, D. W., Chehroudi, B., and Talley, D. G., "Experiments on a Coaxial Injector under an Externally-Forced Transverse Acoustic Field," 53<sup>rd</sup> JANNAF Propulsion / 2<sup>nd</sup> Liquid Propulsion Subcommittee / 1<sup>st</sup> Spacecraft Propulsion Subcommittee Meeting, CPIA, Monterey, CA, 5-8 Dec. 2005.
36. Davis, D. W., and Chehroudi, B., "Shear- Coaxial Jets from a Rocket- Like Injector in a Transverse Acoustic Field at High Pressures," 44<sup>th</sup> AIAA Aerospace Sciences Meeting and Exhibit, AIAA, Washington, DC, 9-12 Jan. 2006.
37. Oswald, M., Smith, J. J., Branam, R., Hussong, J., Schik, A., Chehroudi, B., and Talley, D. G., "Injection of Fluids into Supercritical Environments," Comb. Sci. Tech., to appear 2005.
38. Oswald, M., and Micci, M., "Spreading Angle and Centerline Variation of Density of Supercritical Nitrogen Jets," Atomization and Sprays, Vol. 11, 2002, pp. 91-106.
39. Oswald, M., and Schik, A., "Supercritical nitrogen free jet investigated by spontaneous Raman scattering," Experiments in Fluids, Vol. 27, 1999, pp. 497-506.
40. Zong, N., Meng, H., Hsieh, S.-Y., Yang, V., "A Numerical Study of Cryogenic Fluid Injection and Mixing under Supercritical Conditions," Physics of Fluids, Vol. 16, No. 12, 2004, pp. 4248-4261.
41. Zong, N., Modeling and Simulation of Cryogenic Fluid Injection and Mixing Dynamics under Supercritical Conditions, Ph.D. Thesis, Department of Mechanical and Nuclear Engineering, The Pennsylvania State University, University Park, PA, <http://etda.libraries.psu.edu/>, 2005.
42. Strakey, P. A., Talley, D. G., and Hutt, J. J., "Mixing Characteristics of Coaxial Injectors at High Gas/Liquid Momentum Ratios," Journal of Propulsion and Power, Vol. 17, No. 2, 2001, pp. 402-410.
43. Strakey, P. A., Talley, D. G., Tseng, L. K., Miner, K. I., "Effects of Liquid-Oxygen Post Biasing on SSME Injector Wall Compatibility," Journal of Propulsion and Power, Vol. 18, No. 2, 2002, pp. 240-246.
44. Forstall, W., and Shapiro, A. H., "Momentum and Mass Transfer in Coaxial Gas Jets," J. Applied Mechanics, Trans. ASME, Vol. 72, 1950, pp. 399-408.
45. Chigier, N. A., and Beer, J. M., "The Flow Region Near the Nozzle in Double Concentric Jets," J. of Basic Engineering, Trans. ASME, Vol. 4, 1964, pp. 797-804.

46. Champagne, F. H., and Wygnanski, I. J., "An Experimental Investigation of Coaxial Turbulent Jets," *International Journal of Heat and Mass Transfer*, Vol. 14, 1971, pp. 1445-1464.
47. Ko, N. W. M., and Au, H., "Coaxial Jets of Different Mean Velocity Ratios," *Journal of Sound and Vibration*, Vol. 100, No. 2, 1985, pp. 211-232.
48. Au, H., and Ko, N. W. M., "Coaxial Jets of Different Mean Velocity Ratios, Part 2," *Journal of Sound and Vibration*, Vol. 116, No. 3, 1987, pp. 427-443.
49. Dahm, W., Frieler, C., and Tryggvason, G., "Vortex Structure and Dynamics in the Near Field of a Coaxial Jet," *J. Fluid Mechanics*, Vol. 241, 1992, pp. 371-402.
50. Villermaux, E., Rehab, H., and Hopfinger, E. J., "Breakup Regimes and Self-Sustained Pulsations in Coaxial Jets," *Meccanica*, Vol. 29, 1994, pp. 393-401.
51. Rehab, H., Villermaux, E., and Hopfinger, E. J., "Flow Regimes of Large Velocity Ratio Coaxial Jets," *J. Fluid Mech.*, 1997, pp. 357-381.
52. Rehab, H., Villermaux, E., and Hopfinger, E. J., "Geometrical Effects of Near-Field Flow Structure of Coaxial Jets," *AIAA Journal*, Vol. 36, No. 5, 1998, pp. 867-869.
53. Villermaux, E., "Mixing and Spray Formation in Coaxial Jets," *J. Propulsion and Power*, Vol. 14, No. 5, 1998, pp. 807-817.
54. Lasheras, J. C., and Hopfinger, E. J., "Liquid Jet Instability and Atomization in a Coaxial Gas Stream," *Annual Rev. Fluid Mech.*, Vol. 32, 2000, pp. 275-308.
55. Hopfinger, E. J., and Lasheras, J. C., "Breakup of A Water Jet in High Velocity Co-Flowing Air," *ICLASS-94*, Rouen, France, Paper I-15, July 1994, pp. 110 – 117.
56. Raynal, L., Instabilité et entrainement a l'interface d'une couche de mélange liquid-gaz, Thèse de Doctorat, Université Joseph Fourier, Grenoble, France, 1997.
57. Raynal, L., Villermaux, E., Lasheras, J. C., and Hopfinger, E. J., "Primary Instability in Liquid-Gas Shear Layers," 11<sup>th</sup> Symposium on Turbulent Shear Flows, Grenoble-France, Sept. 8-11, 1997.
58. Lasheras, J. C., Villermaux, E., and Hopfinger, E. J., "Breakup and Atomization of a Round Water Jet by a High Speed annular Air Jet," *J. Fluid Mech.*, Vol. 357, 1998, pp. 351-379.
59. Favre-Marinet, M., Camano, E. B., and Sarboch, J., "Near-Field Coaxial Jets with Large Density Differences," *Experiments in Fluids*, Vol. 26, 1999, pp. 97-106.



60. Favre-Marinet, M., and Camano Schettini, E. B., "The Density Field of Coaxial Jets with Large Velocity Ratio and Large Density Differences," *International Journal of Heat and Mass Transfer*, Vol. 44, 2001, pp. 1913-1924.
61. Farago, Z., and Chigier, N., "Morphological Classification of Disintegration of Round Liquid Jets in a Coaxial Air Stream," *Atomization and Sprays*, Vol. 2, 1992, pp. 137-153.
62. Woodward, R. D., Primary Atomization of Liquid Jets Issuing from Rocket Engine Coaxial Injectors, Ph.D. Thesis, Department of Mechanical Engineering, The Pennsylvania State University, University Park, PA, 1993.
63. Englebert, C., Hardalupas, Y., and Whitlaw, J. H., "Breakup Phenomena in Coaxial Air-Blast Atomizers," *Proc. R. Soc.*, Vol. 451, London, 1995, pp. 189-229.
64. Carreau, J. L., Porcheron, E., LeVisage, D., Prevost, L., and Roger, F., "Liquid Core Characterization of Coaxial Liquid Oxygen/Inert Gas Jets," *Int. J. of Fluid Mech. Research*, Vol. 24, Nos. 4-6, 1997, pp.498-507.
65. Porcheron, E., Carreau, J. L., Prevost, L., LeVisage, D., and Roger, F., "Effect of Density on Coaxial Liquid Jet Atomization," *Atomization and Sprays*, Vol. 12, 2002, pp. 209-227.
66. Miesse, C. C., "The effect of ambient pressure oscillations on the disintegration and dispersion of a liquid jet", *Jet Propulsion*, Vol. 25, 1955, pp. 525-530, and 534.
67. Newman, "A Preliminary Study of the Effects of Vaporization and Transverse Oscillations on Liquid Jet Breakup," NASA CR-72258, 1967.
68. Buffum, F. G., and Williams, F. A. Response of turbulent liquid jets to transverse acoustic fields, *Proceedings of the 1967 Heat Transfer and Fluid Mechanics Institute*, Edited by P. A. Libby, D. B. Olfe, and C. W. Van Atta, 1967, pp. 247-276.
69. Heidmann, M. F. and Groenweg, J. F. "Analysis of the dynamic response of liquid jet atomization to acoustic oscillations," NASA Technical Note, NASA TN D-5339, July, 1969.
70. Rhys, N. O., Acoustic Excitation and Destruction of Liquid Sheets, PhD Thesis, Department of Mechanical and Aerospace Engineering, The University of Alabama in Huntsville, 1999.
71. Ota, J., Sakurai, K., Okamoto, K., and Madarame, H., "Application of Image Analysis with Noise Removal for Supercritical CO<sub>2</sub>," *Proceedings of ICONE*,

- 10<sup>th</sup> International Conference on Nuclear Engineering, Arlington Virginia, 14-18 Apr. 2002.
72. Okamoto, K., Ota, J., Sakurai, K., Madarame, H., "Transient Velocity Distributions for the Supercritical Carbon Dioxide Forced Convection Heat Transfer," *Journal of Nuclear Science and Technology*, Vol. 40, No. 10, 2003, pp. 763-767.
  73. *Omega Temperature Hand Book*, 5<sup>th</sup> ed., Curtis Publishing, Indianapolis, IN, 2004, Chap. Z
  74. Moffat, R. J., "Describing Uncertainties in Experimental Results," *Experimental Thermal and Fluid Science*, Vol. 1, 1988, pp. 3-17.
  75. Wu, P.-K., Tseng, L.-K., and Faeth, G. M., "Primary Breakup in Gas/Liquid Mixing Layers for Turbulent Liquids," *Atomization and Sprays*, Vol. 2, 1992, pp. 295-317.
  76. Davis, D. W. Supercritical Fuel Injection Studies for Advanced Gas Turbine Engines, M.S. Thesis, The Pennsylvania State University, 2001.
  77. Kinsler, L. E., Frey, A. R., Coppens, A. B., Sanders, J. V., *Fundamentals of Acoustics*, 4<sup>th</sup> Ed., J. Wiley and Sons, New York, 2000.
  78. Gendrich, C. P., Koochesfahani, M. M., and Nocera, D.G., "Molecular Tagging Velocimetry and Other Novel Applications of a New Phosphorescent Supramolecule," *Experiments in Fluids*, Vol. 23, 1997, pp. 361-372.
  79. Russ, J. C., *The Image Processing Handbook*, CRC Press, Boca Raton FL, 1992.
  80. Zong, N. and Yang, V., "A Numerical Study of High-Pressure Oxygen/Methane Mixing and Combustion of A Shear Coaxial Jet," 43<sup>rd</sup> AIAA Aerospace Sciences Meeting and Exhibit, AIAA, Washington, DC, 10-13 Jan. 2005.
  81. Eagle, David, BNALib, A BASIC Numerical Analysis Library for Personal Computers, Littleton, CO, [www.vbonline.com](http://www.vbonline.com), 2002.
  82. Glogowski, M., Bar-Gil, M., Puissant, C., Kaltz, T., Milicic, M., and Micci, M., "Shear Coaxial Injector Instability Mechanisms" 30th AIAA/ASME/SAE/ASEE Joint Propulsion Conference, AIAA, Washington, DC, 27-29 Jun. 1994.
  83. Vingert, L., Gicquel, P., Ledoux, M., Care, I, Micci, M., and Glogowski, M., "Atomization in Coaxial-Jet Injectors", in *Liquid Rocket Thrust Chambers: Aspects of Modeling, Analysis, and Design*, edited by Yang, V., Habiballah, M., Hulka, J., and Popp, M., Progress in Astronautics and Aeronautics, AIAA, Washington, DC, 2004, pp. 105-140.

84. Wanhainen, J. P., Feiler, C. E., and Morgan, C. J., "Effect of Chamber Pressure, Flow per Element, and Contraction Ratio on Acoustic-Mode Instability in Hydrogen – Oxygen Rockets," NASA TN D-4733, August 1968.
85. White, F. M., *Fluid Mechanics*, 2<sup>nd</sup> Ed., McGraw-Hill, Inc. New York, 1986.
86. Chehroudi, B., Chen, S. H., Bracco, F., and Onuma, Y., "On the intact core of full-cone sprays," Society of Automotive Engineers, Paper 850126, 1985.

## **Appendix A**

### **Experimental Procedure and Flow Diagram**

The standard operating procedure and an expanded view of the process flow diagram presented in Fig. 3.3 spanning 4 pages here in Figs. A.1 (A) – (D).

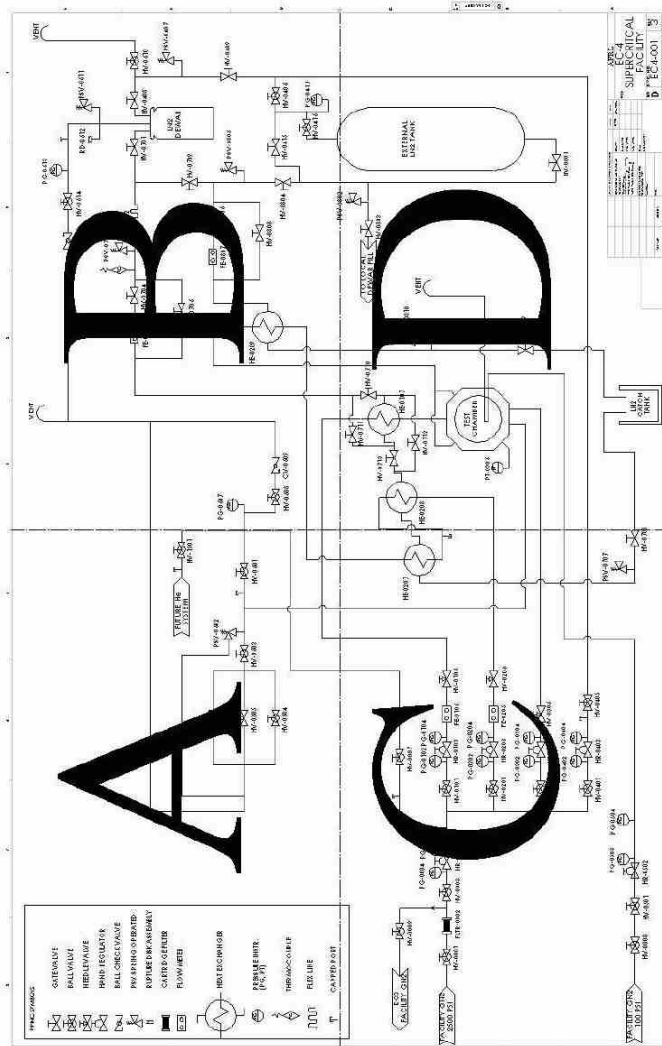


Figure A.1: Process Flow Diagram of the AFRL Supercritical Facility. Regions denoted with “A” corresponds to Fig. A.1(A) and so on.

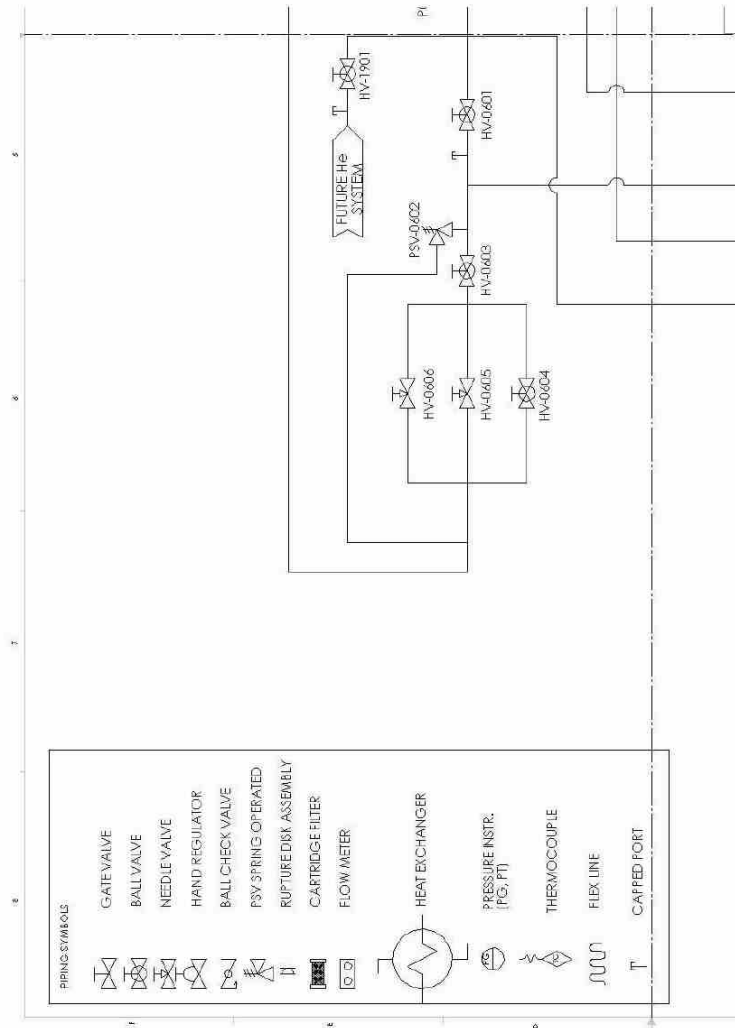


Figure A.2(A): Process Flow Diagram corresponding to region "A" Fig. A.1

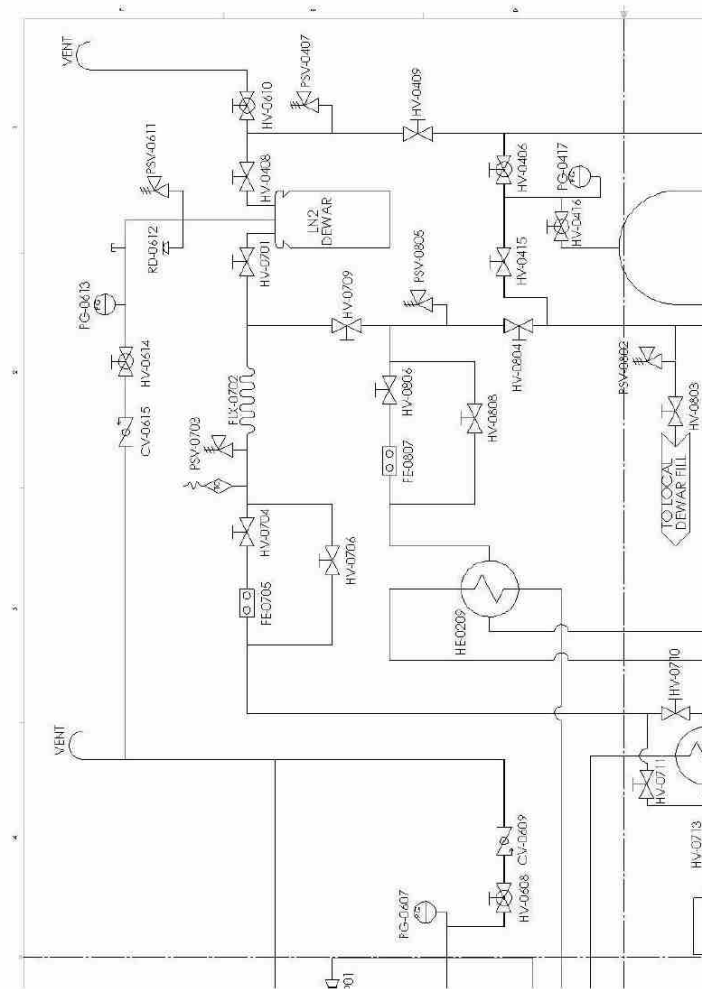


Figure A.3(B): Process Flow Diagram corresponding to region "B" Fig. A.1

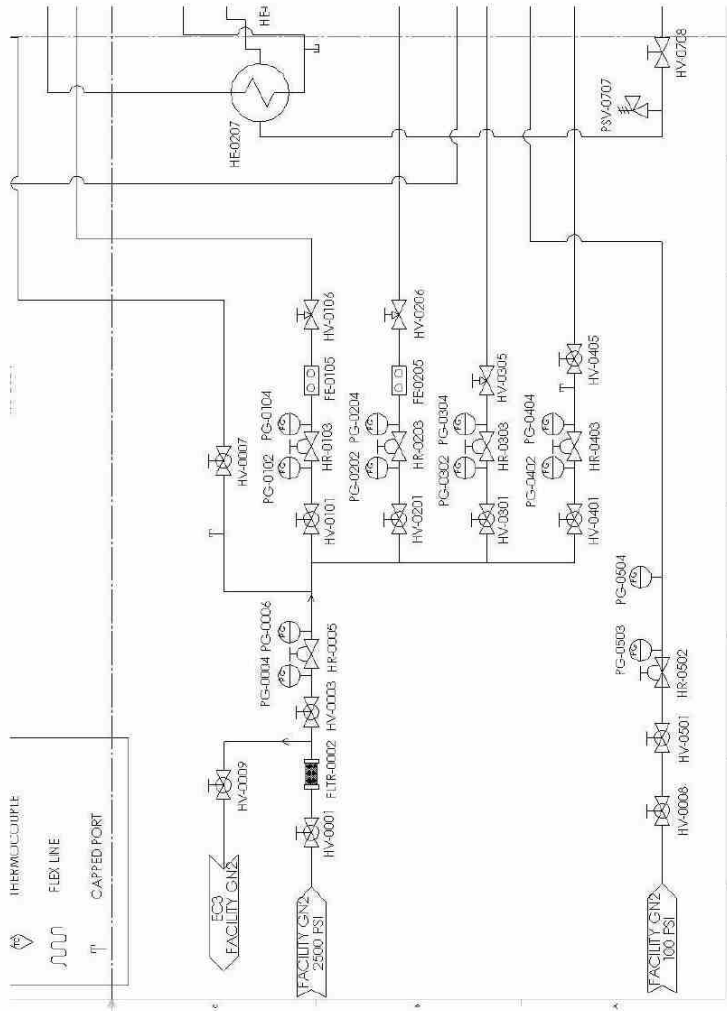


Figure A.4(C): Process Flow Diagram corresponding to region "C" Fig. A.1

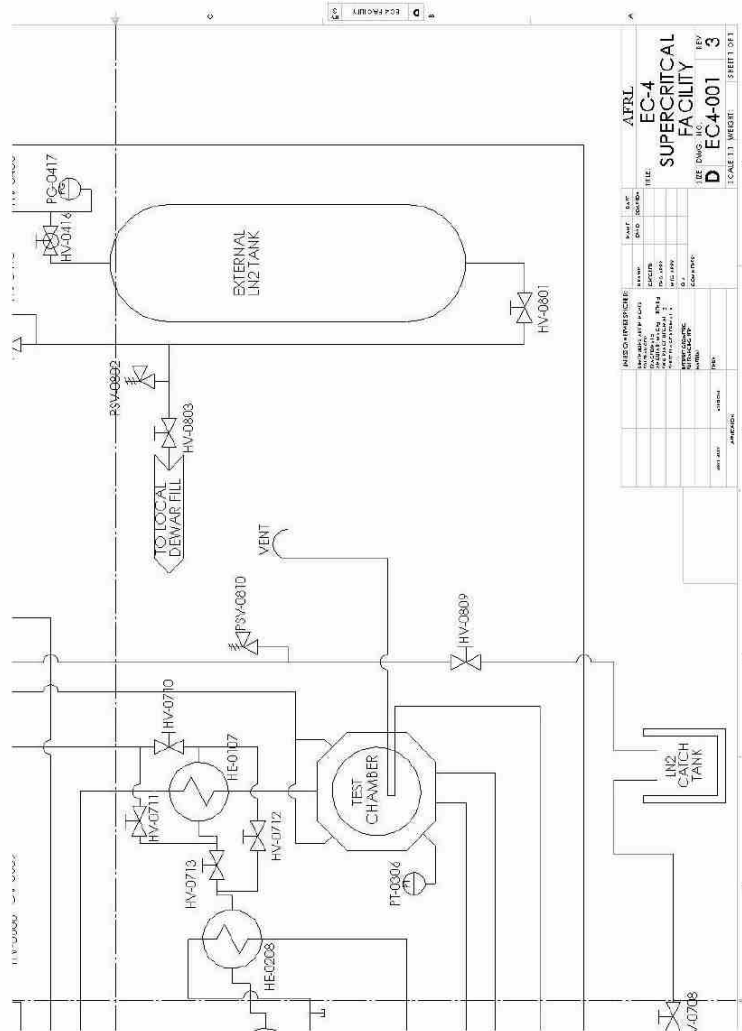


Figure A.5(D): Process Flow Diagram corresponding to region "D" Fig. A.1

<b>BUILDING 8451 EXPERIMENTAL CELL, EC-4 AIR FORCE RESEARCH LABORATORY EDWARDS AFB, CA</b>	<b>PROCEDURE: SOP-PRSA-EC4-0001 REVISION: 0 DATE REVISED: 24 Jun 2004 NUMBER OF PAGES: 25</b>
<div style="border: 1px solid black; padding: 5px; margin: 0 auto; width: 80%;"> <p style="text-align: center;">BUILDING 8451 EXPERIMENTAL CELL, EC-4 OPERATIONS</p> </div> <p style="text-align: center; margin: 5px 0;">PROCEDURE TITLE</p> <div style="border: 1px solid black; padding: 5px; margin: 0 auto; width: 80%;"> <p style="text-align: center;">SUPERCRITICAL COLD FLOW FACILITY OPERATIONS</p> </div>	
<b>PREPARED BY:</b> Test Engineer _____ DATE _____ EC-4 _____	
<b>REVIEW:</b> ERC, Principle Investigator Review _____ DATE _____ Air Force Research Laboratory AFRL, Technical Representative Review _____ DATE _____ Air Force Research Laboratory AFRL, Safety Representative Review _____ DATE _____ Air Force Research Laboratory AFRL, Quality Assurance Review _____ DATE _____ Air Force Research Laboratory	
<b>APPROVAL:</b> AF Program Manager _____ DATE _____ Air Force Research Laboratory ERC Program Manager _____ DATE _____ Air Force Research Laboratory ERC Safety Manager _____ DATE _____ Air Force Research Laboratory Building 8451 Facility Manger _____ DATE _____ Air Force Research Laboratory AFRL Chief, Aerophysics Branch _____ DATE _____ Air Force Research Laboratory AFRL Chief, Safety Branch _____ DATE _____ Air Force Research Laboratory	

Revision	Notes	Prepared By
0	-Initial procedure written	D. Davis June 24, 2004
1	-Added -Deleted	

PERSONNEL

EXPERIMENTAL CELL EC-4

DATE \_\_\_\_\_

AEROPHYICS BRANCH, BLDG 8451  
AUTHORIZATION# \_\_\_\_\_

WORK

The following personnel are designated as test team members, and are charted to perform their assignment as follows:

**Test Conductor (TC)** – Responsible for the timely performance of the test as written and for overall facility and test safety. This includes coordinating and directing the activities of the Red Crew and other test support teams. TC is responsible for coordinating all pretest activities and outside support required, including (but not limited to) security, fire, medical, and safety. TC is responsible for initialing completion on each step of the master test procedure and ensuring all test goals are met and all critical data is acquired. Has authority to perform real-time redlines on test procedures as required to ensure test requirements and goals area met. All safety-related redlines will be coordinated and approved by AFRL and/or ERC Safety.

Name \_\_\_\_\_ Signature \_\_\_\_\_

**Red Crew Leader (RCL)** – Responsible for directing the activities of Red Crew members. Reports directly to the TC and ensures all Red Crew tasks are completed. Responsible for ensuring all RCM's have all required certifications and training. Responsible for ensuring all required equipment is available, accessible, and serviceable.

Name \_\_\_\_\_ Signature \_\_\_\_\_

**Other Test Team Members** – Responsible for performing ancillary duties in support of test, support of anomaly resolution, and other necessary activities.

Name \_\_\_\_\_ Signature \_\_\_\_\_

Name \_\_\_\_\_ Signature \_\_\_\_\_

Name \_\_\_\_\_ Signature \_\_\_\_\_

Name \_\_\_\_\_ Signature \_\_\_\_\_

**ALL TEST TEAM MEMBERS** – Responsible for the safe performance of the test. Have read and understood all portions of the test procedure. Any Test Team Member can declare an emergency or unsafe condition.

\_\_\_\_ 1.

**ABBREVIATIONS AND ACRYONMS**

CPR	- Cardiopulmonary Resuscitation
CV	- Check Valve
EC	- Experimental Cell
ER	- Engineering Request
FE	- Flow Element
FLTR	- Filter
FLX	- Flexible Line
GN2	- Gaseous Nitrogen
HE	- Heat Exchanger
He	- Helium
HR	- Hand Regulator
HV	- Hand Valve
LN2	- Liquid Nitrogen
N2	- Nitrogen
PC	- Chamber Pressure
PG	- Pressure Gauge
PI	- Principle Investigator
PM	- Program Manager
PPE	- Personal Protective Equipment
PSV	- Pressure Safety Valve
PT	- Pressure Transducer
QA	- Quality Assurance
RCL	- Red Crew Leader
RD	- Rupture Disk
SCF	- Supercritical Facility
SOCC	- Site Operations Control Center
SOP	- Standard Operating Procedure
TC	- Test Conductor
TOP	- Test Operation Procedure

___ 2.	<b>TEST DESCRIPTION AND OBJECTIVES</b>
___ 2.1.	<p data-bbox="646 535 743 562"><b>PURPOSE</b></p> <p data-bbox="646 577 1240 682">This procedure performs a stand-alone operation of the EXPERIMENTAL CELL, EC-4. This procedure may be used in conjunction with other Test Operation Procedures (TOP) or Work Authorizations (WA) as required to support operations or checkouts.</p>
___ 2.2.	<p data-bbox="646 682 717 709"><b>SCOPE</b></p> <p data-bbox="646 724 1240 850">This procedure will verify proper configuration before operation including purges and valve configuration and sequential steps to perform the Supercritical Cold Flow (SCF) Operation. Securing the SCF post operation and emergency shutdown are also included in the procedure.</p>
___ 3.	<p data-bbox="646 903 820 930"><b>DOCUMENTATION</b></p> <p data-bbox="646 945 1240 1018">The completion of each applicable event shall be verified by marking to the left of the item number by the TC. Deviations from these procedures will be coordinated with the Test Engineer, TC, RCL</p>
___ 3.1.	<p data-bbox="646 1029 893 1056"><b>APPLICABLE DOCUMENTS</b></p> <p data-bbox="646 1071 1240 1123">AFRL/PR OI 91-202, Environmental, Safety, and Occupational Health (ESOH) Programs, 7 Aug 2000.</p> <p data-bbox="646 1134 1240 1186">Space &amp; Missile Propulsion Division, Chemical Hygiene Plan (CHP), Bldg 8451.</p>
___ 3.2.	<p data-bbox="646 1197 966 1224"><b>REFERENCE DOCUMENTS: NONE</b></p>
___ 3.3.	<p data-bbox="646 1260 808 1287"><b>SPECIFICATIONS</b></p> <p data-bbox="646 1302 1240 1354">Nitrogen Purge Gas: Pressurizing agent, nitrogen, Grade B, Type I, Spec. Mil-P-27401.</p> <p data-bbox="646 1365 966 1396">Water: Facility domestic water supply</p>
___ 3.4.	<p data-bbox="646 1407 755 1434"><b>DRAWINGS</b></p> <p data-bbox="646 1449 950 1480">EC4-001, EC-4 Supercritical Facility</p>

4.	<b>TEST REQUIREMENTS AND RESTRICTIONS</b>									
4.1.	<p><b>TRAINING</b></p> <p>The following training is required for personnel using these procedures:</p> <table border="0" data-bbox="646 535 1117 604"> <tr> <td>CPR &amp; First Aid</td> <td>High Pressure</td> <td>Noise</td> </tr> <tr> <td>Initial HAZCOM</td> <td>Cryogenics</td> <td></td> </tr> <tr> <td>Job Site HAZCOM</td> <td>Lock-Out/Tag-Out</td> <td></td> </tr> </table> <p>(Laser training will be required in the future)</p>	CPR & First Aid	High Pressure	Noise	Initial HAZCOM	Cryogenics		Job Site HAZCOM	Lock-Out/Tag-Out	
CPR & First Aid	High Pressure	Noise								
Initial HAZCOM	Cryogenics									
Job Site HAZCOM	Lock-Out/Tag-Out									
4.2.	<p><b>MAXIMUM PERSONNEL ALLOWED IN EC-4:</b></p> <p>Five (5): Workers – (3) (RCL and TC),  Supervision – (1) (PI, PM, etc.),  Casual (Bio, Safety, QA, etc) – (1)</p>									
4.3.	<p><b>LIST OF EQUIPMENT</b></p> <p>Vapor Detection Equipment: One permanent (fixed) O2 sensor mounted in EC-4 and two (2) portable oxygen sensors (one for each worker in the cell).</p> <p>Mechanics tool kit, torque wrench and Caliper.</p> <p>Ensure all tools associated with this experiment/test/operation are accounted for prior to initiating system/item test. Assure all trash, debris, and FOD is picked up from around the test stand.</p>									
4.4.	<p><b>METEOROLOGICAL LIMITATIONS/ RESTRICTIONS</b></p> <p>A. No hazardous operations will be started when thunderstorms are within 25 nautical miles (28.75 miles) of AFRL unless the operation can meet the requirements for stopping the operation for lightning within 10 nautical miles. Operations in progress may be completed if it is safe to do so; however supervisors must assess individual operations to determine the appropriate action.</p> <p>B. All hazardous operations will be stopped when thunderstorms are within 10 nautical miles (11.5 miles) of the AFRL. The operation should be secured and personnel evacuated to Bldg 8451 and remain indoors.</p> <p>C. All outside work must stop when thunderstorms are within 5 nautical miles (5.75 miles) of the AFRL and all personnel must seek safety in Bldg 8451 until the lightning warning is cancelled.</p>									

_____ 5.	<b>SAFETY REQUIREMENTS</b>
_____ 5.1.	TEST HAZARDS:
	<p>Nitrogen gas (GN2) is used for pressurization of the chamber and production of the supercritical jet in the chamber. Nitrogen gas can cause asphyxiation hazards to personnel working in EC-4. Oxygen deficiency monitors will be used to warn personnel working in EC-4 of the hazard.</p>
	<p>Liquid nitrogen (LN2) is used for temperature conditioning of the supercritical jet in the chamber. This presents a cryogenic hazard to test crew working inside and outside EC-4. LN2 will also convert to GN2.</p>
	<p>The Acoustic test can produce hazardous noise levels (&gt;120 dB). Personnel are required to wear ear muffs to reduce exposure.</p>
_____ 5.2.	PERSONNEL PROTECTIVE CLOTHING REQUIREMENTS
	<p>Test PPE: Fire retardant lab coat or coveralls, safety goggles, safety shoes, leather gloves, and ear muffs (noise protection as required).</p>
	<p>Cryogenic PPE: Cryogenic gloves, Cryogenic Body Apron, Full-Face shield.</p>
_____ 5.3.	TEST AREA ACCESS DURING OPERATIONS
	<p>EC-4 GREEN: Normal test preparation activities. There are no pressure or chemical hazards in the test cell. The RCL will limit access to the affected operational area of interest.</p>
	<p>EC-4 AMBER: Hazardous chemicals in the test cell. No pressure or flows (static condition). RCL will monitor the Test Cell entrance, and prevent access to the cell. Personnel will not be allowed access to the test area unless cleared by the RCL and TC.</p>
	<p>EC-4 RED Hazardous test operations including propellant chill downs, purging operations. The TC will maintain access control to the area. Personnel will not be allowed access to EC-4 unless cleared by the TC.</p>

\_\_\_\_ 6.

**EXPLOSIVE LIMITS: NONE**

\_\_\_\_ 7.

**EMERGENCY PROCEDURES**

In the event of a major nitrogen leak or other emergency that jeopardizes the safety of the operators or other personnel perform Section 20 emergency procedures at the end of this document.

\_\_\_\_ 8.

**SPECIAL INSTRUCTIONS**

Red Crew Member shall notify Test Engineer of any leaks from the system.

Any lines, which require maintenance or re-torquing, should be coordinated with Test Engineering to maintain SCF system cleanliness. Work must be authorized in order to break into clean and sealed systems.

9.		PRETEST PREPARATIONS
9.1.	ALL	DON Test PPE listed in step 5.2
9.2.	RCL	Verify Oxygen Sensor in EC-4 is not at an ALARM condition and is reading greater than 20.0% +2.0% / -0.5% oxygen concentration by volume.
9.3.	RCL	Verify portable oxygen sensors are operational and calibrated.
9.4.	RCL	Turn ON or Verify ON EC-4 Air Handler ventilation system
9.5.	ALL	UNLOCK EC-4 outside door
9.6.	ALL	NOTE any potential hazards in and outside EC-4
9.7.	ALL	Verify GREEN, AMBER, and RED lights are functional and return to GREEN
9.8.	TC	If Acoustic Testing Verify Gain or Turn Gain on Amplifier to the ZERO position
9.9.	TC	If Acoustic Testing, Turn ON Amplifier to allow warm up as per ER_____
9.10.	RCL	If Acoustic Testing, POST Hearing Protection Required signs on the out side of the doors to EC-4, Room 19, foam door and adjacent hallway.
9.11.	TC	Turn on Data Acquisition System and System Electronics.

___ 10.		<b>INITIAL SETUP</b>
___ 10.1.	RCL	CLOSE / Verify CLOSED HV-0001 (EC-3, EC-4 Primary Facility Isolation Valve)
___ 10.2.	RCL	CLOSE / Verify CLOSED HV-0003 (EC-4 Secondary Facility Isolation Valve)
___ 10.3.	RCL	CLOSE / Verify CLOSED HV-0008 (EC-4 Low Pressure Facility Isolation Valve)
___ 10.4.	RCL	CLOSE / Verify CLOSED HV-0009 (EC-3 Secondary Facility Isolation Valve)
___ 10.5.	RCL	CLOSE / Verify CLOSED HV-0701 (LN2 Isolation Valve)
___ 10.6.	RCL	CLOSE / Verify CLOSED HV-0408 (Dewar GN2 Isolation Valve)
___ 10.7.	RCL	OPEN / Verify OPEN HV-0610 (Supply Dewar GN2 Vent Valve)
___ 10.8.	RCL	CLOSE / Verify CLOSED HV-0406 (Tank GN2 Pressurization Isolation Valve)
___ 10.9.	RCL	CLOSE / Verify CLOSED HV-0409 (Dewar Pressurization Vent Isolation Valve)
___ 10.10.	RCL	CLOSE / Verify CLOSED HV-0709 (Dewar LN2 Supply Isolation Valve)
___ 10.11.	RCL	CLOSE / Verify CLOSED HV-0704 (Heat Exchanger LN2 Flow Meter Isolation Valve)
___ 10.12.	RCL	CLOSE / Verify CLOSED HV-0706 (Heat Exchanger LN2 Flow Meter Bypass Valve)
___ 10.13.	RCL	CLOSE / Verify CLOSED HV-0801 (Tank LN2 Isolation Valve) NOTE: Valve located outside
___ 10.14.	RCL	CLOSE / Verify CLOSED HV-0803 (Local Dewar Fill Isolation Valve) NOTE: Valve located outside
___ 10.15.	RCL	CLOSE / Verify CLOSED HV-0804 (Tank-Dewar Separation Valve) NOTE: Valve located outside
___ 10.16.	RCL	CLOSE / Verify CLOSED HV-0415 (Vacuum Jacketed Line Purge Valve) NOTE: Valve located outside
___ 10.17.	RCL	CLOSE / Verify CLOSED HV-0416 (Tank GN2 Pressurization Valve) NOTE: Valve located outside
___ 10.18.	RCL	CLOSE / Verify CLOSED HV-0614 (Dewar Gauge Vent Valve)

___10.19.	RCL	CLOSE / Verify CLOSED HV-1901 (He System Isolation Valve)
___10.20.	RCL	CLOSE / Verify CLOSED HV-0601 (PC Vent PG Isolation Valve)
___10.21.	RCL	OPEN / Verify OPEN HV-0608 (Gauge Vent Valve)
___10.22.	RCL	CLOSE / Verify CLOSED HV-0007 (Upstream Regulator Pressure Valve)
___10.23.	RCL	OPEN / Verify OPEN HV-0603 (Chamber Pressure Build Valve)
___10.24.	RCL	OPEN / Verify OPEN HV-0604 (Primary Chamber Pressure Vent Valve)
___10.25.	RCL	CLOSE / Verify CLOSED HV-0605 (Secondary Chamber Pressure Vent Valve)
___10.26.	RCL	CLOSE / Verify CLOSED HV-0606 (Tertiary Chamber Pressure Vent Valve)
___10.27.	RCL	CLOSE / Verify CLOSED HV-0708 (Heat Exchanger LN2 Throttle Vent Valve)
___10.28.	RCL	CLOSE / Verify CLOSED HV-0809 (Coax Heat Exchanger LN2 Throttle Vent Valve)
___10.29.	RCL	OPEN / Verify OPEN HV-0710 (Primary Co-Flow Valve)
___10.30.	RCL	OPEN / Verify OPEN HV-0711 (Primary Counter Flow Valve)
___10.31.	RCL	OPEN / Verify OPEN HV-0712 (Secondary Counter Flow Valve)
___10.32.	RCL	OPEN / Verify OPEN HV-0713 (Secondary Co-Flow Valve)
___10.33.	RCL	CLOSE / Verify CLOSED HV-0806 (Coax LN2 Flow Meter Isolation Valve)
___10.34.	RCL	CLOSE / Verify CLOSED HV-0808 (Coax LN2 Flow Meter Bypass Valve)
___10.35.	RCL	CLOSE / Verify CLOSED HV-0101 (Center Jet GN2 Isolation Valve)
___10.36.	RCL	CLOSE / Verify CLOSED HV-0106 (Center Jet GN2 Throttle Valve)
___10.37.	RCL	CLOSE / Verify CLOSED HV-0201 (Coax Jet GN2 Isolation Valve)
___10.38.	RCL	CLOSE / Verify CLOSED HV-0206 (Coax Jet GN2 Throttle Valve)
___10.39.	RCL	CLOSE / Verify CLOSED HV-0301 (Chamber Pressurization Isolation Valve)
___10.40.	RCL	CLOSE / Verify CLOSED HV-0305 (Chamber Pressurization Throttle Valve)

___ 10.41.	RCL	CLOSE / Verify CLOSED HV-0401 (Dewar and Tank Pressurization Isolation Valve)
___ 10.42.	RCL	CLOSE / Verify CLOSED HV-0405 (Dewar LN2 Supply Dewar Tank Isolation Valve)
___ 10.43.	RCL	CLOSE / Verify CLOSED HV-0501 (Window Purge Isolation Valve)
___ 10.44.	RCL	Verify and Record Dewar Pressure from PG-0613 (Dewar Pressure Gauge) _____psig
___ 10.45.	RCL	Verify PG-0504 (Window Purge Pressure Gauge) reads 0 psig
___ 10.46.	RCL	Verify PG-0417 (LN2 Tank Pressure Gauge) reads 0 psig
___ 10.47.	RCL	Verify PG-0607 (Chamber Pressure Gauge) reads 0 psig
___ 10.48.	RCL	DECREASE FULLY / Verify FULLY DECREASED HR-0005 (EC-4 Facility Pressure Regulator)
___ 10.49.	RCL	Verify PG-0004 (EC-4 System Inlet Pressure Gauge) reads 0 psig
___ 10.50.	RCL	DECREASE FULLY / Verify FULLY DECREASED HR-0103 (Center Jet GN2 Pressure Regulator)
___ 10.51.	RCL	Verify PG-0102 (Center Jet GN2 System Inlet Pressure Gauge) reads 0 psig
___ 10.52.	RCL	DECREASE FULLY / Verify FULLY DECREASED HR-0203 (Coax Jet GN2 Pressure Regulator)
___ 10.53.	RCL	Verify PG-0202 (Coax Jet GN2 System Inlet Pressure Gauge) reads 0 psig
___ 10.54.	RCL	DECREASE FULLY / Verify FULLY DECREASED HR-0303 (Chamber Pressurization Regulator)
___ 10.55.	RCL	Verify PG-0302 (Chamber Pressurization System Inlet Pressure Gauge) reads 0 psig
___ 10.56.	RCL	DECREASE FULLY / Verify FULLY DECREASED HR-0403 (Dewar and Tank GN2 Pressure Regulator)
___ 10.57.	RCL	Verify PG-0402 (Dewar and Tank GN2 System Inlet Pressure Gauge) reads 0 psig
___ 10.58.	RCL	DECREASE FULLY / Verify FULLY DECREASED HR-0502 (Window Purge Pressure Regulator)
___ 10.59.	RCL	Verify PG-0504 (Window Purge Pressure Gauge) reads 0 psi

___ 11.	WINDOW PURGE	
___ 11.1.	TC	Notify SOCC via hotline in EC-1, EC-2 control room that EC-4 is going into a RED condition for SCF testing.
___ 11.2.	ALL	Verify all personnel are wearing Test PPE
___ 11.3.	RCL	Change EC-4 light to RED.
___ 11.4.	TC	Record Time _____
___ 11.5.	RCL	Verify window purge apparatus is in satisfactory condition
___ 11.6.	RCL	OPEN HV-0008 (EC-4 Low Pressure Facility Isolation Valve)
___ 11.7.	RCL	OPEN HV-0501 (Window Purge Isolation Valve)
<b>CAUTION: Do NOT Increase HR-0502 so that PG-0504 reads greater than 2.0 psig as it will damage PG-0504</b>		
___ 11.8.	RCL	INCREASE HR-0502 (Window Purge Pressure Regulator) until PG-0504(Window Purge Pressure Gauge) reads 1.5 psig +/- 0.5 psig
___ 11.9.	RCL	Permit window purge to continue according to ER _____

_____12.		FACILITY GN2 SETUP
_____12.1.	RCL	OPEN HV-0001 (EC-3, EC-4 Facility Isolation Valve)
_____12.2.	RCL	OPEN HV-0003 (EC-4 Facility Isolation Valve)
_____12.3.	RCL	Verify PG-0004 (EC-4 System Inlet Pressure Gauge) reads a pressure greater than 2000 psig
_____12.4.	RCL	OPEN HV-0007 (Upstream Regulator Pressure Valve)
_____12.5.	RCL	CLOSE HV-0608 (Gauge Vent Valve)
_____12.6.	RCL	INCREASE HR-0005 (EC-4 Facility Pressure Regulator) until PG-0607 (Chamber Pressure Gauge) reads 2000 psig +/- 50 psig.
_____12.7.	RCL	CLOSE HV-0007 (Upstream Regulator Pressure Valve)
_____12.8.	RCL	OPEN HV-0608 (Gauge Vent Valve)
_____12.9.	RCL	Verify PG-0607 (Chamber Pressure Gauge) reads 0 psig
_____12.10.	RCL	CLOSE HV-0608 (Gauge Vent Valve)
_____12.11.	RCL	OPEN HV-0601 (PC Vent PG Isolation Valve)
_____12.12.	RCL	Verify PG-0607 (Chamber Pressure Gauge) reads 0 psig

_____ 13.		CHAMBER PURGE
_____ 13.1.	TC	Record Time _____
_____ 13.2.	RCL	OPEN HV-0301 (Chamber Pressurization Isolation Valve)
_____ 13.3.	RCL	Verify PG-0302 (Chamber Pressurization System Inlet Pressure Gauge) reads 2000 psig +/- 150 psig
_____ 13.4.	RCL	INCREASE HR-0303 (Chamber Pressure GN2 Pressure Regulator) until PG-0304 (Chamber Pressure Purge Pressure Gauge) reads 400 psig +/-100 psig
_____ 13.5.	RCL	OPEN HV-0305 (Chamber Pressurization Throttle Valve) as per ER_____
_____ 13.6.	RCL	CLOSE HV-0603 (Chamber Pressure Build Valve)
_____ 13.7.	RCL	Verify PG-0607 (Chamber Pressure Gauge) indicates that PC is increasing to indicate purge is flowing.
_____ 13.8.	RCL	OPEN HV-0603 (Chamber Pressure Build Valve)

_____ 14.		CENTER JET PURGE
_____ 14.1.	RCL	OPEN HV-0101 (Center Jet GN2 Isolation Valve)
_____ 14.2.	RCL	Verify PG-0102 (Center Jet GN2 System Inlet Pressure Gauge) reads 2000 psig +/- 150 psig
_____ 14.3.	RCL	INCREASE HR-0103 (Center Jet GN2 Pressure Regulator) until PG-0104 (Center Jet Pressure Gauge) reads 400 psig +/-100 psig
_____ 14.4.	RCL	OPEN HV-0106 (Center Jet GN2 Throttle Valve) as per ER_____
_____ 14.5.	TC	Verify FE-0105 (Center Jet GN2 Flow Meter) indicates purge is flowing

_____ 15.	COAXIAL JET PURGE
_____ 15.1.	RCL OPEN HV-0201 (Coax Jet GN2 Isolation Valve)
_____ 15.2.	RCL Verify PG-0202 (Coax Jet GN2 System Inlet Pressure Gauge) reads 2000 psig +/- 150 psig
_____ 15.3.	RCL INCREASE HR-0203 (Coax Jet GN2 Pressure Regulator) until PG-0204 (Coax Jet GN2 Pressure Gauge) reads 400 psig +/-100 psig
_____ 15.4.	RCL OPEN HV-0206 (Coax Jet GN2 Throttle Valve) as per ER_____
_____ 15.5.	TC Verify FE-0205 (Coax Jet GN2 Flow Meter) indicates purge is flowing
_____ 15.6.	RCL OPEN HV-0605 (Secondary Chamber Pressure Vent Valve)
_____ 15.7.	RCL CLOSE HV-0604 (Primary Chamber Pressure Vent Valve)
_____ 15.8.	RCL ADJUST HV-0605 (Secondary Chamber Pressure Vent Valve) and HV-0606 (Tertiary Chamber Pressure Vent Valve) until PG-0607 (Chamber Pressure Gauge) reads INITIAL CHAMBER PRESSURE as per ER_____
_____ 15.9.	RCL Wait for required time to elapse from step 13.1 as per ER_____

16.		SYSTEM CHILL DOWN
16.1.	TC	Verify Red Crew has donned Cryogenic PPE as outlined in Step 5.2
16.2.	RCL	OPEN HV-0801 (Tank LN2 Isolation Valve)
16.3.	RCL	OPEN HV-0804 (Tank-Dewar Separation Valve)
16.4.	RCL	OPEN HV-0409 (Dewar Pressurization Vent Isolation Valve)
16.5.	RCL	CLOSE HV-0610 (Supply Dewar GN2 Vent Valve)
16.6.	RCL	OPEN HV-0701 (LN2 Isolation Valve)
16.7.	RCL	OPEN HV-0408 (Dewar GN2 Isolation Valve)
16.8.	RCL	OPEN HV-0706 (Heat Exchanger LN2 Flow Meter Bypass Valve)
16.9.	RCL	If operating HE-0107 (Cooling Tower) in <b>CO-FLOW</b> as per ER_____
16.9.1.	RCL	CLOSE HV-0711 (Primary Counter Flow Valve)
16.9.2.	RCL	CLOSE HV-0712 (Secondary Counter Flow Valve)
16.10.	RCL	If operating HE-0107 (Cooling Tower) in <b>COUNTER-FLOW</b> as per ER_____
16.10.1.	RCL	CLOSE HV-0710 (Primary Co-Flow Valve)
16.10.2.	RCL	CLOSE HV-0713 (Secondary Co-Flow Valve)
16.11.	RCL	OPEN HV-0808 (Coax LN2 Flow Meter Bypass Valve)
16.12.	RCL	OPEN HV-0401 (Dewar and Tank Pressurization Isolation Valve)
16.13.	RCL	Verify PG-0402 (Dewar and Tank GN2 System Inlet Pressure Gauge) reads 2000 psig +/-150 psig
16.14.	RCL	Increase HR-0403 (Dewar and Tank GN2 Pressure Regulator) until PG-0404 (Dewar, Tank Pressurization Pressure Gauge) reads as per ER_____
16.15.	RCL	OPEN HV-0405 (Dewar LN2 Supply Dewar Tank Isolation Valve)
16.16.	TC	Record Time _____
16.17.	RCL	OPEN HV-0809 (Coax Heat Exchanger LN2 Throttle Vent Valve) as per ER_____
16.18.	RCL	OPEN HV-0708 (Heat Exchanger LN2 Throttle Vent Valve) as per ER_____

___ 16.19.	ALL	ADJUST HR-0403 (Dewar and Tank GN2 Pressure Regulator) to maintain 22 psig +/- 1 psig on PG-0613 (Dewar Pressure Gauge)
___ 16.20.	ALL	Wait Required time for chill down as per ER _____
___ 16.21.	RCL	OPEN HV-0704 (Heat Exchanger LN2 Flow Meter Isolation Valve)
___ 16.22.	RCL	CLOSE HV-0706 (Heat Exchanger LN2 Flow Meter Bypass Valve)
___ 16.23.	RCL	OPEN HV-0806 (Coax LN2 Flow Meter Isolation Valve)
___ 16.24.	RCL	CLOSE HV-0808 (Coax LN2 Flow Meter Bypass Valve)
___ 16.25.	RCL	Remove Cryogenic PPE and don Test PPE as listed in Step 5.2

___ 17.		<b>TESTING</b>
___ 17.1.	RCL	If acoustic testing, Place foam door into position
___ 17.2.	TC	Verify all personnel are wearing ear muffs if acoustic testing.
___ 17.3.	RCL	INCREASE HR-0103 (Center Jet GN2 Pressure Regulator) until PG-0104 (Center Jet Pressure Gauge) reads 1500 psig +/- 50 psig
___ 17.4.	RCL	INCREASE HR-0203 (Coax Jet GN2 Pressure Regulator) until PG-0204 (Coax Jet GN2 Pressure Gauge) reads 1500 psig +/- 50 psig
___ 17.5.	RCL	INCREASE HR-0303 (Chamber Pressurization Regulator) until PG-0304 (Chamber Pressurization Pressure Gauge) reads 1500 psig +/- 50 psig
___ 17.6.	TC	Direct RCL to operate system as per test needs
___ 17.7.	RCL	OPERATE System as directed by test conductor

___ 18.	RCL	<b>SHUT DOWN</b>
___ 18.1.	RCL	OPEN HV-0808 (Coax LN2 Flow Meter Bypass Valve)
___ 18.2.	RCL	CLOSE HV-0806 (Coax LN2 Flow Meter Isolation Valve)
___ 18.3.	RCL	OPEN HV-0706 (Heat Exchanger LN2 Flow Meter Bypass Valve)
___ 18.4.	RCL	CLOSE HV-0704 (Heat Exchanger LN2 Flow Meter Isolation Valve)
___ 18.5.	RCL	CLOSE HV-0001 (EC-3, EC-4 Primary Facility Isolation Valve)
___ 18.6.	RCL	CLOSE HV-0701 (LN2 Isolation Valve)
___ 18.7.	RCL	CLOSE HV-0408 (Dewar GN2 Isolation Valve)
___ 18.8.	RCL	OPEN HV-0610 (Supply Dewar GN2 Vent Valve)
___ 18.9.	RCL	CLOSE HV-0008 (EC-4 Low Pressure Facility Isolation Valve)
___ 18.10.	RCL	CLOSE HV-0801 (Tank LN2 Isolation Valve)
___ 18.11.	RCL	Wait for PG-0004 (EC-4 System Inlet Pressure Gauge) to read 0 psig
___ 18.12.	RCL	CLOSE HV-0003 (EC-4 Secondary Facility Isolation Valve)
___ 18.13.	RCL	Verify PG-0102 (Center Jet GN2 System Inlet Pressure Gauge) reads 0 psig
___ 18.14.	RCL	CLOSE HV-0101 (Center Jet GN2 Isolation Valve)
___ 18.15.	RCL	CLOSE HV-0106 (Center Jet GN2 Throttle Valve)
___ 18.16.	RCL	Verify PG-0202 (Coax Jet GN2 System Inlet Pressure Gauge) reads 0 psig
___ 18.17.	RCL	CLOSE HV-0201 (Coax Jet GN2 Isolation Valve)
___ 18.18.	RCL	CLOSE HV-0206 (Coax Jet GN2 Throttle Valve)
___ 18.19.	RCL	Verify PG-0302 (Chamber Pressurization System Inlet Pressure Gauge) reads 0 psig
___ 18.20.	RCL	CLOSE HV-0301 (Chamber Pressurization Isolation Valve)
___ 18.21.	RCL	CLOSE HV-0305 (Chamber Pressurization Throttle Valve)
___ 18.22.	RCL	Verify PG-0402 (Dewar and Tank GN2 System Inlet Pressure Gauge) read 0 psig
___ 18.23.	RCL	CLOSE HV-0401 (Dewar and Tank Pressurization Isolation Valve)
___ 18.24.	RCL	CLOSE HV-0405 (Dewar LN2 Supply Dewar Tank Isolation Valve)

___ 18.25.	RCL	Verify PG-0504 (Window Purge Pressure Gauge) reads 0 psig
___ 18.26.	RCL	CLOSE HV-0501 (Window Purge Isolation Valve)
___ 18.27.	RCL	Fully DECREASE HR-0005 (EC-4 Facility Pressure Regulator)
___ 18.28.	RCL	Fully DECREASE HR-0103 (Center Jet GN2 Pressure Regulator)
___ 18.29.	RCL	Fully DECREASE HR-0203 (Coax Jet GN2 Pressure Regulator)
___ 18.30.	RCL	Fully DECREASE HR-0303 (Chamber Pressurization Regulator)
___ 18.31.	RCL	Fully DECREASE HR-0403 (Dewar and Tank GN2 Pressure Regulator)
___ 18.32.	RCL	Fully DECREASE HR-0502 (Window Purge Pressure Regulator)
___ 18.33.	RCL	OPEN HV-0608 (Gauge Vent Valve)
___ 18.34.	RCL	Verify PG-0607 (Chamber Pressure Gauge) reads 0 psig
___ 18.35.	RCL	CLOSE HV-0601 (PC Vent PG Isolation Valve)
___ 18.36.	RCL	OPEN / Verify OPEN HV-0603 (Chamber Pressure Build Valve)
___ 18.37.	RCL	OPEN HV-0604 (Primary Chamber Pressure Vent Valve)
___ 18.38.	RCL	CLOSE HV-0605 (Secondary Chamber Pressure Vent Valve)
___ 18.39.	RCL	CLOSE HV-0606 (Tertiary Chamber Pressure Vent Valve)
___ 18.40.	RCL	CLOSE HV-0808 (Coax LN2 Flow Meter Bypass Valve)
___ 18.41.	RCL	OPEN / Verify OPEN HV-0710 (Primary Co-Flow Valve)
___ 18.42.	RCL	OPEN / Verify OPEN HV-0711 (Primary Counter Flow Valve)
___ 18.43.	RCL	OPEN / Verify OPEN HV-0712 (Secondary Counter Flow Valve)
___ 18.44.	RCL	OPEN / Verify OPEN HV-0713 (Secondary Co-Flow Valve)
___ 18.45.	RCL	CLOSE HV-0708 (Heat Exchanger LN2 Throttle Vent Valve)
___ 18.46.	RCL	CLOSE HV-0809 (Coax Heat Exchanger LN2 Throttle Vent Valve)
___ 18.47.	RCL	CLOSE HV-0409 (Dewar Pressurization Vent Isolation Valve)
___ 18.48.	RCL	CLOSE HV-0706 (Heat Exchanger LN2 Flow Meter Bypass Valve)
___ 18.49.	RCL	CLOSE HV-0804 (Tank-Dewar Separation Valve)

___ 19.		<b>LN2 DEWAR FILL</b>
		<b>NOTE: If filling Dewar without testing go through Initial Setup</b>
___ 19.1.	TC	Verify Red Crew has donned Cryogenic PPE as outlined in Step 5.2
___ 19.2.	RCL	OPEN HV-0408 (Dewar GN2 Isolation Valve)
___ 19.3.	RCL	OPEN HV-0801 (Tank LN2 Isolation Valve)
___ 19.4.	RCL	OPEN HV-0804 (Tank-Dewar Separation Valve)
___ 19.5.	RCL	OPEN HV-0709 (Dewar LN2 Supply Isolation Valve)
___ 19.6.	RCL	OPEN HV-0701 (LN2 Isolation Valve) as per ER_____
___ 19.7.	RCL	Monitor Dewar Level until full
___ 19.8.	RCL	CLOSE HV-0701 (LN2 Isolation Valve)
___ 19.9.	RCL	CLOSE HV-0801 (Tank LN2 Isolation Valve)
___ 19.10.	RCL	CLOSE HV-0804 (Tank-Dewar Separation Valve)
___ 19.11.	RCL	CLOSE HV-0709 (Dewar LN2 Supply Isolation Valve)
___ 19.12.	RCL	CLOSE HV-0408 (Dewar GN2 Isolation Valve)
___ 19.13.	TC	Notify SOCC via hotline in EC-1, EC-2 control room that EC-4 is going from a RED condition to GREEN. Testing is complete.
___ 19.14.	RCL	Change EC-4 light from RED to GREEN.

_____20.	RCL	<b>EMERGENCY PROCEDURE (GN2 or LN2 line leak or burst)</b>
		<b>IF OXYGEN DEFICIENCY MONITORS ALARMS:</b>
_____20.1.	ALL	Exit the facility to a safe zone given in safety brief.
_____20.2.	TC	Contact SOCC and report the emergency. Have the SOCC contact the Fire Dept.
_____20.3.	TC	Contact the Facility Manager and isolate the cell or area.
		<b>IF POSSIBLE AND WHEN SAFE, DO THE FOLLOWING:</b>
_____20.4.	RCL	CLOSE HV-0001 (EC-3, EC-4 Primary Facility Isolation Valve)
_____20.5.	RCL	CLOSE HV-0701 (LN2 Isolation Valve)
_____20.6.	RCL	HV-0801 (Tank LN2 Isolation Valve)

## **Appendix B**

### **Tabular Data**

Table B.1 presents the data for the radial temperature and density profiles plotted in Fig. 4.3. The details about the conditions for the individual case numbers correspond to the case numbers in Table 4.1.

Table B.2 contains the dark core length measured from the averaged image, the average dark core length of the individual images, and the root mean square deviation of the dark core length. These three quantities are normalized by the inner-tube diameter of the injector. The details about the conditions for the individual case numbers correspond to the case numbers in Table 4.1.

Table B.1: Radial temperature and density profiles.

CASE 1				CASE 2			
Micrometer Position (mm)	$r/R_1$ -	Average Temperature (K)	Calculated Density ( $\text{kg/m}^3$ )	Micrometer Position (mm)	$r/R_1$ -	Average Temperature (K)	Calculated Density ( $\text{kg/m}^3$ )
18.00	8.46	230.4	22.2	18.00	7.87	242.1	22.5
17.50	6.50	230.4	22.2	17.50	5.91	239.8	22.7
17.30	5.71	225.3	22.7	17.30	5.12	225.3	24.3
17.20	5.31	220.4	23.3	17.20	4.72	209.9	26.3
17.10	4.92	210.2	24.5	17.10	4.33	202.9	27.3
17.00	4.53	199.1	26.1	17.00	3.94	201.9	27.4
16.90	4.13	196.0	26.5	16.90	3.54	201.5	27.5
16.80	3.74	193.9	26.9	16.80	3.15	200.6	27.6
16.70	3.35	190.6	27.4	16.70	2.76	198.2	28.0
16.60	2.95	185.5	28.3	16.60	2.36	192.6	29.0
16.50	2.56	176.3	30.0	16.50	1.97	187.1	30.0
16.40	2.17	167.1	32.0	16.40	1.57	177.2	31.9
16.35	1.97	159.9	33.9	16.30	1.18	110.8	615.7
16.30	1.77	154.0	35.5	16.25	0.98	110.8	616.0
16.25	1.57	110.1	620.5	16.20	0.79	110.4	619.8
16.20	1.38	109.3	627.6	16.15	0.59	110.0	622.8
16.15	1.18	109.1	629.7	16.10	0.39	110.0	623.1
16.10	0.98	109.1	629.7	16.05	0.20	110.0	623.4
16.05	0.79	109.1	629.3	16.00	0.00	110.0	623.3
16.00	0.59	109.1	629.5	15.95	-0.20	110.0	622.8
15.95	0.39	109.1	629.9	15.90	-0.39	110.0	622.8
15.90	0.20	109.0	629.9	15.85	-0.59	110.0	622.6
15.85	0.00	109.1	629.7	15.80	-0.79	110.1	621.9
15.80	-0.20	109.1	629.3	15.75	-0.98	110.2	621.3
15.75	-0.39	109.2	628.5	15.70	-1.18	111.0	614.5
15.70	-0.59	109.2	628.4	15.65	-1.38	127.8	50.5
15.65	-0.79	109.3	627.7				
15.60	-0.98	109.4	627.3				
15.55	-1.18	109.4	627.3				
15.50	-1.38	109.3	627.4				
15.45	-1.57	109.9	622.3				
15.40	-1.77	125.4	48.2				

Table B.1: Radial temperature and density profiles. (continued)

CASE 3				CASE 4			
Micrometer Position (mm)	$r/R_1$ -	Average Temperature (K)	Calculated Density ( $\text{kg/m}^3$ )	Micrometer Position (mm)	$r/R_1$ -	Average Temperature (K)	Calculated Density ( $\text{kg/m}^3$ )
18.00	8.86	250.6	19.7	18.00	8.86	238.5	21.4
17.50	6.89	248.1	20.0	17.50	6.89	236.9	21.6
17.30	6.10	245.9	20.1	17.30	6.10	234.5	21.8
17.20	5.71	241.1	20.6	17.20	5.71	230.9	22.2
17.10	5.31	226.5	22.0	17.10	5.31	220.6	23.3
17.00	4.92	210.1	23.9	17.00	4.92	206.2	25.1
16.90	4.53	205.1	24.5	16.90	4.53	202.6	25.6
16.80	4.13	204.7	24.6	16.80	4.13	202.2	25.7
16.70	3.74	204.3	24.6	16.70	3.74	202.0	25.7
16.60	3.35	203.6	24.7	16.60	3.35	200.9	25.9
16.50	2.95	197.7	25.6	16.50	2.95	191.1	27.4
16.45	2.76	193.1	26.3	16.45	2.76	181.7	29.0
16.40	2.56	189.0	26.9	16.40	2.56	174.9	30.4
16.35	2.36	185.8	27.5	16.35	2.36	168.4	31.8
16.30	2.17	178.6	28.8	16.30	2.17	143.7	39.1
16.25	1.97	160.5	32.8	16.25	1.97	111.8	61.7
16.20	1.77	112.9	57.6	16.20	1.77	109.6	625.5
16.15	1.57	109.3	627.6	16.15	1.57	108.9	630.9
16.10	1.38	109.0	630.1	16.10	1.38	108.8	631.8
16.05	1.18	108.9	630.6	16.05	1.18	108.7	632.7
16.00	0.98	108.5	633.8	16.00	0.98	108.5	634.3
15.95	0.79	107.9	638.5	15.90	0.59	107.8	640.5
15.90	0.59	107.7	640.3	15.85	0.39	107.5	642.6
15.85	0.39	107.8	639.9	15.80	0.20	107.3	644.2
15.80	0.20	107.7	640.4	15.75	0.00	107.1	645.8
15.75	0.00	107.8	639.7	15.70	-0.20	107.6	641.5
15.70	-0.20	107.8	639.8	15.65	-0.39	108.0	638.6
15.65	-0.39	107.8	639.7	15.60	-0.59	108.1	637.5
15.60	-0.59	108.0	638.2	15.55	-0.79	108.4	635.4
15.55	-0.79	108.8	631.2	15.50	-0.98	108.8	632.1
15.50	-0.98	109.0	629.7	15.45	-1.18	109.0	630.7
15.45	-1.18	109.1	629.4	15.40	-1.38	109.0	630.2
15.40	-1.38	109.2	628.6	15.35	-1.57	109.0	630.0
15.35	-1.57	109.3	627.2	15.30	-1.77	109.1	629.6
15.30	-1.77	111.5	59.5	15.25	-1.97	109.2	628.9
15.25	-1.97	147.7	36.5	15.20	-2.17	109.4	627.4
				15.15	-2.36	110.2	619.9
				15.10	-2.56	150.2	36.8

Table B.1: Radial temperature and density profiles. (continued)

CASE 5				CASE 6			
Micrometer Position (mm)	$r/R_1$ -	Average Temperature (K)	Calculated Density ( $\text{kg/m}^3$ )	Micrometer Position (mm)	$r/R_1$ -	Average Temperature (K)	Calculated Density ( $\text{kg/m}^3$ )
18.00	8.86	235.5	52.7	18.00	8.46	230.8	56.2
17.50	6.89	235.1	52.8	17.50	6.50	227.5	57.2
17.30	6.10	233.4	53.2	17.30	5.71	224.4	58.1
17.20	5.71	230.4	54.1	17.20	5.31	210.8	62.9
17.10	5.31	220.6	57.0	17.10	4.92	191.2	71.7
17.00	4.92	204.8	62.6	17.00	4.53	187.3	73.8
16.90	4.53	196.4	66.2	16.90	4.13	189.1	72.8
16.85	4.33	195.3	66.7	16.80	3.74	187.6	73.6
16.80	4.13	194.8	66.9	16.70	3.35	187.8	73.5
16.70	3.74	193.3	67.6	16.60	2.95	183.3	76.1
16.60	3.35	191.5	68.5	16.50	2.56	168.4	87.0
16.50	2.95	188.4	70.1	16.40	2.17	153.2	104.2
16.45	2.76	184.4	72.3	16.30	1.77	138.7	136.6
16.40	2.56	178.1	76.1	16.25	1.57	133.1	164.6
16.35	2.36	172.1	80.3	16.20	1.38	128.7	240.2
16.30	2.17	165.8	85.4	16.15	1.18	127.2	411.3
16.25	1.97	159.0	92.0	16.10	0.98	126.1	454.7
16.20	1.77	151.8	100.9	16.05	0.79	124.8	487.5
16.15	1.57	143.7	115.2	16.00	0.59	123.9	505.1
16.10	1.38	134.8	142.5	15.95	0.39	123.2	517.4
16.05	1.18	128.9	193.5	15.90	0.20	122.5	527.4
16.00	0.98	126.4	426.7	15.85	0.00	122.3	530.0
15.95	0.79	124.6	485.0	15.80	-0.20	122.6	525.6
15.90	0.59	122.8	518.4	15.75	-0.39	123.5	512.6
15.85	0.39	121.4	537.5	15.70	-0.59	124.4	495.7
15.80	0.20	120.9	544.4	15.65	-0.79	126.2	452.4
15.75	0.00	120.8	545.7	15.60	-0.98	126.9	427.3
15.70	-0.20	121.1	542.0	15.55	-1.18	127.5	383.6
15.65	-0.39	121.6	535.8	15.50	-1.38	129.4	214.6
15.60	-0.59	122.1	528.8				
15.55	-0.79	123.2	510.7				
15.50	-0.98	124.8	479.0				
15.45	-1.18	126.5	419.7				
15.40	-1.38	131.3	164.1				
15.35	-1.57	141.9	119.3				

Table B.1: Radial temperature and density profiles. (continued)

CASE 7				CASE 8			
Micrometer Position (mm)	$r/R_1$ -	Average Temperature (K)	Calculated Density ( $\text{kg/m}^3$ )	Micrometer Position (mm)	$r/R_1$ -	Average Temperature (K)	Calculated Density ( $\text{kg/m}^3$ )
18.00	8.86	240.8	51.5	18.0	8.9	241.8	50.9
17.50	6.89	239.3	51.9	17.5	6.9	240.6	51.2
17.30	6.10	237.8	52.2	17.3	6.1	239.8	51.4
17.20	5.71	235.2	52.9	17.2	5.7	237.4	52.0
17.10	5.31	225.6	55.7	17.1	5.3	228.0	54.6
17.00	4.92	202.6	63.7	17.0	4.9	204.9	62.4
16.90	4.53	195.1	67.0	16.9	4.5	197.2	65.6
16.80	4.13	194.3	67.4	16.8	4.1	196.5	65.9
16.70	3.74	193.8	67.6	16.7	3.7	196.2	66.1
16.60	3.35	192.8	68.1	16.6	3.3	195.4	66.4
16.50	2.95	188.5	70.3	16.5	3.0	191.3	68.4
16.40	2.56	170.8	81.6	16.5	2.8	182.7	73.0
16.30	2.17	155.7	96.2	16.4	2.6	171.7	80.3
16.25	1.97	149.0	105.7	16.4	2.4	161.9	88.6
16.20	1.77	141.4	121.1	16.3	2.2	154.0	97.5
16.15	1.57	134.4	145.2	16.3	2.0	146.1	109.7
16.10	1.38	129.7	183.0	16.2	1.8	138.9	126.8
16.05	1.18	127.3	310.1	16.1	1.6	132.5	154.2
16.00	0.98	126.3	429.6	16.1	1.4	128.7	194.3
15.95	0.79	125.9	449.3	16.0	1.2	126.7	394.1
15.90	0.59	125.3	468.2	16.0	1.0	126.1	437.1
15.85	0.39	124.6	485.5	15.9	0.8	125.8	449.7
15.80	0.20	123.6	504.8	15.9	0.6	125.3	464.1
15.75	0.00	123.2	511.8	15.9	0.4	124.9	477.1
15.70	-0.20	124.0	496.6	15.8	0.2	124.6	483.1
15.65	-0.39	124.9	476.7	15.8	0.0	124.5	484.6
15.60	-0.59	125.3	467.9	15.7	-0.2	124.8	479.5
15.55	-0.79	125.7	456.6	15.6	-0.4	125.0	473.0
15.50	-0.98	126.1	441.4	15.6	-0.6	125.3	464.1
15.45	-1.18	126.3	432.4	15.6	-0.8	125.7	452.4
15.40	-1.38	126.8	397.2	15.5	-1.0	126.0	441.2
15.35	-1.57	127.8	231.5	15.4	-1.2	126.4	421.9
15.30	-1.77	129.8	181.4	15.4	-1.4	127.0	349.2
15.25	-1.97	133.4	150.9	15.4	-1.6	128.3	205.0
				15.3	-1.8	130.8	166.9
				15.3	-2.0	134.6	142.7

Table B.1: Radial temperature and density profiles. (continued)

CASE 9				CASE 10			
Micrometer Position (mm)	$r/R_1$ -	Average Temperature (K)	Calculated Density ( $\text{kg/m}^3$ )	Micrometer Position (mm)	$r/R_1$ -	Average Temperature (K)	Calculated Density ( $\text{kg/m}^3$ )
18.00	8.86	243.6	71.3	18.00	8.66	244.3	70.8
17.50	6.89	242.0	71.9	17.50	6.69	243.8	70.9
17.30	6.10	239.3	72.9	17.30	5.91	242.0	71.6
17.20	5.71	237.1	73.8	17.20	5.51	238.3	73.0
17.10	5.31	228.7	77.2	17.10	5.12	223.2	79.3
17.00	4.92	207.5	88.0	17.00	4.72	198.5	93.3
16.90	4.53	192.3	98.4	16.90	4.33	192.8	97.5
16.80	4.13	189.8	100.5	16.80	3.94	191.3	98.7
16.70	3.74	187.9	102.1	16.70	3.54	189.4	100.3
16.60	3.35	186.7	103.2	16.60	3.15	188.0	101.5
16.50	2.95	184.6	105.1	16.50	2.76	182.8	106.3
16.40	2.56	178.8	111.1	16.40	2.36	171.2	119.6
16.35	2.36	173.7	117.0	16.35	2.17	165.7	128.0
16.30	2.17	169.2	123.2	16.30	1.97	160.8	136.8
16.25	1.97	163.5	132.4	16.25	1.77	155.7	148.5
16.20	1.77	158.5	142.5	16.20	1.57	149.2	169.4
16.15	1.57	153.7	155.1	16.15	1.38	142.8	203.5
16.10	1.38	146.5	182.9	16.10	1.18	137.9	259.3
16.05	1.18	140.6	225.3	16.05	0.98	135.0	326.6
16.00	0.98	136.2	296.4	16.00	0.79	133.1	384.3
15.95	0.79	132.8	394.5	15.95	0.59	131.3	430.7
15.90	0.59	130.1	456.2	15.90	0.39	129.3	470.0
15.85	0.39	128.6	482.9	15.85	0.20	128.7	479.4
15.80	0.20	127.9	493.2	15.80	0.00	128.9	476.2
15.75	0.00	127.6	498.5	15.75	-0.20	128.8	479.3
15.70	-0.20	128.5	484.7	15.70	-0.39	129.3	470.7
15.65	-0.39	128.9	477.2	15.65	-0.59	130.5	446.6
15.60	-0.59	129.2	472.7	15.60	-0.79	132.0	414.0
15.55	-0.79	130.2	455.3	15.55	-0.98	132.9	389.3
15.50	-0.98	132.3	407.8	15.50	-1.18	133.8	362.7
15.45	-1.18	135.5	316.8	15.45	-1.38	135.1	322.1
15.40	-1.38	140.5	226.0	15.40	-1.57	137.1	272.9
15.35	-1.57	147.8	176.3	15.35	-1.77	140.6	223.2

Table B.1: Radial temperature and density profiles. (continued)

CASE 11				CASE 12			
Micrometer Position (mm)	$r/R_1$ -	Average Temperature (K)	Calculated Density ( $\text{kg/m}^3$ )	Micrometer Position (mm)	$r/R_1$ -	Average Temperature (K)	Calculated Density ( $\text{kg/m}^3$ )
19.00	12.80	240.1	72.2	18.0	8.5	242.7	71.3
18.50	10.83	239.0	72.6	17.5	6.5	241.3	71.7
17.50	6.89	237.0	73.3	17.3	5.7	241.1	71.8
17.30	6.10	234.7	74.2	17.2	5.3	239.1	72.6
17.20	5.71	232.4	75.2	17.1	4.9	231.2	75.7
17.10	5.31	223.8	78.9	17.0	4.5	206.6	88.0
17.00	4.92	197.4	94.0	16.9	4.1	192.5	97.7
16.90	4.53	186.9	102.3	16.8	3.7	191.4	98.5
16.80	4.13	186.0	103.1	16.7	3.3	191.1	98.8
16.70	3.74	185.5	103.5	16.6	3.0	190.6	99.2
16.60	3.35	184.7	104.2	16.5	2.6	189.7	99.9
16.50	2.95	183.0	105.9	16.4	2.2	182.0	106.9
16.45	2.76	179.5	109.5	16.3	1.8	163.4	131.6
16.40	2.56	172.6	117.6	16.3	1.6	157.8	143.0
16.35	2.36	166.0	127.2	16.2	1.4	151.6	160.3
16.30	2.17	159.9	138.4	16.1	1.2	142.8	203.6
16.25	1.97	155.0	150.1	16.1	1.0	138.8	244.0
16.20	1.77	149.4	168.1	16.0	0.8	137.3	268.4
16.15	1.57	144.0	195.0	16.0	0.6	136.0	298.1
16.10	1.38	140.3	225.4	15.9	0.4	135.2	320.1
16.05	1.18	137.6	263.3	15.9	0.2	132.3	404.4
16.00	0.98	135.7	305.0	15.9	0.0	131.7	419.4
15.95	0.79	134.7	333.5	15.8	-0.2	132.5	400.4
15.90	0.59	134.0	354.3	15.8	-0.4	132.8	390.7
15.85	0.39	133.5	369.8	15.7	-0.6	133.7	366.5
15.80	0.20	133.3	377.2	15.6	-0.8	135.1	321.5
15.75	0.00	133.3	378.0	15.6	-1.0	136.8	279.1
15.70	-0.20	133.4	374.2				
15.65	-0.39	133.7	363.3				
15.60	-0.59	134.5	340.4				
15.55	-0.79	135.8	303.4				

Table B.1: Radial temperature and density profiles. (continued)

CASE 13				CASE 14			
Micrometer Position (mm)	$r/R_1$ -	Average Temperature (K)	Calculated Density ( $\text{kg/m}^3$ )	Micrometer Position (mm)	$r/R_1$ -	Average Temperature (K)	Calculated Density ( $\text{kg/m}^3$ )
18.00	8.96	228.4	21.8	18.00	9.25	225.5	22.4
17.50	6.99	223.8	22.3	17.50	7.28	226.8	22.3
17.30	6.20	221.0	22.6	17.30	6.50	222.1	22.8
17.20	5.81	211.6	23.7	17.20	6.10	219.5	23.1
17.10	5.41	182.2	28.1	17.10	5.71	211.1	24.1
17.00	5.02	145.8	37.2	17.00	5.31	184.5	28.1
16.90	4.63	135.0	41.6	16.90	4.92	152.5	35.5
16.80	4.23	133.5	42.2	16.80	4.53	142.4	39.0
16.70	3.84	132.4	42.8	16.70	4.13	140.0	40.0
16.60	3.44	131.2	43.4	16.60	3.74	137.9	40.9
16.50	3.05	128.7	44.8	16.50	3.35	137.3	41.1
16.40	2.66	118.7	51.7	16.40	2.95	137.1	41.2
16.30	2.26	110.0	61.9	16.30	2.56	127.4	46.2
16.25	2.07	109.0	629.9	16.25	2.36	109.8	623.3
16.20	1.87	108.7	632.2	16.20	2.17	109.1	629.5
16.15	1.67	108.7	632.3	16.15	1.97	109.0	629.9
16.10	1.48	108.7	632.0	16.10	1.77	109.0	630.4
16.05	1.28	108.8	631.9	16.05	1.57	108.9	630.6
16.00	1.08	108.8	632.0	16.00	1.38	108.9	630.9
15.95	0.89	108.8	631.4	15.90	0.98	108.9	630.9
15.90	0.69	108.9	631.1	15.80	0.59	108.9	630.8
15.85	0.49	108.9	631.0	15.70	0.20	108.9	630.8
15.80	0.30	108.9	630.5	15.60	-0.20	108.9	631.1
15.75	0.10	108.9	630.8	15.50	-0.59	108.9	630.9
15.70	-0.10	108.9	631.1	15.40	-0.98	109.0	630.5
15.65	-0.30	108.8	631.2	15.30	-1.38	108.9	630.8
15.60	-0.49	108.9	631.1	15.20	-1.77	108.9	630.7
15.55	-0.69	108.9	631.0	15.10	-2.17	108.9	630.7
15.50	-0.89	108.9	631.1	15.05	-2.36	109.0	630.3
15.45	-1.08	108.8	631.3	15.00	-2.56	109.4	627.0
15.40	-1.28	108.8	631.3				
15.35	-1.48	108.8	631.5				
15.30	-1.67	108.8	631.4				
15.25	-1.87	108.8	631.5				
15.20	-2.07	108.8	631.2				
15.15	-2.26	109.1	629.1				
15.05	-2.66	224.3	22.3				

Table B.1: Radial temperature and density profiles. (continued)

CASE 15			
Micrometer Position (mm)	$r/R_1$ -	Average Temperature (K)	Calculated Density ( $\text{kg/m}^3$ )
18.00	8.96	224.0	23.0
17.50	6.99	221.3	23.3
17.20	5.81	216.8	23.8
17.10	5.41	206.5	25.2
17.00	5.02	171.2	31.3
16.90	4.63	135.9	42.6
16.90	4.63	141.3	40.2
16.80	4.23	132.3	44.4
16.80	4.23	149.6	37.2
16.70	3.84	152.3	36.3
16.60	3.44	153.6	35.9
16.50	3.05	152.4	36.3
16.40	2.66	138.7	41.3
16.40	2.66	135.2	42.9
16.35	2.46	118.2	54.4
16.30	2.26	111.0	63.2
16.25	2.07	109.0	630.2
16.15	1.67	109.0	630.2
16.05	1.28	109.0	630.6
16.00	1.08	109.0	630.2
15.90	0.69	109.0	630.4
15.80	0.30	109.0	630.3
15.70	-0.10	109.0	630.5
15.60	-0.49	109.2	628.8
15.50	-0.89	109.3	628.1
15.40	-1.28	109.2	628.4
15.30	-1.67	109.3	628.3
15.20	-2.07	109.3	628.0
15.15	-2.26	109.8	623.2
15.05	-2.66	122.0	51.1

Table B.1: Radial temperature and density profiles. (continued)

CASE 16				CASE 17			
Micrometer Position (mm)	$r/R_1$ -	Average Temperature (K)	Calculated Density ( $\text{kg/m}^3$ )	Micrometer Position (mm)	$r/R_1$ -	Average Temperature (K)	Calculated Density ( $\text{kg/m}^3$ )
18.00	8.86	234.0	52.8	18.00	8.86	206.6	61.4
17.50	6.89	232.4	53.2	17.50	6.89	205.3	62.0
17.30	6.10	227.9	54.5	17.30	6.10	203.4	62.7
17.20	5.71	223.1	55.9	17.20	5.71	199.5	64.3
17.10	5.31	212.7	59.3	17.10	5.31	185.7	71.0
17.00	4.92	174.6	78.0	17.00	4.92	152.7	98.8
16.90	4.53	141.2	120.0	16.90	4.53	140.2	122.2
16.80	4.13	137.4	131.1	16.80	4.13	138.7	126.4
16.70	3.74	136.2	135.3	16.70	3.74	139.4	124.4
16.60	3.35	136.3	135.2	16.60	3.35	140.8	120.6
16.50	2.95	135.7	137.5	16.50	2.95	140.2	122.2
16.40	2.56	135.0	140.4	16.40	2.56	133.3	148.2
16.30	2.17	131.7	159.0	16.35	2.36	130.2	171.9
16.25	1.97	129.8	177.2	16.30	2.17	128.4	199.7
16.20	1.77	128.5	198.0	16.25	1.97	127.7	222.2
16.15	1.57	127.4	243.8	16.20	1.77	126.8	380.4
16.10	1.38	126.4	422.0	16.15	1.57	126.0	437.1
16.05	1.18	125.7	451.6	16.10	1.38	125.5	458.0
16.00	0.98	124.9	474.9	16.05	1.18	124.7	478.8
15.95	0.79	123.9	498.0	16.00	0.98	123.7	501.4
15.90	0.59	122.5	521.6	15.95	0.79	122.7	518.2
15.85	0.39	121.5	536.7	15.90	0.59	121.8	531.4
15.80	0.20	121.4	537.6	15.85	0.39	121.2	540.6
15.75	0.00	121.7	533.1	15.80	0.20	120.6	548.2
15.70	-0.20	121.7	533.1	15.75	0.00	120.4	549.9
15.65	-0.39	121.5	536.6	15.70	-0.20	120.7	546.9
15.60	-0.59	121.1	542.1	15.65	-0.39	121.1	541.5
15.55	-0.79	121.1	540.9	15.60	-0.59	121.7	533.2
15.50	-0.98	122.2	526.2	15.55	-0.79	122.4	523.7
15.45	-1.18	123.8	500.2	15.50	-0.98	123.2	511.0
15.40	-1.38	125.1	470.7	15.45	-1.18	123.9	497.9
15.35	-1.57	126.7	400.0	15.40	-1.38	124.7	480.9
15.30	-1.77	129.1	186.4	15.35	-1.57	125.3	464.2
15.25	-1.97	132.1	156.2	15.30	-1.77	125.9	443.4
				15.25	-1.97	126.4	418.7
				15.15	-2.36	127.8	215.0

Table B.1: Radial temperature and density profiles. (continued)

CASE 18				CASE 19			
Micrometer Position (mm)	$r/R_1$ -	Average Temperature (K)	Calculated Density ( $\text{kg/m}^3$ )	Micrometer Position (mm)	$r/R_1$ -	Average Temperature (K)	Calculated Density ( $\text{kg/m}^3$ )
18.00	8.86	208.6	60.5	18.0	9.1	211.7	59.7
17.50	6.89	207.4	60.9	17.5	7.1	209.9	60.4
17.30	6.10	203.6	62.4	17.2	5.9	207.7	61.2
17.10	5.31	196.4	65.5	17.1	5.5	204.2	62.5
17.00	4.92	158.2	91.6	17.0	5.1	184.5	71.9
16.90	4.53	136.2	134.0	16.9	4.7	139.8	123.7
16.70	3.74	133.3	147.0	16.8	4.3	133.9	145.6
16.50	2.95	134.0	143.3	16.7	3.9	133.9	145.5
16.30	2.17	127.2	254.1	16.5	3.1	133.2	149.3
16.20	1.77	126.3	418.4	16.3	2.4	129.0	188.6
16.10	1.38	125.0	471.1	16.2	2.0	126.2	430.9
16.00	0.98	123.0	512.6	16.1	1.6	125.2	467.5
15.95	0.79	122.5	521.3	16.0	1.2	124.8	478.2
15.90	0.59	121.7	532.5	15.9	1.0	125.0	471.7
15.85	0.39	119.8	556.5	15.9	0.8	124.4	486.6
15.80	0.20	119.8	556.9	15.9	0.6	124.6	482.8
15.75	0.00	119.5	560.4	15.8	0.4	125.5	457.6
15.70	-0.20	120.0	554.3	15.8	0.2	125.7	453.4
15.65	-0.39	120.2	552.5	15.7	0.0	125.9	444.0
15.60	-0.59	121.0	542.0	15.6	-0.2	125.5	457.4
15.50	-0.98	122.3	523.9	15.6	-0.4	125.5	459.9
15.40	-1.38	124.1	493.2	15.5	-0.8	125.7	452.0
				15.4	-1.2	125.8	448.0
				15.3	-1.6	126.2	429.5

Table B.1: Radial temperature and density profiles. (continued)

CASE 20				CASE 21			
Micrometer Position (mm)	$r/R_1$ -	Average Temperature (K)	Calculated Density ( $\text{kg/m}^3$ )	Micrometer Position (mm)	$r/R_1$ -	Average Temperature (K)	Calculated Density ( $\text{kg/m}^3$ )
18.00	8.86	214.5	83.6	18.00	9.25	225.2	77.2
17.50	6.89	213.0	84.5	17.50	7.28	222.9	78.3
17.30	6.10	208.5	87.0	17.10	5.71	219.9	79.7
17.20	5.71	203.1	90.3	17.00	5.31	215.2	82.0
17.10	5.31	189.8	100.0	16.90	4.92	187.8	100.1
17.00	4.92	148.5	172.3	16.80	4.53	144.4	187.8
16.90	4.53	135.9	302.5	16.70	4.13	140.2	220.2
16.80	4.13	135.2	319.3	16.60	3.74	142.4	201.0
16.70	3.74	135.2	320.5	16.40	2.95	139.4	229.4
16.60	3.35	135.2	321.3	16.20	2.17	136.8	269.3
16.50	2.95	135.1	324.7	16.10	1.77	134.5	328.6
16.40	2.56	134.9	330.7	16.00	1.38	132.6	388.8
16.30	2.17	134.2	350.1	15.95	1.18	130.9	433.7
16.20	1.77	132.9	388.6	15.90	0.98	129.4	464.6
16.15	1.57	132.0	412.5	15.85	0.79	128.3	482.7
16.10	1.38	130.8	440.5	15.80	0.59	127.6	494.3
16.05	1.18	129.0	475.1	15.75	0.39	126.8	506.3
16.00	0.98	127.5	498.2	15.70	0.20	126.8	506.2
15.95	0.79	125.4	525.9	15.65	0.00	126.2	514.5
15.90	0.59	122.6	556.5	15.60	-0.20	126.5	510.3
15.85	0.39	120.8	573.9	15.55	-0.39	126.8	506.4
15.80	0.20	119.7	583.3	15.50	-0.59	127.4	497.4
15.75	0.00	119.5	585.0	15.45	-0.79	128.5	479.5
15.70	-0.20	119.9	581.9	15.40	-0.98	129.2	467.6
15.65	-0.39	120.1	580.1	15.35	-1.18	130.3	447.5
15.60	-0.59	120.7	574.7	15.30	-1.38	131.6	417.5
15.55	-0.79	121.1	570.7				
15.50	-0.98	123.1	551.5				
15.45	-1.18	127.9	492.5				
15.40	-1.38	130.0	457.6				

Table B.2: Dark Core Length Data.

CASE #	Acoustic OFF			Acoustics ON First Mode			Acoustics ON Second Mode		
	Averaged Image L/D1	Average of Instantaneous L/D1	RMS/D1	Averaged Image L/D1	Average of Instantaneous L/D1	RMS/D1	Averaged Image L/D1	Average of Instantaneous L/D1	RMS/D1
1	28.0	34.1	6.9	18.8	31.8	7.9	20.5	30.7	6.9
2	20.9	23.1	4.9	15.1	16.5	-	15.2	19.3	3.2
3	17.4	19.4	1.9	6.7	10.4	2.4	10.9	12.7	1.8
4	15.1	15.9	1.4	7.2	9.5	2.3	11.2	12.6	1.9
5	17.9	19.0	1.8	14.6	16.3	2.1	18.4	19.2	1.5
6	10.4	10.7	2.0	5.5	6.4	1.0	6.3	6.5	1.3
7	5.6	5.8	0.7	4.2	4.5	0.5	3.4	4.0	0.9
8	4.5	4.7	0.5	3.4	3.6	0.5	3.8	4.1	0.5
9	14.6	15.6	2.3	12.2	13.4	1.4	15.0	16.0	2.1
10	7.0	7.7	0.8	5.4	6.0	0.6	5.5	5.9	0.9
11	3.7	4.0	0.4	2.8	3.2	0.7	3.2	3.4	0.5
12	3.0	3.1	0.3	3.0	3.0	0.4	3.0	2.9	0.4
13	20.7	25.7	4.5	18.8	24.2	4.0	16.5	20.7	2.6
14	17.1	18.4	2.1	11.9	15.0	2.0	8.9	9.1	1.5
15	17.9	18.4	1.6	14.9	15.9	1.9	9.7	11.2	1.5
16	21.6	25.0	2.9	17.9	19.9	2.5	17.1	17.4	1.9
17	7.5	8.0	1.0	5.8	6.9	1.3	4.9	5.7	0.9
18	3.6	3.2	0.5	2.8	2.6	0.3	3.4	3.2	0.5
19	3.7	2.9	0.5	4.2	2.7	0.4	3.2	2.5	0.5
20	6.9	9.8	3.6	7.7	12.3	4.0	27.3	29.0	2.8

## VITA

### **Dustin Wayne Davis**

Dustin W. Davis was born on December 3, 1975, and raised in Rockwood, Pennsylvania with humble beginnings. He graduated from Rockwood Area High School in June of 1994. After high school, the author went to The Pennsylvania State University, where he wanted to attend since five years of age. He completed his Bachelor of Science degree in Chemical Engineering, with a focus on Fuel Science in December of 1998. The faculty and courses in Fuel Science inspired him to attend graduate school with the intention of focusing on propulsion and power research in Mechanical Engineering. Upon completion of his Master of Science degree in Mechanical Engineering in August of 2001 and an additional year of course work, he went to the Air Force Research Laboratory at Edwards AFB, CA to perform the experimental work pursuing his doctoral degree in Mechanical Engineering. After three continuous years experimental work at AFRL, the author completed his experiments and doctoral degree.

While in graduate school, Dustin married Holly Beth Lee, and now have two sons Drew Anthony and Parker William. Presently, the author is working at GE Global Research Center in Niskayuna, New York.

# **APPENDIX C**

# *A Priori* Analysis of Subgrid-Scale Models for Large Eddy Simulations of Supercritical Binary-Species Mixing Layers

Nora Okong'o\* and Josette Bellan†  
*Jet Propulsion Laboratory*  
*California Institute of Technology*  
*Pasadena CA 91109-8099*

Models for large eddy simulation (LES) are assessed on a database obtained from direct numerical simulations (DNS) of supercritical binary-species temporal mixing layers. The analysis is performed at the DNS transitional states for heptane/nitrogen, oxygen/hydrogen and oxygen/helium mixing layers. The incorporation of simplifying assumptions that are validated on the DNS database leads to a set of LES equations that requires only models for the subgrid scale (SGS) fluxes, which arise from filtering the convective terms in the DNS equations. Constant-coefficient versions of three different models for the SGS fluxes are assessed and calibrated. The Smagorinsky SGS-flux model shows poor correlations with the SGS fluxes, while the Gradient and Similarity models have high correlations, as well as good quantitative agreement with the SGS fluxes when the calibrated coefficients are used.

## Introduction

Supercritical fluids are of great interest in extraction processes as well as in propulsion devices such as advanced gas-turbine and diesel engines, and liquid rockets. The performance of these devices depends on the efficiency of fluid disintegration and turbulent mixing, which may occur under supercritical conditions. A fluid is here defined to be in a supercritical state when it is at a thermodynamic pressure,  $p$ , or temperature,  $T$ , exceeding its critical (subscript  $c$ ) value,<sup>1</sup>  $p_c$  or  $T_c$ ; therefore, in the supercritical regime there is no longer the possibility of a two phase (i.e. gas/liquid) region.<sup>2</sup> For mixtures, both  $p_c$  and  $T_c$  depend on the composition. The present interest is in fluid mixtures at high pressures that are supercritical for the pure species. Past the critical point of the fluid (where material surfaces no longer exist), the disintegration of fluid jets displays an aspect that Chehroudi et al.<sup>3</sup> call 'fingers', or 'comb-like structures' at transcritical conditions, which have an increasingly gaseous appearance with increasing  $p$ . Similar experimental evidence was produced by Mayer et al.<sup>4,5</sup> for O<sub>2</sub> disintegration. For supercritical free N<sub>2</sub> jets, the experiments of Oswald and Schik<sup>6</sup> also showed sharp density profiles, indicating the occurrence of sharp density gradients.

Results from Direct Numerical Simulations (DNS) showed, as in the experiments, that regions of high density-gradient-magnitude exist in both pre-transitional<sup>7</sup> and transitional<sup>8,9</sup> temporal mixing layers, arising both from the initial density stratification as well as from mixing.<sup>10</sup> These DNS were conducted using real-gas equations of state for non-ideal mixtures in conjunction with realistic transport properties and thermal

\*Scientist, AIAA Member.

†Senior Research Scientist, AIAA Associate Fellow (corresponding author, josette.bellan@jpl.nasa.gov).

diffusion (Soret and Dufour) effects. For modeling fully turbulent supercritical flows at high pressures, Large Eddy Simulation (LES), wherein only the large-scales are simulated and the subgrid scales (SGS) are modeled, presently seems more computationally achievable for practical systems than DNS, which requires all turbulence scales to be resolved. The LES equations are derived by applying a spatial filter to the DNS equations, leading to various unclosed terms, including the SGS fluxes, which arise from filtering the convective terms. Given the distinctive supercritical flow characteristics, it is of interest to inquire whether LES models developed for compressible perfect-gas and incompressible flows can be extended to real-gas non-ideal mixtures.

In this paper, DNS databases for transitional supercritical temporal mixing layers<sup>8,9</sup> are analyzed on an *a priori* basis. In Section I, the LES governing equations are presented, in order to derive the unclosed terms that need to be modeled. Section II summarizes the DNS database, followed by the *a priori* analysis of the database in Section III. The analysis includes explicit modeling for the SGS fluxes and simplifying assumptions for the remaining unclosed terms. Finally, Section IV contains the conclusions and areas for future work.

## I. Governing Equations for Large Eddy Simulations

The LES equations are derived from the DNS set by spatial filtering. The filtering operation is defined as:

$$\bar{\psi}(\vec{x}) = \int_V \psi(\vec{y}) G(\vec{x} - \vec{y}) d\vec{y} \quad (1)$$

where  $G$  is the filter function and  $V$  is the filtering volume;  $G$  has the property that for a spatially constant function, the filtered function is identical to the unfiltered one. For compressible flow, we use Favre filtering, defined as  $\tilde{\psi} = \bar{\rho\psi}/\bar{\rho}$  where  $\rho$  is the density. The governing equations are written for the conservative variables  $\phi = \{\rho, \rho u_i, \rho e_t, \rho Y_\alpha\}$  where  $u_i$  is the velocity component in the  $x_i$ -direction,  $e_t$  is the total energy and  $Y_\alpha$  is the mass fraction for species  $\alpha$ .

### A. DNS Equations

The conservation equations for a mixture of  $N$  species are:

$$\frac{\partial \rho}{\partial t} + \frac{\partial \rho u_j}{\partial x_j} = 0 \quad (2)$$

$$\frac{\partial \rho u_i}{\partial t} + \frac{\partial \rho u_i u_j}{\partial x_j} = -\frac{\partial p}{\partial x_i} + \frac{\partial \sigma_{ij}}{\partial x_j} \quad (3)$$

$$\frac{\partial \rho e_t}{\partial t} + \frac{\partial \rho e_t u_j}{\partial x_j} = -\frac{\partial p u_j}{\partial x_j} - \frac{\partial q_j}{\partial x_j} + \frac{\partial \sigma_{ij} u_i}{\partial x_j} \quad (4)$$

$$\frac{\partial \rho Y_\alpha}{\partial t} + \frac{\partial \rho Y_\alpha u_j}{\partial x_j} = -\frac{\partial J_{\alpha j}}{\partial x_j} - w_\alpha \quad (5)$$

where  $t$  is the time,  $\sigma$  is the viscous stress tensor,  $\mathbf{q}$  is the heat flux,  $e = e_t - e_k$  is the internal energy,  $e_k = u_i u_i / 2$  is the kinetic energy, and  $\mathbf{J}_\alpha$  and  $w_\alpha$  are the species-mass flux and reaction rate of species  $\alpha$ , respectively. Also,

$$\sum_{\alpha=1}^N Y_\alpha = 1, \quad \sum_{\alpha=1}^N J_{\alpha j} = 0, \quad \sum_{\alpha=1}^N w_\alpha = 0 \quad (6)$$

In this paper, the Einstein summation is used for roman indices ( $i, j, k$ ), but not for Greek indices ( $\alpha, \beta$ ). The thermodynamic variables are functions of the flow field  $\phi$ :

$$e = e(\phi), \quad p = p(\phi), \quad T = T(\phi), \quad h = h(\phi)$$

where  $p$ ,  $T$  and the enthalpy  $h$  are computed from the equation of state (EOS); likewise, the transport quantities are functions of  $\phi$ :

$$\sigma_{ij} = \sigma_{ij}(\phi), \quad J_{\alpha j} = J_{\alpha j}(\phi), \quad q_j = q_j(\phi)$$

For a Newtonian fluid,

$$\sigma_{ij} = \mu \left( \frac{\partial u_i}{\partial x_j} + \frac{\partial u_j}{\partial x_i} - \frac{2}{3} \frac{\partial u_k}{\partial x_k} \delta_{ij} \right) \quad (7)$$

where  $\mu$  is the viscosity and  $S_{ij}$  is the rate-of-strain tensor.

The species-mass and heat fluxes originate in Keizer's<sup>11</sup> fluctuation-dissipation theory which is consistent with non-equilibrium thermodynamics, converges to kinetic theory in the low-pressure limit and relates fluxes and forces from first principles. The species-mass and heat fluxes take the form, including Soret and Dufour effects:<sup>12</sup>

$$J_{\alpha j} = - \sum_{\beta=1}^N \Lambda_{\alpha\beta j} \quad (8)$$

$$q_j = -\lambda \frac{\partial T}{\partial x_j} - \frac{1}{2} R_u T \sum_{\beta=1}^N \sum_{\alpha=1}^N \alpha_{IK,\alpha\beta} \frac{m}{m_\alpha m_\beta} \Lambda_{\alpha\beta} \quad (9)$$

$$\Lambda_{\alpha\beta} = \frac{m_\alpha m_\beta}{m} \left( \frac{\rho}{R_u} D_{m,\alpha\beta} Y_\alpha Y_\beta \right) \left[ \frac{m}{m_\beta m_\alpha} R_u \alpha_{IK,\alpha\beta} \frac{1}{T} \frac{\partial T}{\partial x_j} + \frac{1}{m_\alpha} \frac{\partial}{\partial x_j} \left( \frac{\mu_\alpha}{T} \right) - \frac{1}{m_\beta} \frac{\partial}{\partial x_j} \left( \frac{\mu_\beta}{T} \right) \right] \quad (10)$$

$$\frac{\partial}{\partial x_j} \left( \frac{\mu_\alpha}{T} \right) = -\frac{h_{,\alpha}}{T^2} \frac{\partial T}{\partial x_j} + \frac{v_{,\alpha}}{T} \frac{\partial p}{\partial x_j} + R_u \sum_{\beta=1}^N \frac{\alpha_{D\alpha\beta}}{X_\alpha} \frac{\partial X_\beta}{\partial x_j} \quad (11)$$

$$\alpha_{D\alpha\beta} \equiv \frac{1}{R_u T} X_\alpha \frac{\partial \mu_\alpha}{\partial X_\beta} = \frac{\partial X_\alpha}{\partial X_\beta} + X_\alpha \frac{\partial \ln \gamma_\alpha}{\partial X_\beta} \quad (12)$$

For the mixture,  $\lambda$  is the thermal conductivity,  $R_u$  is the universal gas constant,  $m$  is the mixture molar mass, with the molar volume being  $v = m/\rho$ . For the pure species  $\alpha$ ,  $m_\alpha$  is the species- $\alpha$  molar mass,  $\mu_\alpha$  is the chemical potential,  $h_{,\alpha}$  is the partial molar enthalpy,  $v_{,\alpha}$  is the partial molar volume,  $X_\alpha = mY_\alpha/m_\alpha$  is the mole fraction, and  $\gamma_\alpha$  is the fugacity. For the species- $\alpha$ /species- $\beta$  pair,  $\Lambda_{\alpha\beta}$  is the binary species-mass flux ( $\Lambda_{\alpha\beta} = -\Lambda_{\beta\alpha}$ ,  $\Lambda_{\alpha\alpha} = 0$ ),  $\alpha_{IK,\alpha\beta}$  is the Irwing-Kirwood (IK) form of the thermal diffusion factor ( $\alpha_{IK,\alpha\beta} = -\alpha_{IK,\beta\alpha}$ ,  $\alpha_{IK,\alpha\alpha} = 0$ ),  $D_{m,\alpha\beta}$  is the binary diffusion coefficient ( $D_{m,\alpha\beta} = D_{m,\beta\alpha}$ ,  $D_{m,\alpha\alpha} = 0$ ) and  $\alpha_{D\alpha\beta}$  is the mass diffusion factor.

## B. LES Equations

After filtering, and assuming that filtering and differentiation commute (true except near boundaries, where the filter function changes), the governing equations become:

$$\frac{\partial \bar{\rho}}{\partial t} + \frac{\partial \bar{\rho} \tilde{u}_j}{\partial x_j} = 0 \quad (13)$$

$$\frac{\partial \bar{\rho} \tilde{u}_i}{\partial t} + \frac{\partial \overline{\rho u_i u_j}}{\partial x_j} = -\frac{\partial \bar{p}}{\partial x_i} + \frac{\partial \bar{\sigma}_{ij}}{\partial x_j} \quad (14)$$

$$\frac{\partial \bar{\rho} \tilde{e}_t}{\partial t} + \frac{\partial \overline{\rho e_t u_j}}{\partial x_j} = -\frac{\partial \bar{p} u_j}{\partial x_j} - \frac{\partial \bar{q}_j}{\partial x_j} + \frac{\partial \overline{\sigma_{ij} u_i}}{\partial x_j} \quad (15)$$

$$\frac{\partial \bar{\rho} \tilde{Y}_\alpha}{\partial t} + \frac{\partial \overline{\rho Y_\alpha u_j}}{\partial x_j} = -\frac{\partial \bar{J}_{\alpha j}}{\partial x_j} - \bar{w}_\alpha \quad (16)$$

$$\tilde{e}_t = \tilde{e} + \widetilde{u_i u_i}/2, \quad \sum_{\alpha=1}^N \tilde{Y}_{\alpha j} = 1, \quad \sum_{\alpha=1}^N \tilde{J}_{\alpha j} = 0, \quad \sum_{\alpha=1}^N \tilde{w}_{\alpha} = 0 \quad (17)$$

Using the previously adopted notation of denoting the DNS flow field as  $\phi$ , the filtered flow field can now be denoted as  $\bar{\phi}$  and we can define functions of the filtered flow field:

$$e(\bar{\phi}), \quad p(\bar{\phi}), \quad T(\bar{\phi}), \quad h(\bar{\phi}), \quad \sigma_{ij}(\bar{\phi}), \quad J_{\alpha j}(\bar{\phi}), \quad q_j(\bar{\phi})$$

which have the same functional form as in the DNS and that in general differ from their filtered counterparts

$$\tilde{e} = \overline{\rho e(\phi)}/\bar{\rho}, \quad \bar{p} = \overline{p(\phi)}, \quad \bar{T} = \overline{T(\phi)}, \quad \tilde{T} = \overline{\rho T(\phi)}/\bar{\rho}, \quad \tilde{h} = \overline{\rho h(\phi)}/\bar{\rho}, \quad \bar{\sigma}_{ij} = \overline{\sigma_{ij}(\phi)}, \quad \bar{J}_{\alpha j} = \overline{J_{\alpha j}(\phi)}, \quad \bar{q}_j = \overline{q_j(\phi)}$$

Defining the SGS fluxes,

$$\tau_{ij} = \widetilde{u_i u_j} - \tilde{u}_i \tilde{u}_j, \quad \zeta_j = \widetilde{h u_j} - \tilde{h} \tilde{u}_j, \quad \eta_{\alpha j} = \widetilde{Y_{\alpha} u_j} - \tilde{Y}_{\alpha} \tilde{u}_j \quad \text{with} \quad \sum_{\alpha=1}^N \eta_{\alpha j} = 0 \quad (18)$$

the filtered governing equations are:

$$\frac{\partial \bar{\rho}}{\partial t} + \frac{\partial \bar{\rho} \tilde{u}_j}{\partial x_j} = 0 \quad (19)$$

$$\frac{\partial \bar{\rho} \tilde{u}_i}{\partial t} + \frac{\partial \bar{\rho} \tilde{u}_i \tilde{u}_j}{\partial x_j} = -\frac{\partial p(\bar{\phi})}{\partial x_i} + \frac{\partial \sigma_{ij}(\bar{\phi})}{\partial x_j} - \frac{\partial}{\partial x_j} (\bar{\rho} \tau_{ij}) - \frac{\partial}{\partial x_i} [\bar{p} - p(\bar{\phi})] + \frac{\partial}{\partial x_j} [\bar{\sigma}_{ij} - \sigma_{ij}(\bar{\phi})] \quad (20)$$

$$\begin{aligned} \frac{\partial \bar{\rho} \tilde{e}_t}{\partial t} + \frac{\partial \bar{\rho} \tilde{e}_t \tilde{u}_j}{\partial x_j} = & -\frac{\partial p(\bar{\phi})}{\partial x_j} \tilde{u}_j - \frac{\partial q_j(\bar{\phi})}{\partial x_j} + \frac{\partial \sigma_{ij}(\bar{\phi})}{\partial x_j} \tilde{u}_i - \frac{\partial}{\partial x_j} (\bar{\rho} \zeta_j) - \frac{\partial}{\partial x_j} (\bar{\rho} \kappa_j) \\ & - \frac{\partial}{\partial x_j} \{ [\bar{p} - p(\bar{\phi})] \tilde{u}_j \} - \frac{\partial}{\partial x_j} [\bar{q}_j - q_j(\bar{\phi})] + \frac{\partial}{\partial x_j} [\bar{\sigma}_{ij} u_i - \sigma_{ij}(\bar{\phi}) \tilde{u}_i] \end{aligned} \quad (21)$$

$$\frac{\partial \bar{\rho} \tilde{Y}_{\alpha}}{\partial t} + \frac{\partial \bar{\rho} \tilde{Y}_{\alpha} \tilde{u}_j}{\partial x_j} = -\frac{\partial J_{\alpha j}(\bar{\phi})}{\partial x_j} - \tilde{w}_{\alpha} - \frac{\partial}{\partial x_j} (\bar{\rho} \eta_{\alpha j}) - \frac{\partial}{\partial x_j} [\bar{J}_{\alpha j} - J_{\alpha j}(\bar{\phi})] \quad (22)$$

where  $\kappa_j = \widetilde{e_k u_j} - \tilde{e}_k \tilde{u}_j$ . These equations contain several unclosed terms that cannot be directly computed from the filtered flow field. To compute these terms, we pursue two closure approaches: explicit models for the SGS fluxes, and simplifying assumptions for the remaining terms. The assumptions and models will be assessed in Section III on a DNS database, described below, of a binary non-reacting temporal mixing layer.

## II. Description of DNS database

The database consists of supercritical temporal mixing layer simulations of binary ( $N = 2$ ) mixtures, namely, heptane/nitrogen (HN), oxygen/hydrogen (OH) and oxygen/helium (OHe). The pure species properties are listed in Table 1. For each layer, the lighter molar mass species is indexed as species 1 while the heavier molar mass species is indexed as species 2; the notation is simplified as  $D \equiv D_{21}$ ,  $\alpha_{IK} \equiv \alpha_{IK,21}$ ,  $\alpha_D \equiv \alpha_{D,21}$ ,  $\eta_j \equiv \eta_{2j}$ . The flows are non-reacting, i.e.  $w_{\alpha} \equiv 0$ .

A detailed description of the DNS methodology has been given by Miller et al.<sup>7</sup> and Okong'o and Bellan<sup>8</sup> for C<sub>7</sub>H<sub>16</sub>/N<sub>2</sub> layers and by Okong'o et al.<sup>9</sup> for

Table 1. Pure species properties.

Species	$m$ (g/mol)	$T_c$ (K)	$p_c$ (MPa)
H <sub>2</sub>	2.016	33.0	1.284
He	4.003	5.19	0.227
N <sub>2</sub>	28.013	126.3	3.399
O <sub>2</sub>	31.999	154.6	5.043
C <sub>7</sub> H <sub>16</sub>	100.205	540.2	2.74

the O<sub>2</sub>/H<sub>2</sub> layers. The conservation equations were numerically solved using a fourth-order explicit Runge-Kutta time integration and a sixth-order compact scheme with eighth-order filter for spatial derivatives;<sup>20</sup> the filtering is required to maintain numerical stability for long-time integrations and is applied at interior points only. The computations were parallelized using three-dimensional domain decomposition and message passing, and an efficient parallel tridiagonal solver.<sup>21</sup> The configuration, initial and boundary conditions, EOS, and transport property relations are summarized below.

### A. Configuration, initial and boundary conditions

The temporally developing mixing layer configuration is depicted in Figure 1 for heptane/nitrogen, as an example, showing the definition of the streamwise ( $x_1$ ), cross-stream ( $x_2$ ) and spanwise ( $x_3$ ) coordinates. The layer is not symmetric in extent in the  $x_2$  direction, to accommodate the larger layer growth in the lighter fluid side. The free-stream density ( $\rho_1$  or  $\rho_2$ ) is calculated for each pure species at its free-stream temperature ( $T_1$  or  $T_2$ ) and at the initial uniform pressure ( $p_0$ ). The vorticity thickness is defined as  $\delta_\omega(t) = \Delta U_0 / (\partial \langle u_1 \rangle / \partial x_2)_{max}$  where  $\langle u_1 \rangle$  is the ( $x_1, x_3$ ) planar average of the streamwise velocity, and  $\Delta U_0 = U_1 - U_2$  is the velocity difference across the layer. The choice

$$U_1 = \frac{2M_{c,0}a_{s1}}{\left[1 + \left(\frac{a_{s1}}{a_{s2}}\right) \sqrt{\frac{\rho_1 Z_1}{\rho_2 Z_2}}\right]}, U_2 = -\sqrt{\frac{\rho_1 Z_1}{\rho_2 Z_2}} U_1 \quad (23)$$

was made with the intent of keeping the ultimate vortex stationary in the computational domain,<sup>7</sup> although the relations of Papamoschou and Roshko<sup>16</sup>

$$U_1 = \frac{2M_{c,0}a_{s1}}{\left[1 + \left(\frac{a_{s1}}{a_{s2}}\right) \sqrt{\frac{\rho_1}{\rho_2}}\right]}, U_2 = -\sqrt{\frac{\rho_1}{\rho_2}} U_1 \quad (24)$$

were also used for some simulations reported here. Here  $M_{c,0}$  is the convective Mach number and  $Z = p / (\rho T R_u / m)$  is the compression factor indicating departures from perfect gas ( $Z = 1$ ) behavior. The specification of  $M_{c,0}$  therefore determines  $\Delta U_0$ . Given the initial streamwise velocity profile  $u_1$  based on  $U_1$  and  $U_2$ ,  $(\partial \langle u_1 \rangle / \partial x_2)_{max}$  and hence  $\delta_{\omega,0} \equiv \delta_\omega(0)$  are calculated. The specified value of the initial flow Reynolds number,  $Re_0 = (1/2)(\rho_1 + \rho_2) \Delta U_0 \delta_{\omega,0} / \mu_R$ , chosen so as to enable the resolution of all relevant length scales, is then used to calculate  $\mu_R$ . The grid spacing is an approximately linear function of  $Re_0$ .

The simulations are started with error-function profiles for the mean streamwise velocity, mass fraction and temperature, upon which are imposed spanwise and streamwise vorticity perturbations<sup>17, 18</sup> of strengths  $F_{2D}$  and  $F_{3D}$  respectively, whose streamwise ( $\lambda_1$ ) and spanwise ( $\lambda_3$ ) wavelengths are  $\lambda_1 = C \delta_{\omega,0}$  and  $\lambda_3 = 0.6 \lambda_1$ , where  $C = 7.29$  is the most unstable wavelength for incompressible flow. For the simulations reported here, listed in Table 2, other values of  $C$  obtained from stability analyses<sup>9</sup> were also used:  $C = 4.57$  for the shortest (estimated) unstable wavelength for the C<sub>7</sub>H<sub>16</sub>/N<sub>2</sub> layer, or  $C$  corresponding to the most unstable wavelength for O<sub>2</sub> layers. The grid is chosen for all simulations so as to accommodate four wavelengths in the streamwise and spanwise directions, and the evolution of the layer is meant to encompass roll-up and two pairings of the four initial spanwise vortices into an ultimate vortex.

The boundary conditions are periodic in the streamwise and spanwise directions, and of outflow type for real gas in the cross-stream direction, as derived by Okong'o and Bellan.<sup>19</sup> The outflow type conditions are

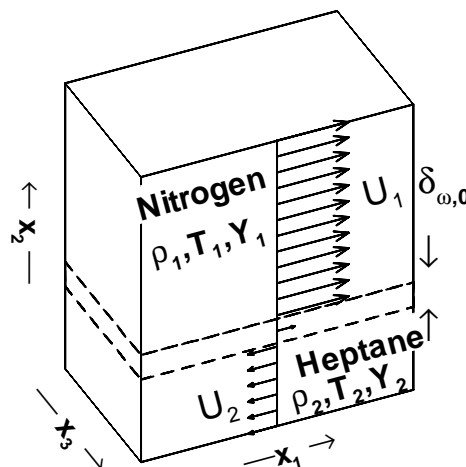


Figure 1. Sketch of the C<sub>7</sub>H<sub>16</sub>/N<sub>2</sub> mixing layer configuration.

**Table 2. Simulation parameters for supercritical temporal mixing layer database**

Run	HN400	HN500	HN600	HN800	OH750	OH550	OH500	OHe600
Species 2	C <sub>7</sub> H <sub>16</sub>	O <sub>2</sub>	O <sub>2</sub>	O <sub>2</sub>	O <sub>2</sub>			
Species 1	N <sub>2</sub>	N <sub>2</sub>	N <sub>2</sub>	N <sub>2</sub>	H <sub>2</sub>	H <sub>2</sub>	H <sub>2</sub>	He
$T_2$ (K)	600	600	600	600	400	400	235	235
$T_1$ (K)	1000	1000	1000	1000	600	600	287	287
$\rho_2/\rho_1$	12.88	12.88	12.88	12.88	24.40	24.40	24.51	12.17
$p_0$ (atm)	60	60	60	60	100	100	100	100
$Re_0$	400	500	600	800	750	550	500	600
$\lambda_1/\delta_{\omega,0}$	7.29	7.29	7.29	4.57	7.29	10.35	10.61	9.31
$L_1$ (m)	0.200	0.200	0.200	0.125	0.200	0.284	0.284	0.255
$L_2$ (m)	0.232	0.232	0.232	0.148	0.200	0.284	0.284	0.255
$L_3$ (m)	0.120	0.120	0.120	0.075	0.120	0.170	0.170	0.153
$N_1$	192	240	288	240	352	352	352	352
$N_2$	224	288	336	272	352	352	352	352
$N_3$	112	144	176	144	208	208	208	208
$\Delta x$ ( $10^{-4}$ m)	10.71	8.36	6.97	5.23	5.77	8.19	8.39	7.36
$F_{2D}$	0.1	0.1	0.1	0.1	0.1	0.1	0.1	0.05
$F_{3D}$	0.05	0.05	0.05	0.05	0.05	0.025	0.025	0.0125
$t_{trans}^*$	150	155	135	100	150	270	290	220
$Re_{m,trans}$	972	1250	1452	1258	1507	1907	1772	2004

All simulations have  $M_{c,0}=0.4$ ,  $L_1 = 4\lambda_1$  and  $L_3 = 0.6L_1$ .  $N_i$  is the number points in the  $x_i$ -direction,  $\Delta x = \max\{\Delta x_1, \Delta x_2, \Delta x_3\}$ .

essential to maintain numerical stability since the initial perturbation causes large pressure waves that must be allowed out of the domain with minimal reflection.

## B. Equation of state

The pressure is calculated from the well-known Peng-Robinson (PR) EOS, given  $T$  and the PR molar volume ( $v_{PR}$ ), as

$$p = \frac{R_u T}{(v_{PR} - b_m)} - \frac{a_m}{(v_{PR}^2 + 2b_m v_{PR} - b_m^2)}, \quad (25)$$

where  $a_m$  and  $b_m$  are functions of  $T$  and  $X_\alpha$ . At high pressures,  $v_{PR}$  may differ significantly from the actual molar volume  $v$ .<sup>1</sup> Both  $v_{PR}$  and the volume shift ( $v_S = v - v_{PR}$ ) can be calculated from the PR EOS given  $p$ ,  $T$  and  $X_\alpha$ ,<sup>13</sup> although for the C<sub>7</sub>H<sub>16</sub>/N<sub>2</sub> system  $v_S$  is negligible. All thermodynamic quantities, including  $\alpha_D$ ,  $h$ ,  $C_p = (\partial h/\partial T)_{p,X}$  and the speed of sound ( $a_s$ ), are calculated from the EOS using standard thermodynamic relations.<sup>7,8,14</sup> The implementation of the EOS to calculate  $p$  and  $T$  from  $\rho$ ,  $e$  and  $Y_\alpha$  uses an iterative scheme<sup>14</sup> for O<sub>2</sub>/H<sub>2</sub> and O<sub>2</sub>/He, and an energy fit<sup>8</sup> for C<sub>7</sub>H<sub>16</sub>/N<sub>2</sub>.

## C. Transport coefficients

The viscosity, the Schmidt number ( $Sc = \mu/(\rho\alpha_D D)$ ) and the Prandtl number ( $Pr = \mu C_p/(m\lambda)$ ) were calculated from high-pressure single-species transport properties using mixing rules, as in Harstad and Belan.<sup>15</sup> The calculated values were correlated, as summarized in Table 3, and these correlations are then used

**Table 3. Transport properties for binary mixtures.**  $T_R = (T_1 + T_2)/2$ ,  $T$  in Kelvin.

System	C <sub>7</sub> H <sub>16</sub> /N <sub>2</sub>	O <sub>2</sub> /H <sub>2</sub>	O <sub>2</sub> /He
$\mu = \mu_R (T/T_R)^n$	$n = 0.7$	$n = 0.75$	$n = 0.59$
$Sc \equiv \mu / (\rho \alpha_D D)$	$1.5 - Y_2$	$\left[ \begin{array}{l} (1.334 - 0.668Y_2 - 0.186Y_2^2 - 0.268Y_2^6) \\ \times [1 + (88.6/T)^{1.5}] \end{array} \right]$	Eq. 41
$Pr \equiv \mu C_p / (m \lambda)$	$0.5 Sc / \exp(-1.5Y_2)$	$1.335/T^{0.1}$	Eq. 40
$\alpha_{IK}$ or $\alpha_{BK}$	$\alpha_{IK} = 0.1$ (Ref. 12 )	$\alpha_{BK} = 0.2$ (Refs. 15, 30 )	$\alpha_{BK} = 0.25$
$T$ Range	500K–1100K	200K–800K	100K–900K
$p$ Range	40 atm–80 atm	~100atm	~100atm

to compute the transport properties  $\mu$ ,  $D$  and  $\lambda$ . One of the thermal diffusion factors is specified, then the other is calculated from

$$\alpha_{BK} = \alpha_{IK} - \frac{1}{R_u T} \frac{m_2 m_1}{m} \left( \frac{h_{,2}}{m_2} - \frac{h_{,1}}{m_1} \right) \quad (26)$$

where  $\alpha_{BK}$  is the Bearman-Kirkwood (BK) form of the thermal diffusion factor.

### III. Results

The database used for the *a priori* analysis is summarized in Table 2. Note that the grid spacing is uniform with  $\Delta x_1 \simeq \Delta x_2 \simeq \Delta x_3$ ; we denote  $\Delta x = \max\{\Delta x_i\}$ . The flow fields are filtered using a cubic-top hat filter, for which the filtered value is simply the volume-average. The filter width used is  $\bar{\Delta}$ , with  $\bar{\Delta}/\Delta x=4$  or 8. Further filtering is performed at the test-filter width  $\hat{\Delta}$ , with  $\hat{\Delta}/\bar{\Delta}=1$  or 2. All calculations are performed on the DNS grid. The analysis is carried out at the transitional states listed in Table 2. The differing thermodynamics of the various species-systems preclude matching of the initial density stratification ( $\rho_2/\rho_1$ ) or of the transitional momentum thickness<sup>9,14</sup> within the regimes of practical interest, since there is not a simple relationship between the initial conditions and the transitional state. As a result, the O<sub>2</sub> layers ended up with higher momentum-thickness Reynolds number,  $Re_m$ , at the transitional state, with the O<sub>2</sub>/He layer having the highest value of 2004. While the HN layers have lower initial  $\rho_2/\rho_1$ , they have higher density gradient magnitude  $|\nabla \rho| \delta_{\omega,0} / (\rho_2 - \rho_1)$  at the transitional state, due to their higher mixture non-ideality.<sup>10</sup> Since the appropriate LES resolution ( $\Delta x_{LES}$ ) depends on the gradients of the filtered flow field, the implication is that HN LES may require higher resolution relative to DNS (i.e., less grid coarsening, smaller  $\bar{\Delta}/\Delta x_{DNS}$  and  $\Delta x_{LES}/\Delta x_{DNS}$ ) than LES for the other species systems considered.

#### A. LES assumptions

Following a protocol previously used for an atmospheric two-phase mixing layer,<sup>22</sup> we evaluate the following LES assumptions, with a view to simplifying Eqs. 20–22:

$$\tilde{e} = e(\bar{\phi}), \quad \bar{T} = T(\bar{\phi}), \quad \tilde{T} = T(\bar{\phi}), \quad \bar{p} = p(\bar{\phi}), \quad \tilde{h} = h(\bar{\phi}) \quad (27)$$

$$\bar{\sigma}_{ij} = \sigma_{ij}(\bar{\phi}), \quad \bar{J}_{\alpha j} = J_{\alpha j}(\bar{\phi}), \quad \bar{q}_j = q_j(\bar{\phi}), \quad \overline{u_i \sigma_{ij}} = \tilde{u}_i \sigma_{ij}(\bar{\phi}) \quad (28)$$

$$\bar{\rho} \kappa_j = \frac{1}{2} (\overline{\rho u_i u_i u_j} - \overline{\rho u_i u_i} \tilde{u}_j) = \bar{\rho} \tau_{ij} \tilde{u}_i \quad (29)$$

The LES assumptions tested are listed in Table 4, where the slopes from least-squares fit of the model (RHS) to the terms (LHS) are tabulated. Correlations between the models and terms (not shown) were excellent (typically above 98%), being somewhat lower for the larger filter width. Correspondingly, compared to the values at the smaller filter width, the slopes in Table 4 also show greater deviation from the ideal value

of unity at the larger filter width. The thermodynamic assumptions (Eq. 27) have less than 1% error on all the flow fields. The assumptions for the viscous, heat and species-mass fluxes are almost as accurate, with errors of about 4%. The model for the triple correlation (Eq. 29) appears to be the least accurate assumption, with errors of up to 10%. Therefore, it would appear that the filtered thermodynamic quantities (internal energy, temperature, pressure and enthalpy) and the filtered viscous, heat and species-mass fluxes can be adequately modeled from the filtered flow field. The same results were previously obtained in an atmospheric-pressure perfect-gas mixing layer,<sup>22</sup> although here the species-mass and heat fluxes have a much more complicated functional form (Eqs. 8 and 9), including Soret and Dufour (thermal diffusion) effects.

Incorporating the validated LES assumptions, Eqs. 19–22 become:

$$\frac{\partial \bar{\rho}}{\partial t} + \frac{\partial \bar{\rho} \tilde{u}_j}{\partial x_j} = 0 \quad (30)$$

$$\frac{\partial \bar{\rho} \tilde{u}_i}{\partial t} + \frac{\partial \bar{\rho} \tilde{u}_i \tilde{u}_j}{\partial x_j} = -\frac{\partial p(\bar{\phi})}{\partial x_i} + \frac{\partial \sigma_{ij}(\bar{\phi})}{\partial x_j} - \frac{\partial}{\partial x_j} (\bar{\rho} \tau_{ij}) \quad (31)$$

$$\frac{\partial \bar{\rho} \tilde{e}_t}{\partial t} + \frac{\partial \bar{\rho} \tilde{e}_t \tilde{u}_j}{\partial x_j} = -\frac{\partial p(\bar{\phi})}{\partial x_j} \tilde{u}_j - \frac{\partial q_j(\bar{\phi})}{\partial x_j} + \frac{\partial \sigma_{ij}(\bar{\phi})}{\partial x_j} \tilde{u}_i - \frac{\partial}{\partial x_j} (\bar{\rho} \zeta_j) - \frac{\partial}{\partial x_j} (\bar{\rho} \tau_{ij} \tilde{u}_i) \quad (32)$$

$$\frac{\partial \bar{\rho} \tilde{Y}_\alpha}{\partial t} + \frac{\partial \bar{\rho} \tilde{Y}_\alpha \tilde{u}_j}{\partial x_j} = -\frac{\partial J_{\alpha j}(\bar{\phi})}{\partial x_j} - \bar{w}_\alpha - \frac{\partial}{\partial x_j} (\bar{\rho} \eta_{\alpha j}) \quad (33)$$

Eqs. 30–33 still contain unclosed terms, namely the SGS fluxes, that will be modeled explicitly.

## B. SGS-flux models

The three basic models for the SGS fluxes ( $\tau_{ij}$ ,  $\eta_{\alpha j}$ ,  $\zeta_j$ ) are<sup>22</sup> the Smagorinsky (SM) model, the Gradient (GR) model and the Scale-Similarity (SS) model. For the *a priori* analysis, only constant coefficient versions of these models can be considered, although dynamic-coefficient versions should also be studied in a *posteriori* LES.<sup>23</sup> Because dynamic models are based on the same concept as the SS model, the *a priori* evaluation of that model should provide reasonable indications of the likely performance of dynamic models. Although in this paper we will calibrate the constant-coefficients, it should be kept in mind that other effects that cannot be studied *a priori*, such as the interaction of the resolved flow with the SGS, may dictate a different value in actual LES. Note that the calibration will consider the same coefficient value for all SGS fluxes, although practical implementation may require different values for different fluxes, in addition to the spatial and temporal variation of coefficients that is afforded by dynamic modeling.<sup>23</sup>

The SM model, which is based on the gradient-diffusion (eddy-viscosity) concept, is<sup>24</sup>

$$\tau_{ij} - \frac{1}{3} \tau_{kk} \delta_{ij} = -C_{SM} \bar{\Delta}^2 S(\bar{\phi}) \left[ S_{ij}(\bar{\phi}) - \frac{1}{3} S_{kk}(\bar{\phi}) \delta_{ij} \right] \quad (34)$$

$$\eta_{\alpha j} = -C_{SM} \bar{\Delta}^2 S(\bar{\phi}) \frac{1}{2} \frac{\partial \tilde{Y}_\alpha}{\partial x_j}, \quad \zeta_j = -C_{SM} \bar{\Delta}^2 S(\bar{\phi}) \frac{1}{2} \frac{\partial \tilde{h}}{\partial x_j} \quad (35)$$

where  $S^2(\phi) = S_{mn}(\phi) S_{mn}(\phi)$ . The Yoshizawa<sup>25</sup> (YO) model for  $\tau_{kk}$  is

$$\tau_{kk} = C_{YO} \bar{\Delta}^2 S^2(\bar{\phi}) \quad (36)$$

The GR model, derived from a Taylor series expansion, is<sup>26</sup>

$$\tau_{ij} = C_{GR} \bar{\Delta}^2 \frac{\partial \tilde{u}_i}{\partial x_k} \frac{\partial \tilde{u}_j}{\partial x_k}, \quad \zeta_j = C_{GR} \bar{\Delta}^2 \frac{\partial \tilde{h}}{\partial x_k} \frac{\partial \tilde{u}_j}{\partial x_k}, \quad \eta_{\alpha j} = C_{GR} \bar{\Delta}^2 \frac{\partial \tilde{Y}_\alpha}{\partial x_k} \frac{\partial \tilde{u}_j}{\partial x_k}, \quad \sigma_{SGS}^2 = C_{GR} \bar{\Delta}^2 \frac{\partial \tilde{\psi}}{\partial x_k} \frac{\partial \tilde{\psi}}{\partial x_k} \quad (37)$$

Table 4. Slopes from least squares fit of RHS/LHS. For quantities with more than one component, the slope listed is that with the largest deviation from unity.

Run	HN400	HN500	HN600	HN800	OH750	OH550	OH500	OHe600
$t_{trans}^*$	150	155	135	100	150	270	290	220
$Re_{m,trans}$	972	1250	1452	1258	1507	1907	1772	2004
$\tilde{e} = e(\bar{\phi})$ ( $\bar{\Delta}/\Delta x=4$ )	1.0001	1.0001	1.0001	1.0001	1.0000	1.0000	1.0000	1.0002
$\tilde{e} = e(\bar{\phi})$ ( $\bar{\Delta}/\Delta x=8$ )	1.0002	1.0002	1.0002	1.0002	1.0001	1.0001	1.0001	1.0006
$\bar{T} = T(\bar{\phi})$ ( $\bar{\Delta}/\Delta x=4$ )	0.9982	0.9989	0.9986	0.9983	0.9999	0.9999	0.9999	0.9999
$\bar{T} = T(\bar{\phi})$ ( $\bar{\Delta}/\Delta x=8$ )	0.9949	0.9968	0.9961	0.9953	0.9998	0.9998	0.9999	0.9998
$\tilde{T} = T(\bar{\phi})$ ( $\bar{\Delta}/\Delta x=4$ )	0.9992	0.9947	0.9994	0.9993	1.0005	1.0006	1.0003	1.0005
$\tilde{T} = T(\bar{\phi})$ ( $\bar{\Delta}/\Delta x=8$ )	0.9977	0.9985	0.9983	0.9980	1.0015	1.0018	1.0009	1.0015
$\bar{p} = p(\bar{\phi})$ ( $\bar{\Delta}/\Delta x=4$ )	0.9996	0.9998	0.9996	0.9996	1.0001	1.0001	1.0001	1.0002
$\bar{p} = p(\bar{\phi})$ ( $\bar{\Delta}/\Delta x=8$ )	0.9987	0.9993	0.9987	0.9986	1.0003	1.0003	1.0003	1.0005
$\tilde{h} = h(\bar{\phi})$ ( $\bar{\Delta}/\Delta x=4$ )	0.9999	1.0000	0.9999	0.9999	1.0000	1.0000	1.0000	1.0002
$\tilde{h} = h(\bar{\phi})$ ( $\bar{\Delta}/\Delta x=8$ )	0.9998	0.9999	0.9998	0.9998	1.0001	1.0001	1.0001	1.0005
$\bar{\sigma}_{ij} = \sigma_{ij}(\bar{\phi})$ ( $\bar{\Delta}/\Delta x=4$ )	0.9924	0.9969	0.9972	0.9912	1.0053	1.0038	0.9987	1.0171
$\bar{\sigma}_{ij} = \sigma_{ij}(\bar{\phi})$ ( $\bar{\Delta}/\Delta x=8$ )	0.9764	0.9867	0.9853	0.9610	1.0095	1.0057	0.9935	1.0273
$\bar{J}_{\alpha j} = J_{\alpha j}(\bar{\phi})$ ( $\bar{\Delta}/\Delta x=4$ )	1.0086	1.0080	1.0099	1.0111	1.0035	1.0046	1.0032	1.0018
$\bar{J}_{\alpha j} = J_{\alpha j}(\bar{\phi})$ ( $\bar{\Delta}/\Delta x=8$ )	0.9709	0.9861	0.9886	0.9653	1.0046	1.0078	1.0045	0.9964
$\bar{q}_j = q_j(\bar{\phi})$ ( $\bar{\Delta}/\Delta x=4$ )	1.0330	1.0253	1.0258	1.0456	1.0046	1.0053	1.0036	1.0027
$\bar{q}_j = q_j(\bar{\phi})$ ( $\bar{\Delta}/\Delta x=8$ )	1.0389	1.0344	1.0326	1.0365	1.0067	1.0093	1.0052	0.9971
$\bar{u}_i \bar{\sigma}_{ij} = \tilde{u}_i \sigma_{ij}(\bar{\phi})$ ( $\bar{\Delta}/\Delta x=4$ )	1.0196	0.9980	1.0070	1.0112	1.0131	1.0093	1.0063	1.0026
$\bar{u}_i \bar{\sigma}_{ij} = \tilde{u}_i \sigma_{ij}(\bar{\phi})$ ( $\bar{\Delta}/\Delta x=8$ )	1.0235	0.9854	0.9787	0.9325	1.0217	1.0197	1.0132	0.9941
$\bar{\rho} \kappa_j = \bar{\rho} \tau_{ij} \tilde{u}_i$ ( $\bar{\Delta}/\Delta x=4$ )	0.9788	1.0453	0.9818	0.9535	0.9859	0.9946	1.0054	1.0099
$\bar{\rho} \kappa_j = \bar{\rho} \tau_{ij} \tilde{u}_i$ ( $\bar{\Delta}/\Delta x=8$ )	0.9611	1.0845	0.9658	0.9070	0.9682	0.9862	1.0156	1.0131

where the SGS standard deviation,  $\sigma_{SGS}$ , of a generic variable  $\psi$  is defined as

$$\sigma_{SGS}^2(\tilde{\psi}) = \tilde{\psi}\tilde{\psi} - \tilde{\psi}\tilde{\psi}, \quad \sigma_{SGS}(\bar{\psi}) = \overline{\psi\psi} - \bar{\psi}\bar{\psi} \quad (38)$$

(Note:  $\sigma_{SGS}(\tilde{u}_1) = \tau_{11}$ ,  $\sigma_{SGS}(\tilde{u}_2) = \tau_{22}$ ,  $\sigma_{SGS}(\tilde{u}_3) = \tau_{33}$ .) Theoretically,  $C_{GR}$  is proportional to the moments of inertia of the filtering volume; for a cubic top-hat filter  $C_{GR} = 1/12$ .

The SS model, which postulates similarity between the SGS and the small resolved scale, is<sup>27</sup>

$$\tau_{ij} = C_{SS}(\widehat{\tilde{u}_i \tilde{u}_j} - \widehat{\tilde{u}_i} \widehat{\tilde{u}_j}), \quad \zeta_j = C_{SS}(\widehat{\tilde{h} \tilde{u}_j} - \widehat{\tilde{h}} \widehat{\tilde{u}_j}), \quad \eta_{\alpha j} = C_{SS}(\widehat{\tilde{Y}_\alpha \tilde{u}_j} - \widehat{\tilde{Y}_\alpha} \widehat{\tilde{u}_j}), \quad \sigma_{SGS}^2 = C_{SS}(\widehat{\tilde{\psi} \tilde{\psi}} - \widehat{\tilde{\psi}} \widehat{\tilde{\psi}}) \quad (39)$$

where the overhat ( $\widehat{\quad}$ ) denotes (unweighted) filtering at the test-filter level  $\hat{\Delta}$ . Two test filter widths are considered, leading to models SS1 ( $\hat{\Delta}/\bar{\Delta} = 1$ ) and SS2 ( $\hat{\Delta}/\bar{\Delta} = 2$ ). While scale-similarity would imply that  $C_{SS} = 1$ , the actual value is filter-width dependent.<sup>22, 28, 29</sup>

Least squares fits of the exact SGS fluxes to the SGS-flux models produced the slope (exact/model) and correlation for each SGS quantity; the model coefficient is the slope from the least squares fit. For each SGS model, the calibrated SGS coefficient for a given run and filter width is obtained by averaging the slopes obtained for each SGS quantity. The SM coefficient is based on 12 SGS quantities (6 independent  $\tau_{ij}$ , 3  $\zeta_j$ , 3  $\eta_j$ ), whereas the GR and SS coefficients are based on an additional 6 SGS standard deviations. Due to the

**Table 5. Slopes from least-squares fit of SGS models to SGS quantities (slope=exact/model), OHe600,  $\bar{\Delta}/\Delta x=8$ . The SM model  $\tau_{ij}$  is compared to the exact ( $\tau_{ij} - \tau_{kk}\delta_{ij}/3$ ). For  $\bar{\rho}\tau_{kk}$  using the YO model, the slope is 0.2275 and the correlation is 0.8332.**

SGS quantity	SM	GR	SS ( $\hat{\Delta}/\bar{\Delta} = 1$ )	SS ( $\hat{\Delta}/\bar{\Delta} = 2$ )
$\bar{\rho}\tau_{11}$	0.0633	0.1269	1.4741	0.5141
$\bar{\rho}\tau_{22}$	0.0241	0.1241	1.5030	0.5667
$\bar{\rho}\tau_{33}$	0.0160	0.1210	1.4826	0.5574
$\bar{\rho}\tau_{12}$	0.0366	0.1133	1.3331	0.4572
$\bar{\rho}\tau_{13}$	0.0241	0.1158	1.4547	0.5348
$\bar{\rho}\tau_{23}$	0.0160	0.1143	1.5005	0.6108
$\bar{\rho}\zeta_1$	0.1662	0.1200	1.4647	0.5132
$\bar{\rho}\zeta_2$	0.0607	0.1143	1.4389	0.4802
$\bar{\rho}\zeta_3$	0.0522	0.1119	1.4371	0.4812
$\bar{\rho}\eta_1$	0.1683	0.1201	1.4641	0.5132
$\bar{\rho}\eta_2$	0.0591	0.1145	1.4378	0.4805
$\bar{\rho}\eta_3$	0.0509	0.1122	1.4360	0.4810
$\sigma_{SGS}^2(\tilde{u}_1)$	-	0.1200	1.4174	0.5088
$\sigma_{SGS}^2(\tilde{u}_2)$	-	0.1213	1.4535	0.5516
$\sigma_{SGS}^2(\tilde{u}_3)$	-	0.1190	1.4596	0.5602
$\sigma_{SGS}^2(\tilde{T})$	-	0.1204	1.7133	0.7200
$\sigma_{SGS}^2(\tilde{Y}_2)$	-	0.1136	1.5360	0.6143
$\sigma_{SGS}^2(\bar{p})$	-	0.1224	1.4021	0.5197
Average slope	0.0622	0.1180	1.4671	0.5369
Std. dev. of slopes	0.0577	0.0044	0.0230	0.0636
Average correlation	0.2313	0.9602	0.9492	0.8322

strong density variation, the actual calibration is performed for the product of density and SGS flux, that appears in Eqs. 31–33. The slopes and the average of the correlations are listed for OHe600 in Table 5. The correlations for the SS and GR models are typically better than 95% (better than 80% for SS2), whereas the correlations for the SM model are at best 50% and are typically about 20%. Whereas the GR and SS slopes have a narrow distribution, as indicated by their small standard deviation of the slopes, there is wide variation among SM slopes, with the standard deviation of the SM slopes being comparable in magnitude to the average. These characteristics of OHe600 are typical of all layers at both filter widths.

Figures 2 and 3 compare the different SGS-flux models in terms of their averages in homogeneous ( $x_1, x_3$ ) planes for OHe600. The calibrated coefficient values (that is, the average slopes) from Table 5 are used for the comparison. The Smagorinsky model has poor agreement with the exact (computed) SGS fluxes for all components, consistent with the low correlations; its deficiencies cannot be remedied by simply using different coefficient values for the different types of fluxes. However, the Yoshizawa model correlates quite well (over 80%) with  $\tau_{kk}$ , and in this case, where  $\tau_{kk}$  dominates in  $\tau_{ij}$ , the combination with the Smagorinsky model yields good predictions of  $\tau_{11}$ ,  $\tau_{22}$ , and  $\tau_{33}$ . In marked contrast to the Smagorinsky model, the Similarity and Gradient models clearly have both qualitative and quantitatively good agreement with the exact SGS fluxes for all components.

The calibrated coefficients for all layers in Table 2 are tabulated in Table 6. The calibrated coefficients are here compared to determine possible statistical equality of the values (based on t-tests with 5% confidence

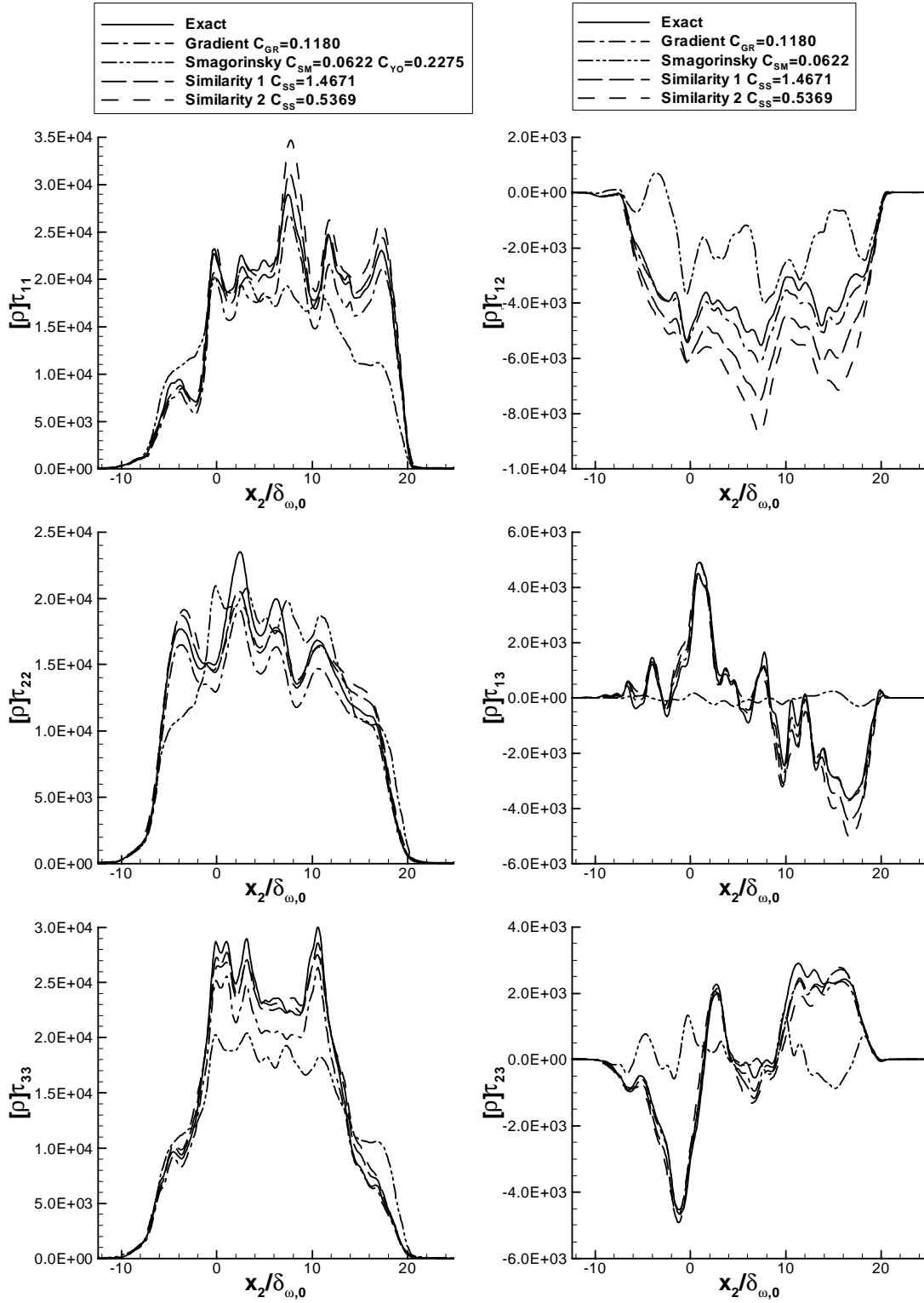


Figure 2. SGS fluxes and models for OHe600 with  $\bar{\Delta}/\Delta x=8$ , averages in homogeneous planes. ( $[\rho] \equiv \bar{\rho}$ )

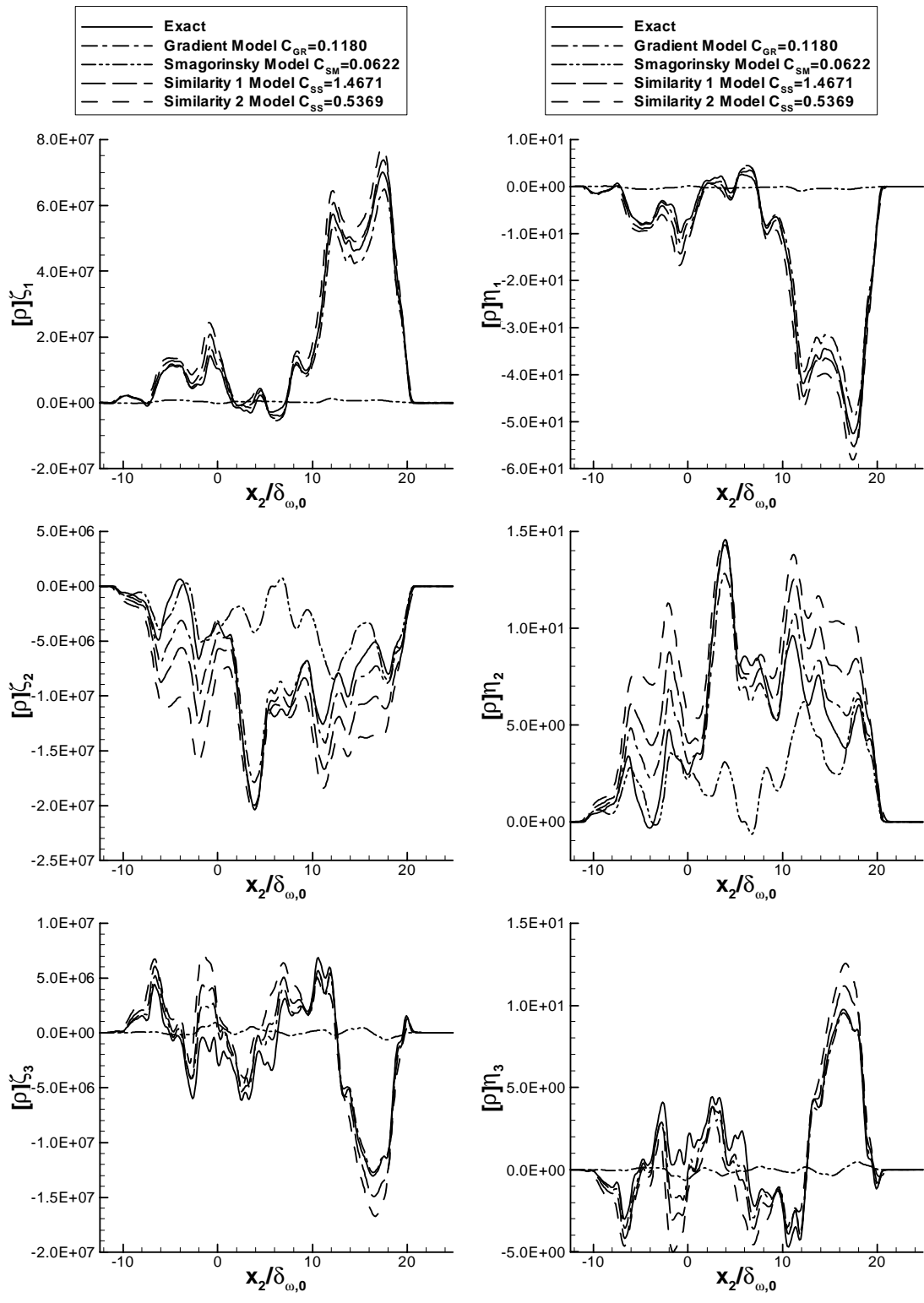


Figure 3. SGS fluxes and models for OHe600 with  $\bar{\Delta}/\Delta x=8$ , averages in homogeneous planes. ( $[\rho] \equiv \bar{\rho}$ .)

**Table 6. Model coefficients calibrated from transitional states**

Run	HN400	HN500	HN600	HN800	OH750	OH550	OH500	OHe600
$t_{trans}^*$	150	155	135	100	150	270	290	220
$Re_{m,trans}$	972	1250	1452	1258	1507	1907	1772	2004
$C_{YO} \left( \frac{\bar{\Delta}}{\Delta x} = 4 \right)$	0.2751	0.2687	0.2583	0.2612	0.2396	0.2383	0.2398	0.2477
$C_{YO} \left( \frac{\bar{\Delta}}{\Delta x} = 8 \right)$	0.2751	0.2634	0.2471	0.2506	0.2144	0.2150	0.2137	0.2275
$C_{SM} \left( \frac{\bar{\Delta}}{\Delta x} = 4 \right)$	0.0726	0.0735	0.0655	0.0409	0.1442	0.1315	0.1293	0.0711
$C_{SM} \left( \frac{\bar{\Delta}}{\Delta x} = 8 \right)$	0.0742	0.0687	0.0579	0.0423	0.1232	0.1169	0.1138	0.0622
$C_{GR} \left( \frac{\bar{\Delta}}{\Delta x} = 4 \right)$	0.1372	0.1397	0.1346	0.1344	0.1284	0.1280	0.1275	0.1328
$C_{GR} \left( \frac{\bar{\Delta}}{\Delta x} = 8 \right)$	0.1254	0.1257	0.1193	0.1180	0.1115	0.1118	0.1112	0.1180
$C_{SS} \left( \frac{\hat{\Delta}}{\Delta} = 1, \frac{\bar{\Delta}}{\Delta x} = 4 \right)$	1.3352	1.3293	1.2938	1.2954	1.1312	1.1048	1.0983	1.2388
$C_{SS} \left( \frac{\hat{\Delta}}{\Delta} = 1, \frac{\bar{\Delta}}{\Delta x} = 8 \right)$	1.6891	1.6069	1.5399	1.5661	1.2920	1.2560	1.2448	1.4671
$C_{SS} \left( \frac{\hat{\Delta}}{\Delta} = 2, \frac{\bar{\Delta}}{\Delta x} = 4 \right)$	0.4934	0.4904	0.4705	0.4676	0.3845	0.3685	0.3655	0.4426
$C_{SS} \left( \frac{\hat{\Delta}}{\Delta} = 2, \frac{\bar{\Delta}}{\Delta x} = 8 \right)$	0.6998	0.6260	0.5770	0.5870	0.4469	0.4303	0.4243	0.5369

level). The YO coefficients range from 0.2137 to 0.2751, with the lower values for OH at the larger  $\bar{\Delta}/\Delta x$ , while the HN values show little filter-width dependence. At fixed  $\bar{\Delta}/\Delta x$ , the OHe600 coefficient lies between the HN and OH values, and is approximately equal to the average coefficient computed over all layers; this behavior was also observed for all the other models. Except for the SM model, where the trend is reversed, for a given  $\bar{\Delta}/\Delta x$ , the HN values are higher than the OH values. The range of coefficient values is 0.0409–0.1442 (SM), 0.1112–0.1397 (GR), 1.0988–1.6891 (SS1) and 0.3655–0.6998 (SS2). For the SM model, the coefficients are statistically independent of run and filter width, because the underlying the SM coefficients have a large spread of slopes (large standard deviation, e.g. Table 5 for OHe600). This result indicates that the correlation of the SM model with the SGS-fluxes is too poor for this calibration procedure to produce a meaningful coefficient.

For the GR and SS models, the statistical equivalence of the coefficients in Table 6 mirrors the closeness of numerical values, due to the small variation (small standard deviation) in the underlying slopes. For both models, the coefficients are filter-width dependent for each run. At either  $\bar{\Delta}/\Delta x$ , the three OH coefficients are (statistically) equal, the HN coefficients are also generally equal, and OHe600 is generally equal to the closest HN value (HN600 or HN800). For the GR model, the HN400 and HN500 values at  $\bar{\Delta}/\Delta x = 8$  are equal to the OH values at  $\bar{\Delta}/\Delta x = 4$ . For the SS1 model, the HN values at  $\bar{\Delta}/\Delta x = 4$  are equal to the OH750 value at  $\bar{\Delta}/\Delta x = 8$ . For the SS2 model, the OHe600 value at  $\bar{\Delta}/\Delta x = 4$  is equal to the OH values at  $\bar{\Delta}/\Delta x = 8$ . Based on the  $\bar{\Delta}/\Delta x$ - and run-dependence of the GR coefficients, it is anticipated that dynamic modeling, wherein the model coefficient is computed during the LES from the LES flow field, will be required. Because dynamic modeling is based on the SS model with  $C_{SS}=1$ , the fact that the SS1 coefficient values are closer to unity than are the SS2 values suggests that  $\hat{\Delta} = \bar{\Delta}$  has the greater potential for dynamic modeling. An *a posteriori* study is needed to determine the sensitivity of the LES to the model coefficients.

## IV. Summary and conclusions

Large Eddy Simulation (LES) equations have been derived for compressible real-gas non-ideal-mixture flows, by applying a spatial filter to the Direct Numerical Simulation (DNS) equations. The LES equations

contain unclosed terms that cannot be computed directly from the filtered flow field, including the SGS fluxes that arise from filtering the convective terms. Using an existing DNS database of supercritical binary-species temporal mixing layer simulations, explicit models for the SGS fluxes and simplifying assumptions for the remaining unclosed terms were assessed *a priori*. The DNS database consists of transitional states of high pressure heptane/nitrogen, oxygen/hydrogen and oxygen/helium layers. The various assumptions were found to be valid, and the filtered thermodynamic quantities as well as the filtered viscous, species-mass and heat fluxes were found to be well-approximated by using the DNS functional form on the filtered flow field; the species-mass and heat fluxes contain Soret and Dufour effects, respectively. For modeling the SGS fluxes, constant-coefficient versions of Smagorinsky, Gradient and Similarity models were assessed and calibrated on the DNS database. The Smagorinsky model showed poor correlation with the exact SGS fluxes, while the Gradient and Similarity models had high correlations. Furthermore, the calibrated coefficients for the Gradient and Similarity models yielded good quantitative agreement with the SGS fluxes. However, comparison among the layers in the DNS database revealed that, statistically speaking, the calibrated coefficients were not generally valid. Future studies involve assessing the LES models *a posteriori* to determine their predictive ability in reproducing the temporal and spatial evolution of the filtered flow field, with particular interest on the sensitivity of the results to the value of the SGS-flux model coefficients.

## V. Acknowledgments

This work was conducted at the Jet Propulsion Laboratory (JPL), California Institute of Technology (Caltech) and sponsored by the National Aeronautics and Space Administration (NASA) Fluid Microgravity Program under the direction of Dr. Walter Duval, by the Air Force Office of Scientific Research under the direction of Dr. Julian Tishkoff, and by the Army Research Office under the direction of Dr. David Mann, through interagency agreements with NASA. The computational resources were provided by the JPL Supercomputing Center. The authors would like to thank Dr. Kenneth Harstad of JPL for the transport property fits.

## Appendix. Transport properties for O<sub>2</sub>/He mixtures

For O<sub>2</sub>/He mixtures, the Prandtl number is approximated as

$$\text{Pr} = 0.68 + 0.0283\xi - 0.5017\xi^2 - 0.5390\xi^3 + \Delta \text{Pr} \quad (40)$$

where

$$\xi = \min(0.5, Y_2 - 0.81\theta^{0.35}), \quad \theta = (T - 100) / 800, \quad 0 \leq \theta \leq 1, \quad (T \text{ in Kelvin})$$

For  $0.02 \leq \theta \leq 0.368$ ,  $\Delta \text{Pr} = 2.42Y_2^{14.6} \max(0.0, -0.23(1 + \ln \theta))$ , otherwise  $\Delta \text{Pr} = 0$ .

For O<sub>2</sub>/He mixtures, the Schmidt number is approximated as

$$\begin{aligned} Sc &= \Sigma(Y_2) \left[ 1 + (114/T)^{1.5} \right] / (1 + \Delta_s) \\ T < 200\text{K}: \Sigma &= (1.292 - 0.757Y_2 + 0.444Y_2^2 - 0.757Y_2^3) \\ T > 200\text{K}: \Sigma &= (1.318 - 0.772Y_2 + 0.453Y_2^2 - 0.772Y_2^3) \end{aligned} \quad (41)$$

For  $p < 30$  MPa,  $\Delta_s = \min(0.08, 0.1264 + 0.226Y_R) + 0.1 \exp(-2400\theta^{4.5})$  where  $Y_R = Y_2 - \min(1, 0.5 + 0.78\theta^{0.6})$ , otherwise  $\Delta_s = 0$ .

## References

<sup>1</sup>Prausnitz, J., Lichtenthaler, R., and de Azevedo, E., *Molecular Thermodynamics for Fluid-Phase Equilibrium*, Prentice-Hall, 1986.

- <sup>2</sup>Hirshfelder, J., Curtis, C., and Bird, R., *Molecular Theory of Gases and Liquids*, John Wiley and Sons, 1964.
- <sup>3</sup>Chehroudi, B., Talley, D., and Coy, E., "Initial Growth Rate and Visual Characteristics of a Round Jet into a Sub- to Supercritical Environment of Relevance to Rocket, Gas Turbine and Diesel Engines," AIAA 99-0206, 37th AIAA Aerospace Sciences Meeting Conference and Exhibit, January 11-14, 1999, Reno, NV.
- <sup>4</sup>Mayer, W., Schik, A., Schweitzer, C., and Schaffler, M., "Injection and Mixing Processes in High Pressure LOX/GH<sub>2</sub> Rocket Combustors," AIAA 96-2620, AIAA/ASME/SAE/ASEE 32nd Joint Propulsion Conference, July 1-3, 1996, Lake Buena Vista, FL.
- <sup>5</sup>Mayer, W., Ivancic, B., Schik, A., and Hornung, U., "Propellant Atomization in LOX/GH<sub>2</sub> Rocket Combustors," AIAA 98-3685, AIAA/ASME/SAE/ASEE 34th Joint Propulsion Conference and Exhibit, July 13-15, 1998, Cleveland, OH.
- <sup>6</sup>Oschwald, M. and Schik, A., "Supercritical Nitrogen Free Jet Investigated by Spontaneous Raman Scattering," *Experiments in Fluids*, Vol. 27, 1999, pp. 497-506.
- <sup>7</sup>Miller, R., Harstad, K., and Bellan, J., "Direct Numerical Simulations of Supercritical Fluid Mixing Layers Applied to Heptane-Nitrogen," *Journal of Fluid Mechanics*, Vol. 436, 2001, pp. 1-39.
- <sup>8</sup>Okong'o, N. and Bellan, J., "Direct Numerical Simulation of a Transitional Supercritical Binary Mixing Layer: Heptane and Nitrogen," *Journal of Fluid Mechanics*, Vol. 464, 2002, pp. 1-34.
- <sup>9</sup>Okong'o, N. and Bellan, J., "Real Gas Effects of Mean Flow and Temporal Stability of Binary-Species Mixing Layers," *AIAA Journal*, Vol. 41, No. 12, December 2003, pp. 2429-2443.
- <sup>10</sup>Okong'o, N. and Bellan, J., "Turbulence and Fluid-Front Area Production in Binary-Species, Supercritical, Transitional Mixing Layers," *Physics of Fluids*, Vol. 16, No. 5, May 2004, pp. 1467-1492.
- <sup>11</sup>Keizer, J., *Statistical Thermodynamics of Nonequilibrium Processes*, Springer-Verlag, New York, 1987.
- <sup>12</sup>Harstad, K. and Bellan, J., "An All-Pressure Fluid-Drop Model Applied to a Binary Mixture: Heptane in Nitrogen," *International Journal of Multiphase Flow*, Vol. 26, No. 10, 2000, pp. 1675-1706.
- <sup>13</sup>Harstad, K. and Bellan, J., "Behavior of a Polydisperse Cluster of Interacting Drops Evaporating in an Inviscid Vortex," *International Journal of Multiphase Flow*, Vol. 23, No. 5, 1997, pp. 899-925.
- <sup>14</sup>Okong'o, N., Harstad, K., and Bellan, J., "Direct Numerical Simulations of O<sub>2</sub>/H<sub>2</sub> Temporal Mixing Layers Under Supercritical Conditions," *AIAA Journal*, Vol. 40, No. 5, May 2002, pp. 914-926.
- <sup>15</sup>Harstad, K. and Bellan, J., "Isolated Fluid Oxygen Drop Behavior in Fluid Hydrogen at Rocket Chamber Pressures," *International Journal of Heat and Mass Transfer*, Vol. 41, 1998, pp. 3537-3550.
- <sup>16</sup>Papamoschou, D. and Roshko, A., "The Compressible Turbulent Shear Layer: An Experimental Study," *Journal of Fluid Mechanics*, Vol. 197, 1988, pp. 453-477.
- <sup>17</sup>Moser, R. and Rogers, M., "Mixing Transition and the Cascade to Small Scales in a Plane Mixing Layer," *Physics of Fluids A*, Vol. 3, No. 5, 1991, pp. 1128-1134.
- <sup>18</sup>Moser, R. and Rogers, M., "The Three-Dimensional Evolution of a Plane Mixing Layer: Pairing and Transition to Turbulence," *Journal of Fluid Mechanics*, Vol. 247, 1993, pp. 275-320.
- <sup>19</sup>Okong'o, N. and Bellan, J., "Consistent Boundary Conditions for Multicomponent Real Gas Mixtures Based on Characteristic Waves," *Journal of Computational Physics*, Vol. 176, 2002, pp. 330-344.
- <sup>20</sup>Kennedy, C. and Carpenter, M., "Several New Numerical Methods for Compressible Shear Layer Simulations," *Applied Numerical Mathematics*, Vol. 14, 1994, pp. 397-433.
- <sup>21</sup>Muller, S. M. and Scheerer, D., "A Method to Parallelize Tridiagonal Solvers," *Parallel Computing*, Vol. 17, 1991, pp. 181-188.
- <sup>22</sup>Okong'o, N. and Bellan, J., "Consistent Large Eddy Simulation of a Temporal Mixing Layer Laden with Evaporating Drops. Part 1: Direct Numerical Simulation, Formulation and *A Priori* Analysis," *Journal of Fluid Mechanics*, Vol. 499, 2004, pp. 1-47.
- <sup>23</sup>Leboissetier, A., Okong'o, N., and Bellan, J., "Consistent Large-Eddy Simulation of a Temporal Mixing Layer Laden with Evaporating Drops. Part 2: *A Posteriori* Modeling," *Accepted, Journal of Fluid Mechanics*, 2004.
- <sup>24</sup>Smagorinsky, J., "Some Historical Remarks on the Use of Nonlinear Viscosities," *Large Eddy Simulation of Complex Engineering and Geophysical Flows*, edited by B. Galperin and S. Orszag, chap. 1, Cambridge University Press, 1993, pp. 3-36.
- <sup>25</sup>Yoshizawa, A., "Statistical Theory for Compressible Turbulent Shear Flows, With the Application to Subgrid Modeling," *Physics of Fluids*, Vol. 29, No. 7, 1986, pp. 2152-2164.
- <sup>26</sup>Clark, R., Ferziger, J., and Reynolds, W., "Evaluation of Subgrid-Scale Models Using an Accurately Simulated Turbulent Flow," *Journal of Fluid Mechanics*, Vol. 91, No. 1, 1979, pp. 1-16.
- <sup>27</sup>Bardina, J., Ferziger, J., and Reynolds, W., "Improved Subgrid Scale Models for Large Eddy Simulation," AIAA 80-1357, 1980.
- <sup>28</sup>Liu, S., Meneveau, C., and Katz, J., "On the Properties of Similarity Subgrid-Scale Models as Deduced from Measurements in a Turbulent Jet," *Journal of Fluid Mechanics*, Vol. 275, 1994, pp. 83-119.
- <sup>29</sup>Pruett, C., Sochacki, J., and Adams, N., "On Taylor-Series Expansions of Residual Stress," *Physics of Fluids*, Vol. 13, No. 9, September 2001, pp. 2578-2589.
- <sup>30</sup>Harstad, K. and Bellan, J., "The  $D^2$  Variation For Isolated LOX Drops and Polydisperse Clusters in Hydrogen at High Temperature and Pressures," *Combustion and Flame*, Vol. 124, No. 4, 2001, pp. 535-550.

# Vortex identification in high-pressure flows

N. A. Okong'o and J. Bellan

*Jet Propulsion Laboratory, California Institute of Technology, Pasadena, CA 91109-8099, USA and  
TEL: 1-818-354-6959, FAX: 1-818-393-6682, josette.bellan@jpl.nasa.gov*

(Dated: April 7, 2006)

High-pressure flows have distinctive visual features compared to low-pressure flows, particularly regions of high-pressure-gradient magnitude resulting both from dynamic turbulent effects and from thermodynamic mixing of species. Identifying a vortex may thus need a quantitative measure beyond that of visual observations. Several quantitative measures previously proposed for vortex identification are tested using an existing Direct Numerical Simulation database, and it is shown that the second invariant of the velocity-gradient tensor best captures the vortical features of the flow.

PACS: 47.27.Cn, 47.27.Eq

High-pressure flows occur in nature and in manufactured items; prominent examples are the flow in the atmosphere of Jupiter and other large gaseous planets, and diesel, gas turbine and rocket engines. Understanding the atmosphere of gaseous planets relies on measurements where the information consists mainly of visual and thermal images of the flow over the planet. Also, validation of recently proposed models of high-pressure flows [1–3] requires comparison with measurements, which are mainly of visual nature [4]. The interpretation of flow structures observed in these images is based on experience with low pressure flows, typically modeled as incompressible or compressible perfect-gas flows, whereas at high pressures the fluid might no longer behave as a perfect gas and will additionally exhibit significant variation in fluid properties such as density and temperature. Therefore, the identification of flow structures, in particular, vortices, based on low-pressure behavior may lead to misidentification in the high-pressure situation. In this study, we develop quantitative criteria for the identification of coherent structures, especially vortices, from previously generated flow field data, to complement or supersede the determination of flow structures by visual inspection of instantaneous fields or flow animations. The focus is on correlating visual images of flow features with various quantities computed from the flow field data.

The quantities considered are the deformation tensor,  $D_{ij} = u_{i,j} = \partial u_i / \partial x_j$ , the strain rate  $S_{ij} = (u_{i,j} + u_{j,i})/2$  and the rotation tensor  $\Omega_{ij} = (u_{i,j} - u_{j,i})/2$  which are the symmetric and anti-symmetric part of the deformation tensor, and the vorticity  $\omega_i = \epsilon_{ijk} u_{j,k}$ . Path lines and stream lines have also been used for vortex identification, but are not considered here as they are not Galilean invariant, i.e. they are reference-frame dependent. Besides magnitude, other quantities based on  $\mathbf{D}$ ,  $\mathbf{S}$  and  $\mathbf{\Omega}$  can be defined using matrix analysis. For a 3-by-3 matrix,  $\mathbf{A}$ , the characteristic equation

$$\gamma^3 - I_1 \gamma^2 + I_2 \gamma - I_3 = 0 \quad (1)$$

has 3 eigenvalues  $\gamma_i(\mathbf{A})$ , ordered as  $|\gamma_1| \leq |\gamma_2| \leq |\gamma_3|$ , where  $I_i(\mathbf{A})$  are the three invariants of  $\mathbf{A}$

$$I_1 = A_{ii}, \quad I_2 = (1/2)(I_1^2 - \text{tr}(\mathbf{A}^2)), \quad I_3 = \det \mathbf{A}. \quad (2)$$

The characteristic equation 1 can have (i) all real roots that are distinct, (ii) all real roots of which at least two are equal, or (iii) one real root and a conjugate pair of complex roots. Regions with complex roots are defined by  $\Delta(\mathbf{A}) > 0$ , where

$$\Delta = 27I_3^2 + (4I_1^3 - 18I_1I_2)I_3 + (4I_2^3 - I_1^2I_2^2) \quad (3)$$

is the discriminant of  $\mathbf{A}$ . Furthermore, if  $\mathbf{A}$  is symmetric, all its roots are real.

While the vorticity magnitude  $|\omega|$  might seem the most obvious indicator of vortical activity, subjective selection of the  $|\omega|$  values to isolate the structures of interest from near-wall or free-stream regions of high vorticity [5–7] makes this criterion arbitrary. Chong et al. [8] used  $\mathbf{D}$  to classify three-dimensional flow patterns defined by instantaneous streamlines for compressible and incompressible flow; they conclude that  $\Delta(\mathbf{D}) > 0$  in the vortex cores. For incompressible flow ( $I_1(\mathbf{D}) = u_{i,i} = 0$ ,  $I_2(\mathbf{D}) = -(1/2)u_{i,j}u_{j,i}$ ), Jeong and Hussain [5] propose that  $I_2(\mathbf{D}) > 0$  inside the vortex cores as a restriction of  $\Delta(\mathbf{D}) > 0$ . Jeong and Hussain [5] also used, for incompressible flow, the eigenvalues of the symmetric tensor  $\mathbf{S}^2 + \mathbf{\Omega}^2$  to identify a vortex. They argued that a local pressure minimum in a plane requires two positive eigenvalues of the pressure Hessian  $p_{,ij}$  which appears in the strain transport equation for incompressible flow

$$\frac{DS_{ij}}{Dt} - \nu S_{ij,kk} + \Omega_{ik}\Omega_{kj} + S_{ik}S_{kj} = -\frac{1}{\rho}p_{,ij}. \quad (4)$$

Neglecting the first two terms also appearing in that equation, they considered  $\Omega_{ik}\Omega_{kj} + S_{ik}S_{kj} = \mathbf{S}^2 + \mathbf{\Omega}^2$  to determine the existence of a local pressure minimum due to vortical motion. They identified the vortex core as a region with  $\Lambda_2 \equiv \gamma_2(\mathbf{S}^2 + \mathbf{\Omega}^2) < 0$ . Analysis of the strain transport equation for high-pressure flows with strong density gradients [9] reveals that the additional terms arising in compressible flow are in general non-negligible; moreover, the vortex cores no longer coincide with local pressure minima.

Therefore, there are four quantities that could potentially be used for identifying vortical features: (1) The discriminant of  $\mathbf{D}$ ,  $\Delta(\mathbf{D})$ ; (2) The second invariant of  $\mathbf{D}$ ,

$I_2(\mathbf{D})$ ; (3) The intermediate eigenvalue of  $\mathbf{S}^2 + \mathbf{\Omega}^2$ ,  $\Lambda_2$ ; and (4) The vorticity magnitude,  $|\omega|$ . Inside the vortex cores,  $\Delta > 0$  [8] and  $I_2 > 0$ ,  $\Lambda_2 < 0$  [5].

Comparative studies of these quantities for incompressible flows have yielded mixed results [6, 7, 10–12], with ensuing proposals for more complicated methods such as pressure-based schemes [6], non-local analysis [7], eigenvalue analysis [10] or strain-based analysis of fluid trajectories [11]. The assumptions underlying these schemes are based on incompressible flow, and have not been validated for compressible high-pressure flows. However, Grinstein [13] and Fureby and Grinstein [14] successfully performed flow visualizations for atmospheric-pressure compressible jets using iso-surfaces of  $|\omega|$  and  $\Lambda_2$ . While it is unlikely that a fully automatic feature identification scheme can be easily developed for high-pressure flows, aiding the interpretation of results by using flow visualization to isolate regions of unusual activity is a viable and worthwhile goal. In the present study, we plot iso-surfaces of the four listed quantities using a database of transitional states of a high-pressure mixing layer and assess their ability to demarcate flow structures from the background flow.

The database consists of direct numerical simulation (DNS) data of high-pressure binary-species temporal mixing layers undergoing transition to turbulence [2, 3]; the turbulence characteristics of the database, listed in Table I, have been previously been examined in detail [9]. The mixing layer has two counter-flowing streams, with species 1 in the upper stream and species 2 in the lower stream. The coordinates are: streamwise ( $x_1$ ), cross-stream ( $x_2$ ) and spanwise ( $x_3$ ). The boundary condi-

TABLE I: Simulation parameters for supercritical temporal mixing layer database

Run	HN500	HN600	HN800	OH500	OH750
Species 2	C <sub>7</sub> H <sub>16</sub>	C <sub>7</sub> H <sub>16</sub>	C <sub>7</sub> H <sub>16</sub>	O <sub>2</sub>	O <sub>2</sub>
Species 1	N <sub>2</sub>	N <sub>2</sub>	N <sub>2</sub>	H <sub>2</sub>	H <sub>2</sub>
$T_2$ (K)	600	600	600	235	400
$T_1$ (K)	1000	1000	1000	287	600
$\rho_2/\rho_1$	12.88	12.88	12.88	24.51	24.40
$p_0$ (atm)	60	60	60	100	100
$Re_0$	500	600	800	500	750
$\lambda_1/\delta_{\omega,0}$	7.29	7.29	4.57	10.61	7.29
$L_2$ (m)	0.232	0.232	0.148	0.284	0.200
$N_1$	240	288	240	352	352
$N_2$	288	336	272	352	352
$N_3$	144	176	144	208	208
$\Delta x/\delta_{\omega,0}$	0.122	0.102	0.076	0.122	0.084
$t_{trans}^*$	155	135	100	290	150
$Re_{m,trans}$	1250	1452	1258	1772	1507

All simulations have convective Mach number of 0.4,  $\delta_{\omega,0} = 6.86 \times 10^{-3}$  m,  $L_1 = 4\lambda_1$  and  $L_3 = 0.6L_1$ .  $L_i$  is the domain length and  $N_i$  is the number points in the  $x_i$ -direction,  $\Delta x = \max\{\Delta x_1, \Delta x_2, \Delta x_3\}$ ,  $t^* = t\Delta U_0/\delta_{\omega,0}$ .

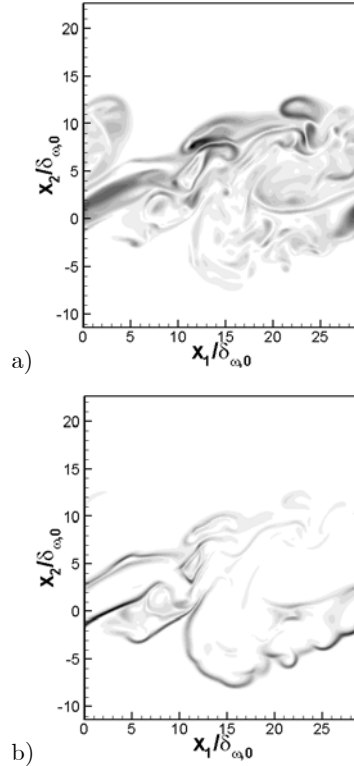


FIG. 1: Contours for HN600 in the  $x_3 = L_3/16$  plane: (a) vorticity magnitude and (b) density gradient magnitude.

tions are periodic in the  $x_1$ - and  $x_3$ -directions, and of outflow type for real gas in the  $x_2$ -direction [15]. The grid is chosen for all simulations so as to accommodate four wavelengths of the initially imposed vorticity perturbations, of wavelengths  $\lambda_1$  and  $\lambda_3 = 0.6\lambda_1$  in the  $x_1$ - and  $x_3$ -directions respectively, and the evolution of the layer encompasses roll-up and two pairings of the four initial spanwise vortices into an ultimate vortex. The layer is not symmetric in extent in the  $x_2$ -direction, to accommodate the larger layer growth in the lighter fluid side. The free-stream density ( $\rho_1$  or  $\rho_2$ ) is calculated for each pure species at its free-stream temperature ( $T_1$  or  $T_2$ ) and at the initial uniform pressure ( $p_0$ ). Error-function profiles are used for the initial mean streamwise velocity, mass fraction and temperature. The vorticity thickness is defined as  $\delta_\omega(t) = \Delta U_0 / (\partial \langle u_1 \rangle / \partial x_2)_{max}$  where  $\langle u_1 \rangle$  is the  $(x_1, x_3)$  planar average of the streamwise velocity, and  $\Delta U_0 = U_1 - U_2$  is the velocity difference across the layer.  $U_1$  and  $U_2$  are selected to keep the ultimate vortex stationary in the computational domain [1, 16, 17]. The specified value of the initial flow Reynolds number,  $Re_0 = (1/2)(\rho_1 + \rho_2)\Delta U_0\delta_{\omega,0}/\mu_R$  is used to calculate the reference viscosity  $\mu_R$ . The grid spacing is an approximately linear function of  $Re_0$ , and the number of nodes is high enough to resolve all flow scales [2, 3]. The momentum thickness-based Reynolds number,  $Re_m = Re_0\delta_m/\delta_{\omega,0}$ , listed in Table I at the transitional times,  $t_{trans}^*$ , is larger than that typical of

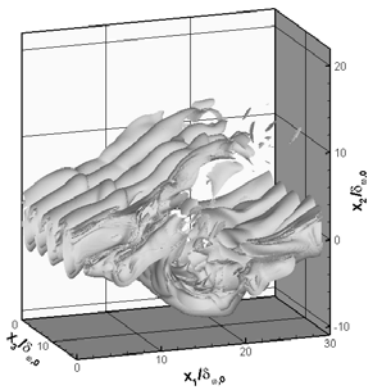


FIG. 2: Iso-surfaces for HN600: density gradient magnitude (at 10% of maximum value).

the laminar regime.

The transitional states of the flow contain vortical structures found in fully turbulent flow, as well as high density gradient structures which are created both by the distortion of the initial density interface between the two streams and by mixing of the fluid in the two streams (Fig. 1), depicting a flow similar to that experimentally visualized at the edge of round jets [4]. The three-dimensional counterpart of the density-gradient-magnitude of Fig. 1 is plotted in Fig. 2. The four vortex identification methods discussed above were examined using the DNS database and selected iso-surfaces of the four quantities are plotted in Fig. 3.

The criteria  $\Delta > 0$  (Fig. 3a) and  $\Lambda_2 < 0$  (Fig. 3c)

yield only a few small localized structures. In contrast, plotting iso-surfaces of  $I_2 > 0$  (Fig. 3b) yields structures distributed throughout the layer; the long thin structures correspond to the initial streamwise vortices that have been distorted by the flow and lie along the high-density-gradient magnitude regions. Shorter structures with a more random orientation indicate turbulence within the flow. Structures identified using iso-surfaces of  $|\omega|$  (Fig. 3d) appear to be confined to the edges of the layer and seem to be a subset of those in Fig. 3b. In comparing the four methods, the  $I_2 > 0$  method appears to produce the most realistic structures, and seems to capture structures in all regions of the flow.

Illustrated in Fig. 4 are vortical features from several simulations listed in Table I; the vortical features are identified using the second invariant criterion. The diversity of the features is noticeable. This bodes well on the ability of this method to distinguish specific features of the flow, and thus to both be able to extract vortical features from visual data and to enable appropriate comparisons between experiments and numerical simulations for the purpose of model validation.

This work was conducted at the Jet Propulsion Laboratory (JPL), California Institute of Technology (Caltech) and sponsored by the National Aeronautics and Space Administration (NASA). Portions of the iso-surface generation program were developed at the National Center for Supercomputing Applications at the University of Illinois at Urbana-Champaign. Computations were performed at the JPL Supercomputing Center.

- 
- [1] R. Miller, K. Harstad and J. Bellan, "Direct Numerical Simulations of supercritical fluid mixing layers applied to heptane-nitrogen," *J. Fluid Mech.* **436**,1-39 (2001).
  - [2] N. Okong'o and J. Bellan, "Direct Numerical Simulation of a transitional supercritical binary mixing layer: heptane and nitrogen," *J. Fluid Mech.* **464**,1 (2002).
  - [3] N. Okong'o, K. Harstad and J. Bellan, "Direct numerical simulations of O<sub>2</sub>/H<sub>2</sub> temporal mixing layers under supercritical conditions," *AIAA Journal* **40**(5), 914 (2002).
  - [4] B. Chehroudi, D. Talley and E. Coy, "Visual characteristics and initial growth rates of round cryogenic jets at subcritical and supercritical pressures," *Phys. Fluids* **14**(2), 850 (2002).
  - [5] J. Jeong and F. Hussain, "On the identification of a vortex," *J. Fluid Mech.* **285**, 69 (1995).
  - [6] S. Kida and H. Miura, "Identification and analysis of vortical structures," *European Journal of Mechanics B, Fluids*, **17**(4), 471 (1998).
  - [7] R. Cucitore, M. Quadrio and A. Baron, "On the effectiveness and limitations of local criteria for the identification of a vortex," *European Journal of Mechanics B, Fluids*, **18**(2), 261 (1999).
  - [8] M. S. Chong, A. E. Perry and B. J. Cantwell, "A general classification of three-dimensional flow fields," *Phys. Fluids A* **2**(5), 765 (1990).
  - [9] N. Okong'o and J. Bellan, "Turbulence and fluid-front area production in binary-species, supercritical, transitional mixing layers", *Phys. Fluids* **16**(5), 1467 (2004).
  - [10] K. Horiuti, "A classification method for vortex sheet and tube structures in turbulent flows," *Phys. Fluids* **13**(12), 3756 (2001).
  - [11] G. Haller, "An objective definition of a vortex," *J. Fluid Mech.* **525**, 1 (2005).
  - [12] J.-Z. Wu, A.-K. Xiong and Y.-T. Yang, "Axial stretching and vortex definition," *Phys. Fluids* **17**, 038108 (2005).
  - [13] F. F. Grinstein, "Vortex dynamics and entrainment in rectangular free jets," *J. Fluid Mech.* **437**, 69 (2001).
  - [14] C. Fureby and F. Grinstein, "Large Eddy Simulation of high-Reynolds-number free and wall-bounded flows," *J. Comp. Phys.* **181**, 68 (2002).
  - [15] N. Okong'o and J. Bellan, "Consistent boundary conditions for multicomponent real gas mixtures based on characteristic waves," *J. Comp. Phys.* **176**, 330 (2002).
  - [16] D. Papamoschou and A. Roshko, "The compressible turbulent shear layer: An experimental study," *J. Fluid Mech.* **197**, 453 (1988).
  - [17] N. Okong'o and J. Bellan, "Real gas effects of mean flow and temporal stability of binary-species mixing layers," *AIAA Journal* **41**(12), 2429 (2003).

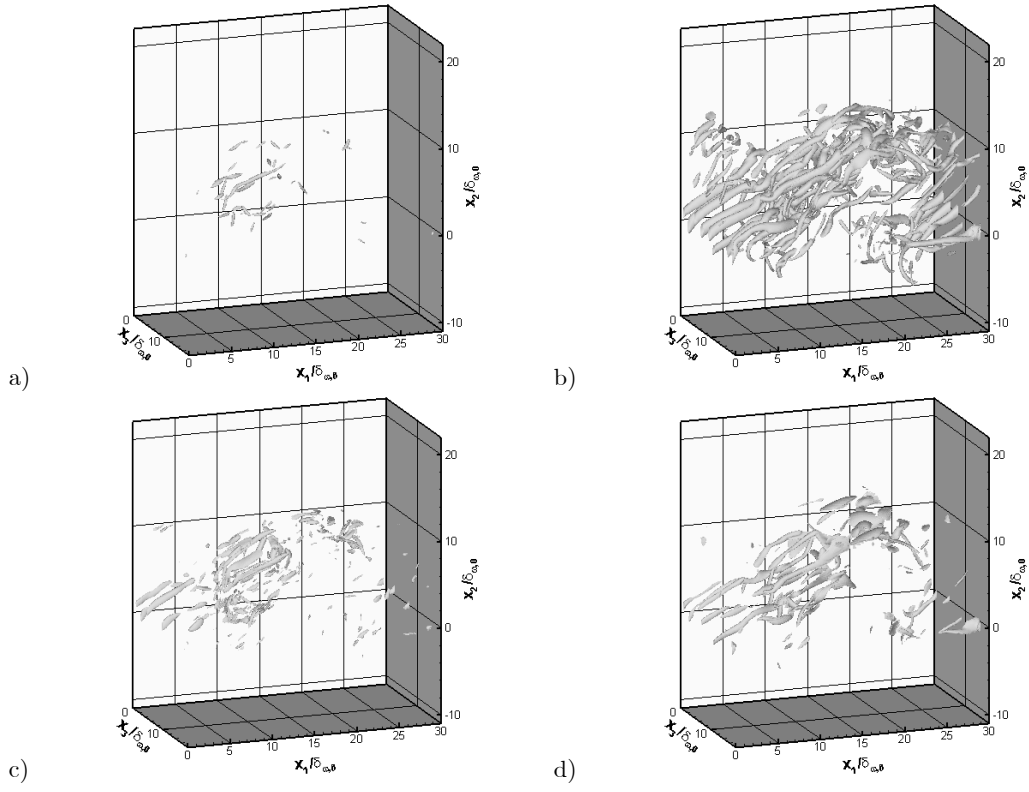


FIG. 3: Iso-surfaces for HN600: a)  $\Delta > 0$ , b)  $I_2 > 0$ , c)  $\Lambda_2 < 0$ , and d)  $|\omega|$  (at 20% of maximum value). Levels are:  $\Delta (\delta_{\omega,0}/\Delta U_0)^6 = 9.14 \times 10^{-3}$ ,  $I_2 (\delta_{\omega,0}/\Delta U_0)^2 = 0.10$ ,  $\Lambda_2 (\delta_{\omega,0}/\Delta U_0)^2 = -1.83 \times 10^{-2}$ ,  $|\omega|^2 (\delta_{\omega,0}/\Delta U_0)^2 = 1.4711$ .

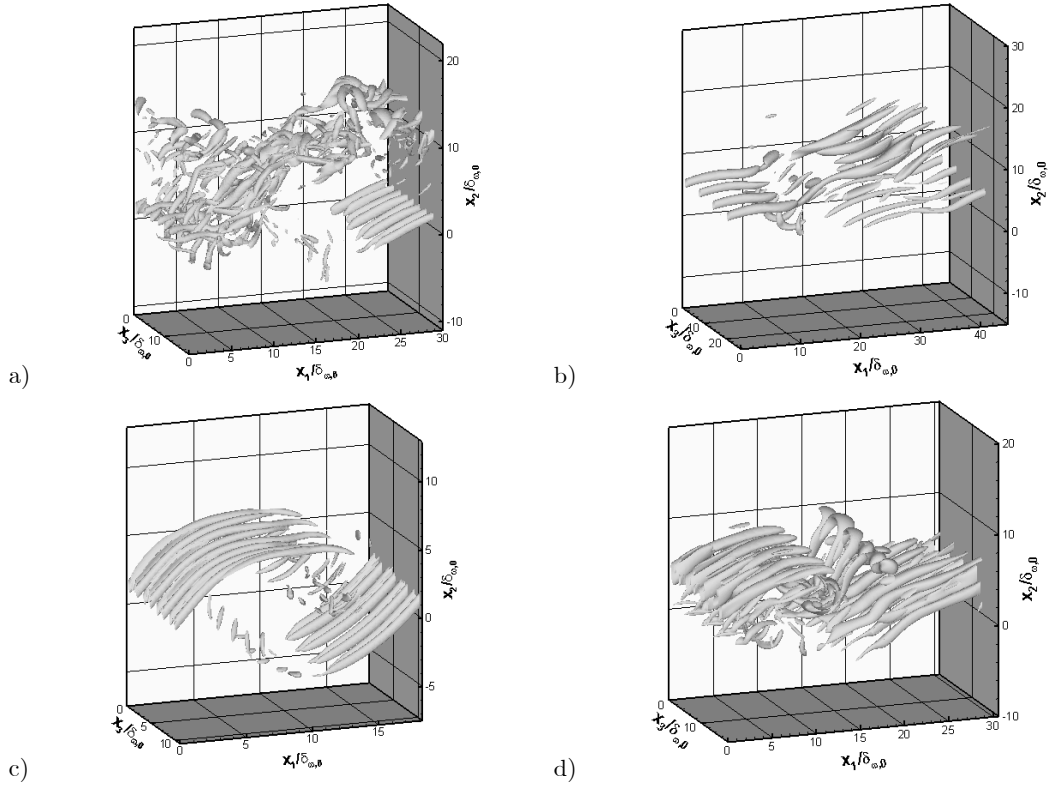


FIG. 4: Iso-surfaces of  $I_2 > 0$ : (a) HN500, (b) OH500, (c) HN800, and (d) OH750. Levels are  $I_2 (\delta_{\omega,0}/\Delta U_0)^2 = 0.07$ (HN500),  $0.12$ (HN800),  $0.016$ (OH500),  $0.018$ (OH750).

**AFRL-PR-ED-TR-2006-0040**  
**Primary Distribution of this Report:**

AFRL/PRSA (3 CD + 2 HC)  
Douglas G. Talley  
104 N. Mercury Blvd.  
Edwards AFB CA 93524

ERC, Inc. (1 CD + 1 HC)  
Dustin W. Davis  
104 N. Mercury Blvd.  
Edwards AFB CA 93524

ERC, Inc. (1 CD + 1 HC)  
Bruce Chehroudi  
104 N. Mercury Blvd.  
Edwards AFB CA 93524

Jet Propulsion Laboratory (1 CD + 1 HC)  
Josette Bellan  
4800 Oak Grove Drive  
Pasadena CA 91109

Jet Propulsion Laboratory (1 CD + 1 HC)  
Nora Okong'o  
4800 Oak Grove Drive  
Pasadena CA 91109

AFRL/PR Technical Library (2 CD + 1 HC)  
6 Draco Drive  
Edwards AFB CA 93524-7130

Chemical Propulsion Information Agency (1 CD)  
Attn: Tech Lib (Dottie Becker)  
10630 Little Patuxent Parkway, Suite 202  
Columbia MD 21044-3200

Defense Technical Information Center  
(1 Electronic Submission via STINT)  
Attn: DTIC-ACQS (Pat Mawby)  
8725 John J. Kingman Road, Suite 94  
Ft. Belvoir VA 22060-6218